Nano- and Micro-Fabrication for Single-Molecule Biological Studies

Proefschrift

ter verkrijging van de graad van doctor
aan de Technische Universiteit Delft,
op gezag van de Rector Magnificus prof. ir. K.C.A.M. Luyben,
voorzitter van het College voor Promoties,
in het openbaar te verdedigen op dinsdag 16 oktober 2012 om 15.00 uur
door

Zhuangxiong HUANG

Magistri in Scientia

geboren te Raoping, Guangdong, China.

Dit proefschrift is goedgekeurd door de promotor:
Prof. dr. N.H. Dekker

Samenstelling promotiecommissie:

Rector Magnificus,	voorzitter
Prof. dr. N.H. Dekker,	Technische Universiteit Delft, promotor
Prof. dr. C. Dekker,	Technische Universiteit Delft
Prof. dr. P.M. Sarro,	Technische Universiteit Delft
Prof. dr. G.J.L. Wuite,	Vrije Universiteit Amsterdam
Dr. E. Schäffer,	Technische Universität Dresden
Dr. E.W.J.M van der Drift,	Technische Universiteit Delft
Dr. E.A. Abbondanzieri,	Technische Universiteit Delft

Keywords: nanofabrication, surface functionalization, single molecule techniques, zero-mode waveguides, fluorescence microscopy, birefringent particles, optical torque wrench, micromirror, 3D tracking, microfluidics.

Casimir PhD series, Delft-Leiden 2012-24
ISBN: 978-90-8593-132-4

Printed: Proefschriftmaken.nl || Uitgeverij BOXPress

Contents

Chapter 1

Introduction

Over the last decade, single-molecule techniques have proven their wide applicability in the study of biological systems. Single-molecule techniques have the potential to overcome the limitations associated with conventional bulk techniques. Observing a single molecule allows for the exploration of the concealed heterogeneity of the system (this scenario can be compared to a triangular prism dispersing a light passing through it, see Figure 1), direct observation of dynamical state changes without required synchronization, as well as detection in many unexplored regimes (e.g. fluctuating behaviors) that are measurable only in single/few-molecule systems. This offers the opportunity to study the detailed dynamics of complex biological systems and to address many questions inaccessible at the bulk level. In addition, a single-molecule experiment, as its name implies, in principle requires just minute quantities of samples to study.

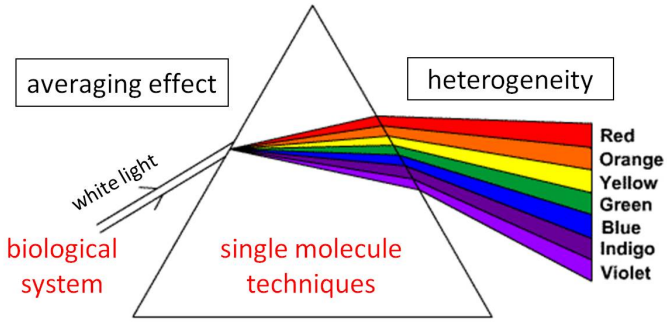

Figure 1. Single-molecule techniques can be compared to a triangular prism dispersing a light passing through it. As known to us, white light is actually color; it's an averaging effect from different single colors. So averaging is sometimes misleading and even cheating. This is also often the case in biological studies. Heterogeneity is a general feature in biological system; therefore it is very important to look into individuals for details in order to ensure a correct understanding of the biological system. Single-molecule techniques are therefore required for this purpose.

Single-molecule techniques typically make use of tools that consist of essential parts at nano- and micro-meter scale, which is in general determined by the size of single biomolecule or single cell to be investigated. This reasoning could be understood from our daily life experience, as illustrated in Figure 2.

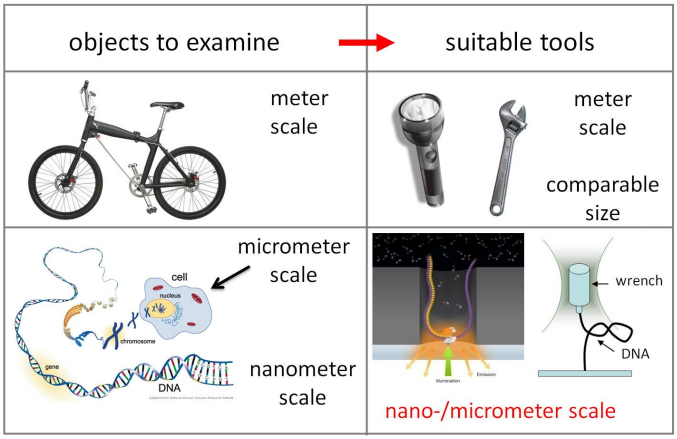

Figure 2. Reasoning of why single-molecule biological studies require tools at nano- and micro-meter scale can be found from our daily life experience: in order to examine and fix objects such as bike, we need tools with size comparable to the size of parts to be examined on the objects. Similarly, in order to manipulate a cell or single biomolecule for instance DNA, we need tools that have comparable size, which is in the range of nanometer to micrometer. In other words, nano- and micro-meter scale structures are the most suitable physical tools for manipulate and study single molecules and single cells.

In general, nano- and micro-structures can be fabricated using modern nanolithography techniques. Figure 3 shows a peek into our in-house nanolithography facility. All the nano- and micro-structures that will be presented in this thesis were fabricated using this facility.

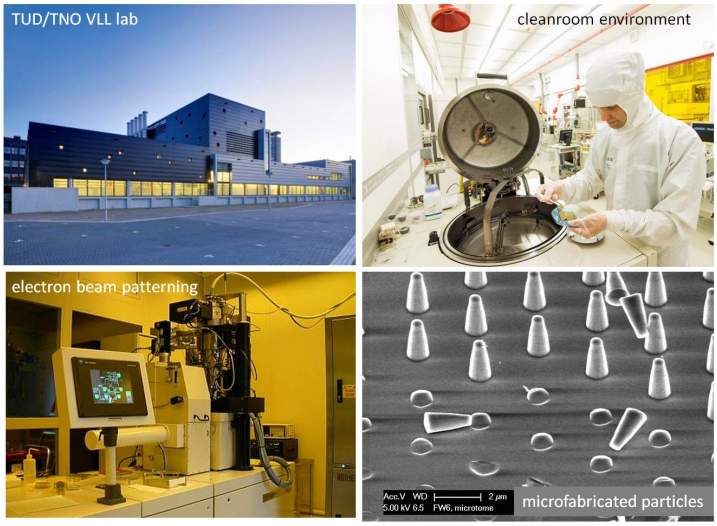

Figure 3. Our in-house nanolithography facility: Van Leeuwenhoek Laboratory co-founded by TNO and TU Delft (*top-left*). It has a cleanroom environment of class 10000 (*top-right*). It is equipped with an electron beam patterning machine (*bottom-left*), which is the most essential element of nanolithography. (*bottom-right*) an example of nano- and micro-structures fabricated using this facility.

The nano- and micro-structures that I've developed for single-molecule biological studies can be divided into two categories (as illustrated in Figure 4): one is for visualization and imaging; the other is for manipulation, measurement, probing and sensing. Generally speaking, my main contributions to the works involving these nano- and micro-structures are as following: first, I designed and fabricated these structures, and functionalized their surfaces to interface with biological systems under investigation. In addition, I have developed various theoretical models for calibration and optimization of the structures, and for proper use of them. Last but not least, I have also been involved in construction of the setups in which these structures are used.

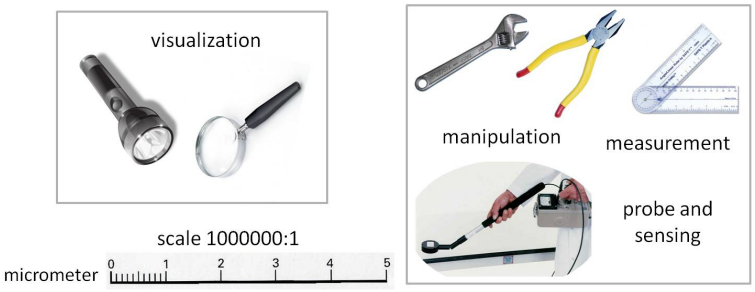

Figure 4. My categories of nano- and micro-meter scale structures for single-molecule biological studies. Imitations of daily tools are presented for understanding of applications of the structures I developed.

For the category of visualization/imaging, I have developed zero-mode waveguides for single-molecule fluorescence study of DNA polymerizing enzymes (Figure 5, *left*), and V-groove micromirrors for 3D tracking of single molecules/particles (Figure 5, *right*).

A zero-mode waveguide (Figure 5, *top-left*) is just a tiny hole in metal cladding layer on a glass coverslip. This hole is so small that illumination light cannot propagate through this hole. In such way a very tiny evanescent field is confined around the bottom [1, 2]. Zero-mode waveguide has been used in commercial DNA sequencer (PacBio, CA, USA) to visualize individual incorporation of dye-labeled nucleotides [1]. In our project (Figure 5, *bottom-left*), we are interested to study an important enzyme called telomerase, which is involved in most cancer diseases. Similar to DNA sequencer, we plan to study the kinetics of the enzyme by visualizing individual labeled nucleotides being incorporated. In order to detect the signal of the single labeled nucleotide being incorporated, the background noise level due to the fast diffusing free labeled nucleotides should be much lower than the signal. This set the upper limit of the concentration of labeled nucleotides that can be used for a given size of illumination spot. Zero-mode waveguides can confine the illumination spot so small that we can apply biologically-relevant high concentration of the labeled nucleotides while keeping the background level low, which is required for a meaningful study of telomerase enzyme, and is very difficult to achieve by conventional fluorescent techniques. The progress I have made so far towards single-molecule fluorescence studies of telomerase kinetics in zero-mode waveguides will be presented in Chapter 2.

V-groove micromirror (Figure 5, *top-right*) has been used for 3D imaging and particle tracking [3]. In 3D visualization, the precision in z localization is usually much worse

compared to the localization in x-y plane. A straightforward solution to this problem is to project z-axis to a horizontal axis through a micromirror; in such way the precision in z localization will be improved to be comparable to the localization in horizontal plane. In our lab, we are mainly interested in combing micromirror with magnetic tweezers so that biological events along DNA can also be visualized (Figure 5, *bottom-right*). As will be presented in Chapter 3, I have developed a perfect 45 degree micromirror for such purpose. In addition, we have also been developing a novel method for particle localization in micromirror with improved precision.

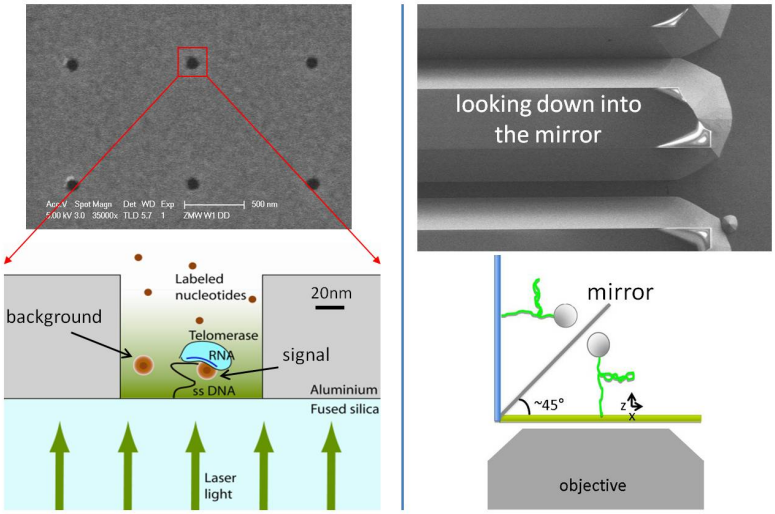

Figure 5. Nano- and micro-structures for visualization and imaging of single biomolecules. (*left*) Zero-mode waveguide: (*top-left*) SEM image of ZMW device, and (*bottom-left*) experimental configuration of using ZMW for single-molecule fluorescent studies of telomerase. (*right*) V-groove micromirror: (*top-right*) SEM image of V-groove micromirror device, and (*bottom-right*) experimental configuration of combing a micromirror with magnetic tweezers for visualization of biological events along DNA.

For category of manipulation, measurement, probing and sensing, the nano- and micro-structures that I have developed includes PDMS-based microfluidic device for live-cell immobilization and imaging (Figure 6, *left*), and birefringent microcylinders used in optical torque wrench for torsional manipulation and measurement of single biomolecules and for sensing (Figure 6, *right*).

PDMS-based microfluidic device has been used to restrict movement of E. coli cells for the study of cell growth and death [4]. This type of study requires hours and even days of continuous imaging. Therefore, the movement of cells should be restricted otherwise the cells would swim away from the field of view in seconds. A challenge is to develop a method to restrict movement of E. Coli cells without disturbing their activities. Surface chemical adhesion of cells is difficult to meet this requirement. Therefore, we have developed a PDMS microstructure (Figure 6, *left*), which consist of channels with width slightly smaller than the cell diameter, so that cells will be mechanically clamped and the movement will be greatly restricted in the channels. As will be demonstrated later, the cells in these channels are indeed

able to grow and divide. Our microfluidic devices are fabricated using electron beam lithography, as this provides excellent control over the shape and size of growth channels in a wide range required to study a variety of (sub) micron-sized bacterial species. This will be the content of discussion in Chapter 4.

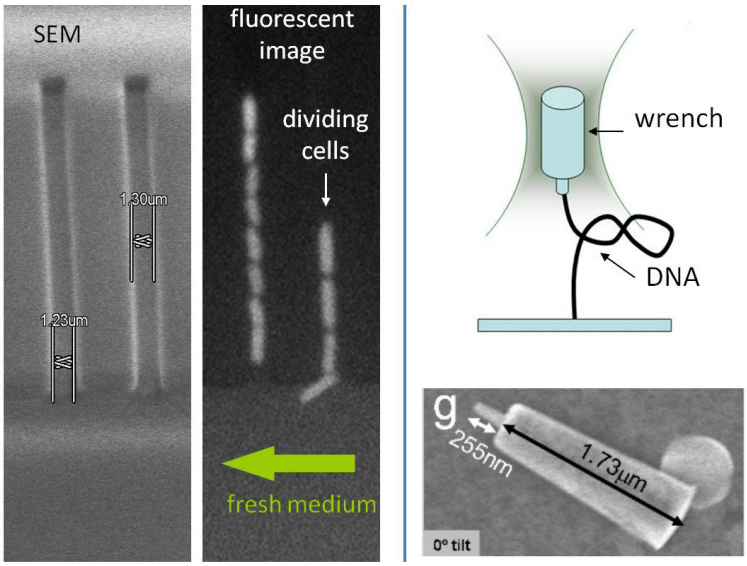

Figure 6. Nano- and micro-structures for manipulation, measurement, probing and sensing. (*left*) PDMS-based microfluidic channels for live-cell immobilization and imaging: SEM image of the device and fluorescent movie of growing cells immobilized in the microfluidic channels. (*top-right*) A typical experimental configuration of optical torque wrench using a birefringent dielectric particle for single-molecule biophysical studies. (*bottom-right*) SEM image of a fabricated birefringent quartz microcylinder.

The Optical Torque Wrench (OTW) is a special type of optical tweezers that uses birefringent dielectric particles [5], and has proved to be one of the most promising tools for torsional manipulation and torque measurement of single biomolecules [6, 7]. Optical tweezers uses a laser focus spot to trap a micron-sized dielectric particle. In a typical experimental configuration for biophysical study, a single biomolecule is attached to a dielectric particle in optical trap; by moving the focus spot, the particle can be moved, and therefore the biomolecule can be manipulated and measured. The main difference between OTW and conventional optical tweezers is that OTW uses a birefringent dielectric particle, which can be rotated by controlling the polarization of trapping laser, and therefore is able to apply and measure torque on the biomolecule attaching to the particle. As shown in Figure 6 (*right panel*), typically birefringent particle is fabricated into cylinder shape [6, 7], so that the long axis of the cylinder will align with the direction of laser propagation in optical trap. Also the extraordinary optical axis is designed to be perpendicular to cylinder's long axis, so that when the laser polarization is rotated, the cylinder will follow, and thus the biomolecule attached to the cylinder can be twisted. I have developed protocols for fabrication and surface functionalization of birefringent microcylinders (Chapter 5 and Chapter 8) [7]. In addition, I

have also developed the theory for setup calibration (Chapter 6) [8] and for understanding of the kinetics of trapped microcylinders in OTW (Chapter 6 - 8) [8, 9]. Furthermore, on the basis of understanding this kinetic feature, we have devised and demonstrated that birefringent microcylinder in OTW can also be used for probing and sensing environmental parameters, and for detecting single perturbation events with high signal-to-noise ratio and adjustable sensitivity (Chapter 7) [9]. Last but not least, progress, experimentally and theoretically, towards the study of single flagellar motor using OTW will be discussed in Chapter 8.

References

1 Eid, J., et al., Real-Time DNA Sequencing from Single Polymerase Molecules. Science, 2009. 323(5910): p. 133-138.

2 Crut A., et al., Controlling the surface properties of nanostructures for single-molecule studies of polymerases. Nanotechnology, 2008. 19, 465301.

3 McMahon MD, et al., 3D Particle Trajectories Observed by Orthogonal Tracking Microscopy. ACS Nano, 2009. 3 (3), pp 609–614.

4 Wang P., et al., Robust Growth of Escherichia coli. Current Biology, 2010. 20:1099-1103.

5 La Porta A., et al., Optical Torque Wrench: Angular Trapping, Rotation, and Torque Detection of Quartz Microparticles. Phys. Rev. Lett. 2004. 92: 190801.

6 Deufel C., et al., Nanofabricated quartz cylinders for angular trapping: DNA supercoiling torque detection. Nature Methods, 2007. 4: 223 – 225.

7 Huang Z., et al., Electron Beam Fabrication of Micron-Scale Birefringent Quartz Cylinders for Use in Optical Trapping. ACS Nano, 2011. 5:1418–1427.

8 Pedaci F., et al., Calibration of the optical torque wrench. Optics Express, 2012. 20:3787-3802.

9 Pedaci F., et al., Excitable Particles in an Optical Torque Wrench. Nature Physics, 2011. 7:259–264.

Chapter 2

Nano-Fabrication and the Surface Treatment of Zero-Mode Waveguides towards Single-Molecule Fluorescence Studies of Telomerase

Zhuangxiong Huang, Yun-Hsuan Chen, Aurélien Crut, Daniel A. Koster, Susanne Hage,

Serge Donkers and Nynke Dekker

Telomerase is an important ribonucleoprotein reverse transcriptase involved in cancers and aging problems. However, the elementary kinetics of this enzyme has not yet been clearly unveiled, mainly due to the disadvantage of the bulk techniques available for telomerase studies. Zero-mode waveguide (ZMW) is a powerful technique for studying single-molecule dynamics at biologically-relevant concentrations. Employing this technique, we might be able to investigate the molecular kinetics of telomerase and address the questions inaccessible in bulk experiments. In this chapter, I will discuss the preliminary experiments that we have done aiming towards the assay of telomerase kinetics in ZMWs: Optical setup for telomerase assay using ZMWs has been constructed. ZMW have been successfully fabricated and characterized. A method for surface treatment of ZMW has been developed in order to make ZMW able to tether DNA substrates for telomerase assay, and more importantly able to reduce the non-specific transient adsorption of labeled nucleotides. The telomerase activity with labeled nucleotides has also been demonstrated.[*]

[*] Part of this chapter has been published as A. Crut, D.A. Koster, Z.-X. Huang, S. Hage, and N.H. Dekker, *Nanotechnology* **19**, 465301 (2008).

2.1 Introduction

Telomeres & Telomerase

During cell division, the genomic information stored in a parent cell's chromosomes must be replicated and propagated to each daughter cell. The replication process, in which the genetic material of each chromosome is duplicated, is faithfully carried out by an enzyme called DNA polymerase. In most prokaryotes, chromosomes are circular and the DNA replication can be completed without any problem. In contrast, for eukaryotes in which the genetic material is stored in linear form, the replication of chromosome is by nature incomplete, since DNA polymerases are incapable to start at the exact extremity of DNA. As shown in **Figure 1**, the replication of parent DNA (black strands) requires a RNA primer (pink) binding to the very end of each strand. This RNA primer will finally be removed, resulting in a shorter daughter DNA (blue).

Consequently, eukaryotes suffer attrition of DNA sequences from the ends of their chromosomes with every cell cycle. Without some other mechanism, such attrition would eventually lead to loss of genetic information, halting cell division. This is known as the DNA end-replication problem (**Figure 1**) [1].

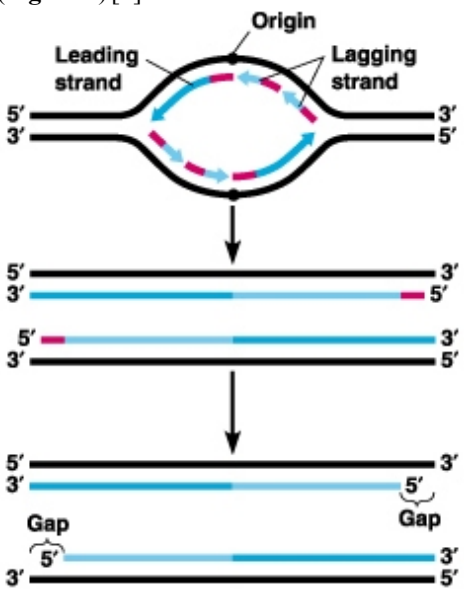

Figure 1. DNA end-replication problem. Replication of the parent DNA (black strands) occurs within replication bubbles initiated around replication origins encoded in DNA sequence. DNA replication requires RNA primers (pink) and is performed by polymerases in the 3'->5' direction. As the replication bubble grows, RNA primers unbind and are replaced by DNA, except the only one remaining at the 5' end of each daughter DNA molecule (blue). The unbinding of these two primers results in a gap that polymerases cannot fill. Therefore, both daughter DNA molecules generated are shorter than the parent molecule.

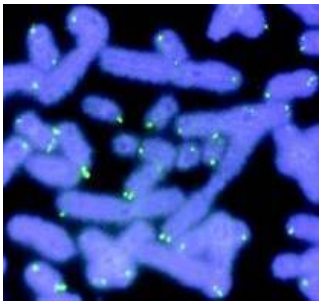

Figure 2. Telomeres (green) are the ends of chromosomes (blue). [edited from Ref. 22]

The identification of telomere structure and the discovery of the telomerase enzyme by Greider and Blackburn [2] made clear how cells overcome the end-replication problem. The ends of the eukaryotic chromosomes (**Figure 2**, shown in green), known as telomeres, (which comes from Greek – telos meaning "end" and meros meaning "part") [3] are actually elongated by an RNA-templated DNA polymerase called telomerase.

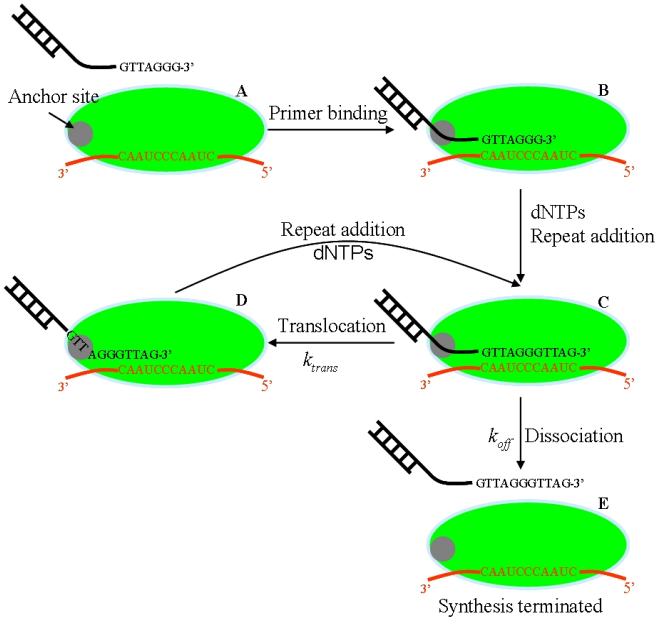

Figure 3. Mechanism of the action of human telomerase. [edited from Ref. 8] (A) Telomerase enzyme (green oval), RNA template (shown in red), and chromosomal terminus (shown in black). (B) Telomeric DNA binds to telomerase by base pairing with the templating domain sequence of the telomerase RNA, plus additional interaction with the telomerase anchor site. (C) Telomerase extends the telomeric DNA by polymerization of dNTPs using its RNA template. (D) Translocation of the extended DNA product to a new position allows synthesis of telomeric repeats. (E) The extended DNA product dissociates from telomerase and the synthesis process is terminated.

The telomeres consist of tandem repeats of a non-coding sequence, functioning as a disposable buffer to protect the genome. The exact sequence of the telomere repeats (5'-TTAGGG in all vertebrates) is determined by the inner RNA template (**Figure 3**, sequence within the red strand) that telomerase (**Figure 3**, green oval) uses to extend DNA (**Figure 3**, black strand). This mechanism restores the chromosome ends that were shortened during DNA replications [3 - 21].

In cells containing active telomerase, such as germ-line cells, the lengthening and shortening processes are largely kept in balance, and the telomere length homeostasis is regulated by telomere-binding proteins [14]. However, telomerase is not active in most human somatic tissues [11]. Therefore, normal human cells typically undergo a finite number of cells divisions and ultimately enter a non-dividing state called replicative senescence. In other words, we are destined to age. It has been demonstrated that the life-span of normal human cells can be extended at least 20 times longer by introduction of telomerase into these cells [18], which also has important implications for biological and medical research.

However, having active telomerase in cells is not necessarily good in all circumstances. Although telomerase plays a crucial role in normal cell growth, it has also been implicated in many cancers. More than eighty percent of cancer cells have an overabundant supply of telomerase, which allows them to continue dividing forever. Cancerous cells are therefore effectively immortal, and their constant multiplication leads to the formation of tumors [3, 11, 12, 19, 23]. For this reason, telomerase inhibition has been viewed as a promising way to limit cancer cell division and tumor production [11, 23].

Telomerase Kinetics

Since telomerase is a crucial target for cancer therapy and age-related disease treatment, the detailed study of its action at the molecular level has attracted a great deal of attention and played an important part in the research of the biological function of telomere and telomerase [21].

As shown in **Figure 3**, the proposed mechanism of human telomerase [8, 10, 21, 24] involves initial binding of telomeric DNA to the active site by base-pairing with the RNA template and an additional interaction with the anchor site on the protein component of telomerase. Nucleotides in a sequence complementary to the RNA template are then incorporated into the DNA until the telomeric DNA is elongated to the 5'-boundary of the template* (**Figure 3**(C)). This template boundary is the position at which the extended DNA is most likely to either dissociate from the telomerase (rate constant: k_{off}), terminating the synthesis (**Figure 3**(E)), or translocate back to the beginning position of the RNA template

* Strictly speaking, before reaching the 5'-boundary and translocation back to the beginning position of the RNA template (type II translocation), the DNA product can also (i) dissociate from the enzyme, (ii) stay bound without further elongation, (iii) be shifted, together with the RNA template, to accommodate the addition of the next nucleotide (This is called type I translocation, distinguishing from the type II translocation in which DNA re-positions relative to the RNA template)[21].

(rate constant: k_{trans}), starting next cycle of DNA synthesis (**Figure 3**(D)). The probability of the telomerase dissociating from a given DNA per telomeric repeat synthesized is usually referred to as telomerase's "repeat addition processivity" [8, 25, 26], which is about 0.3~0.4 for human telomerase in vitro [8, 25]. Repeat addition processivity is one of the most important parameters to characterize the length distribution of DNA products extended by human telomerase.

Despite its importance, to date, studying the dynamics of telomerase in detail has proved difficult. Numerous bulk biochemical approaches have been reported [24, 27, 28], but these techniques are limited to studying the average behavior produced by a large number of reactants. Since these many parallel reactions are not easily coordinated, quantifying the dynamics from a mixture of extended products with varying lengths remains challenging. In addition, correctly assembling and purification of a large amount of active enzymes, as usually required in bulk biochemical assays, also faces great challenges.

Single-Molecule Techniques

Single-molecule techniques have the potential to overcome the limitations associated with bulk techniques in studies of telomerase kinetics. Observing a single molecule allows for the exploration of the concealed heterogeneity of the system, direct observation of dynamical state changes without required synchronization, as well as detection in many unexplored regimes (*e.g.* fluctuating behaviors) that are measurable only in single/few-molecule systems. This offers the opportunity to study the detailed dynamics of complex systems and to address many questions inaccessible at the bulk level. In addition, a single-molecule experiment, as its name implies, in principle requires just minute quantities of active enzyme.

Nowadays, several approaches allow the observation and/or manipulation of individual bio-molecules. Examples of these approaches include Atomic Force Microscopy (AFM) [29], magnetic tweezers [30], optical tweezers [31], and fluorescence microscopy [32-35], *etc.* The choice of the most appropriate technique among those quoted above depends on the precise biological process that one wishes to study. In this project, we choose to use single-molecule fluorescence microscopy (SMFM) [8, 32-42] to investigate the kinetics of the telomerase enzyme. This technique has the potential to visualize the incorporation of single fluorescently-labeled nucleotides by an individual enzyme.

Questions to Address by SMFM

SMFM techniques provide a great opportunity to advance the understanding of the remarkable telomerase enzyme.

For instance, by following the activity of a single telomerase enzyme in real time, the poorly-established rate at which telomerase works can be precisely measured. It will also be possible to assess whether every telomeric repeat is incorporated at the same rate and how the rate depends on the length of the telomeric DNA already synthesized. In addition, the processivity of telomerase, which plays a crucial role in telomere maintenance and telomere length homeostasis in vivo [21], can likewise be determined. Repetition of these experiments will establish the distributions of telomerase incorporation rate and processivity. Analysis of

these distributions may further reveal the mechanistic details of telomerase activity and their corresponding functions. Moreover, the exact rate constants for translocation and dissociation may also be determined by studying the telomere extension rate as a function of nucleotide concentration. This may yield specific information on the interactions between the DNA and the telomerase enzyme.

It has been thought that the telomeric DNA primer, the RNA template and the catalytic protein component of the telomerase complex, besides providing the basic functions for nucleotide incorporation as shown in **Figure 3**, also structurally influence the telomerase repeat addition processivity [21]. By introducing mutations to these components, our experiment will permit a quantitative analysis of how they influence the dynamics of telomerase activity and their relative importance.

Finally, as the experiment is further developed, we may be able to address questions that are even more complicated, *e.g.* the role of telomere-binding proteins in telomerase activity. In yeast and mammals, the telomeric repeat sequences are associated with a group of specialized telomere-binding proteins to protect chromosome ends from degradation and from end-to-end joining events. At the same time, these proteins regulate telomerase activity to achieve telomere length homeostasis [14]. In humans, six telomere-binding proteins, TRF1, TRF2, hRap1, TIN2, TPP1, and POT1, form the shelterin complex, which is a constitutive component of human telomeres [14, 16]. Studying how shelterin proteins regulate the telomerase activity on the single-molecule level will shed light on the development of effective telomerase inhibitors in cancer research.

2.2 Experimental Configuration

To observe the real-time incorporation of fluorescent nucleotides on a DNA molecule by telomerase, we have constructed a fluorescence setup based on zero-mode waveguide (ZMW) arrays, which is a very powerful tool for single-molecule fluorescent studies as demonstrated in various important applications including real-time DNA sequencing [47], real-time detection of methylated bases during DNA sequencing [48], real-time translation by ribosome [49], lambda-repressor oligomerization kinetics [36], plasma membrane dynamics [50], and lipid membranes rigidity and bending modulus [51] *etc.*

In our planned experiment, as shown in **Figure 4**, telomerase kinetics could be monitored by anchoring single-strand telomeric DNA (**Figure 4**, ssDNA) to the bottom of ZMW, so that a telomerase within the ZMW can extend the free end of the anchored ssDNA. Some of the nucleotides to be incorporated will be fluorescently labeled, and thus the DNA extension process can be observed using either a fast photodiode or a CCD camera.

In order to detect the signal of the single labeled nucleotide being incorporated, we need to make sure that the background noise level due to the fast diffusing labeled nucleotides is much lower than the signal (*i.e.* fluorescence from a single labeled nucleotide being incorporated, **Figure 4**). This sets the upper limit of the concentration of labeled nucleotides that can be used for a given size of illumination spot. Similarly, for a given concentration of labeled nucleotides, the smaller the illumination spot, the lower the background level. Using

ZMW we can confine the illumination spot so small to the extent that we can apply biologically-relevant high concentration of the labeled nucleotides, which is impossible in conventional fluorescent technique.

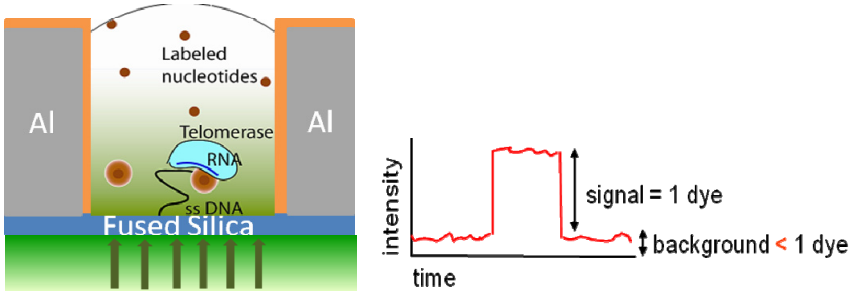

Figure 4. Experimental configuration (left) and expected measured signal (right).

Zero-Mode Waveguides

Simply speaking, a zero-mode waveguide is a small hole (usually about 80~140 nm in size) in a metal film deposited on a microscope coverslip (**Figure 4**). This kind of metal-clad waveguide exhibits a cut-off wavelength above which no propagating modes of electromagnetic wave exist inside the waveguide. This cut-off wavelength is determined by the size and shape of the waveguide. For a square ZMW (or a circular ZMW), the cut-off wavelength is about twice of its width (or diameter). Wavelengths longer than the cut-off value are evanescent and their intensity decays exponentially along the length of the waveguide, enabling a reduction in the conventional probe volume by at least three orders of magnitude. For ZMWs of about 100 nm in diameter, the effective observation volumes are found to be the order of 100 zepto-litters, corresponding to a micro-molar resolution.

ZMWs were initially used for real-time DNA sequencing from single polymerase molecules [47]. Since then, it has been a great interest among biophysicists to extend their applicability to other nucleotide-processing enzymes. In our lab, we are mainly interested in the fluorescence study of telomerase kinetics, namely, using ZMWs to visualize individual labeled nucleotides being incorporated by telomerase.

As just discussed, the main advantage of using ZMWs for fluorescence study is that ZMWs have very small observation volumes, ensuring very low background noise levels and very high working concentrations. In our study of telomerase kinetics, it is indeed necessary to apply relatively-high physiological concentrations (μM) of labeled nucleotides, not only because we want to gain physiologically-relevant insights into telomerase kinetics, but also because it is critical for efficient detection of nucleotide incorporation events. If the nucleotide concentration is too low, the rate of DNA synthesis will become very slow, and it may take a very long time to observe a subsequent incorporation event after one is observed. This may also be troublesome if the telomerase loses its activity after a relatively short time.

Another advantage of ZMWs resulting from its reduced detection volume is the temporal resolution. The temporal resolution of conventional optical configurations for single-molecule

kinetics studies is basically limited by the time it takes for background fluorophores to diffuse out of the observation volume, usually on the order of several hundred microseconds. While in ZMW, the average residence times for molecules in the small probe volume are only a few microseconds, three orders of magnitude faster than many enzymatic reaction rates.

In addition, millions of such ZMWs can be made on a single coverslip, resulting in massive parallelism. Admittedly, if many waveguides are observed in parallel with a CCD camera, temporal resolution will be limited by the detector readout speed as discussed above. However, as long as the number of CCD pixels is not too large, a temporal resolution can still be sufficiently achieved to resolve the millisecond rates of enzymatic reaction. For our camera (iXonEM DV887ECS-BV, Andor Technology, South Windsor, CT, USA) of which the readout speed is 0.1ns/pixel, the maximum number of pixel for this requirement is given on the order of 104, or 27μm×27μm in frame resolution (this allows a parallel detection of an array of couples of hundred ZMWs).

Last but not least, the small detection volume essentially requires only a very minute amount of enzyme (e.g. active telomerase) for activity assay. Given that the metal (aluminum) surface of the ZMW array could be specifically passivated [43, 44, 46] and thus few enzymes are stuck on the metal surface, the required number of enzymes (only needed in the small ZMW holes) can be greatly minimized. This is very important for experiments with telomerase, which is usually particularly difficult to obtain in large amount or at a high concentration.

Surface Treatments

In our planned experiments, as shown in **Figure 4**, we need to immobilize DNA molecules on the glass floor surfaces of ZMWs. Besides, the non-specific adsorption of telomerase enzymes, labeled nucleotides and other bio-molecules that will be present in the reaction solution to the surface of glass floor and aluminum wall should be prohibited, because the non-specific bound enzymes may lose or change their activities due to the interactions with the surface of glass or aluminum, and the transient binding of labeled nucleotides to the surface will produce fluorescent spikes which might be very difficult to distinguish from nucleotide incorporation events. For this purpose, a specific surface treatment of the ZMW is required. Our strategy for the specific surface treatment is to coat the glass surface and aluminum surface differently.

Functionalization of Glass Surface

For the glass floor in ZMW, we use poly ethylene glycol (PEG) to coat the surfaces. PEG is a hydrophilic but uncharged polymer. PEG coating layers prove excellent in resisting non-specific protein adsorption, and have proved highly suitable for the studies of nucleic acids-protein interactions [40, 41, 45]. The resistance mechanism is mainly ascribed to steric repulsion and excluded volume effects which prevent direct contact of proteins with the bare surface [39]. Importantly, since the resistance of protein non-specific adsorption does not arise from the charge repulsion as in many other coating techniques (*e.g.* BSA surface), the neutral PEG surface repels proteins of both negative and positive charges equally well.

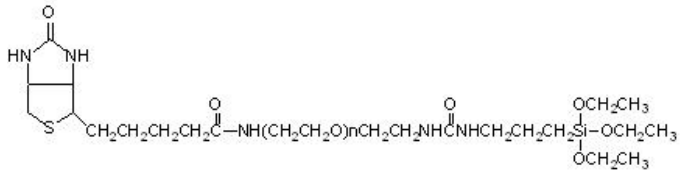

Figure 5. Molecular structures of Biotin-PEG-Silane.

In practice, we use Biotin-PEG-Silane (MW 3400, Laysan Bio, Inc., see **Figure 5**) to create a dense monolayer, which thickness can be estimated to be only ~ 5 nm from the radius of gyration of PEG molecules [39]. Compared to the size of ZMWs (about 100nm), this thickness is nearly negligible and thus the PEG layer will not occupy too much space in the ZMWs. Each PEG molecule has biotin functional group for tethering of DNA molecule via strong streptavidin-biotin linkages, which have a very high association constant ($K_a \sim 10^{15} M^{-1}$) and a dissociation time of several tens of hours [39]. More importantly, it has been demonstrated that silane groups can form stable bonds with glass surfaces via Si-O-Si bond formation, but do not significantly modify aluminum surfaces under appropriate reaction conditions [52]. In order words, the coating of Biotin-PEG-Silane occurs only on the glass bottom of the ZMW, where DNA molecules will be selectively tethered.

Passivation of Aluminum Surface

Aluminum is an active metal. When it is exposed to air, the aluminum surface will be oxidized into a condensed alumina layer. The main concern of aluminum surface passivation is to inhibit the transient binding of labeled nucleotides on the surface alumina, which is believed mainly due to surface charge interactions.

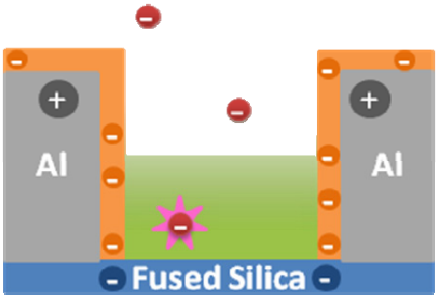

Figure 6. Passivation of aluminum surface. When aluminum surface is coated with negative charged polymers (in orange), it will repel the negative charged labeled nucleotides.

The charge of a molecule or surface in buffered solution depends on its isoelectric point (pI) and the pH of the buffer. The isoelectric point is the pH value at which a molecule or surface carriers no net electrical charge. When a molecule is in a solution with pH lower (higher) than its pI, the molecule is positive (negative) charged. The pH of the buffers we use typically range from 6.5 to 7.5. In ZMW, silicon dioxide has pI = 1.7 - 3.5, and alumina has pI

= 8 – 9 (data from ref. 53). So the glass surface in negatively charged and alumina surface is positively charged.

It is known that in normal buffer range nucleotides are negatively charged. It is also believed and experimentally demonstrated that for the dyes (ATTO-532 or TAMARA) we use, the charge of the labeled nucleotide is mainly determined by the nucleotide itself， especially when the nucleotides are modified to have 6 phosphate groups. In other words, the labeled nucleotides used for our experiment are negatively charged, the same as glass surface but different from alumina surface. Therefore, due to charge interaction, the non-specific adsorption of labeled nucleotides to aluminum walls is much more severe than the glass floor in ZMW [52].

Our strategy, as shown in **Figure 6**, is to coat aluminum with negatively charged polymers such as polyvinylphosphonic acid (PVPA) and PAA/PEI polyelectrolyte multilayer, both of which have proved very excellent to reduce the non-specific transient binding of labeled nucleotides in ZMW [46, 52].

Super-Telomerase

The human telomerase samples under study are so-called 'super-telomerase', provided by the Lingner Group of EPFL in Switzerland. These samples are prepared as cell extracts which have massive telomerase activity (>200-fold increase in telomerase activity was observed) conferred by co-overexpression of hTR and hTERT [54]. The term 'super-telomerase' does not imply that the telomerase has different properties, but only that it is highly expressed.

Oligonucleotide

Table 1 (edited from Ref. 5). Dissociation rate and half life of the base-pairing between telomerase and the six permutated sequences of oligonucleotide 5'-(TTAGGG)3-3'.

Oligonucleotide sequence	Dissociation rate k_{off}(min^{-1}) 22°C	Half life $t_{1/2}$ (min)
5'-(TTAGGG)3-3'	<0.00058	>1200
5'-(TAGGGT)3-3'	0.0022	315
5'-(AGGGTT)3-3'	0.020	35
5'-(GGGTTA)3-3'	0.047	15
5'-(GGTTAG)3-3'	0.020	35
5'-(GTTAGG)3-3'	0.019	36

The biotin-oligonucleotide construct with human telomeric sequence, Biotin-5'-$(TTAGGG)_3$-3' (biotin-tDNA), which is specifically designed for human telomerase assay, is provided by Biolegio Company. The 5' end of the oligonucleotide is labeled with a biotin group, so that it can be tethered on the bottom glass surface of ZMWs via biotin-streptavidin coupling. The free 3' end of the oligonucleotide will be available for the binding of a telomerase, which will extend the oligonucleotide in the 5'->3' direction. The sequence of this

oligonucleotide is well selected. As shown in Table 1, it has the highest affinity for the base-pairing with telomerase among all the sequence permutations of 5'-$(TTAGGG)_3$-3'.

Fluorescently-Labeled Nucleotides

As mentioned above, we will label the nucleotides under study with fluorophores so that they can be visualized by fluorescence microscopy. A nucleotide used for DNA synthesis is a chemical compound that consists of a heterocyclic base, a sugar, and 3 phosphate groups. Commercially available labeled nucleotides usually have fluorophores chemically attached directly to the base. However, this type of labeled nucleotide is not the most appropriate for the experiments that we have in mind (**Figure 4**). This is because when such a nucleotide is incorporated onto DNA, its fluorophore becomes a permanent part of the DNA strand. The physical bulk of the fluorophore side chain on the DNA product takes up space and may sterically hinder the telomerase from further incorporating nucleotides. Also fluorophores accumulate on the DNA products and thus the accumulated fluorescence signal may interfere with the observation of upcoming fluorescent nucleotides to be incorporated.

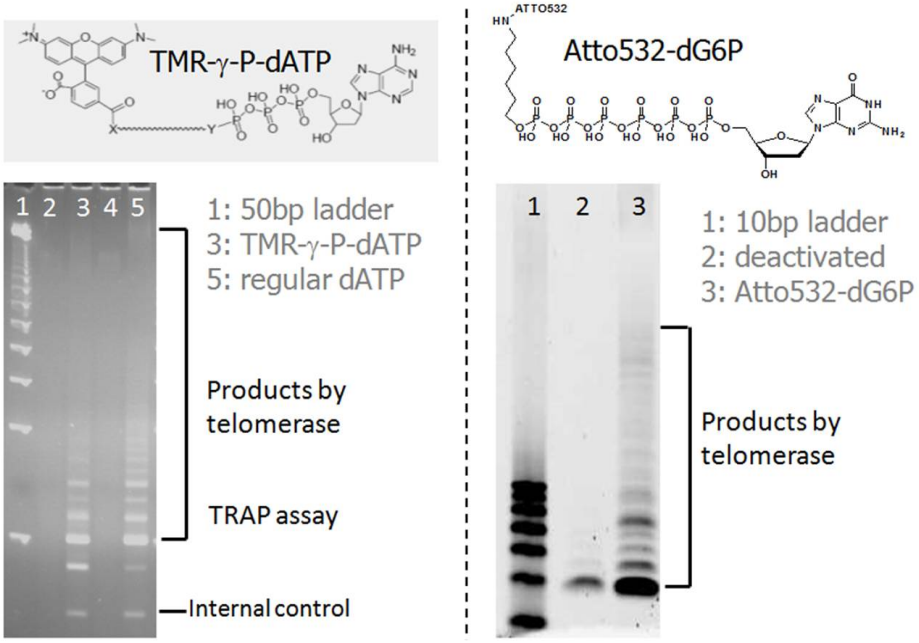

Figure 7. Terminal phospholinked nucleotides and their incorporation by human telomerase. (*left*) TMR-γ-dATP (kindly provided by Visigen Biotechnology Company): TMR dye is labeled on the γ-phosphate. TMR-γ-dATP can be incorporated by human telomerase. The resulting telomeric DNA repeats are visible as a ladder-like pattern in the left gel image (lane 3). A control experiment using regular dATP was performed for comparison (land 5). (*right*) ATTO532-dG6P (custom-synthesized by Jena Bioscience GmbH): the triphosphate moiety of the nucleotide is extended to six phosphates in order to increase incorporation efficiencies [47, 54], and the ATTO532 dye is tagged to the terminal phosphate. As shown in the gel image on the right, ATTO532-dG6P can also be incorporated by human telomerase producing telomeric DNA repeats (lane 3).

In contrast, when the fluorophore is tagged to the terminal phosphate group of the nucleotide (**Figure 7**, *top-left*), the labeled nucleotide can still be fluorescently detected when being incorporated, but the fluorophore, along with the phosphate chain, will be naturally cleaved and quickly diffuse away when the nucleotide is incorporated [55]. In our planned experiment, we will use this type of labeled nucleotide to investigate the process of DNA-incorporation by telomerase. This not only has the advantage of resulting in a fluorophore-free telomeric DNA, which avoids the potential artifacts sterically induced on telomerase activity by a fluorophore-packed DNA, but it also prevents the accumulated fluorescence from overwhelming the signal accompanying the incorporation of the most recent nucleotide.

So far, we have tested, in chronological order, two types of terminal phospholinked nucleotides as shown respectively in **Figure 7**. Although the first type of phospholinked nucleotide (TMR- γ -P-dATP, **Figure 7**, *left*) can be incorporated by telomerase processively, we nevertheless have included several advanced features in the latter type of phospholinked nucleotide (Atto532 -dG6P, **Figure 7**, *right*), including (1) a brighter and more stable dye Atto532, (2) a longer phosphate chain which has been reported to increase incorporation efficiencies and enzyme processivity [47, 54], and (3) 'G' base instead of 'A' base: so that in each telomeric repeat (TTAGGG) added by the telomerase under study, we can observe more fluorescent pulses (3 vs 1). Besides, the feature of three successive fluorescent 'G' pulses can also be used for signal proofreading - as a contrast, a single isolated 'A' fluorescent pulse is difficult to distinguish from spurious signals due to transient surface binding of nucleotide.

For the test of the incorporation of phospholinked nucleotides by human telomerase ('super-telomerase' from Lingner Group), we used a commercial kit (TRAPEZE® Telomerase Detection Kit, S7700, Millipore) with a slightly modified protocol: in the first step of TRAP protocol - 'Addition of Telomeric Repeats By Telomerase' [56], the phospholinked nucleotides under test were used to replace the corresponding regular nucleotides (*i.e.* TMR- γ -P-dATP to replace dATP, and Atto532 -dG6P to replace dGTP), while in the second step of TRAP protocol - 'Amplification of TS-Telomerase Product By PCR' [56], excessive regular nucleotides were added to make sure the PCR reaction was not inhibited by modified nucleotides. The resulting gel images of the TRAP assay for TMR- γ -P-dATP and Atto532 -dG6P are shown in **Figure 7** on the left and right, respectively. The clearly visible telomeric DNA repeats (products by telomerase with phospholinked nucleotides) in both gel images demonstrate that both phospholinked nucleotides can be incorporated by human telomerase.

2.3 Optical Setup

A dual-mode (wide-field & focused-spot) optical setup for the single-molecule fluorescence studies in ZMWs has been constructed. As shown in **Figure 8**, we utilize a 532nm green light from a diode-pumped laser (500 mW max.; GCL-050-L-0.5%, Crystalaser, Reno, NV, USA). A neutral density filter wheel is used to tune the laser intensity, and a 15X beam expander is used to expand the laser beam from 0.36 mm to 5 mm in diameter. Following the beam expander, the excitation light is first linearly polarized by a polarizing

beamsplitter cube and then converted by a λ/4 plate into circularly-polarized. An additional λ/2 plate was placed right before the polarizing beamsplitter cube for further tuning of the light intensity. The circularly-polarized light is preferred for our optical setup because the illumination profile inside ZMWs created by circularly-polarized light is much more isotropic than that by linearly-polarized light [39]. Subsequently, a flipping lens which is employed to switch the optical configuration from wild-field illumination (flipping on) to focused-spot illumination (flipping off). Then the excitation light will be conveyed to an inverted microscope (IX71, Olympus, Japan), in which the incoming light is reflected by a dichroic mirror, going through the objective (PlanApo 60X/1.45oil TIRFM, Olympus, Japan), and illuminating the sample. The emitted fluorescence from the sample is collected through the same objective. In contrast to the excitation light, the resulting fluorescence will pass through the dichroic mirror to the detection modules. We found that ZMW device is basically a highly reflective aluminum-coated mirror. Most of the excitation light (532 nm) is reflected back onto the dichroic mirror, while the dichroic mirror cannot filter out all the 532 nm light. In practice, an additional filter is needed to further attenuate the 532 nm component in the fluorescence signal prior to detection.

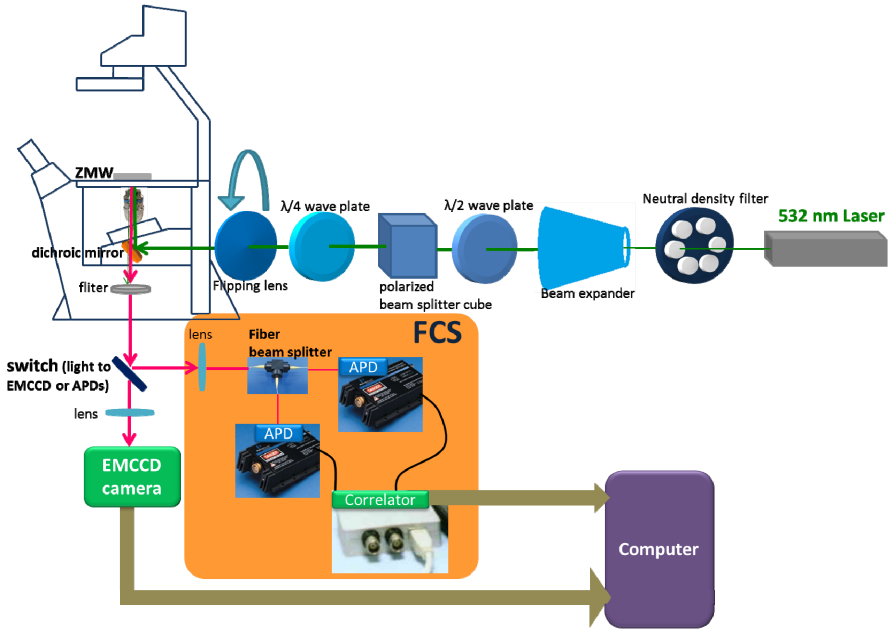

Figure 8. Schematic of dual-mode optical setup for single-molecule fluorescence studies in ZMWs. The illumination profile can be switched between wide field and focused spot. The wide-field illumination is used for massive parallel measurements of ZMW array in EMCCD. The focused-spot illumination is used for measurement on single ZMW using either an EMCCD (slow, for coarse alignment) or APDs (high speed, for data acquisition). The APDs are configurated specifically for FCS measurement of single ZMW.

Our setup is equipped with both EMCCD and APDs for detection of the fluorescence signal. A built-in switch in the IX71inverted microscope is used for selection between two detection modules. The EMCCD camera (iXonEM DV887ECS-BV, Andor Technology, South Windsor, CT) is used for massive parallel measurements of a large array of ZMWs with wide-field illumination. The APDs are configurated specifically for Fluorescence Correlation Spectroscopy (FCS of a single ZMW with focused-spot illumination. In this module, the fluorescence signal is focused and collected by a fiber of 50 μm in diameter, which also works as a pinhole to allow only the signal from one ZMW to be detected. The signal is then split equally into two parts by a free space beam splitter (FOBS-12P-111-50/125-MMM-550/650-50/50-35-3S3S3S-3-1, OZ Optics) and directed toward identical APDs (SPCM-AQRH-14-FC, PerkinElmer). A USB correlator (Flex02-12D/C, Correlator.com) is used for the calculation of cross-correlation function between the signals from two APDs. The reason to use two APDs instead of one for FCS measurement is to avoid the afterpulsing signal that always appears in auto-correlation graph using only one APD. Afterpulsing signal can affect up to microseconds [60], which is an important time scale for FCS measurement of ZMW [57]. In principle, FCS measurements on individual ZMWs can also be carried out using EMCCD, especially when high-speed (faster than ms) processes are not of interest. It has been demonstrated that by only using a subregion of the EMCCD (*e.g.* 2x2 pixels) it is even possible to perform FCS measurement with 20 μs time resolution [61]. However, for the sake of convenience, we perform FCS measurements exclusively with APDs, and only use EMCCD for coarse pre-alignment of ZMW with respect to the illumination spot. In order to stabilize the laser beam path and the focus spot for FCS measurement, the entire optical path is compactly isolated from air flow using home-made absorptive painted foils.

2.4 ZMW Fabrication and Device Assembly

ZMW arrays have been fabricated using electron beam lithography with the facilities in Kavli Nanolab Delft. Two different approaches have been developed to shape the ZMW structures, namely, dry-etching method (adapted from Ref. 38), and lift-off method (adapted from Ref. 57). Here we describe both methods in detail, and compare them. The process of ZMW device assembly after fabrication will also be presented in this section.

ZMW Fabrication: Dry-Etching Method

Substrates cleaning: Fused silica cover slides (Corning 7980 5G UV Grade Fused Silica 1" square x .007" +000/-.001" thick, optically polished both sides 40/20 scratch/dig < 7 Angstroms; FS-224, Valley Design Corp. USA) were immersed in a cleaning solution containing 30 mL NH_4OH (27 %) and 150 mL water. The cleaning solution was heated to 75 °C, and supplemented with 30 mL of H_2O_2 (30 %). This is known as RCA cleaning (**Figure 9**, Step 1). After 10 min, the slides were rinsed thoroughly with water, dried with nitrogen, and treated with oxygen plasma (Tepla 100, TePla AG, Germany).

Aluminum deposition and resist coating: A layer of aluminum (typically 100-120 nm thick) was evaporated on the slides (**Figure 9**, Step 2). Evaporation was performed in a Temescal FC-2000 evaporation system, at a rate of 3 Å/s, at room temperature and with base pressure of about 1×10^{-6} mbar. The samples were then spin-coated with ZEP-520A (ZEON Corporation, Japan) electron beam resist at a rotation speed of 5000 rpm for 1 min, and baked on a hot plate for 30 min at 175 °C. This procedure results in a resist layer with a thickness of about 300 nm (**Figure 9**, Step 3).

E-beam exposure and resist development: The samples were exposed (**Figure 9**, Step 4) with an electron beam pattern generator (Leica EBPG 5000+). A beam of approximately 3.3 nA at 100 kV acceleration (which corresponds to an estimated beam size of approximately 6 nm), a beam step size of 5 nm, and a dose of approximately 350 μC/cm^2 were typically used. The samples were developed (**Figure 9**, Step 5) in xylene for 3 min, with mild agitation. They were rinsed with isopropanol immediately after development and dried with nitrogen.

Dry Etching: The pattern was transferred into the aluminum using an Alcatel GIR 300 RIE etcher (**Figure 9**, Step 6). We typically etched for 4 minutes using a mixture of 12.5 sccm N_2, 10 sccm BCl_3, and 5 sccm Cl_2. During etching, the pressure in the chamber was regulated to 16 μbar, the table temperature was maintained at 50 °C, and the RF power equaled 50 W. The samples were rinsed with distilled water immediately after etching and dried with nitrogen. Finally, the resist was removed by sonication for 1 min in dimethylacetamide (**Figure 9**, Step 7), and the samples were rinsed with isopropanol and dried with nitrogen.

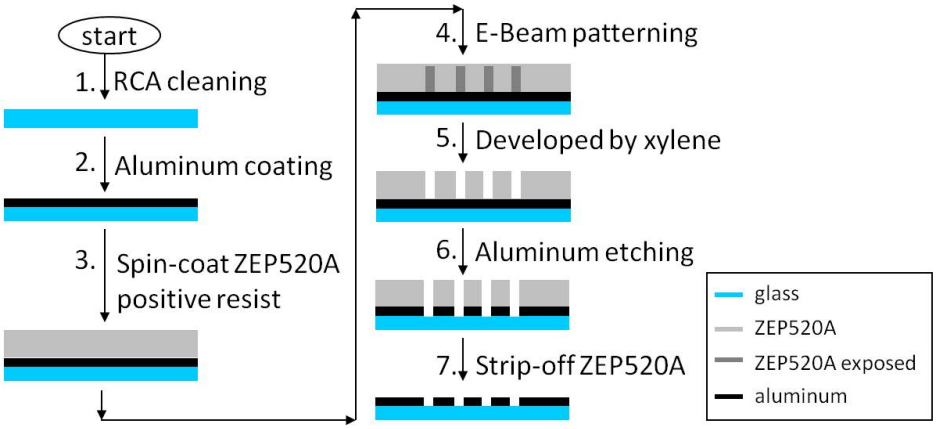

Figure 9. Schematic of the fabrication of zero-mode waveguides using a positive tone process (dry-etching method).

ZMW Fabrication: Lift-off Method

Fabrication of the ZMW arrays was performed on a 100 mm diameter fused silica wafer (Corning 7980, OD: 100mm +/- 0.2mm, THK: 170um +/- 25um, Polished Both Sides, 20/10, No bevel, max chip <0.005", Supplier: Mark Optics Inc., Santa Ana, USA).

First, the wafer was ultrasonically cleaned (**Figure 10**, Step 1) in fuming nitric acid (100% HNO_3) for 10 min, rinsed in deionized (DI) water and spun dry. Then, the wafer surface was primed for resist adhesion using hexamethyldisilazane by spin-coating at 2000 rpm for 55 s (**Figure 10**, Step 2). After priming, a 300-nm layer of NEB-22A2E negative electron-beam resist (Sumitomo Chemical Co.) was spin-coated onto the wafer at 2000 rpm for 55 s and baked for 3 min at 110°C (**Figure 10**, Step 3). Followed the spin-coating of resist, a 20 nm gold layer is deposited (**Figure 10**, Step 4) on top of the resist using a resistive thermal evaporator (Leybold-Heraeus L560). Evaporation was initialized when the chamber pressure dropped below 10^{-5} mbar, and the evaporate rate was kept around 1.5 Å/s. This gold layer serves as a reflective layer to facilitate the focusing on the electron beam lithography machine (Leica EBPG 5000+) and additionally provides a charge dissipation path during electron beam exposure. At this point, the sample is ready for patterning.

Feature patterning (**Figure 10**, Step 5) is performed on a Leica EBPG 5000+ (acceleration voltage 100 kV, aperture 400 μm, at a current of nominally 1.6 nanoAmpere). One ZMW was exposed as a 10x10 nm^2 single pixel using a square pattern with edge length equal to beam step size. This method enables the use of dose as a direct control for finished feature size. Under these settings, ZMWs with diameters ranging from 80 to 140 nm were obtained from doses from 4000 to 20000 $\mu C/cm^2$ respectively.

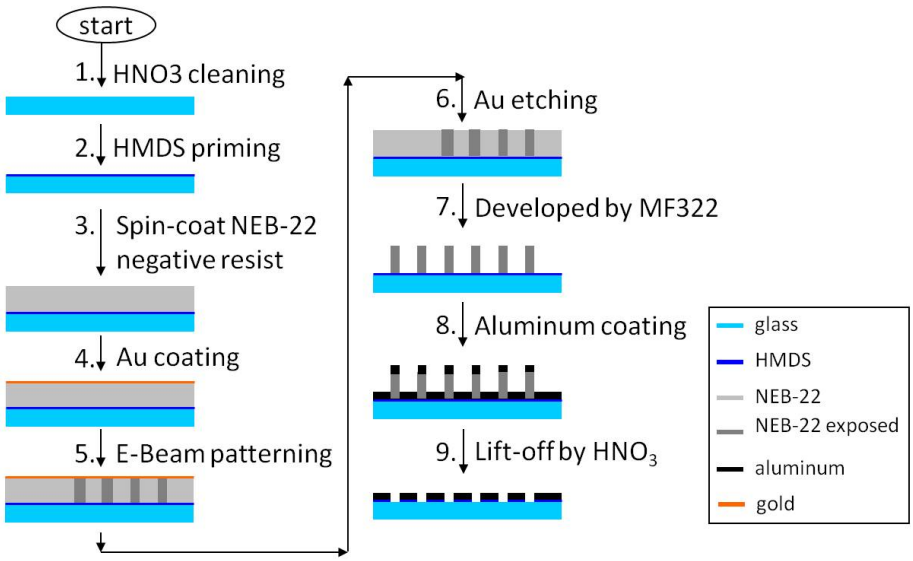

Figure 10. Schematic of the fabrication of zero-mode waveguides using a negative tone process (lift-off method).

Following electron beam exposure, the resist was baked at 105 °C for 3 min and the gold overcoat was removed (**Figure 10**, Step 6) by immersing the wafer in gold etchant TFA (Transene, USA) for ~20 s, rinsing with DI water, and spinning dry. Next, the development was done for 1 min in Microposit MF322 solution (Rohm and Haas), followed by a 15 s

soaking in 1:10 diluted MF322 solution (**Figure 10**, Step 7). The wafer was then rinsed in DI water and spun dry.

Before aluminium deposition, the wafer submitted to 5 seconds descuming oxygen plasma in a microwave plasma system (Tepla 100, TePla AG, Germany) under the following conditions: the microwave power equaled 100 W and the pressure was kept at 1 mbar with a 104-sccm O_2 flow.

A 100-nm layer of aluminium was then deposited onto the wafer using a Temescal FC-2000 evaporation system (**Figure 10**, Step 8). The pressure set-point to start evaporation was $2x10^{-6}$ mbar, and the evaporation rate was maintained at 2 Å/s.

The structures were then finished by immersing the wafer in an ultrasonic bath of fuming nitric acid (100% HNO3) for 10 min, rinsed in deionized (DI) water and spun dry. At this point, ZMW arrays were fabricated (**Figure 10**, Step 9), and the wafer was ready for dicing into individual chips.

Prior to wafer dicing, a 2-μm layer of AZ5214E photoresist (MicroChemicals GmbH) was spin-coated onto the wafer at 2000 rpm for 55 s and baked for 1 min at 90°C. This thick photoresist layer protected the aluminum surface from scratching by debris particles during dicing. The wafer was diced into individual 6×6 mm^2 square chips using a Disco Dicing Saw (model: DAD3220) with a resin/diamond sintered blade (Disco P1A series). After dicing, the dies were removed from the adhesive tape manually and stored in vacuum. The protective photoresist layer was removed just before use of the ZMW chip. This was done by immersing the chip in an ultrasonic bath of fuming nitric acid (100% HNO_3) for 10 min, rinsed in deionized (DI) water and spun dry.

Comparison of Two Fabrication Methods

Generally speaking, both dry-etching method and lift-off method produce sufficient good results. However, in practice, we find that lift-off method is much easier to find 'one-fits-all' universal settings for machining ZMWs of different sizes, much easier to scale up to whole-wafer processing, and much more reproducible.

The disadvantages of dye-etching method are mainly due to the inhomogenity nature of plasma dry etching. For example, we observed that the etch rate depends on the size of ZMW. This effect is known as RIE-lag, and a possible explanation for this is that the incoming reactive ions in the ZMW hole are partly captured by the sidewalls or deflected by the electrostatic fields of the sidewalls [58]. The fact that different size of ZMW requires different etching time causes serious inconvenience when different sizes of ZMWs need to be made on one single wafer: there're always some ZMWs either underetched (aluminum is not etched through) or overetched (ZMW size becomes larger).

Moreover, besides the RIE-lag effect, plasma dry etching in general also subjects to another intrinsic inhomogenity called macro-loading effect, i.e., the etching rate increases monotonically with the radial distance from the wafer center. This effect can be explained by the depletion of reactant along its transportation course from outside edge to the wafer center, and it depends greatly on the loading ratio (i.e. the ratio of mask opening for etching) [59].

Last but not least, in practice we also found that for a given dry etching settings, the etch results were not always reproducible. One of the main reasons might be that the etcher is cross-contaminated from other processings, which is a common problem of shared general-purpose facilities.

Due to the above-mentioned problems, the dry-etching method has gradually faded out in use. Most of the recent experimental results, which will be presented in the following sections, are taken from ZMWs prepared by lift-off method only.

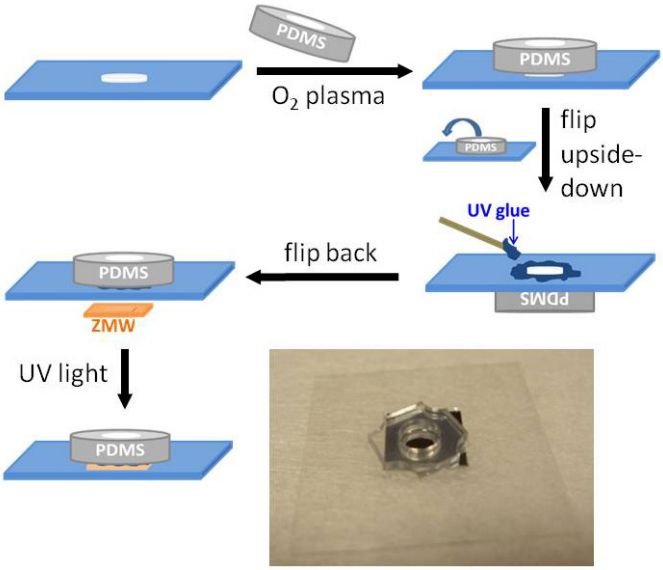

Figure 11. Flow chart and photo (*bottom-right*) of a ZMW device assembly prior to microscope imaging.

ZMW Device Assembly

After fabrication (and surface functionalization, optionally), the ZMW chips (6×6 mm^2) were then mounted to special microscope slides which were bound to PDMS gaskets, as shown in **Figure 11**. The detailed procedure is as following: A 3 mm diameter hole is drilled into the center of a microscope glass coverslip (MENZEL-GLASER, 18×18 mm) using a Danville PrepStart sandblaster system. Then the glass coverslip is cleaned with acetone and subsequently isopropyl alcohol in an ultrasound sonicator, and blown dry with a nitrogen gas gun. In the meantime, a PDMS gasket is prepared by cutting and peeling a single PDMS well (3 mm in diameter, 1 mm in depth) off from a CultureWell Chambered Coverglass (CWCS 50R-1.0, Grace Bio-Labs). During cutting and peeling, take a good care to keep the PDMS gasket clean. Then the next step is to bind the PDMS gasket and the glass coverslip together. This is done by exposing briefly (*ca.* 5-15 s) the clean coverslip and the PDMS gasket simultaneously to oxygen plasma in a microwave plasma system (PLASMA- PREEN I,

Plasmatic Systems Inc.). The two exposed surfaces are then aligned with respect to the holes, brought into contact and pressed slightly. It is thought that the when exposed to plasma silanol groups (-OH) are developed on both the PDMS and glass surfaces, and when the two surfaces are brought into contact they form covalent siloxane bonds (Si-O-Si) after baking. The PDMS and attached coverslip are then baked for 30 minutes at 85 °C, and ready to be glued to a ZMW chip. For gluing, UV-cured adhesive (Norland Optical Adhesive 81) is applied as little as possible (while still sufficient to completely surround the hole) to the opposite side of the coverslip (with respect to the PDMS gasket) using a toothpick. Then a ZMW chip is aligned with respect to the center of the aperture, and brought into contact with the coverslip. A home-made chip holder was made to assist the process of alignment and bringing two surfaces into contact. To fully cure the adhesive, the ZMW device is placed under a UV lamp (NORLAND wavelength 365 nm), illuminating for 1 hour through the PDMS onto the adhesive sandwiched between the glass and ZMW chip. At this point the ZMW device assembly is complete (**Figure 11**, *bottom-right*), and the device is ready for subsequent surface functionalization and further experiments.

2.5 ZMW Characterization

Characterization of the fabricated ZMW structures was conducted by Scanning Electron Microscopy (SEM) and Fluorescence Correlation Spectroscopy (FCS). SEM was used to visualize and measure the dimensions of ZMW structures. FCS was used to characterize the illumination profile inside the ZMWs.

Scanning Electron Microscopy

Figure 12 shows the SEM images of a typical example of ZMW device in use. Both the top-view (**Figure 12**, *left*) and cross-section images (**Figure 12**, *right*) of ZMWs were taken in a FEI/Philips XL30S/FEG system. For cross-section imaging, the ZMWs were pre-sculpted using a focused ion beam (FIB) system (STRATA DualBeam DB235 from FEI).

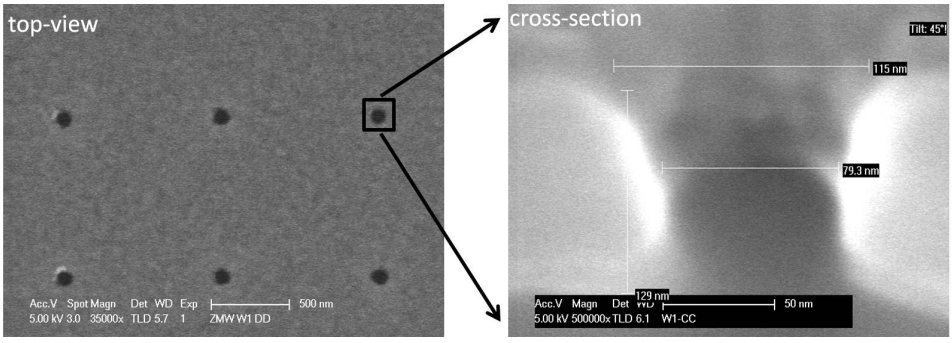

Figure 12. SEM images of fabricated ZMWs in use. (*left*) top-view image of ZMW array. (*right*) cross-section image of a single ZMW.

Our fabrication protocol enables manufacturing ZMWs in dense uniform arrays. Different pitches of ZMW arrays were designed to serve different applications. For ZMWs used with camera for massive parallel detection, we chose a pitch of 1.06 μm (**Figure 12**, *left*), which equals 2 wavelengths (532nm laser), and will be projected as exactly 4-pixel size onto the EMCCD (16 μm pixel size, 60X magnification). For single-ZMW measurements using APDs (for FCS, or high temporal resolution), the ZMW are arrayed at a larger pitch, such as 5.3 μm, which is sufficient large that when a ZMW is illuminated by a focus spot, the illumination on neighboring ZMWs can be ignored. Also a pitch of 5.3 μm will be projected (60X magnification) onto the imaging plane as *ca.* 300 μm, which is more than enough to make sure the fiber entrance (50 μm diameter) can only collect fluorescent signal from a single ZMW.

The cross-section image of ZMW (**Figure 12**, *right*) shows a small tapering near the entrance, while the sidewalls are basically straight at the base of the structure. It is thought [57] that the tapering on top is attributed to shadowing effect from the resist pillar during the aluminum deposition step. Since the optical confinement in ZMW is mainly located at the base of the structure, it is believed [57] the tapering near the ZMW entrance has little impact on the performance of the ZMW.

Fluorescence Correlation Spectroscopy

FCS measurements and fitting of FCS curves to theoretical model were performed to characterize the optical confinement of ZMWs. For each measurement, an 8 μl of the ATTO532-dG6P solution with a working concentration of 10 μM (in 50 mM MOPS-acetate buffer pH 7.5, with 75 mM potassium acetate, 5 mM dithiothreitol, and 0.05% of Tween-20.) was loaded in the reaction well defined by the hole in PDMS gasket (**Figure 11**). Approximately 300 μW of laser power (532 nm wavelength) was fed into the objective. Measurement of each correlation curve lasted 120 s.

To fit the FCS curves, we used the empirical model developed by K. T. Samiee, *et. al.* [36, 62] given as:

$$G(\tau) = G(0)\left[\frac{\pi}{4}\left(\left(1-2\frac{\tau}{\tau_d}\right)\exp\left(\frac{\tau}{\tau_d}\right)erfc\left(\sqrt{\frac{\tau}{\tau_d}}\right)+\frac{2}{\sqrt{\pi}}\sqrt{\frac{\tau}{\tau_d}}\right)-\frac{\sqrt{\pi}}{2}erf\left(R\sqrt{\frac{\tau}{\tau_d}}\right)\sqrt{\frac{\tau_d}{\tau}}\frac{1}{\left(1+R^2\right)^2}\right] \quad (1)$$

where $G(0)$ is the amplitude ($G(0) = N/(N+B)^2$, with N being the average occupation number of molecule in the observation volume (V_{obs}), and B being the constant background signal), τ_d is the diffusion time ($\tau_d = L^2/D$, with L being the decay length of the observation volume in ZMW, and D being the diffusion constant), and R is the ratio of the decay constant (L) to the height of the ZMW (H): $R = L/H$. In this model, there're three free parameters: $G(0)$, τ_d and R.

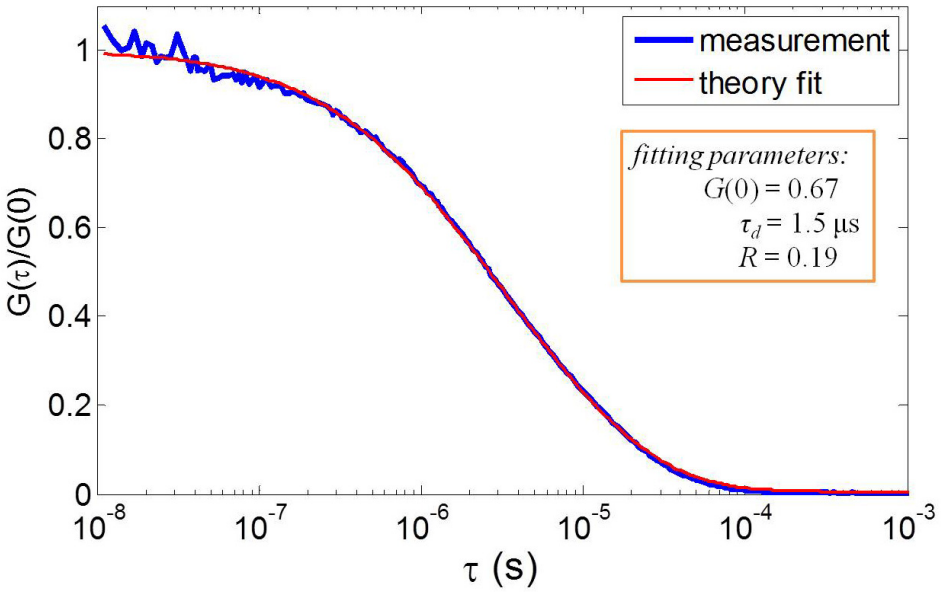

Figure 13. FCS curve of a ZMW with a diameter of 80 nm. The measurement (in blue) was performed using 10 μM of ATTO532-dG6P solution, and each curve was recorded for duration of 120 s. About 300 μW of laser power was fed into the objective, resulting in an intensity of about 600 kHz in each APD. The FCS curve is fitted (in red) by equation (1), with $G(0) = 0.67$, $\tau_d = 1.5$ μs, and $R = 0.19$.

Figure 13 shows an example of FCS curves of a ZMW with a diameter of 80nm (the same ZMW device as shown in **Figure 12**). The theory fit gives $G(0) = 0.67$, $\tau_d = 1.5$ μs, and $R = 0.19$, from which, in combination with the ZMW dimensions measured by SEM, we can gain many insights into the illumination profile in ZMW, and even the physical properties of the labeled nucleotides.

From the wavelength (λ = 532 *nm*) and ZMW diameter (d = 80 *nm*), the decay length ($L = \frac{1}{6}\left[\frac{1}{(1.7d)^2} - \frac{1}{\lambda^2}\right]^{-\frac{1}{2}}$, Ref. 39) can be calculated: L = 23 nm. From the cross-section image of the ZMW (**Figure 12**, *right*), we also know that the height of the ZMW is 115 nm, so one should expect $R = L/H = 0.2$, which agrees very well with the fitted value (R = 0.19) from the FCS curve.

The observation volume is given as: $V_{obs} = \pi d^2 L/8 = 5.9\text{x}10^4$ nm^3. Accordingly the occupation number is calculated to be $N = V_{obs}C = 0.35$, which indicates that even at 28 μM concentration, such ZMW still shows single occupancy of labeled nucleotide). From occupation number, in combination with the fitted parameter $G(0) = 0.67$, we can then calculate the constant background signal: $B = 0.37$, which is not unreasonable because the ZMW is illuminated with very high power (*ca.* 300 μW), and the detection intensity is quick high (2 x 600 kHz, or about 1.6 MHz molecule brightness).

Also, from τ_d = 1.5 μs, and L = 23 nm, the diffusion constant (D) of ATTO532-dG6P can be determined to be 3.7 x 10^{-6} cm^2/s (in comparison, Alexa488 dye in similar condition has a diffusion constant of 2.6 x 10^{-6} cm^2/s [57]).

2.6 ZMW Surface Functionalization

To serve the single-molecule fluorescent studies of telomerase, ZMW surfaces need to be selectively functionalized, namely, the ZMW glass floor needs to be coated with Biotin-PEG-Silane for specific tethering of DNA, while the aluminum surfaces need to be passivated by negative-charged inert polymers to avoid transient binding of labeled nucleotides. Here we describe in detail our method of selective treatments of ZMWs. Characterization and evaluation of the treated surfaces of ZMWs will also be presented.

Biotin-PEG-Silanization

Surface functionalization of ZMW chip was performed before device assembly for the convenience of sample handling. Biotin-PEG-Silane coating is applied to ZMW glass floor prior to the passivation of aluminum surface, because we found that in our method Biotin-PEG-Silane coating is very specific to glass, and it can serve as a mask to ensure that the subsequent surface passivation occurs on aluminum surface only.

Selective coating of Biotin-PEG-Silane on the glass floor of ZMWs was accomplished as follows (protocol adapted from Ref. 52). The fabricated ZMW chips are cleaned in an ultrasonic bath of fuming nitric acid (100% HNO_3) for 10 min, rinsed in deionized (DI) water and blown dried by N_2 gas gun. Then the ZMW chips are subjected to brief oxygen plasma in a microwave plasma system (Tepla 100, TePla AG, Germany) to activate the glass surface for silanization. Subsequently, the Biotin-PEG silanization is carried out by immersing the ZMW chips in a Biotin-PEG-Silane (MW 3400, Laysan Bio, Inc.) solution in 270 : 1 (w/w) ethanol : methanol solvent for 3 hours at 4°C. Then the ZMW chips are rinsed with methanol, thoroughly washed with DI water, and blown dried with N_2 gas gun. At this point, the ZMW chips are selectively functionalized with Biotin-PEG-Silane and ready for subsequent aluminum surface passivation.

Aluminum Surface Passivation

For aluminum surface passivation, we have tested two different types of polymers, namely, polyvinylphosphonic acid (PVPA, negatively-charged) and PAA/PEI polyelectrolyte multilayer (PAA is positively-charged, and PEI is negatively-charged).

The PVPA coating (adapted from Ref. 46) is achieved by immersing the ZMW chips (pre-functionalized with Biotin-PEG-Silane) in preheated 2% (vol/vol) aqueous solution of PVPA (MW 24000, 30%, Polyscience, Inc. Cat#24297) for 2 min at 90°C. Then the ZMW chips are soaked in DI water, blown dried with N_2 gas, and annealed in dry oven at 85°C for 4 hours. Extended annealing improves the adhesion of PVPA coating to aluminum.

The procedure (adapted from Ref. 52) of PAA/PEI multilayer coating consists of consecutive immersion of the ZMW chips (pre-functionalized with Biotin-PEG-Silane) for 3 min in 20 mg/ml Polyacrylic acid (PAA, ACROS ORGANICS, 185012500) and 20 mg/ml Polyethylenimine (PEI, SIGMA-ALDRICH, P3143, pH 7.5 adjusted with HCl) at room temperature, each step followed by thoroughly ringing with DI water, in the order: PAA/PEI/PAA/PEI/PAA (**Figure 15**).

Characterization of the Treated Surfaces

Extensive tests have been performed to characterize the treated ZMW surfaces and evaluate their performance.

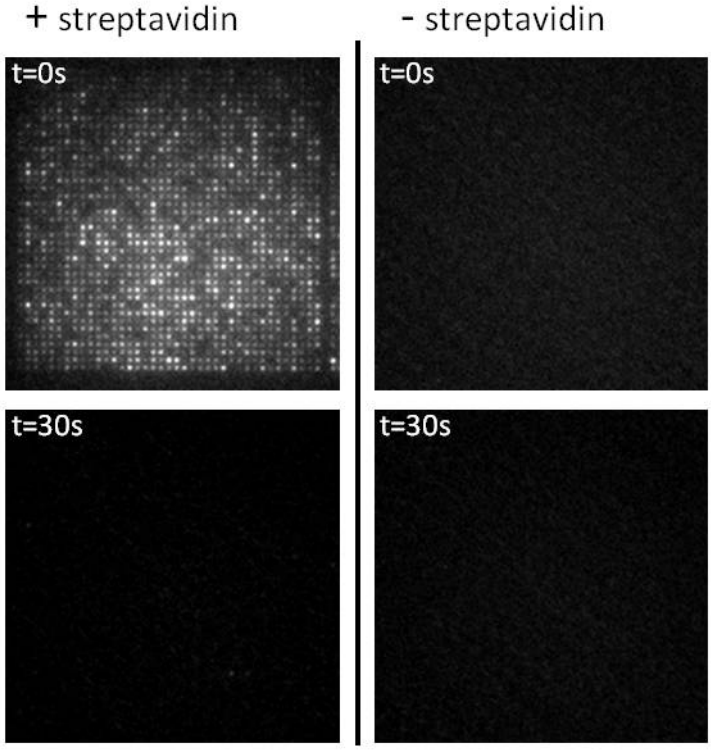

Figure 14. Specific tethering of DNA in ZMWs. (*top-left*) The fluorescence (white) comes from the fluorescently-labeled oligonucleotides tethered inside ZMWs via biotin-streptavidin linkages. This image was taken upon switching on the laser power. (*bottom-left*) Fluorescence lost after 30 s due to photobleaching under continuous strong excitation (*ca.* 40 mW laser power injected into objective). This proves that the fluorescently-labeled oligonucleotides present only on the surfaces inside ZMWs, but not in the bulk solution. Also detailed analysis of time-resolved fluorescence intensity from individual ZMWs indicated that in most ZMWs only one or two oligonucleotides present (data not shown). (*right*) A control experiment, in which all the procedures for sample preparation remained the same except that the streptavidin was missing, shows that non-specific adsorption of DNA on treated surfaces in ZMWs is very low and basically undetectable.

We first investigated to what extent specific tethering of DNA in ZMWs can be achieved. To do so, ZMW test chips were coated with Biotin-PEG-Silane and PAA/PEI multilayer following the procedures described above, and then assembled into final devices with PDMS incubation wells (**Figure 11**). Subsequently, 8 µl of 100 nM streptavidin in loading buffer (50 mM MOPS-acetate buffer pH 7.5, with 75 mM potassium acetate, 5 mM dithiothreitol, and 0.05% of Tween-20) was loaded onto the ZMW device (for a negative control experiment, this step was skipped), incubated in a humid environment for 10 min at room temperature, and rinsed 5 times with loading buffer. Then the ZMW device was incubated with 100nM biotinylated fluorescently-labeled oligonucleotides (5'Biotin-ttagggttagggttaggg-TMR) in loading buffer for 15 min at 4 °C, followed by 5 times rinsing with loading buffer. The last volume of loading buffer remained on the ZMW device, which was then mounted onto our optical setup (**Figure 8**) for taking fluorescent movies of the ZMWs. The first frame (upon switching on laser power), and a frame 30 s later of the movie taken from ZMWs incubated with streptavidin (or without streptavidin as negative control) and oligonucleotides was shown in **Figure 14** left panel (and right panel for negative control). The big difference between the positive (with streptavidin) and negative (without streptavidin) results demonstrates a highly specific tethering of DNA in ZMWs. Also further investigations prove that non-specific adsorption of streptavidin on PAA/PEI multilayer (the coatings on the sidewalls of ZMWs) is very low and basically undetectable (data not shown). To sum up these observations, we can conclude that tethering of DNA is specific only on the glass floors of ZMWs via linkages in the form of DNA-biotin-streptavidin-biotin-PEG-glass.

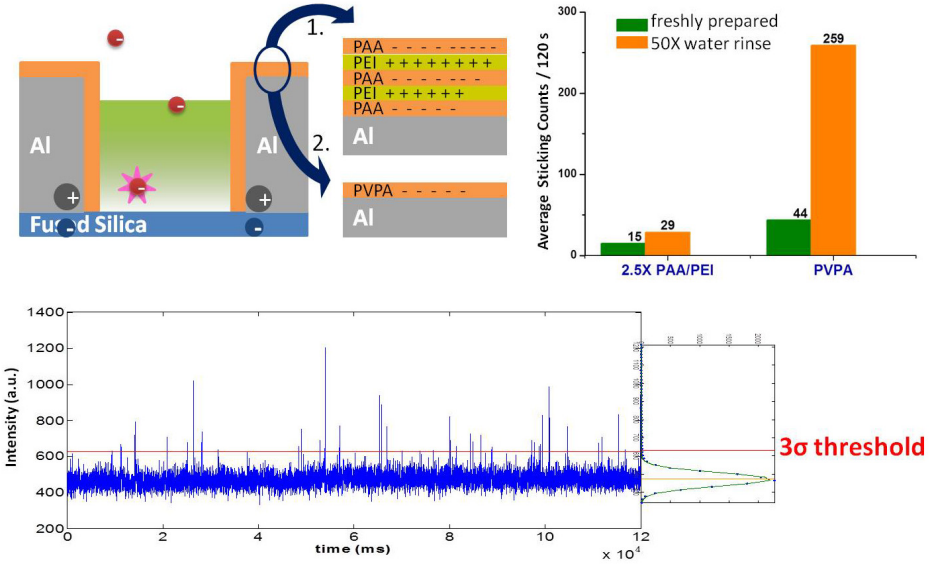

Figure 15. Transient adsorption of fluorescently-labeled nucleotides on treated ZMW surfaces. (*top-left*) Schematics for the two types of treated ZMW surfaces under investigation; (*top-right*) Average number of transient adsorption events from a surface-treated ZMW: PVPA vs PAA/PEI, freshly-prepared vs after 50X rinse. (*bottom*) A fluorescent trace from a single ZMW. The 3σ threshold is also plotted for demonstration.

Another important aspect of the performance of surface treatment is to what extent the transient adsorption of phospholinked nucleotide on ZMW surfaces can be reduced. For this evaluation, both types of surface-treated ZMWs (**Figure 15**, *top-left*) have been investigated: one is treated with PAA/PEI multilayer (in combination with Biotin-PEG-Silane), and the other is treated with PVPA (also in combination with Biotin-PEG-Silane). To characterize the transient adsorption of labeled nucleotides on treated ZMW surfaces, an 8 μL of 0.5 μM Atto532-dG6P (in 50 mM ACES buffer pH 7.1, with 75 mM potassium acetate, 5 mM dithiothreitol, and 1mM calcium chloride; similar condition as planned experiment for telomerase study) was loaded to a surface-treated ZMW device, and the fluorescent signals from individual ZMWs were recorded by EMCCD for 2min with a bin time of 10 ms. Then by analyzing the fluorescent trace of a single ZMW (**Figure 15**, *bottom*), the number of transient adsorption events can be measured. This was done by counting the number of fluorescent spikes (N_{spike}) above 3 standard deviations from the mean. Since in theory, there are 12 (±3) out of the total 12000 data points above the 3σ threshold can still be attributed to normal distribution. We then count the number of transient adsorption events as $N_{adsorption} = N_{spike} - 12$, which are then plotted in **Figure 15** (*top-right*) for different tests. From this plot, we can see that PAA/PEI multilayer coating can reduce the transient adsorption of labeled nucleotides more significantly than PVPA coating. Also the performance of PAA/PEI multilayer coating appears very stable, while in contrast the quality of PVPA coating is deteriorated rapidly after a practical amount of water rinsing. More importantly, the frequency of transient adsorption of Atto532-dG6P on PAA/PEI treated ZMW surface (*ca.* 20-30 in 120 s) is much lower than a typical incorporation rate of labeled nucleotides by DNA polymerizing enzyme in a similar reaction condition (*e.g. ca.* 240 - 480 in 120 s by phi29 DNA polymerase [47]). Therefore, we decided to use PAA/PEI multilayer in combination with Biotin-PEG-Silane for surface treatments of our ZMW devices.

2.7 Conclusion

We have successfully developed several key fundamental elements towards single-molecule studies of telomerase kinetics in ZMWs. We have designed a biotin-labeled oligonucleotide specifically for human telomerase assay in ZMW: it can be immobilized on the ZMW floor via its biotin group, and it has the highest affinity for base-pairing with telomerase. We have also designed and acquired two types of special modified nucleotides for this assay: fluorescently phospholinked nucleotides (TMR-γ-dATP and Atto532-dG6P), and we have demonstrated that both phospholinked nucleotides can be incorporated processively by human telomerase. We have constructed an optical setup specifically for single-molecule fluorescence studies in ZMWs. This setup can operates in two different modes, namely, massive parallel detection mode (using wide-field illumination and EMCCD detection), and high-speed single spot mode (using focused illumination spot and APD for high speed detection). We have successfully developed methods for nano-fabrication of ZMWs. We have also performed extensive characterizations on our ZMW devices using SEM (device geometric profiles), and FCS (detection volume, fluorophore working concentration). Our characterization results show that we are able to controlledly fabricate ZMWs with a suitable

size (*ca.* 80nm in diameter) for single-molecule fluorescent studies at biologically relevant concentration (> 1μM), which is very important for meaningful studies of telomerase kinetics. Finally, we have demonstrated a method for successful surface treatment of ZMWs, by which the DNA substrates can be tethered specifically onto the glass floor of ZMWs, and more importantly, the non-specific transient adsorption of labeled nucleotides on ZMW surfaces has been reduced to a sufficient low level (one order of magnitude lower than the typical rate of nucleotide incorporation).

2.8 References

1. Olovniko, A.M., Theory of Marginotomy - Incomplete Copying of Template Margin in Enzymic-Synthesis of Polynucleotides and Biological Significance of Phenomenon. Journal of Theoretical Biology, 1973. 41(1): p. 181-190.
2. Greider, C.W. and E.H. Blackburn, Identification of a Specific Telomere Terminal Transferase-Activity in Tetrahymena Extracts. Cell, 1985. 43(2): p. 405-413.
3. Bailey, S.M. and J.P. Murnane, Telomeres, chromosome instability and cancer. Nucleic Acids Research, 2006. 34(8): p. 2408-2417.
4. Wenz, C., et al., Human telomerase contains two cooperating telomerase RNA molecules. Embo Journal, 2001. 20(13): p. 3526-3534.
5. Wallweber, G., et al., Interaction of human telomerase with its primer substrate. Biochemistry, 2003. 42(2): p. 589-600.
6. Strahl, C. and E.H. Blackburn, Effects of reverse transcriptase inhibitors on telomere length and telomerase activity in two immortalized human cell lines. Molecular and Cellular Biology, 1996. 16(1): p. 53-65.
7. Rivera, M.A. and E.H. Blackburn, Processive utilization of the human telomerase template - Lack of a requirement for template switching. Journal of Biological Chemistry, 2004. 279(51): p. 53770-53781.
8. Ren, X.J., et al., Analysis of human telomerase activity and function by two color single molecule coincidence fluorescence spectroscopy. Journal of the American Chemical Society, 2006. 128(15): p. 4992-5000.

9. Lin, J., D.L. Smith, and E.H. Blackburn, Mutant telomere sequences lead to impaired chromosome separation and a unique checkpoint response. Molecular Biology of the Cell, 2004. 15(4): p. 1623-1634.
10. Lee, M.S. and E.H. Blackburn, Sequence-Specific DNA Primer Effects on Telomerase Polymerization Activity. Molecular and Cellular Biology, 1993. 13(10): p. 6586-6599.
11. Kim, N.W., et al., Specific Association of Human Telomerase Activity with Immortal Cells and Cancer. Science, 1994. 266(5193): p. 2011-2015.
12. Kim, M.M., et al., A low threshold level of expression of mutant-template telomerase RNA inhibits human tumor cell proliferation. Proceedings of the National Academy of Sciences of the United States of America, 2001. 98(14): p. 7982-7987.
13. Kelleher, C., et al., Telomerase: biochemical considerations for enzyme and substrate. Trends in Biochemical Sciences, 2002. 27(11): p. 572-579.
14. Hug, N. and J. Lingner, Telomere length homeostasis. Chromosoma, 2006. 115(6): p. 413-425.
15. Feng, J.L., et al., The RNA Component of Human Telomerase. Science, 1995. 269(5228): p. 1236-1241.
16. De Lange, T., Shelterin: the protein complex that shapes and safeguards human telomeres. Genes & Development, 2005. 19(18): p. 2100-2110.
17. Chan, S.R.W.L. and E.H. Blackburn, Telomeres and telomerase. Philosophical Transactions of the Royal Society of London Series B-Biological Sciences, 2004. 359(1441): p. 109-121.
18. Bodnar, A.G., et al., Extension of life-span by introduction of telomerase into normal human cells. Science, 1998. 279(5349): p. 349-352.
19. Blackburn, E.H., C.W. Greider, and J.W. Szostak, Telomeres and telomerase: the path from maize, Tetrahymena and yeast to human cancer and aging. Nature Medicine, 2006. 12(10): p. 1133-1138.
20. Blackburn, E.H., Telomere states and cell fates. Nature, 2000. 408(6808): p. 53-56.

21. Lue, N.F., Adding to the ends: what makes telomerase processive and how important is it? Bioessays, 2004. 26(9): p. 955-962.
22. Lindstrom, U.M., et al., Artificial human telomeres from DNA nanocircle templates. Proceedings of the National Academy of Sciences of the United States of America, 2002. 99(25): p. 15953-15958.
23. De Lange, T. and T. Jacks, For better or worse? Telomerase inhibition and cancer. Cell, 1999. 98(3): p. 273-275.
24. Chen, J.L. and C.W. Greider, Determinants in mammalian telomerase RNA that mediate enzyme processivity and cross-species incompatibility. Embo Journal, 2003. 22(2): p. 304-314.
25. Huard, S., T.J. Moriarty, and C. Autexier, The C terminus of the human telomerase reverse transcriptase is a determinant of enzyme processivity. Nucleic Acids Research, 2003. 31(14): p. 4059-4070.
26. Greider, C.W., Telomerase Is Processive. Molecular and Cellular Biology, 1991. 11(9): p. 4572-4580.
27. Kim, N.W. and F. Wu, Advances in quantification and characterization of telomerase activity by the telomeric repeat amplification protocol (TRAP). Nucleic Acids Research, 1997. 25(13): p. 2595-2597.
28. Weizmann, Y., et al., Magneto-mechanical detection of nucleic acids and telomerase activity in cancer cells. Journal of the American Chemical Society, 2004. 126(4): p. 1073-1080.
29. Giessibl, F.J., Advances in atomic force microscopy. Reviews of Modern Physics, 2003. 75(3): p. 949-983.
30. Gosse, C. and V. Croquette, Magnetic tweezers: Micromanipulation and force measurement at the molecular level. Biophysical Journal, 2002. 82(6): p. 3314-3329.
31. Neuman, K.C. and S.M. Block, Optical trapping. Review of Scientific Instruments, 2004. 75(9): p. 2787-2809.
32. Xie, X.S. and J.K. Trautman, Optical studies of single molecules at room temperature. Annual Review of Physical Chemistry, 1998. 49: p. 441-480.

33. Xie, X.S., Single-molecule spectroscopy and dynamics at room temperature. Accounts of Chemical Research, 1996. 29(12): p. 598-606.
34. Weiss, S., Fluorescence spectroscopy of single biomolecules. Science, 1999. 283(5408): p. 1676-1683.
35. Moerner, W.E. and D.P. Fromm, Methods of single-molecule fluorescence spectroscopy and microscopy. Review of Scientific Instruments, 2003. 74(8): p. 3597-3619.
36. Samiee, K.T., et al., lambda-repressor oligomerization kinetics at high concentrations using fluorescence correlation spectroscopy in zero-mode waveguides. Biophysical Journal, 2005. 88(3): p. 2145-2153.
37. van Oijen, A.M., et al., Single-molecule kinetics of lambda exonuclease reveal base dependence and dynamic disorder. Science, 2003. 301(5637): p. 1235-1238.
38. Levene, M.J., et al., Zero-mode waveguides for single-molecule analysis at high concentrations. Science, 2003. 299(5607): p. 682-686.
39. Kuzmenkina, E., Protein folding dynamics: single-molecule studies of Ribonuclease HI on biocompatible surfaces, in Fakultät für Naturwissenschaften. 2005, Universität Ulm. p. 1-118.
40. Ha, T., et al., Initiation and re-initiation of DNA unwinding by the Escherichia coli Rep helicase. Nature, 2002. 419(6907): p. 638-641.
41. Ha, T., Single-molecule fluorescence resonance energy transfer. Methods, 2001. 25(1): p. 78-86.
42. Braslavsky, I., et al., Sequence information can be obtained from single DNA molecules. Proceedings of the National Academy of Sciences of the United States of America, 2003. 100(7): p. 3960-3964.
43. Lee, L.M., et al., Self-aligned immobilization of proteins utilizing PEG patterns. Nanotechnology, 2006. 17(4): p. S29-S33.
44. Green, M.L., et al., Preparation of Poly(Ethylene Glycol)-Grafted Alumina. Journal of Materials Science Letters, 1993. 12(18): p. 1425-1427.
45. Rasnik, I., S.A. Mckinney, and T. Ha, Surfaces and orientations: Much to FRET about? Accounts of Chemical Research, 2005. 38(7): p. 542-548.

46. Korlach J. et al., Selective aluminum passivation for targeted immobilization of single DNA polymerase molecules in zero-mode waveguide nanostructures, PNAS, 2008. 105(4): 1176-1181.
47. Eid, J., et al., Real-Time DNA Sequencing from Single Polymerase Molecules. Science, 2009. 323(5910): p. 133-138.
48. Flusberg, B.A., et al., Direct detection of DNA methylation during single-molecule, real-time sequencing. Nature Methods, 2010. 7(6): p. 461.
49. Uemura, S., et al., Real-time tRNA transit on single translating ribosomes at codon resolution. Nature, 2010. 464(7291): p. 1012.
50. Moran-Mirabal, J.M., et al., Cell investigation of nanostructures: zero-mode waveguides for plasma membrane studies with single molecule resolution. Nanotechnology, 2007. 18(19).
51. Samiee, K.T., et al., Zero mode waveguides for single-molecule spectroscopy on lipid membranes. Biophysical Journal, 2006. 90(9): p. 3288-3299.
52. Rank, D.R., et al., Articles having localized molecules disposed thereon and methods of producing same. United States Patent Application 20080176769.
53. http://en.wikipedia.org/wiki/Isoelectric_point
54. Cristofari, G. and Lingner, J., Telomere length homeostasis requires that telomerase levels are limiting. The EMBO Journal, 2006. 25(3): p. 565-574.
55. Korlach J. et al., Long, Processive Enzymatic DNA Synthesis Using 100% Dye-Labeled Terminal Phosphate-Linked Nucleotides, Nucleosides, Nucleotides and Nucleic Acids, 2008. 27(9): p. 1072-1082.
56. Manual for TRAPEZE® Telomerase Detection Kit - S7700: http://www.millipore.com/userguides/tech1/s7700
57. Foquet, M. et al., Improved fabrication of zero-mode waveguides for single-molecule detection. Journal of Applied Physics, 2008. 103: p. 034301.
58. Jansen, H. et al., Rie Lag in High Aspect Ratio Trench Etching Of Silicon. Mieroeleetronie Engineering, 1997. 35: p. 45-50.
59. Karttunen, et al., Loading Effects in Deep Silicon Etching. P Soc Photo-Opt Ins, 2000, 4174, 90-97.

60. Zhao, M. et al., Afterpulsing and Its Correction in Fluorescence Correlation Spectroscopy Experiments. Appl. Opt. 2003. 42: p. 4031-4036.
61. Burkhardt, M. et al., Electron multiplying CCD based detection for spatially resolved fluorescence correlation spectroscopy. Opt. Express, 2006. 14: 5013-5020.
62. Liao, D. et al., Single molecule correlation spectroscopy in continuous flow mixers with zero-mode waveguides. Opt. Express, 2008. 16: 10077-10090.

Chapter 3

Towards 3D Single Molecule Tracking Using Microfabricated Mirrors

Zhuangxiong Huang, David Dulin, Jelmer Cnossen, Jacob Kerssemakers, Sumit Sachdeva,

Matthew Pierotti and Nynke H. Dekker

In order for molecular biologists to fully study subcellular processes, fluorescence microscopy techniques capable of tracking single molecules or particles in 3D are highly desired. Though many methods have been devised to solve this problem, there is typically a trade-off between factors such as design complexity, accuracy, and temporal resolution. In this report, we discuss our work on the development of a technique implementing microfabricated mirrors to reflect axial planes into the imaging plane of the system. Advantages of this technique include its simplicity and modularity, that it simultaneously allows tracking in 3 dimensions, and that by reflecting the axial plane into the image plane we may approach typical planar tracking accuracy in the order of 1 nm. We will first present our approaches for microfabrication of mirrors, then discuss in detail our novel tracking algorithm.

3.1 Introduction

In the last twenty years, technological advances have allowed molecular biologists to perform single molecule studies on the machinery of the cell. These studies are significant because the technical precision required for such experiments yields information with high resolution in both space and time. Additionally, they avoid averaging results over large populations, allowing for one to study highly transient states with potentially critical functionality. Such information provides new insight into important subcellular processes such as signal transduction networks and the central dogma of molecular biology. Several types of techniques for studying single molecule systems have gained prominence in this field, in particular fluorescence microscopy.

Fluorescence microscopy has become a cornerstone of single molecule studies for its ability to study systems both in vitro and in vivo. For example, it has been used to observe the hand-over-hand motion of the translational motor myosin [1], diffusion of membrane proteins [2], and the movement of β-actin mRNA during transport from the nucleus to cytoplasm [3]. To perform these studies, particularly those conducted in vivo, very high demands are placed on the ability to image and more specifically to localize and track an object of interest, which may itself be a single molecule spanning several nanometers. As a result, methods have been developed with localization precision on the order of one nanometer in a 2D imaged plane. However, biological processes occur in a 3D environment, it would be ideal to have accurate localization in all 3 dimensions. Since the microscope projects the 3D world onto a 2D image, finding the Z coordinate requires additional measurements and processing. A variety of methods have been developed to perform 3D imaging and localization using fluorescence microscopy, but there are significant differences between them.

First of all, a number of methods for 3D imaging using fluorescence are based on confocal microscopy (such as Hell et al. [4]), in which a scanning laser is used to excite only a small part of the sample. This greatly reduces the background noise coming from out-of-focus fluorophores. Compared to wide-field microscopy, confocal microscopy is well suited to 3D scanning of larger structures, but suffers from higher photon damage to the sample and a slower speed (as it takes time to move the beam back and forth over the sample).

In recent years, a few novel methods for acquiring Z positions of fluorophores have emerged. The main idea behind these methods is to modify the point spread function (PSF) using various optical methods in such a way that it contains information about the Z position that can be extracted. Astigmatic lenses are used to create an elliptical point-spread-function, whose shape depends on the Z position. The Z position can then be extracted by fitting this PSF to the image. This method has been used in 3D tracking of quantum dots (Holtzer et al. [5]) and localization microscopy, by Huang et al. [6] in their STORM method (Stochastic optical reconstruction microscopy). Toprak et al. [7] use bifocal microscopy, in which two light paths with a different focal depth produce two images. The Z position of emitters is then inferred from the sizes of the spots on each image. Sun et al. [8] also use a bifocal approach, but unlike Toprak et al. [7] their approach is set up in such a way that a displacement in Z of the molecule causes a displacement in Y in the measured images. Quirin et al. [9] and Rama

et al. [10] use a spatial light modulator (SLM) device to create a point-spread-function with 2 spots that rotate when the Z coordinate of the emitter is changed. Interestingly, these localization methods can be combined with fluorophore blinking techniques, to be able to isolate and localize each molecule individually (this is referred to as super-resolution fluorescence microscopy, used in methods such as PALM [11], STORM [12], or their successors [13]).

As mentioned, each of the listed methods has modified the regular optical system in such a way that the PSF depends on Z. However, this information about Z comes at a cost. Some of the considerations are: The Z accuracy can be much lower than the X & Y accuracy (e.g. in the astigmatic method); Splitting or modification of the optical path results in a loss of photons along the way (in the bifocal methods or methods using an SLM); It complicates the optical system, leaving less room for additional features (such as in multicolor imaging). To conclude, room for improvements in 3D localization remains.

Micromirrors for 3D Tracking

A conceptually simple solution to the problem of z-localization of a fluorophore is a smart placement of mirror surfaces. Figure 1 (*left*) illustrates that with mirrors oriented at 45° to the imaged plane, the reflections of a fluorescent object will translate z-motion of the object to motion relative to the mirror surface, denoted as the x axis. Localization of the true fluorophore image will give an x,y position, which in turn will allow for the calculation of z position from the localization of the reflections following simple geometrical arguments. Therefore, the localization accuracy in z could be in principle as good as the accuracy in x axis, which is in the order of 1 nm.

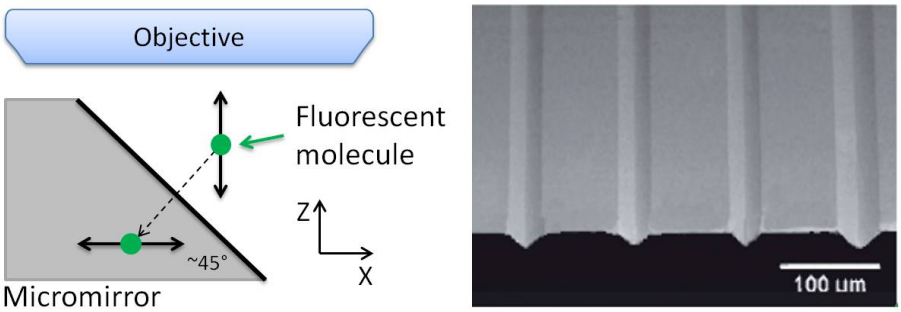

Figure 1. Micromirror. (*left*) A schematic of the micromirror design illustrating the concept of reflecting the plane oriented along the optical axis of the objective into the imaging plane. (*right*) SEM image of microfabricated V-groove micromirrors as made by Hajjoul et al. [14].

The use of this idea in fluorescence microscopy was introduced by McMahon et al. [15] who used a pyramidal micromirror well to do fast 3D particle tracking. In addition to 3D tracking, 3D live cell imaging using V-groove micromirrors (Figure 1, r*ight*) was demonstrated by Hajjoul et al. [14]. V-groove micromirror is particularly attractive for its modularity: it is compatible with flow cells so that life cells can be flooded into the V-groove channels after construction; it can be combined with typical epifluorescence microscopy

setups without any modification to the optics. Additionally, it is interesting to note that the micromirrors actually increase the number of photons collected, which determines the limit of the localization accuracy.

So far, micromirrors have been typically fabricated by wet etching of (100) or (110) silicon wafers to reveal the {111} crystal planes, whose angle relative to the wafer surface plane are 54.7° for (100) wafer, and 35.3° for (110) wafer [16]. If an exact 45° mirror is desired, in theory, one could try to wet-etch a (100) silicon wafer to reveal {110} crystal planes. However we find, both in practice and in literature, that the resulting {110} facets either are too rough to be used as a mirror [17], or do not appear as straight plane anymore [18]. A better strategy for making 45° mirrors is to reveal {111} crystal planes on silicon wafers that are cut 9.7° off the [l00] axis [19]. One of the main advantages of this approach is that the fabrication protocol that applies to regular (100) silicon wafers can be used without any modification for the off-axis wafers. Our fabrication protocol and results for both regular 54.7° mirrors and perfect 45° mirrors will be presented in details in section 3.2.

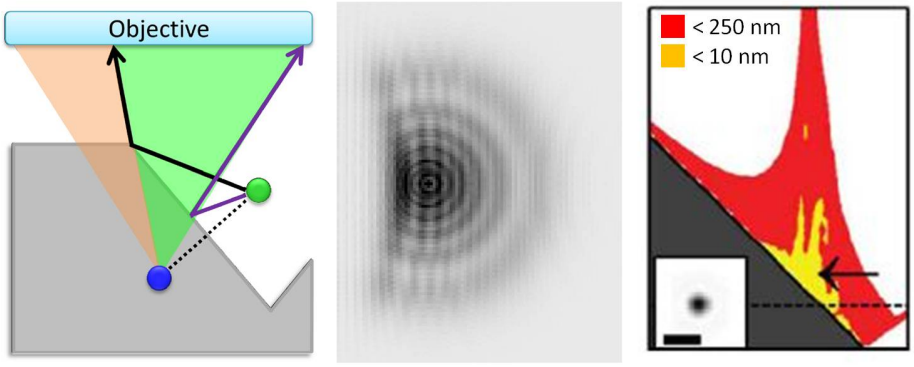

Figure 2. The limited height of the micromirrors allows for some rays to pass the mirror plane unreflected (*left*), causing asymmetric aberrations in the reflected images (*middle*). The green sphere indicates the bead and the blue sphere represents the position of the virtual bead image created by reflections. The pink triangle indicates the light paths that would normally travel to the objective, but are now cut-off due to the finite size of the left mirror surface. (*right*) Simulation results of Berglund et al. [20]: typical contour plot showing the regions where absolute tracking errors are below 10 nm (yellow region) and below 250 nm (red region).

Although the idea of reflecting the axial plane into the image plane so as to approach typical planar tracking accuracy of ~1 nm sounds straightforward, previous work on tracking diffraction-limited fluorescent beads using pyramidal micromirror wells [15] indicated that a systematic error in tracking could reach up to 20% of the total distance traveled when typical localization techniques such as center of mass and Gaussian fitting are used. They determined that the origin of this error is largely the geometry of the micromirror setup. Berglund et al. [20] performed several optics simulations taking into account this geometrical effect as well as diffractive effects (Figure 2, *left* and *middle*). From their simulations they concluded that one could reduce the tracking error to around 10 nm by adjusting the numerical aperture and mirror angle, and by using only objects located deep within a well (Figure 2, *right*). However, their predictions are based on errors using center-of-mass tracking method, which is in nature

more suitable for symmetric diffraction pattern (e.g. Airy-disk) than for images with asymmetric aberrations: because it is asymmetric the actual particle position will not be at the center of the shape (Figure 2, *middle*). Therefore, we have been developing novel tracking algorithms for micromirrors to attempt to increase z-axis accuracy when the PSF is truncated, and to avoid restrictions from mirror angle, numerical aperture, and especially object location. This work will be presented in section 3.4.

3.2 Micromirror Fabrication

We have developed a protocol based on electron-beam lithography and silicon wet etching for fabrication of micromirrors using either regular (100) silicon wafers (4-inch, University Wafer, USA) for 54.7° mirrors, or off-axis cut silicon wafers (<100> off 9.7° to <110> ± 0 9°, 4-inch, Virginia Semiconductor Inc. USA) for 45° mirrors. Here we will describe our process flow in details (Figure 3).

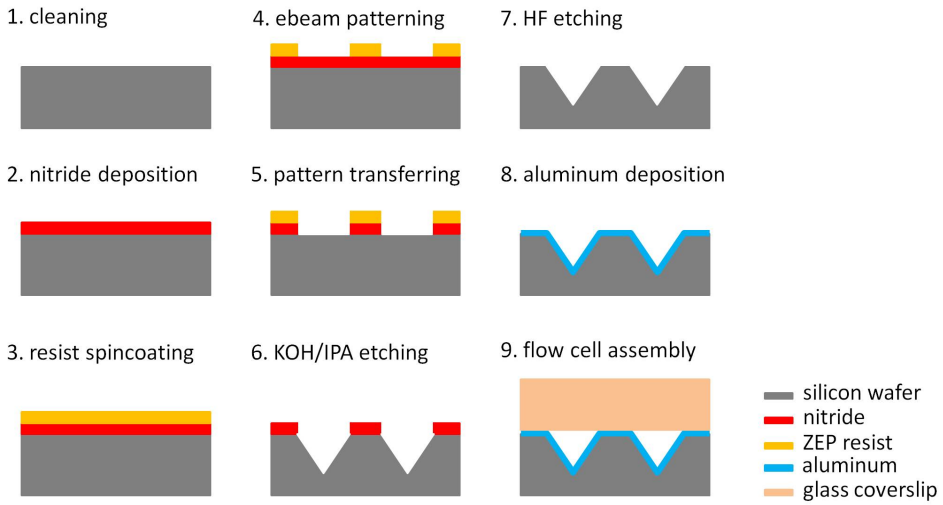

Figure 3. Process flow for the fabrication of micromirrors. (step 1) Clean silicon wafer. (steps 2-5) Nitride mask is patterned using electron beam lithography and prepared for wet etching. (steps 6-7) Wet etch of silicon substrate in KOH/IPA hot bath to form micro-channels and reveal mirror facets. (step 8) Aluminum is deposited on micromirror surface to enhance reflectivity. (step 9) Micromirror is assembled into flow cell.

First, the wafer was ultrasonically cleaned (Figure 3, step 1) in fuming nitric acid (100% HNO3) for 10 min, rinsed in deionized (DI) water and spun dry. Then a 50 nm Si_3N_4 layer was deposited at 300°C on the polished side of the wafer (Figure 3, step 2) using a PECVD system (Plasmalab 80 Plus, Oxford Instruments Plasma Technology, UK). Followed the Si_3N_4 deposition, a 450-nm layer of ZEP520A positive electron-beam resist (ZEON Corporation,

Japan) was spin-coated onto the wafer at 2000 rpm for 55 s and baked for 3 min at 175°C. At this point, the sample is ready for patterning (Figure 3, step 3).

Feature patterning is performed on a Leica EBPG 5000+ (acceleration voltage 100 kV, aperture 400 μm). A beam of approximately 257 nA (which corresponds to an estimated beam size of approximately 135 nm), a beam step size of 100 nm, and a dose of approximately 200 $\mu C/cm^2$ were typically used. Following electron-beam exposure, the sample was developed in N-amylacetate for 90 s with mild agitation. They were then rinsed with isopropanol for about 10 s immediately after development and dried with nitrogen. At this point, the patterns were revealed (Figure 3, step 4) and ready to be transferred to the Si_3N_4 layer to define a wet-etch mask.

The pattern in the resist was transferred into the Si_3N_4 mask layer (Figure 3, step 5) using an inductively-coupled-plasma (ICP) reactive-ion etcher (Adixen AMS100 I-speeder) with a mixture of 20 sccm C_4F_8 and 10 sccm CH_4, diluted in 100 sccm He. The ICP source power equaled 2500 W, and the substrate bias RF power equaled 300 W. The pressure was maintained as low as possible, ~1 Pa. The temperature was maintained at 0 °C for the sample holder and 200 °C for the chamber. Under these settings, the etching rate of Si_3N_4 was ~80 nm/min. Therefore, 1 min is typically sufficient to complete the pattern transferring. After pattern transferring, the resist was removed by sonication for 1 min in dimethylacetamide, rinsed with isopropanol and dried with nitrogen. At this point, the wafer was ready for dicing into individual chips.

Prior to wafer dicing, a 2-μm layer of AZ5214E photoresist (MicroChemicals GmbH) was spin-coated onto the wafer at 2000 rpm for 55 s and baked for 1 min at 90°C. This thick photoresist layer protected the Si_3N_4 mask surface from scratching by debris particles during dicing. The wafer was diced into individual 24mm×60 mm (standard glass coverslip size) rectangular plates using a Disco Dicing Saw (model: DAD3220) with a 50 μm blade (Disco NBC-Z series). After dicing, the silicon plates were removed from the adhesive tape manually and the protective photoresist layer was removed by immersing the silicon plates in an ultrasonic bath of acetone (alternatively, fuming HNO_3) for 10 min, rinsed in deionized (DI) water and spun dry. At this point the silicon plates were ready for wet etching.

Following the dicing, the silicon plates were anisotropically etched in a KOH/IPA bath (4 parts of KOH 36% wt/wt aqueous solution mixed with 1 part of IPA) at 80°C for 30 min, yielding V-groove channels (Figure 3, step 6) on the patterned areas (long strips along <110> direction). During etching, the solution was continuously stirred using a magnetic stirrer and the temperature was well regulated to avoid overheating (note that the boiling point of IPA is only 82.5°C). The etching rate of silicon along <100> direction under these conditions is about 1 μm/min. The etch stop for KOH is the Si (111) crystal plane, whose angle relative to the (100) surface plane is 54.7° (Figure 4, *left*). For (100) silicon wafers, the maximum possible depth of a channel (along <110> direction) is determined by the channel width, e.g. the maximum possible depth for a channel width of 60 μm is 30 μm /sin54.7° = 24.5 μm. We typically set the total etching time to slightly over-etch the channels so as to make sure the maximum possible depth of the channels was reached. For off-axis wafer, since the wafer surface is not an exact (100) crystal plane, there will be some undercutting under the Si_3N_4 mask, resulting in widening of the channels, e.g. a 45-μm design width of the channel (along

<110> direction) will have a widening of about 8 μm after 45 min of wet etching in KOH/IPA hot bath (Figure 4, *right*). In contrast, the widening of the channels on a (100) wafer is hardly visible under the same etching conditions (Figure 4, *left*). It would be recommended to take into account the widening when designing mask patterns for etching of off-axis wafers.

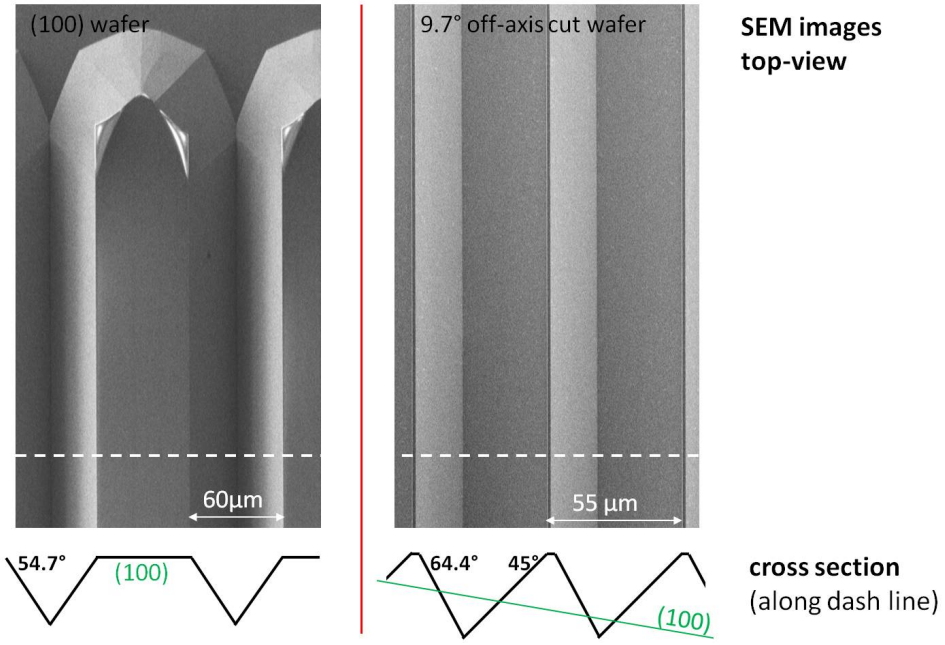

Figure 4. SEM images of micromirrors fabricated using our process flow (Figure 3) (*left*) micromirror fabricated using (100) silicon wafer (Si_3N_4 mask not removed): the V-groove channels were formed by wet etching of silicon through strip-like mask openings along <110> direction. The mirror facets were defined by the etch stop at (111) planes, which were revealed symmetrically about the centerline of the channels, and have an identical 54.7° angle relative to the (100) plane (wafer surface). The surface topology of the micromirror (along white dash line) is plot below the SEM image. The resulting channel width is the same as the designed width in mask openings (60 μm). In other words, the undercutting under the Si_3N_4 mask is basically ignorable. (*right*) micromirror fabricated using 9.7° off-axis cut silicon wafer (Si_3N_4 mask removed): similar to wet etching of (100) wafer, the mirror channels were defined by strip-like mask openings along <110> direction, and the mirror facets were also revealed on (111) planes, which have either 54.7°-9.7°=45° or 54.7°+9.7°=64.4° relative to the wafer surface. So the V-groove is asymmetric, as illustrated by the plot of surface topology below the SEM image. The off-axis cut wafer suffered from significant undercutting under the Si_3N_4 mask. In this specific example, the designed width of the channels was 45 μm (and pitch equals 55 μm), while the resulting channel width after 45 min of wet etching was about 53 μm, i.e. about 8-μm undercutting in total.

Following wet etching, the silicon plates were immersed in a 10% HF aqueous solution for 20 min to remove contaminant particles (byproducts of KOH wet-etching) and to remove the Si_3N_4 mask layer (Figure 3, step 7), rinsed in deionized (DI) water and spun dry. At this point atomically flat and mirror-like surfaces were created on the walls of V-groove channels.

To enhance the surface reflectivity, a 200-nm layer of aluminium was then deposited onto the micromirror surfaces (Figure 3, step 8) using a Temescal FC-2000 evaporation system.

The pressure set-point to start evaporation was $2x10^{-6}$ mbar, and the evaporation rate was maintained at 2 Å/s. If it is desired to passivate the aluminum surface to avoid erosion, a layer of 1000 nm SiO_2 can be deposited using a PECVD system (Plasmalab 80 Plus, Oxford Instruments Plasma Technology, UK). At this point, the V-groove micromirror plate was ready to be assembled into a flow cell.

The first step of flow-cell assembling is to fabricate the inlet and outlet ports. This was done by drilling two through holes of ~1-2 mm in diameter at the two ends of the V-groove channels, using a Danville PrepStart sandblaster system. Then, the V-groove micromirror surface was glued to a cover glass of the same size (24mm×60 mm) using a UV-cured adhesive (Norland Optical Adhesive 81). The adhesive was applied as little as possible and only on the non-channel area. To fully cure the adhesive, the micromirror flow cell is placed under a UV lamp (NORLAND wavelength 365 nm), illuminating for 1 hour through the cover glass onto the adhesive sandwiched between the glass and micromirror plate. At this point, the micromirror flow-cell assembly is completed (Figure 3, step 9), and the device is ready to connect with tubings and be mounted on a microscope for further experiments.

3.3 Fluorescence Imaging using Micromirror

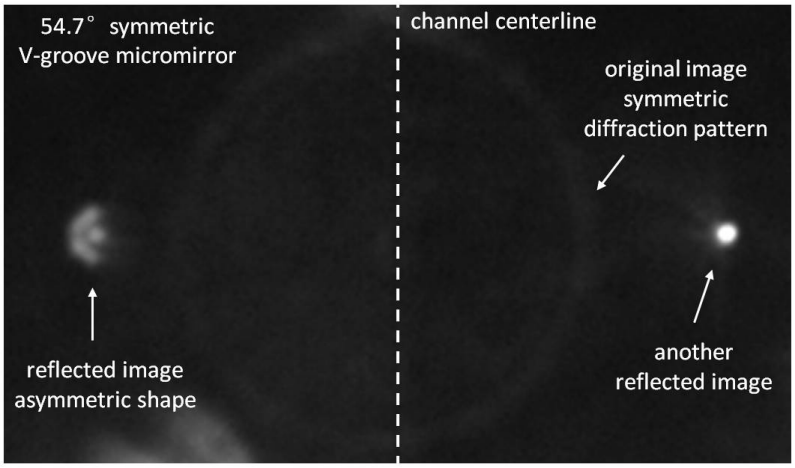

Figure 5. Image of a fluorescent particle in a 54.7°-symmetric V-groove micromirror: the centerline of the V-groove channel is presented as a dash line. The original image of the particle appears as a big symmetric diffraction disk, indicating that the particle is out of focus. The mirror-reflected images appear asymmetric due to asymmetric aperture cut-off imposed by micromirror geometry (Figure 2, *left*).

We now demonstrate the applicability of micromirror flow-cell assembly for imaging of fluorescent particles. To do so, a flow-cell assembly using a 54.7°-symmetric micromirror (Figure 4, *left*) was filled with a dilute aqueous solution of 40-nm fluorescent particles (FluoSpheres F8766, 1% solids, Invitrogen), and mounted on a wide-field fluorescence

microscope (IX71, Olympus, Japan) equipped with a mercury arc lamp, a 60X 1.45N.A. objective (PlanApo 60X/1.45oil TIRFM, Olympus, Japan), and an Andor EM-CCD camera for detection (iXonEM DV887ECS-BV, Andor Technology, South Windsor, CT). Figure 5 shows a frame from a typical movie of a single fluorescent particle diffusing in a micromirror channel. In this specific case, the particle is out of focus; therefore its original image appears as a big symmetric diffraction circle. The particle has two additional images due to reflections on mirror facets. These two reflected images appear brighter and smaller because their virtual positions are closer to the focal plane. As also explained previously (Figure 2, *left*), due to the asymmetric aperture cut-off imposed by micromirror geometry, the reflected images appear asymmetric.

3.4 3D Tracking Algorithm

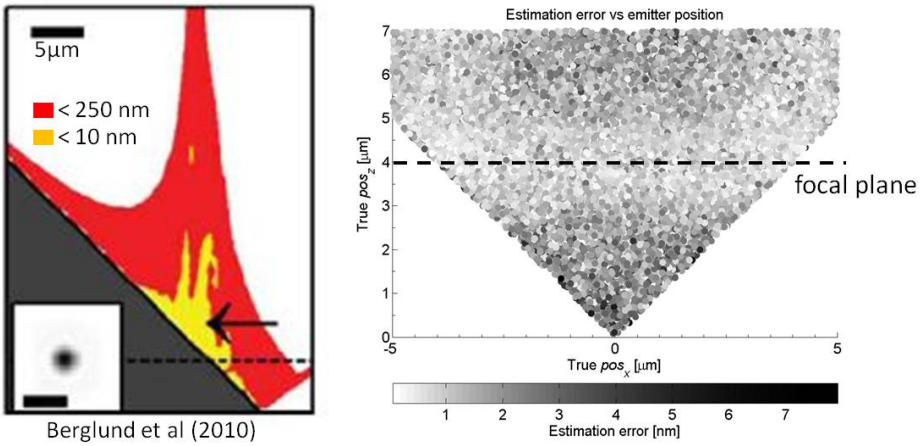

Figure 6. Numerical simulation results of position-dependent tracking error in micromirror. (*left*) a typical contour plot of tracking error using Berglund's center-of-mass method [20]: showing the regions where absolute tracking errors are below 10 nm (yellow region) and above 10nm but below 250 nm (red region). In this simulation: N.A.= 0.95, mirror angle = 45°. (*right*) a typical grey-scale plot of tracking error using our MLE method: the tracking error remains below 10nm everywhere in the mirror channel, showing much less position dependency. In this simulation: N.A.= 1.2, mirror angle = 45°.

Our method for 3D tracking of single molecule using micromirror is described in detail in J. Cnossen's master thesis [21]. Briefly speaking, our tracking algorithm is based on maximum likelihood estimation (MLE), namely, fitting the image data to a parameterized optical model to provide estimates for parameters (particle position: X, Y, Z) that result in such particular image. MLE is believed to make optimal use of the information embedded in the image data [22]. Our parameterized optical model is developed based on the work done by Berglund et al [20], accounting for optical aberrations and the fact that the mirror geometry causes an asymmetric angular truncation within the imaging system (Figure 2, *left*). Despite

using a similar optical model, our MLE approach for obtaining particle position information from image data is fundamentally different from Berglund's center-of-mass fitting method. For an asymmetrically-truncated point spread function (Figure 2, *middle*), the center of the shape is by nature not the same as the projected position of the point source, and the distance between these two is typically larger for a larger diffraction pattern (i.e. further out of focus). This is the systematic error in Berglund's center-of-mass tracking method. As shown in Figure 6 (*left*), in Berglund's method, to achieve tracking errors less than 10 nm, the particle needs to be restricted in a small region near the mirror surface (less asymmetric truncation in diffraction pattern) and close to the focal plane (smaller diffraction pattern). In contrast, our MLE tracking method has no such systematic error and the tracking accuracy is much less position-dependent (Figure 6, *right*).

3.5 Conclusion

We have developed a method based on electron beam lithography and wet etching of single-crystal silicon for the fabrication of V-groove micromirrors. 54.7°-symmetric V-groove micromirror was fabricated using regular (100) silicon wafer. To fabricate a mirror facet 45° relative to wafer surface, an off-axis cut silicon wafer (<100> off 9.7° to <110>) was used. We have demonstrated that our V-groove micromirrors could be assembled into flow cell structures for imaging single fluorescent particles. We have also been developing a novel algorithm based on maximum likelihood estimation for 3D tracking of single molecule/particle using micromirrors. Our simulation results demonstrated that our MLE tracking method outperformed center-of-mass tracking method as developed by Berglund et al.

3.6 References

1. Yildiz A., et al., Myosin V Walks Hand-Over-Hand: Single Fluorophore Imaging with 1.5-nm Localization, Science, 300 (5628): 2061-2065, 2003.
2. Ghosh, R.N. et al., Automated detection and tracking of individual and clustered cell surface low density lipoprotein receptor molecules, Biophysical Journal, 66(5):1301-1318, 1994.
3. Grunwald D., et al., In vivo imaging of labeled endogenous β-actin mRNA during nucleocytoplasmic transport, Nature, 467: 604-607, 2010.
4. Hell, S.W. et al., Diffraction-unlimited three-dimensional optical nanoscopy with opposing lenses, Nature Photonics, 3(7):381-387, 2009.

5. Holtzer, L., et al., Nanometric three-dimensional tracking of individual quantum dots in cells, Applied Physics Letters, 90(5):053902, 2007.
6. Huang B., et al., Three-dimensional super-resolution imaging by stochastic optical reconstruction microscopy. Science, 319(5864):810-813, 2008.
7. Toprak, E., et al., Three-dimensional particle tracking via bifocal imaging. Nano letters, 7(7):2043-5, 2007.
8. Sun, Y. et al., Parallax: high accuracy three-dimensional single molecule tracking using split images, Nano letters, 9(7):2676-82, 2009.
9. Quirin, S., et al., Optimal 3D single-molecule localization for super-resolution microscopy with aberrations and engineered point spread functions, PNAS, 109(3):675-9, 2012.
10. Rama, S. et al., Three-dimensional, single-molecule fluorescence imaging beyond the diffraction limit by using a double-helix point spread function, PNAS, 106(9), 2009.
11. Betzig, E., et al., Imaging intracellular fluorescent proteins at nanometer resolution. Science, 313(5793):1642-5, 2006.
12. Bates, M. et al., Multicolor super-resolution imaging with photo-switchable fluorescent probes, Science, 317(5845):1749-53, 2007.
13. Burnette, D.T., et al., Bleaching/blinking assisted localization microscopy for superresolution imaging using standard fluorescent molecules. PNAS, 108(52):21081-6, 2011.
14. Hajjoul, H., et al., Optimized micromirrors for three-dimensional single-particle tracking in living cells, Applied Physics Letters, 98(24):243701, 2011.
15. McMahon, M.D., et al., 3D particle trajectories observed by orthogonal tracking microscopy. ACS nano, 3(3):609-614, 2009.
16. Hajjoul, H., et al., Lab-on-Chip for fast 3D particle tracking in living cells, Lab on a Chip, 9: 3054–3058, 2009.
17. Resnik D., et al., The role of Triton surfactant in anisotropic etching of {1 1 0} reflective planes on (1 0 0) silicon, J. Micromech. Microeng, 15:1174–1183, 2005.

18. Xu Y.W., et al., Formation of ultra-smooth 45° micromirror on (1 0 0) silicon with lowconcentration TMAH and surfactant: Techniques for enlarging the truly 45° portion, Sensors and Actuators A, 166:164–171, 2011.
19. Strandman C., et al., Fabrication of 45° Mirrors Together with Well-Defined V-Grooves Using Wet Anisotropic Etching of Silicon, Journal of Microelectromechanical Systems, 4:213-219, 1995.
20. Berglund, A. J. et al., Theoretical model of errors in micromirror-based three-dimensional particle tracking, Optics Letters, 35(11):1905-1907, 2010.
21. Cnossen, J., 3D Single Molecule Localization Using Micromirrors, Master Thesis, TU Delft, 2012.
22. Mortensen, K. I. et al., Optimized localization analysis for single-molecule tracking and super-resolution microscopy, Nature Methods, 7 (5):377-381, 2010.

Chapter 4

Electron Beam Fabrication of a Microfluidic Device for Studying Submicron-Scale Bacteria

Charl Moolman†, Zhuangxiong Huang†, Sriram Tiruvadi Krishnan, and Nynke H. Dekker

(†=equal contribution)

The ability to restrict the movement of cells in a controlled manner using microfluidics, allows one to study individual cells and gain added insight into aspects of their physiology and behaviour that can potentially be hidden in ensemble averaging experiments. For example, the use of micron-sized growth channels that restrict movement of Escherichia coli (E. coli) has yielded novel insights into cell growth and death. A similar approach could be applied to many other species of bacteria. However, since the size of bacteria is dependent on the growth conditions and a significant fraction of bacterial species has dimensions in the sub-micron range, a readily-fabricated device with sub-micron features is required. Here we describe a detailed fabrication protocol of such a device that has growth channels with widths ranging from 0.3 μm to 0.8 μm. This range yields a versatile device that can potentially be used to study a variety of submicron-sized bacteria. The device is fabricated using electron beam lithography, as this provides excellent control over the shape and size of these different growth channels and facilitates the rapid-prototyping of new designs. We demonstrate that the structures can successfully be fabricated in both silicon and polydimethylsiloxane. To illustrate the utility of our microfluidic device, we confirm the wettability of the growth channels using fluorescence microscopy and as a proof-of-principle show that the sub-micron scale bacterium Lactococcus lactis can be grown in the growth channels for several generations.*

* This chapter has been submitted for publication.

4.1 Introduction

The use of microfluidics in biological research has gained much popularity in recent years. Subfields that have been impacted by this technology range from tissue engineering (1), cancer stem cell research (2), gene expression of embryonic stem cells (3), protein interactions (4), diagnostic medicine (5) as well as microbial physiology and behaviour (6 - 8), to name but a few. A specific contribution to the field of microbiology is the ability to observe and manipulate single cells with excellent control. Individual cells can significantly differ from one another in terms of their biochemistry and genetics (9). The ability to observe individual cells under controlled conditions provides one with the ability to investigate the individual functioning of cells as well as their mutual behaviour (10 - 16). Additionally, the use of microfluidics has facilitated the study of molecular behaviour inside individual cells, as demonstrated by Taniguchi et al. (17) in their study of protein and mRNA expression at the single-molecule level inside individual living cells.

Recently Wang et al. (18) utilized a microfluidic device (which they named "the mother machine") to quantitatively study steady-state growth and division of individual Escherichia coli (E. coli) cells at a defined reproductive age. Such a device made it possible to study a large number of cells that inherit the same cell pole over multiple generations. In their design, cells were confined in growth channels oriented perpendicularly to a trench through which growth medium was pumped. The width and height of the channels were similar to the dimensions of E. coli, which has a diameter of ca. 1 μm and a length of ca. 2.5 μm in typical growth conditions (19, 20). Cells were immobilized, without chemical fixation, at the far end of such a growth channel (ca. 25 μm in length) due to the walls on the sides and the other cells that grew in front of them. The length of the growth channel was chosen so as to ensure sufficient supply of nutrients to the bacteria by diffusion. This type of immobilization scheme allows one to study numerous different cells for extensive periods of time.

A microfluidic device that allows one to investigate multiple individual bacteria in a precise manner is a powerful tool for microbial studies and can potentially be used to research various processes in different species of bacteria, including ones that are significantly smaller than E. coli. Many bacterial species have sub-micron scale dimensions, including e.g. Mycoplasma (diameter 0.2 - 0.4 μm (21)), Prochlorococcus (diameter 0.5 - 0.7 μm (22)), and Lactococcus lactis (diameter of ca. 0.75 - 0.95 μm (23)), for which growth channels would require significantly reduced widths. A single device with growth channels of variable widths would furthermore provide maximal flexibility for studying different types of bacteria under for example various growth conditions without further modifications. A recent advance along these lines described the fabrication of sub-micron channels in agarose (24). However, both this approach as well as the device utilized by Wang et al. are fabricated using conventional photolithography. While this is a widely available and convenient technique, for the fabrication of devices with smaller dimensions it becomes more cumbersome and alternative approaches such as electron beam lithography (EBL) (25) become more suitable. EBL can readily fabricate smaller features (ca. 20 nm in lateral dimensions) compared to conventional photolithography (ca. 1 μm) (26), while simultaneously affording greater control of the

structure size and shape. An additional advantage of EBL is the reduced time from design to final device, which is convenient in a research environment where it is frequently required to change and improve a device on a relatively short time scale. The structural control and rapid-prototyping needs are thus more easily met by EBL than by conventional photolithography.

Here we present an EBL and poly(dimethylsiloxane) (PDMS) (27) soft-lithography (28) protocol for the fabrication of such a microfluidic device for microbial studies. PDMS has a number of attractive features, which makes it an excellent material for fabricating microfluidic devices (26). Here we make use of the fact that sub-micron sized structures down to ca. 100 nm can be made in PDMS (29). It is worthwhile to remark that even smaller structures, sub-100 nm, can be fabricated in PDMS using a composite two-layer process consisting out of a thick "typical" PDMS layer and a thin h-PDMS ("hard" PDMS) layer (30).

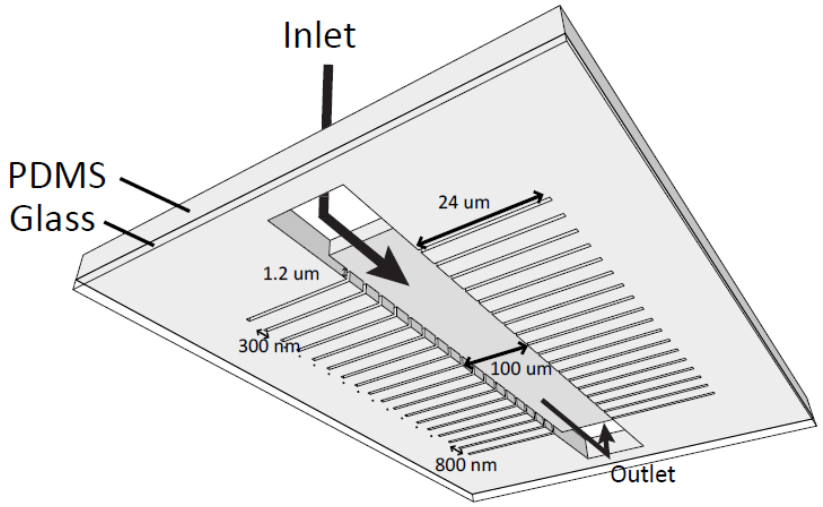

Figure 1. Schematic overview of the final PDMS device together with bound cover glass (not to scale). Dimensions are as follows: the main trench has a width of 100 µm and a length of 12.5 mm, growth slits are 24 µm long and 1.2 µm deep, while their widths range from 0.3 µm to 0.8 µm.

We have designed a device that contains channels of variable widths ranging from 0.3 µm to 0.8 µm (Figure 1). This range of widths takes into consideration the typical range of sizes of sub-micron scale bacteria. We demonstrate successful fabrication by characterizing both the silicon (Si) and the PDMS structure using scanning electron microscopy (SEM). We demonstrate the utilization of the device by injecting fluorescent dye into the channels and imaging the resulting fluorescence, and we also show that the gram-positive bacterium, Lactococcus lactis (L. lactis), can successfully be loaded into the channels and grown for several generations as a proof-of-principal.

4.2 Device Fabrication

The fabrication of the device contains three principal steps (Figure 2). Firstly, we etch the pattern of the device into a 4" silicon (Si) wafer (Figure 2, Step 1). We accomplish this by employing EBL together with specific dry etching protocols. Secondly, we use PDMS to create a negative mold of the structure that was fabricated in the Si wafer (Figure 2, Step 2). Finally, we make use of this PDMS mold to fabricate the final device in PDMS (Figure 2, Step 3). To optimize yield, we employ a wafer that is far larger than the size of a single device structure. This allows us to perform all steps of the fabrication procedure while preparing multiple individual devices (in our current protocol 24 in total) in parallel. The only step excepted from the parallel approach is the final bonding step (of glass to PDMS), which is carried out for each device individually. A slightly different approach would involve the fabrication of a negative (as opposed to a positive) Si mold, thereby reducing the number of PDMS steps. We do not favor such a protocol as one would need to fabricate the small growth channels ca. 25 μm into the Si wafer. In the following subsections we describe the fabrication in Si (section 2.1) and PDMS in detail (section 2.2).

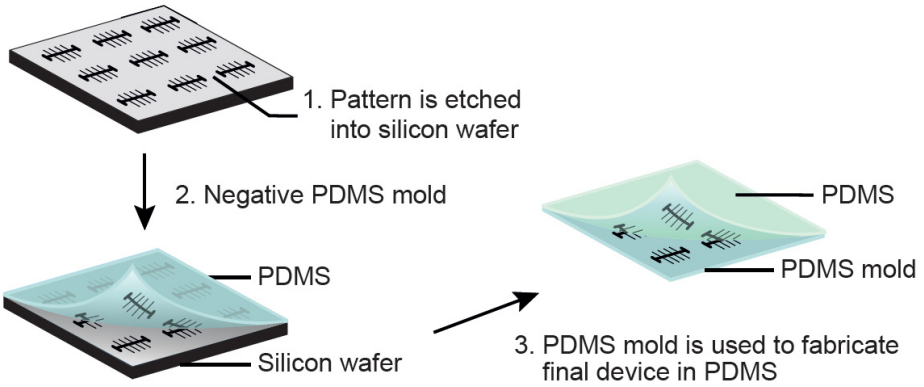

Figure 2. Schematic overview of the three principal steps. (Step 1) The patterns are etched into a 4" silicon wafer. (Step 2) The silicon wafer is used as a mold to fabricate the negative structures in PDMS. (Step 3) The PDMS mold is subsequently used to fabricate the final structures in PDMS. For simplicity we depict only 9 structures (whilst typically a wafer contains 24).

Fabricating the structure in silicon: EBL and dry etching

The main steps we perform in fabricating the structures in Si are depicted in Figure 3. We fabricate the structures into a 4" diameter Si wafer (University Wafer, USA). We first fabricate the small growth channels, followed by the main trench. In the first step, we ultrasonically clean the wafer in fuming nitric acid (100% HNO_3) for 15 min (Figure 3, Step 1), rinse in deionized (DI) water, and spin dry. We then subsequently prime the wafer surface for resist adhesion using hexamethyldisilazane (HMDS) by spin-coating at 3000 rpm for 1

min (Figure 3, Step 2). After this, we spin-coat a layer of approximately 2.2 µm thick poly(methyl methacrylate) (PMMA) 950K A11 positive electron-beam resist onto the wafer at 3000 rpm for 1 min and bake it for 2 min at 100°C and for 10 min at 175°C. (Figure 3, Step 3).

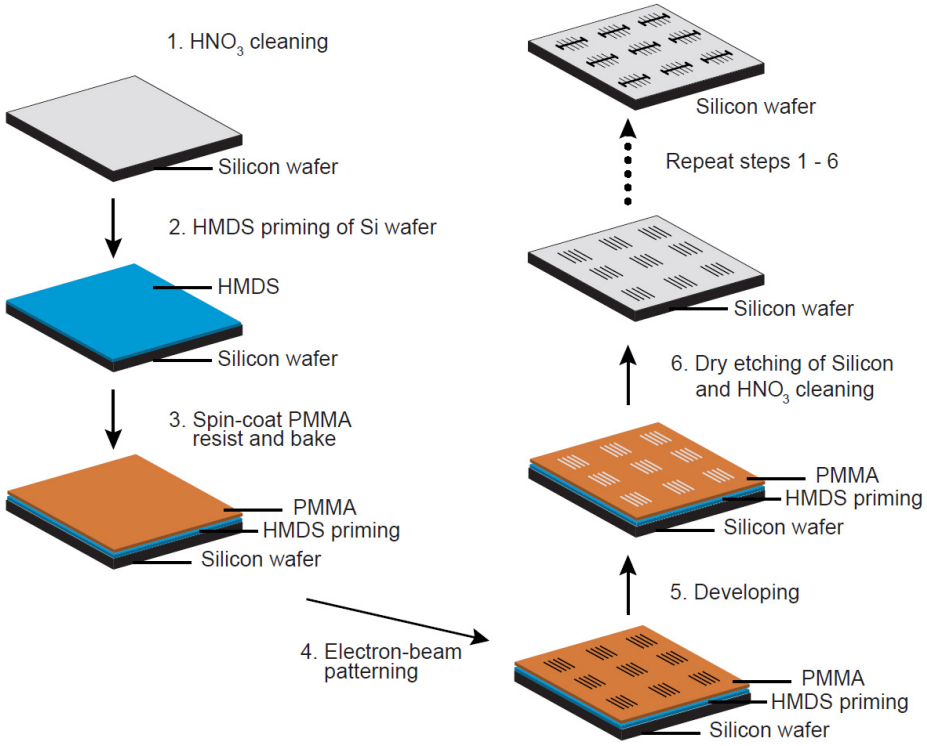

Figure 3. Schematic of the fabrication of multiple structures in Si with sub-micron size growth channels using EBL and dry etching. The growth channels are etched first, followed by the main trench. The steps to conduct this are as follows. (Steps 1-3) A 4" silicon wafer is cleaned and prepared for electron beam patterning. (Steps 4-5) Specific regions of the PMMA is exposed to the electron beam and developed. (Step 6) Dry etching of the structures into the wafer is performed. This whole process is then repeated to etch the main trench into the silicon wafer.

The first pattern, i.e. the small growth channels, can now be written into the wafer (Figure 3, Step 4). We make use of a Leica EBPG 5000+ (acceleration voltage 100 kV, aperture 400 µm) to write the pattern on the wafer. Here we use a spot size of ca. 25 nm and a current of ca. 46 nA. We choose the beam step size (BSS) to be 20 nm and the dose 1400 µC/cm^2.

Following electron beam exposure, we develop the exposed PMMA (Figure 3, Step 5) by using methyl isobutyl ketone (MIBK) and isopropyl alcohol (IPA). We place the wafer in a beaker containing a 3:1 ratio of IPA and MIBK and leave it in there for 60 s. Directly afterwards, we place the wafer in a beaker containing IPA only. We leave the wafer in there for 30 s and subsequently spin it dry. At this point we clean the wafer by a method known as

descum. We expose the wafer to an O_2 plasma in a microwave plasma system (Tepla 100). We set the microwave power to 100 W and keep the pressure at approximately 0.15 mbar.

Following the O_2 plasma cleaning we perform the dry etching of the growth channels (Figure 3, Step 6). We do this by using an inductive coupled plasma (ICP) reactive-ion etcher (RIE) (Adixen AMS 100 I-speeder) with a mixture of 15 sccm sulfur hexafluoride(SF_6), 20 sccm octafluorocyclobutane(C_4F_8), 10 sccm methane(CH_4) that is diluted in 100 sccm helium (He). We set the ICP power to 2000 W, and the capacitive coupled plasma (CCP) power (biased power) to 250 W. We maintain the sample holder at 0 °C during the entire process, and the wall of the main chamber at 200 °C to inhibit polymer deposition on the wall of the main chamber. We fix the sample holder height at 200 mm and maintain the pressure as low as possible (ca. 1 Pa). We perform this etching process for 3 min. At an etching rate of ca. 390 nm/min it results in approximately 1.2 µm deep growth channels.

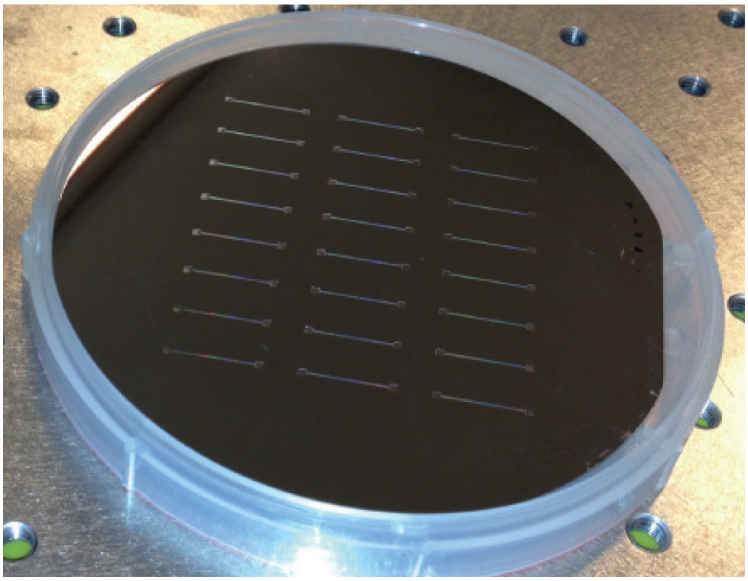

Figure 4. Image of the final Si wafer following the fabrication. One can clearly observe the 24 structures etched into the Si wafer. Here the main trench as well as inlet outlet ports are clearly visible. The side growth channels are too narrow to be visualized in this manner.

Next we fabricate the main trench together with the inlet and outlet. The procedure for this is nearly identical to the previous procedure, with two main differences. Firstly we perform the patterning with the spot size being bigger, ca. 113 nm, at a current of ca. 193 nA and an increased BSS of 100 nm. Secondly, we make use of an adapted dry etching process, so that the sidewalls of the growth channels are protected during the etching of the main trench.

We utilizing what is known as the Bosch deep reactive ion etching (DRIE) process (31) to etch the main trench. This type of etching is different than the previous method in the way that the etching process consists of repeating etching (SF_6) and passivation cycles (C_4F_8). The

passivation step ensures that the sidewalls of the structure being etched are protected during the etching process. The reader is referred to the following references (31, 32) for a more thorough description. We maintain the sample holder at 10 °C during the entire etching process. We keep the pressure at approximately 0.04 mbar. We perform the etching step with 200 sccm SF_6 for 7 s with the ICP power 2000 W and the CCP power off. We execute the passivation step with 80 sccm C_4F_8 for 2 s with the ICP power 2000 W and the CCP power set in chopped low frequency (LF) bias mode: 80 W, ON 10 ms, OFF 90 ms. We repeat this etching cycle for 5 min. The etching rate for Si is approximately 5μm/min, which for these settings results in the ca. 25 μm deep trench. After this, we again clean the wafer in 100% HNO_3 for 15 min, spin it dry and rinse with DI water. An example wafer after all the fabrication steps have been performed is depicted in Figure 4.

Characterization and silanization of the Si fabricated structure

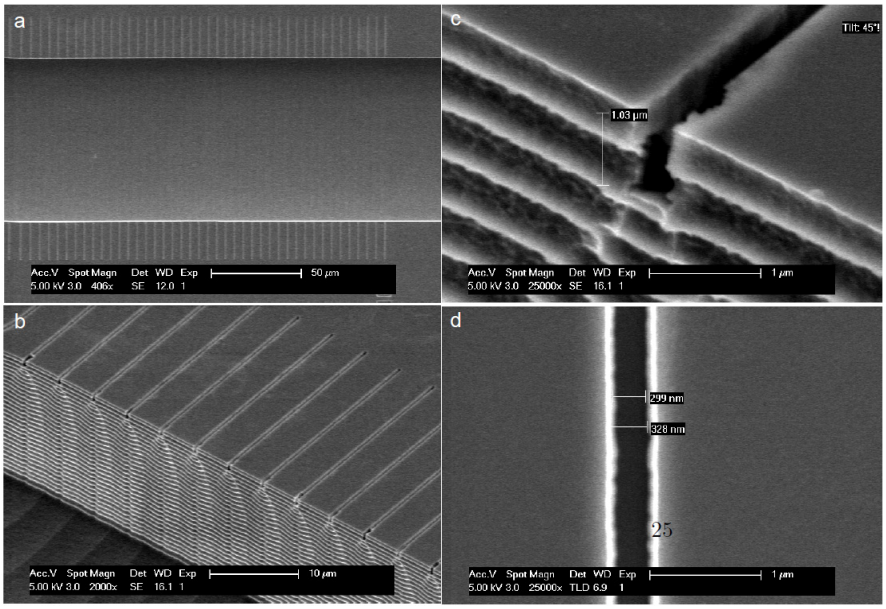

Figure 5. SEM images of fabricated sub-micron channels in silicon. (a) Top overview of a part of the main trench and the small growth channels. For illustration purposes we only show the small channels, but obtained similar results for the bigger growth channels. Here one clearly observes the control of the etching process as shown by the sharp boundaries of the structures. (b) Side view of a part of the main trench and the small growth channels. It is evident from this image that the etching resulted in the appropriate structures. (c, d) Zooming in on one of the small channels to illustrate its dimensions. The scalloping effect seen in (b) and (c) has to do with the repeating passivation and etching cycles of the Bosch process.

We validate the fabrication of the structure in Si by SEM using a FEI/Philips XL30S/FEG. Four different SEM images are shown in Figure 5. A top and side view of a portion of the main trench together with the smallest growth channels (i.e. 0.3 μm) are shown (Figure 5a, b). As can be seen from the images, the etching process is successful and we maintain good

control of the structures. The scalloping effect that is visible at the side of the trench is a result of the Bosch DRIE etching process. Zooming in on one of the small channels one can see that the height and depth correspond to the expected values (Figure 5 c, d). This implies that the PMMA provides sufficient protection during the etching process. We could potentially also fabricate shallower channels by etching for a shorter time. We could then utilize a thinner PMMA protection layer since the desired channel depth determines the thickness of the protection layer.

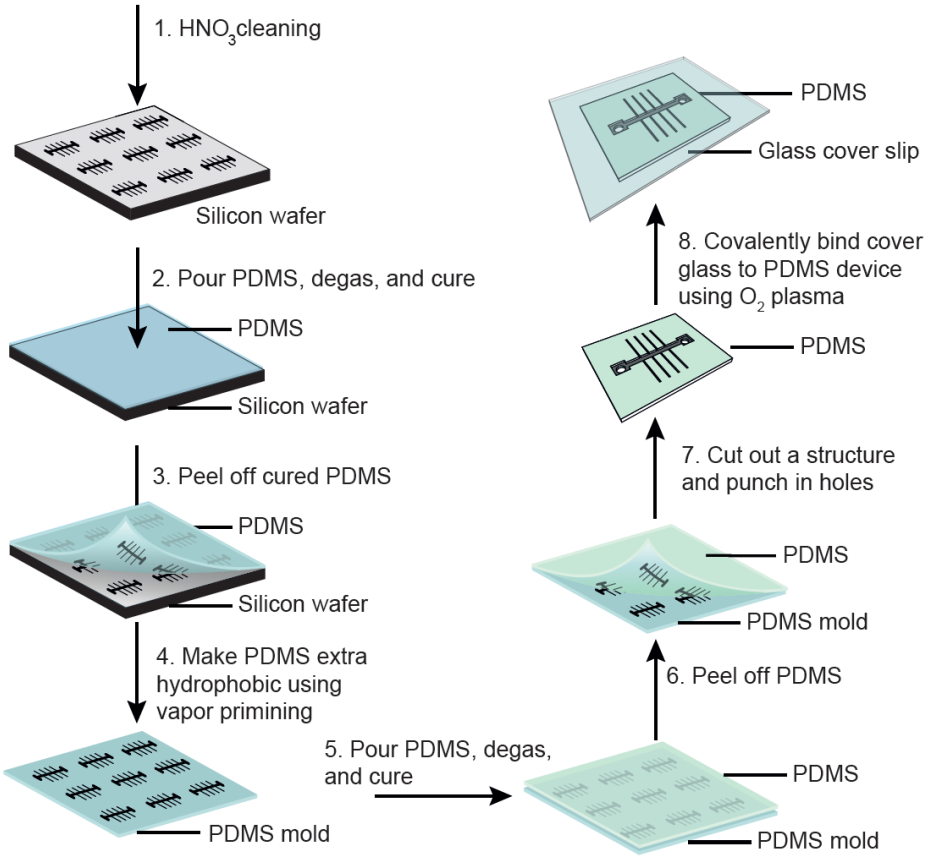

Figure 6. Schematic of the fabrication of multiple structures in PDMS with sub-micron sized growth channels. (Step 1) The wafer is cleaned with HNO_3. (Step 2-3) A 1:5 ratio PDMS is poured on the wafer, cured, and carefully peeled off. (Step 4) A silanization step is performed on the resulting PDMS mold. (Step 5) A 1:10 ratio PDMS is poured on the PDMS mold and cured. (Steps 6) The two PDMS layers are carefully separated from one other. (Step 7) A single structure is cut out, and an inlet and outlet ports are punched. (Step 8) PMDS and a clean cover glass are bound together using O_2 plasma.

The final step we perform before the wafer can be used as a mold is a silanization step. This is necessary to reduce the adhesion between PDMS and Si in the curing step and is

achieved as follows. We expose the wafer to an O_2 plasma for 10 s. We then immediately place the wafer in a desiccator together with 15 µL of silanizing agent (tridecafluoro-1,1,2,2-tetrahydrooctyl trichlorosilane) (TFOCS) (33). We place the desiccator under a vacuum, which results in evaporation of the silanizing agent and formation of a monolayer on the surface of the Si wafer. This layer renders the Si wafer extremely hydrophobic, preventing the PDMS from adhering to it. After 2 hours under vacuum, the Si wafer is ready to be used as a mold.

Fabricating the PDMS microfluidic device

To fabricate the final PDMS microfluidic device, we first utilize the Si wafer as a mold to fabricate a PDMS negative of the structures. We then subsequently use the PDMS negative mold to fabricate the final structures in PDMS. A total of eight principal steps yield the final microfluidic device in PDMS (Figure 6).

We perform the following steps in order to fabricate the structures in PDMS. If the Si wafer is stored for longer than 24 h, we first ultrasonically clean it in 100% HNO_3 for 15 min, rinse with DI water and spin it dry (Figure 6, Step 1). Secondly, we prepare PDMS (Mavom Chemical Solutions DC Sylgard 184 elastomer kit) by mixing an elastomer base and curing agent in a ratio of 1:5 to obtain a relatively stiff mold. After we mix the PDMS thoroughly, we pour it over the clean Si wafer and degas it in a desiccator (Figure 6, Step 2). We subsequently bake the PDMS and Si wafer for 2 h at 85 °C, and afterwards leave it for ca. 30 min to cool down. We finally carefully peel off the PDMS from the Si wafer (Figure 6, Step 3).

Fabrication and characterization of the PDMS mold

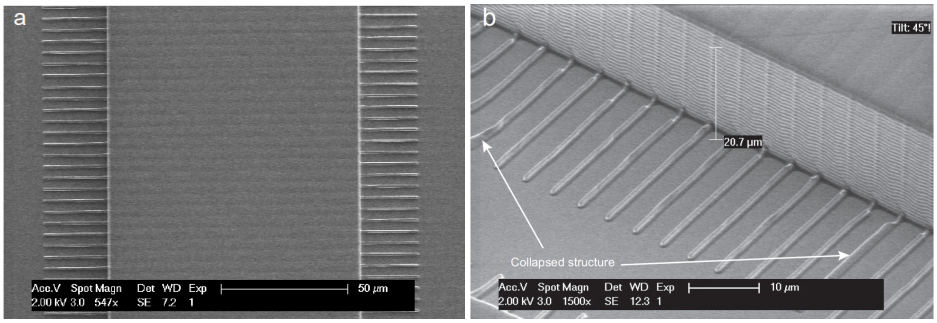

Figure 7. SEM image of PDMS mold with a thin layer of gold on its surface. (a) A top view of the biggest channels. (b) A side view of the smallest channels. In both images it is clear that the structures are successfully replicated from silicon into PDMS.

To verify the successful replica of the structure onto PDMS, we investigate the structure with a SEM. Before we perform the SEM imaging, we first coat the PDMS with a thin layer of gold (Au) as to avoid charging during the imaging process. SEM images are made using a FEI/Philips XL30S/FEG (Figure 7). One can observe from the top view of the largest growth channels (Figure 7a) as well as a side view of the smallest channels (Figure 7b) that the

structures are successfully created in PDMS. We do observe that some growth channels do collapse, pointed out in the figure. This is likely due to a combination of the PDMS being a soft material and the relatively high aspect ratio of the channels (0.3 μm: 1.2 μm). Since there are enough upright channels (Figure 7) that can be used as a mold for the next step, this is not a major concern. As pointed out above, we can vary the depth of the growth channels by etching for a shorter time. This would result in shallower channels and potentially increasing the yield. A different approach to circumvent channel collapse would be to utilize h-PDMS as to make a second layer as described by Odom et al. (30). This approach has been shown to increase the yield when fabricating sub-100 nm size structures using soft lithography.

We perform a further silanization process (Figure 6, Step 4), to reduce the adhesion between the two PDMS layers after the curing process.

Finalization of the PDMS device

Finally we fabricate the positive structures in PDMS. We mix PDMS in a 1:10 ratio, degas, and pour it onto the previously cured PDMS mold (Figure 6, Step 5). We then again degas and allow to cure for 2 h at 85 °C. Once the curing is complete, we leave the PDMS to cool down for at least 30 min. Subsequently we carefully separate the two PDMS layers from each other (Figure 6, Step 6). At this point the PDMS mold can be stored for later use.

The cured PDMS layer contains 24 positive structures, each of which can be used in an experiment. To study an organism under the microscope utilizing the device, the PDMS should have an inlet and outlet port for media exchange, as well as a cover glass sealing the device. This bound cover glass is not only necessary to perform microscopy but also ensures that there is no leakage of the medium when pumped through the device. To fabricate the inlet and outlet ports we first carefully cut out a single PDMS device and punch holes at the two sides of the main trench using a 0.75 mm Harris Uni-Core puncher (Figure 6, Step 7). To bind the cover glass to the PDMS we expose clean cover glass (ultra-sonicated in acetone and IPA) and the PDMS devices at the same time to an O_2 plasma using a microwave plasma system (Plasma-Preen I, Plasmatic Systems Inc.) (Figure 6, Step 8). We then bring the two exposed surfaces into contact and press slightly. It is believed that when the surfaces are exposed to plasma, silanol groups (−OH) are developed, which form covalent siloxane bonds (Si−O−Si) when the two surfaces are brought into contact (34, 35). We then bake the PDMS and attached cover slips for ca. 30 min at 85 °C, after which they are ready to be used in an experiment. In the following section we demonstrate the utilization of this device in two types of experiments.

4.3 Utilizing the PDMS Device

Having successfully fabricated functional structures in Si, transferred these into PDMS with the expected dimensions, and fabricated the inverse in PDMS that includes the final structures, we verify that the final fabricated device (Figure 8a) can indeed be successfully utilized in measurements. To do so, we performed the following two types of experiments.

Firstly we verified that the different size growth channels can indeed be wetted. We accomplished this by injecting a fluorescent dye into the device, and imaging the resulting fluorescence using a fluorescence microscope. We then use a new device to demonstrate that bacteria can indeed be loaded into the growth channels. For this experiment we inject L. lactis into the device to confirm that these cells fit well into the respectively sized channels (ca. 0.8 μm) and also subsequently grow and divide.

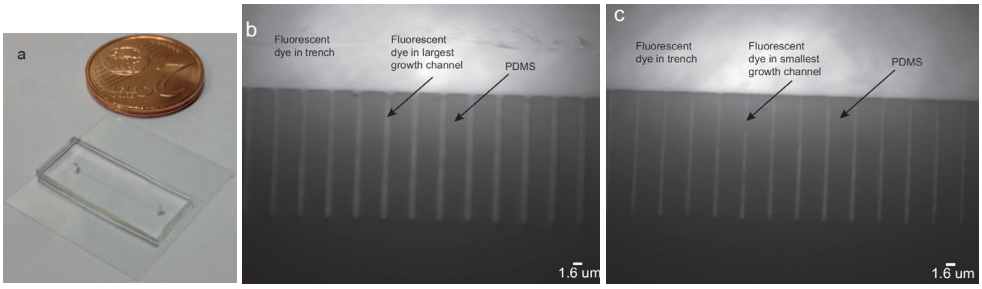

Figure 8. An example of the final PDMS device as well as fluorescence images of a fluorescent dye inside the device. (a) The actual final PDMS device as is used in experiments. (b) Presence of fluorescent dye in largest channel, nominally 0.8 μm, (c) Presence of fluorescent dye in smallest channel, nominally 0.3 μm. One observes that the dye is able to enter the growth channels. A control experiment where the fluorescent signal was measured in the absence of the fluorescent dye (data not shown here), showed no significant fluorescence in the trench or growth channels. The microscope setup used during the experiments consists of a commercial Nikon Ti, a custom laser illumination path, and a personal computer (PC) running Nikon NIS elements. The sample was illuminated with a Cobolt Fandango 515 nm continuous wave (CW) diode-pumped solid-state (DPSS) laser. A Nikon CFI Apo TIRF 100x oil (NA 1.49) objective is used for imaging. The inhomogeneity of the light intensity observed is due to the Gaussian profile of the laser beam. We performed a control experiment (data not shown here) by measuring the fluorescence signal in the absence of the fluorescent dye. During these conditions no significant fluorescence signal was detected in the trench or growth channels. This observation supports our conclusion that the signal detected as shown in the above images are due to the fluorescent dye in the trench and growth channels.

Demonstrating the wettability of the device using a fluorescent dye

We make use of a fluorescent dye (Invitrogen Alexa Fluor 514 Goat Anti-Rabbit IgG 2 mg/mL) to illustrate the functionality of the devices by injecting liquid in the growth channels as illustrated in the following. Firstly, we attached tubing to the inlet and outlet of the device. We inject a standard buffer, namely phosphate buffered saline (PBS) (Sigma, 0.01M PBS - NaCl 0.138 M, KCl 0.0027 M, pH 7.4), into the device. We take care that the PBS exits the outlet tubing. After this, we simultaneously autoclave (120 °C for 15 minutes) the device and tubing. This is done both to ensure sterile conditions when working with microorganisms, and to remove any air bubbles that are present inside the channels of the device. After the autoclaving process is complete, we flush through 50 μL bovine serum albumin (BSA) (10 mg/mL New England Biolabs) through the device and allow it to incubate for at least 15 min. This surface passivation step is done to reduce unwanted sticking of the specimen being studied to the glass and PDMS surfaces. After this incubation period we injected the dye (diluted 1:50 in PBS) into the device and image on a fluorescence microscope.

We are successful in wetting the growth channels as shown in Figure 8b, c. For illustration purposes we show only the largest growth channels, ca. 0.8 μm, (Figure 8b) and smallest ones, ca. 0.3 μm, (Figure 8c). One can clearly observe the size difference between the channels and that in both the cases dye was successfully injected into the channels.

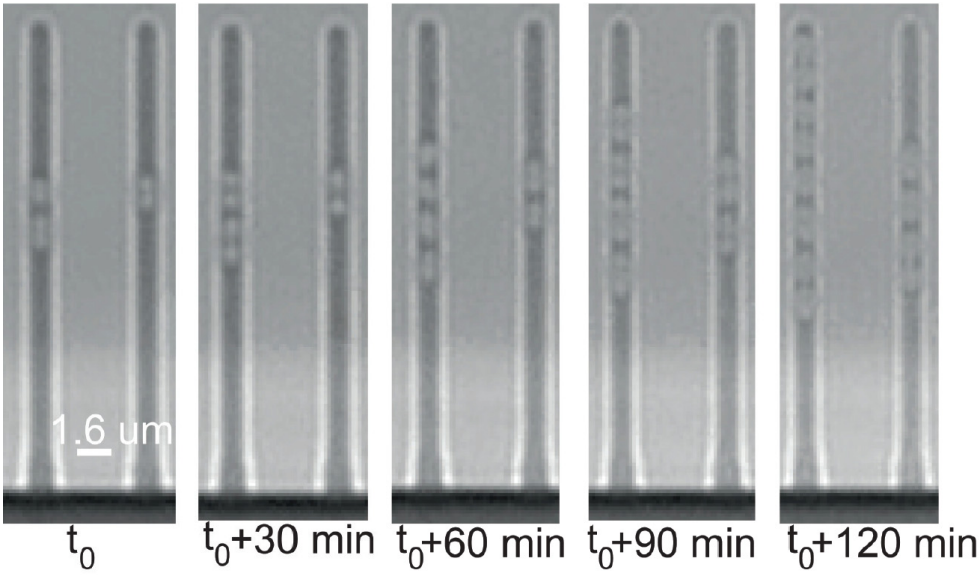

Figure 9. Time points (every 30 min starting at t_0) of a 2 h time series measurement of L. Lactis in the microfluidic device. Cultures were grown directly from plate in Luria-Bertani (LB) at 30 °C until an OD600 ≈ 0.2 was reached. The cell culture was then concentrated by centrifugation and injected into the PDMS device. A syringe pump is used to inject fresh LB medium. Bright field images were acquired every 5 minutes by making use of the same Nikon Ti microscope and objective as was used during the fluorescence experiments. Measurements were performed at room temperature (ca. 23 °C). One can clearly observe growth and division during these two hours. Looking at the first slit, for example one observes the initial two cells becoming 8 cells in 2 h.

Growth of L. lactis in the microfluidic device

Here we demonstrate that sub-micron bacteria can be successfully observed in this device. We use L. lactis for this purpose since it has a diameter of ca. 0.8 μm and should be immobilized in the largest growth channels of this microfluidic device.

We successfully inject the cells into the device and load them into the growth channels by means of centrifugation (Figure 9). The cells depicted are found in the largest size growth channels (ca. 0.8 μm), as was expected given the nominal size of L. lactis. During the course of the experiment the cells remained essentially immobilized. Here we show example time points of approximately 30 min intervals to demonstrate the growth of L. lactis over time. One can clearly observe cell growth in the sample growth channels shown. As is evident from these time points, the cells grew for approximately two generations during the 2 h

measurement duration. The doubling time of these bacteria were estimated from this measurement to be ca. 60 min under these conditions.

4.4 Conclusion

We have presented a detailed protocol based on EBL together with specific dry etching procedures for the fabrication of a microfluidic device suited to study submicron-sized bacteria. In comparison to approaches based on conventional optical lithography, our method provides greater versatility and control of the dimensions of the growth channels while satisfying the rapid-prototyping needs in a research environment. The widths of the submicron growth channels allow for the potential immobilization and study of different size bacteria with widths ranging from 0.3 μm to 0.8 μm. We verified by means of SEM that these structures are successfully transferred from Si into PDMS as well as from PDMS into PDMS. As a proof-of-principle, we demonstrated that the bacterium L. lactis can successfully be loaded and imaged over a number of generations in this device. Similar devices could potentially be used to study other submicron-sized organisms under conditions where the height and shape of the growth channels are crucial to the experimental design.

Acknowledgements: The authors thank Felix Hol, Fabai Wu, Peter Galajda, Jaan Mannik, Simon van Vliet, Mats Wallden and Johan Elf for initial help with the fabrication process, Luping Xu and Peipei Chen for initial help with loading of the cells, Arnold van Run, Hozanna Miro, and Marc Zuiddam for technical assistance with the fabrication instruments, Francesco Pedaci for his help with the acquisition of the SEM images, Greg Schneider for initial help with the silanization procedure, Serge Donkers for initial help with L. lactis, and Jelle van der Does, Dimitri de Roos and Jaap Beekman for help with instrumentation, Melanie Romer for her help with the illustrations. We would also like to thank the reviewers for their insightful comments and suggestions to improve the manuscript. This work was supported by the Netherlands Organization for Scientific Research (NWO), Delft University of Technology, and the European Union via the MitoSys project.

4.5 References

1 S. M. Kim, S. H. Lee and K. Y. Suh, Lab on a chip, 2008, 8, 1015.

2 Y. Huang, B. Agrawal, D. Sun and J. Kuo, Biomicrofluidics, 2011, 5, 013412.

3 J. Zhong, Y. Chen, J. Marcus, A. Scherer, S. Quake, C. Taylor and L. Weiner, Lab on a chip, 2008, 8, 68.

4 S. Maerkl and S. Quake, Science, 2007, 315, 233.

5 P. Yager, T. Edwards, E. Fu, K. Helton, K. Nelson, M. R. Tam and B. H. Weigl, Nature, 2006, 442, 412.

6 T. Danino, O. Mondragon-Palomino, L. Tsimring and J. Hasty, Nature, 2010, 463, 326.

7 J. Mannik, R. Driessen, P. Galajda, J. E. Keymer and C. Dekker, PNAS, 2009, 106, 14861.

8 M. Gan, J. Su, J. Wang, H. Wu and L. Chen, Lab on a chip, 2011, 11, 4087.

9 D. B. Weibel, W. R. Diluzio and G. M. Whitesides, Nat. Rev. Microbiol., 2007, 5, 209–218.

10 H. Yin and D. Marshall, Curr. Opin. Biotechnol., 2011, 23, 1.

11 M. E. Lidstrom and D. R. Meldrum, Ann. Biomed. Eng., 2003, 1, 158.

12 M. R. Bennett and J. Hasty, Nat Rev Genet., 2009, 10, 628.

13 Y. Wang and Z. Chen, Microchimica Acta, 2010, 168, 177.

14 R. N. Zare and S. Kim, Annu. Rev. Biomed. Eng., 2010, 12, 187.

15 S. Cookson, N. Ostroff, W. Pang, D. Volfson and J. Hasty, Mol. Syst. Biol., 2005, 1, 2005.0024.

16 P. Guo, E. W. Hall, R. Schirhagl, H. Mukaibo, C. R. Martin and R. N. Zare, Lab on a chip, 2012, 12, 558.

17 Y. Taniguchi, P. Choi, G. Li, H. Chen, M. Babu, J. Hearn, A. Emili and X. Xie, Science, 2010, 329, 533.

18 P. Wang, L. Robert, J. Pelletier, W. L. Dang, F. Taddei, A. Wright and S. Jun, Curr. Biol., 2010, 20, 1099–1103.

19 N. Grossman, E. Z. Ron and C. L. Woldringh, J. Bacteriol., 1982, 152, 35.

20 D. Nelson and K. Young, J. Bacteriol., 2000, 182, 1714.

21 H. Zhao, U. Dreses-Werringloer, P. Davies and P. Marambaud, BMC Res Notes, 2008, 1, 38.

22 F. Partensky, W. R. Hess and D. Vaulot, Microbiol Mol Biol Rev, 1999, 63, 106.

23 A. Kokkinosa, C. Fasseas, E. Eliopoulos and G. Kalantzopoulos, Le Lait, 1998, 78, 491.

24 J. R. Moffitt, J. B. Lee and P. Cluzel, Lab on a chip, 2012, 12, 1487.

25 M. Altissimo, Biomicrofluidics, 2010, 4, 026503.

26 D. Qin, Y. Xia and G. M. Whitesides, Nat. Protoc., 2010, 5, 491.

27 J. McDonald, D. Duffy, J. Anderson, D. Chiu, H. Wu, O. Schueller and G. Whitesides, Electrophoresis, 2000, 21, 27.

28 G. Whitesides and E. Ostuni, Annu. Rev. Mater. Sci., 2001, 28, 153.

29 M. Bender, U. Plachetka, J. Ran, A. Fuchs, B. Vratzov, H. Kurz, T. Glinsner and F. Lindner, J. Vac. Sci. Tech. B, 2004, 22, 3229.

30 T. Odom, J. Love, D. Wolfe, K. Paul and G. Whitesides, Langmuir, 2002, 18, 5314.

31 H. V. Jansen, M. J. de Boer, S. Unnikrishnan, M. C. Louwerse and M. C. Elwenspoek, J. Micromech. Microeng., 2009, 19, 033001.

32 J. Wei, Ph.D. thesis, Delft University of Technology, 2010.

33 D. C. Duffy, J. C. McDonald, O. J. Schueller and G. M. Whitesides, Anal. Chem., 1998, 70, 4974.

34 M. Eddings and M. Johnson, J. Micromech. Microeng., 2008, 18, 067001.

35 S. Bhattacharya, A. Datta and J. Berg, J. MEMS, 2005, 14, 590.

Chapter 5

Electron Beam Fabrication of Birefringent Microcylinders

Zhuangxiong Huang†, Francesco Pedaci†, Maarten van Oene, Matthew J. Wiggin,

and Nynke H. Dekker (†=equal contribution)

Numerous biological and biotechnological applications rely on the use of micron- and nanometer-scale particles, benefiting tremendously from quantitative control of their physical and chemical properties. Here, we describe the use of electron beam lithography for the design, fabrication and functionalization of micron-scale birefringent quartz cylinders for use in sensing and detection. We demonstrate excellent control of the cylinders' geometry, fabricating cylinders with heights of 0.5-2 μm and diameters of 200–500 nm with high precision while maintaining control of their side-wall angle. The flexible fabrication allows cylinders to be selectively shaped into conical structures or to include centered protrusions for the selective attachment of biomolecules. The latter is facilitated by straightforward functionalization targeted either to a cylinder's face or to the centered protrusion alone. The fabricated quartz cylinders are characterized in an optical torque wrench, permitting correlation of their geometrical properties to measured torques. Lastly, we tether individual DNA molecules to the functionalized cylinders and demonstrate the translation and rotational control required for single-molecule studies.*

* This chapter has been published as Z. Huang†, F. Pedaci†, M. van Oene, M. Wiggin, and N.H. Dekker, *ACS Nano* **5**, 1418–1427 (2011) , (†=equal contribution).

5.1 Introduction

A variety of micron-sized particles find application in biological separation,[1] biophysical techniques such as magnetic and optical tweezers,[2-4] the preparation of colloidal suspensions and the study of their physical properties,[5, 6] or the construction of artificial devices such as nanoscale swimmers.[7] Both the physical and chemical properties of such particles, *e.g.* their ferromagnetic or paramagnetic character, value of their dielectric constant, and surface coating, play a role in their applicability. Birefringent particles, based on materials capable of exchanging spin angular momentum with light (Figure 1a), are also of great interest. They have been exploited in microrheology as sensors to measure properties of the surrounding fluid,[8-10] in microfluidics as micron-scale pumps for flow generation,[11] and in the torque spectroscopy of single biomolecules[12, 13] through their key role in the optical torque wrench.

Several methods exist for the production of birefringent particles, resulting in a variety of forms such as vaterite microspheres,[14, 15] tetragonal lysozyme crystals,[16, 17] organic semiconductor platelets,[18] $LiNbO_3$ microcrystals,[19] organic dye microcrystals,[20] and micro-fabricated quartz microcylinders.[13, 21] For applications in single-molecule torque spectroscopy, which form the primary motivation for our work, quartz constitutes a particularly suitable material,[13, 21, 22] a consequence of its chemical stability and biological inertness, the facility with which it can be coated, and the control of its geometry.

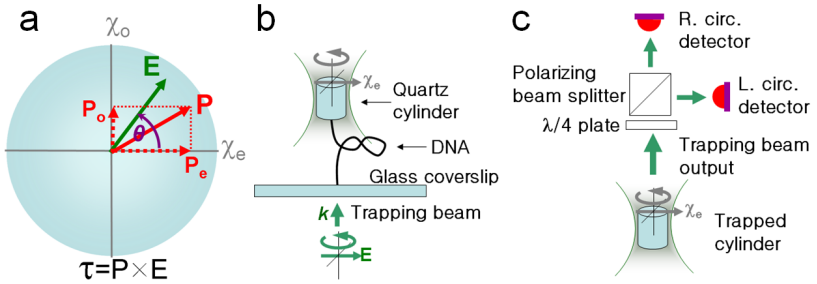

Figure 1. Schematic of an optical torque wrench. (a) The electric susceptibilities differ along the extraordinary axis (χ_e) and the ordinary axis (χ_o) of a birefringent material. Hence, unless the electric field is aligned with either axis, the induced dipole P (red vector) is not co-linear with external electric field E (green vector), resulting in the generation of torque τ. (b) Use of an optical torque wrench for the study of DNA. A birefringent quartz cylinder having its extraordinary axis perpendicular to its cylindrical axis is maintained in an optical trap as shown. Here k indicates the propagation direction of the trapping laser beam. The top surface of the cylinder is chemically functionalized to permit the binding of DNA via multiple bonds. The DNA's other extremity is attached to a glass coverslip in a flow cell, likewise via multiple bonds. By controlled rotation of the trapping beam's linear polarization, the cylinder can be rotated, generating twist in the DNA. (c) Meanwhile, the torque exerted by the trapping laser on the cylinder is measured by a torque detector that records the imbalance in the intensities of the right and left circular components of the transmitted beam.

La Porta *et al.*[22] have pioneered the use of birefringent particles in an optical torque wrench (OTW), schematically illustrated in Figure 1. When a birefringent particle is trapped in a focused laser beam, the polarization of the trapping beam can be used to apply a torque to the particle, allowing it to be aligned or continuously spun[23] (Figure 1b). Moreover, in such a configuration the torque exerted on a birefringent particle can be measured directly from the change in angular momentum of the light beam (Figure 1c).[13, 21, 22] In a particularly elegant implementation of an OTW, the birefringent particles are formed from quartz cylinders: such cylinders will align their long axis with the direction of laser propagation,[16, 24] thereby confining two rotational degrees of freedom. Provided that the quartz extraordinary axis is perpendicular to the cylinder's long axis, the third rotational degree of freedom can be controlled by the polarization of the trapping beam. Controlled rotation of the trapping beam polarization results in rotation of the cylinder and, if the cylinder is tethered to a well-anchored DNA, to the build-up of twist in DNA[12] (Figure 1a,b).

Typically, optical lithography has been employed in the fabrication and functionalization of such cylinders, as reported by Deutel *et al.*[21] and Gutierrez-Medina *et al.*[13] However, the use of optical lithography for making quartz cylinders comes with a number of limitations. Importantly, it restricts the smallest feature sizes to ~300–400 nm.[13] Here, we report a novel, electron beam lithography-based approach to the nanofabrication and functionalization of quartz cylinders that presents a number of advantages. First, electron beam lithography is capable of patterning a wide range of feature sizes. These can be as small as few nanometers, making it possible to fabricate smaller cylinders with great ease. Simultaneously, our electron beam-based approach remains very well-suited for the fabrication of larger quartz cylinders, especially those with high aspect ratios. Second, our approach comes with great versatility: cylinders may be modified into having a slightly conical shape or fabricated to include a nanometer-scale centered protrusion for the controlled binding of DNA (thereby reducing overall precession). Third, our approach introduces selective surface functionalization following, rather than prior to, the removal of the etching mask, implying that the choice of etching mask is independent of the chemistry of functional groups and affording a wider choice of etching geometries and cylinder shapes. Using this approach, we demonstrate the fabrication of quartz cylinders with lateral dimensions in the range of 0.5-2 μm and axial dimensions in the range of 200-500 nm. The cylinders can be made to high uniformity (4.2% relative standard deviation (RSD) in volume, and a control of their side angles can to within an error of 0.3°). We further fabricate cylinders including centered protrusions on one of their two faces, and demonstrate excellent control of cylinder functionalization, functionalizing either a single face of a cylinder or only the centered protrusion itself. We present extensive characterization of the cylinders via scanning electron microscopy, biochemical analysis, and optical microscopy. The characterization is completed by introducing the cylinders into an OTW, where we correlate their physical properties to the measured torque signals. We then demonstrate, using well-controlled tethering of DNA to the functionalized cylinders, successful force and torque spectroscopy on an individual biomolecule.

5.2 Methods

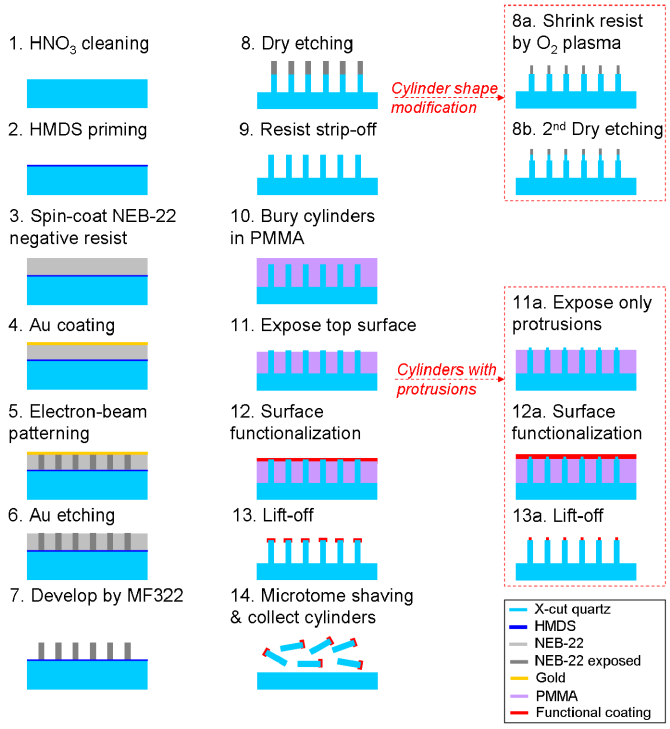

Figure 2. Schematic of the fabrication and selective functionalization of micron-scale quartz cylinders using negative-tone electron beam lithography. (Step 1) A single-crystal quartz wafer is cleaned and prepared for patterning. (Steps 2-4) A negative electron beam resist is coated onto the wafer and prepared for electron beam patterning. (Steps 5-7) Electron beam exposure and development of resist posts. (Steps 8-9) Dry etching and formation of the quartz cylinders. (Steps 10-13) Selective functionalization of the top surface of the quartz cylinders. (Step 14) Shaving off and collecting of the quartz cylinders. (Steps 8a,b) The formation of centered protrusions. (Steps 11a-13a) Selective functionalization of the quartz cylinders with centered protrusions. For further details, see Methods.

Fabrication and Functionalization of Quartz Cylinders: Fabrication of the quartz cylinders was performed on 100 mm diameter x-cut single-crystal quartz wafers (University Wafer, USA) and comprised 14 principal steps (Figure 2).

In the first step, the wafers were ultrasonically cleaned in fuming nitric acid (100% HNO_3) for 10 min (Figure 2, Step 1), rinsed in deionized (DI) water and spun dry. Then, the wafer surface was primed for resist adhesion using hexamethyldisilazane by spin-coating at 1000 rpm for 55 s (Figure 2, Step 2). When fabricating small cylinders (height < 0.8 μm, Figure 3a-c), after priming, a 380 nm layer of NEB-22A2E negative electron-beam resist (Sumitomo Chemical Co.) was spin-coated onto the wafer at 1000 rpm for 55 s and baked for 3 min at

110°C (Figure 2, Step 3). When fabricating larger cylinders (height > 1.5μm, Figure 3d-f), it was necessary to apply a thicker layer of resist. In this case, the solution of NEB-22A2E resist was first spread out on the wafer by spin-coating at 500 rpm for 4 s, after which the resist solution was concentrated by evaporating the solvent on the wafer for 3 min in the spin-coater. The wafer was subsequently spun at 1000 rpm for 55 s, and baked for 3 min at 110°C. The layer of NEB-22A2E resist prepared by this method has a uniform-film thickness of about 1.4-1.6 μm, which greatly exceeds the maximum possible spin-coated thickness as determined by the resist solvent content and specified by the resist supplier. Followed the spin-coating of resist, a 20 nm gold layer is deposited on top of the resist (Figure 2, Step 4) using a resistive thermal evaporator (Leybold-Heraeus L560). This gold layer serves as a reflective layer to facilitate the focusing on the electron beam lithography machine (Leica EBPG 5000+) and additionally provides a charge dissipation path during electron beam exposure. At this point, the sample is ready for patterning.

Feature patterning (Figure 2, Step 5) is performed on a Leica EBPG 5000+ (acceleration voltage 100 kV, aperture 400 μm). The cylinders were exposed as single pixels, whereby the pixel size was adjusted by defocusing a small electron spot to reduce the irregularity of the feature shape. Nominal pixel diameters of 200 nm (Figure 3c), 300 nm (Figure 3a-b), and 500 nm (Figure 3d-f) were achieved by defocusing electron spots with currents of 9 nA, 12nA, and 38nA (corresponding to estimated 12 nm, 14 nm, and 24 nm before defocusing, respectively). Doses equaled 5000 $\mu C/cm^2$ with a 20 nm beam step size (BSS) (for 200 nm and 300 nm pixels) or 100 $\mu C/cm^2$ with a 200 nm BSS (for 500 nm pixels). The beam settling time was set to 10 μs to minimize the overall patterning time (per billion cylinders, machine time was ~10 h for 200 nm and 300 nm pixel sizes, and ~8.5 h for 500 nm pixel sizes). Cylinders were arranged in a hexagonal array with pitches of 1 μm (for 200 nm or 300 nm cylinders) or 3 μm (for 500 nm cylinders), yielding a total of 0.4 - 0.8 billion cylinders.

Following electron beam exposure, the resist was baked at 105 °C for 3 min and the gold overcoat was removed by immersing the wafer in gold etchant TFA (Transene, USA) for ~20 s (Figure 2, Step 6), rinsing with DI water, and spinning dry. Next, the development was done for 1 min in Microposit MF322 solution (Rohm and Haas), followed by a 15 s soaking in 1:10 diluted MF322 solution (Figure 2, Step 7). The wafer was then rinsed in DI water and spun dry. The wafers were then dry-etched (Figure 2, Step 8) in an inductive-coupled-plasma (ICP) reactive-ion etcher (Adixen AMS100 I-speeder) with a mixture of 20 sccm C_4F_8 and 10 sccm CH_4, diluted in 100 sccm He. The ICP source power equaled 2500 W, and the substrate bias RF power equaled 300 W, except for the etching of cone-shaped cylinders (Figure 3d), where the RF bias power equaled 250 W. The pressure was maintained as low as possible, ~1 Pa. The temperature was maintained at 0 °C for the sample holder and 200 °C for the chamber. Under these settings, for both the 300 W and 250 W RF bias power, the etching rate of quartz was ~170 nm/min at wafer center and ~200 nm/min at a radial distance of 30 mm from wafer center, and the etch selectivity of the quartz relative to the resist masks was ~3:1.

For the fabrication of cylinders with centered protrusions (Figure 3f), two additional steps followed dry etching. First, the wafer was exposed to O_2 plasma in a microwave plasma system (Tepla 100, TePla AG, Germany) to shrink the size of the resist residues (Figure 2, Step 8a).[13] The microwave power equaled 100 W and the pressure was kept at 0.15 mbar with a 30-sccm O_2 flow. This resulted in isotropic etching of the resist at a nearly uniform rate of

~10 nm/min across the wafer. Second, the wafer was reloaded into the reactive-ion etcher to undergo an additional C_4F_8 plasma etching for 90 s using the same settings as above (Figure 2, Step 8). This resulted in the formation of small protrusions (Figure 2, Step 8b).

Following the C_4F_8 plasma etching, the wafer was cleaned by O_2 plasma (Figure 2, Step 9), in the Adixen etcher to remove residues of the resist mask and Teflon-like polymers deposited during the dry etching process.

We next proceeded with selective surface functionalization (Figure 2, Steps 10-13). First, to bury the cylinders, the wafers were spin-coated with a layer of PMMA 950k resist (Figure 2, Step 10) that was determined to initially exceed the height of the quartz cylinders by ~100 nm. And then its thickness was reduced by exposure to O_2 plasma (settings as in Step 8a of Figure 2). For cylinders without protrusions (Figure 3b-d), the final PMMA thickness was ~10-30 nm thinner than the cylinder height, just exposing the cylinders' top surface for functionalization (Figure 2, Step 11). For cylinders with protrusions, the resist thickness was reduced to a lesser extent so that only the protrusions were accessible for surface functionalization (Figure 2, Step 11a; Figure 5b). In both cases, the exposed surfaces were amino-functionalized by immersing in 1% Vectabond (Vector Laboratories, Burlingame, CA) in isopropanol for 5 min, followed by rinsing with DI water and drying by spinning (Figure 2, Steps 12, 12a). A further step yielded the desired functional group on the surface: for example, to obtain biotinylated cylinders the wafer of amino-functionalized cylinders was immersed in 2 mg/ml EZ-Link Sulfo-NHS-LC-LC-Biotin (Pierce Chemical Co.) dissolved in Na_2CO_3 buffer (100 mM, pH 8.5) for 2 hours, followed by rinsing with DI water and spinning dry. Finally, the PMMA resist was removed with acetone in an ultrasonic bath for 5 min (Figure 2, Steps 13, 13a), and the wafer was rinsed with DI water and spun dry.

In the final step of the protocol, the quartz cylinders were shaved off from the wafer (Figure 2, Step 14) using a clean microtome blade (DT315D50, C. L. Sturkey, Inc.) [21] and stored in TE buffer (10 mM Tris-HCl, 1 mM EDTA, pH 7.5).

Size Measurement of Quartz Cylinders: Characterization of the quartz cylinders (Figure 3) was conducted via scanning electron microscopy (SEM) using a Hitachi S4800 and a FEI/Philips XL30S/FEG. A wafer of 300 nm cylinders (Figure 2a,b) was used to characterize the uniformity of cylinder dimensions across a wafer (Figure 4). In this measurement, 20 SEM images of individual cylinders were obtained from different radial positions on the wafer. Dimensions of the cylinders were directly deduced from the SEM images with an accuracy of ~8 nm per pixel.

Testing the Functionalization of Quartz Cylinders: The functionalization of the quartz cylinders' top surfaces was tested (Figure 5a) by the binding specificity of fluorescently-labeled biotinylated oligonucleotides (biotin-5'-ttagggttagggttaggg-TAMRA, Biolegio). Using the same approach, we also tested the functionalization of the cylinders with centered protrusions (Figure 5c); the latter result was confirmed by direct SEM imaging the binding of 200 nm biotinylated microspheres (FluoSpheres F8767, Invitrogen) onto the functionalized cylinder protrusions (Figure 5d).

To bind labeled oligonucleotides, the wafer of selectively-biotinylated cylinders (with or without protrusions) was first treated with 10 μg/ml streptavidin (Sigma) in PBS buffer (137 mM NaCl, 2.7 mM KCl, 10 mM Na_2HPO_4, 1.76 mM KH_2PO_4, pH 7.4) for 20 min, rinsed

with DI water and spun dry. Next, 1 mg/ml bovine serum albumin (BSA; Sigma) in PBS buffer was applied onto the wafer for 20 min to prevent nonspecific binding, followed by DI water rinsing and spinning dry. Then, labeled oligonucleotides (10 nM, in PBS buffer) were incubated with the cylinders for 20 min, followed by rinsing with DI water and spinning dry. Subsequently, the wafer of cylinders was imaged using a wide-field fluorescence microscope (IX71, Olympus, Japan) equipped with a 532 nm diode-pumped laser (GCL-050-L-0.5%, Crystalaser, USA). To do so, the wafer was mounted up-side-down on the microscope. Movies (0.1 s exposure time) were recorded, for which the first frames are shown in Figure 5a (cylinders without protrusions), Figure 5c (cylinders with protrusions).

To test the binding specificity with biotin-labeled microspheres, we employed the same wafer as above. Therefore, the wafer was first ultrasonically cleaned to remove any remaining organic coating in fuming nitric acid for 10 min, rinsed in DI water and spun dry. Next, the cylinders were selectively re-functionalized with Vectabond and EZ-Link Sulfo-NHS-LC-LC-Biotin as above (Figure 2, Steps 11a-13a). The wafer was then treated with streptavidin and BSA. A solution of 200 nm biotinylated microspheres was incubated with the wafer for 20 min, followed by rinsing with DI water and spinning dry. The specific binding of biotinylated microspheres was then visualized by SEM (Figure 5d).

OTW Instrumentation: To constitute the OTW,[10] the laser (Coherent CompassTM CW Nd:VO4 1064-4000M) was linearly polarized and focused by a 60X objective (CFI-PLAN-APO-VC-60XA-WI, Nikon) into a custom-made glass flow cell mounted onto piezo-actuators (P-517.3CD, Physik Instrumente). We used a fast electro-optical modulator (EOM; LM 0202-LT, LINOS) in combination with a quarter-wave plate (PWPS-1064-10-4, CVI Melles Griot) as a polarization control system. The torque transferred to the trapped particle was measured optically (Figure 1c) by two identical fast intensity detectors (DET10C/M, Thorlabs) from the imbalance of the two circular components of the polarization at the trap output, separated using a quarter-wavelength plate and a polarizing beam splitter (PBS-1064-100, CVI Melles Griot). The linear displacement of the quartz cylinder in the trap (and hence the force), as well as its height above the surface, were detected via a position-sensitive device (PSD; DL100-7PCBA3, Pacific Silicon Sensor). To obtain constant force, the force measurement was fed back to the piezo-actuators to adjust the linear displacement of the trapped particle, clamping the force at a specified setpoint. For measurements of quartz cylinders in the OTW, the power entering the objective equaled 100 mW and data was acquired at 100 kHz.

Flow Cell Assembly and DNA Constructs: Flow cells were assembled from microscope cover slips with a parafilm spacer. For experiments on quartz cylinders alone, the bottom surface was coated with nitrocellulose (0.01% (wt/vol) in amyl acetate), followed by an incubation of 10 mg/ml BSA for 30 min to prevent nonspecific adhesion of quartz cylinders (pre-passivated with 5 mg/ml BSA for 20 min prior to introduction into the flow cell). For experiments on quartz cylinders bound to DNA, an incubation of the flow cell with 0.1 mg/ml anti-digoxigenin (Roche) in PBS for 30 min (to provide for DNA attachment) preceded the BSA incubation.

We used 7.9 kb dsDNA molecules ligated at their two extremities to ~0.6 kb PCR fragments functionalized with multiple biotin and digoxigenin groups, respectively.[25] dsDNA

constructs were incubated in the passivated flow cell for 30 min in Tethering Buffer (320 mM NaCl, 10 mM Tris-HCl, 1 mM EDTA, pH 7.5) and then again for 30 min in the presence of an additional 0.1 mg/ml streptavidin. Then the quartz cylinders (with biotinylated protrusions), which had been pre-passivated in 5 mg/ml BSA for 20 min, were added, to be followed by an additional 30 min incubation. Following each incubation step, the flow cell was flushed thoroughly with Tethering Buffer. After the final flushing step, only the dsDNA-tethered cylinders remained in the flow cell.

5.3 Results and Discussions

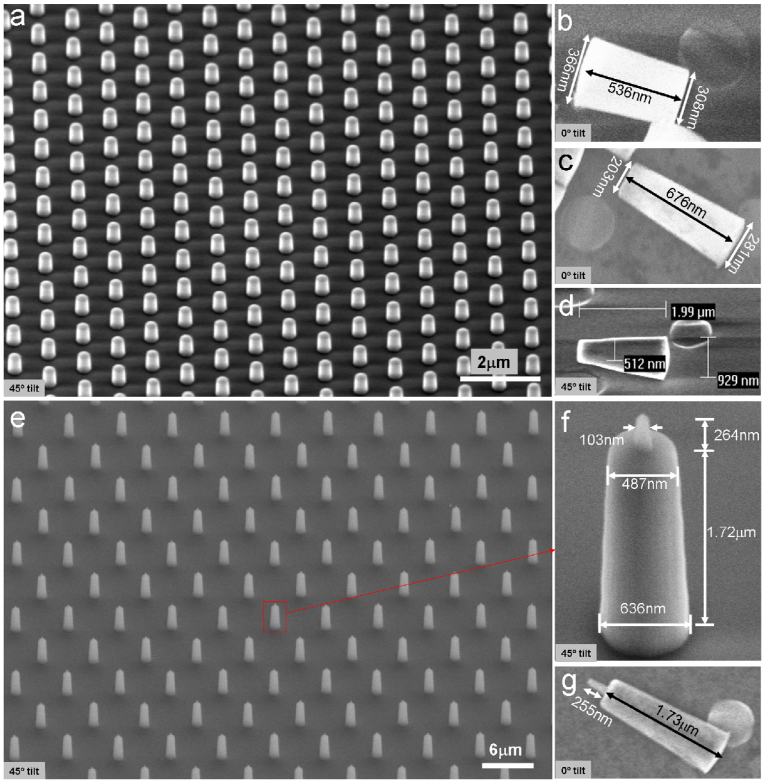

Figure 3. SEM images of fabricated quartz particles. (a) Fabricated quartz cylinders (nominal top diameter: 300-nm) arranged in a hexagonal array pattern on the wafer. (b) A single quartz cylinder after microtome shaving off the wafer (from the same wafer as in (a)). The microtome shaving consistently produces an evenly cut surface at the base of the quartz cylinder, and the cross section of the cut surface demonstrates a round shape at the cylinder's base. (c) A cylinder with a smaller diameter (nominal top diameter: 200 nm) and a higher aspect ratio. (d) A larger cylinder (nominal top diameter: 500 nm) fabricated with a slightly more conical shape. (e)-(g): Larger cylinders

(nominal top diameter: 500 nm) with centered protrusions. (e) Demonstration that the centered protrusions were fabricated consistently on all cylinders in the patterned area. (f) A typical feature size of the centered-protrusion cylinder. (g) A single cylinder with a centered protrusion following microtome shaving. In all panels, the tilt angle of the wafer surface for SEM imaging is indicated in the bottom-left corner.

Control of the Physical Properties of Quartz Cylinders: Ideally, quartz cylinders for application in OTW should have the following properties. First, the cylinder's aspect ratio (height: diameter) should be sufficient large[16] to allow for tight confinement of the long axis of the cylinder along the propagation direction of trapping beam. Second, depending on the specific application, the cylinder size should be tunable: for example, if stronger trapping and larger torques are desired, larger cylinders are appropriate; conversely, smaller cylinders have the advantage of lower noise in the measured torque signal and a smaller drag (resulting in a faster response time). Third, it should be straightforward to attach DNA (or other biomolecules), and preferably so to the center of the cylinder's top or bottom surface.[13] Otherwise, when the DNA is stretched, the cylinder will precess and dramatically increase the noise in the torque measurement.

Fine control of the dimensions and the resulting geometry of the quartz cylinders necessitate a thorough understanding of the physical processes involved in patterning and etching. Using the protocols described in the Methods and illustrated in Figure 2, we were able to fulfill these criteria and fabricate uniform arrays of quartz micro-cylinders (Figure 3a,e show images of such arrays) in a wide variety of sizes and geometries. For instance, It was possible to control cylinder height (a range of 0.5-2 μm was fabricated; Fig 3a-d), cylinder diameter (a range of 200-500 nm was fabricated; Figure 3a-d), the angle of the cylinder side wall (Figure 3b-d), and whether or not the cylinder included any protrusions from its center for controlled binding of DNA (Figure 3e-g). We now discuss the control of these parameters.

To control of the diameter of cylinder's top surface, it suffices to control the electron beam pattering. We typically found the difference between the cylinder's diameter (as measured by SEM) and the nominal diameter of the defocused spot of the electron beam to be less than 6% for all wafers of cylinders (Figure 3b-d, f-g). The shape of the cylinder's cross section, which is likewise defined by electron beam's patterning spot, was similarly easily controlled and exhibited a uniformly round shape over all cylinders sizes tested on various wafers (Figure 3b,c,g).

To control the height (and hence the aspect ratio) of the quartz cylinders, we relied on control of the total etching time, which was demonstrated to be a reliable parameter: for instance, provided that the same machine settings were employed, the etching rate of the C_4F_8 plasma was found to be quite reproducible on different wafers. Additionally, we also found that for cylinders with heights ranging between 0.5–2 μm, the etching rate remained approximately stable throughout the time course, *i.e.* any RIE lag could be ignored.26 However, the etching rate did vary across the wafer, increasing monotonically with the radial distance from the wafer center (5 ± 2% per 10 mm, as measured by SEM analysis over all wafers). This behavior (known as macro-loading effect[27]) results from the depletion of reactant along its transportation course from outside edge to the wafer center and may be alleviated by increasing the supply of reactants and/or decreasing the etch rate. In practice, to acquire cylinders of sufficiently uniform height, we simply employed a subsection of the wafer area (*e.g.* a circular area at the wafer center, or, preferably, a circular annulus, which

has a smaller radial range for the same patterning area). An alternative approach would be to divide the wafer into compartments and to collect the cylinders separately from each.

In addition to the cylinders' height and diameter, we control their side-wall angle. This parameter can be tuned with ease by tuning the substrate bias power during C_4F_8 plasma dry etching. For example, for a resist mask with features of 500 nm diameter, 1.4 μm height, and 3 μm hexagonal pitch, reducing the bias power from 300 W to 250 W decreased the cylinder side wall angle from ~88º to ~84º while leaving the etch rate unchanged (Figure 3d). This dependence of the side wall angle on the substrate bias power may derive from competition between ion bombardment and simultaneous fluorine-carbon polymer deposition: under reduced substrate bias power the side-wall would experience weaker bombardment, permitting a more rapid accumulation of polymer on the side-wall and a concomitant reduction in side-wall angle.[26, 28] We note further that the observed insensitivity of the etching rate to the bias power suggests that the etching process is predominantly governed by chemical reactions on the surface,[27] in agreement with the above observation of the macro-loading effect.

We note that the above-mentioned guidelines do not take into account the design of the resist mask pattern. However, as the dry etching rate depends on the local geometry, this is also a parameter of interest. Optimization of C_4F_8 plasma conditions was essential in order to guarantee the reproducibility of the dry etching recipe: however, instead of re-optimizing the etching conditions for different resist mask patterns, we found that we could also adapt the local geometry to maintain approximately uniform C_4F_8 plasma settings. Initially, the machine settings for C_4F_8 plasma dry etching (Methods) were optimized for a resist mask with a thickness of 380 nm, encoding for 300 nm diameter features in a 1 μm-pitch hexagonal array (yielding cylinders as in Figure 3a,b). Identical etching settings could be applied to resist masks that had a smaller feature diameter (*e.g.* 200 nm, Figure 3c), resulting in the same etching rates and side-wall angles. However, when the resist mask had a larger thickness (1.4 μm) and encoded a larger feature diameter (500 nm), we observed an undesirable deposition of Teflon-like polymer onto the quartz, as opposed to quartz etching.

By examining the role of pattern geometry, we can both understand and reduce unwanted polymeric deposition. First, larger and thicker mask features have an increased resist surface area exposed to etching plasma. For a given array pitch, an increase in the exposed resist surface results in an increased amount of resist erosion and a concomitant reduction of the local fluorine-to-carbon ratio. This would tend to favor the deposition of fluorine-carbon polymers over quartz etching. Second, such geometric conditions result in a higher aspect ratio of the etched area between resist mask features, for which a lower etching rate typically ensues.[29, 30] This is mainly attributed to a decrease in the transport rate of incoming etching species to the bottom of the etched feature.[29, 30] If the increase in mask feature size causes the etch rate to fall below the rate of polymer deposition, the latter will be favored. To successfully circumvent this difficulty, we increased the array pitch of the resist mask to achieve more-or-less equivalent geometries, yielding a resist mask pattern with 500 nm feature diameter, 1.4 μm thickness, and 3 μm pitch (in which both the ratio of the exposed resist surface to the etched quartz surface and the aspect ratio of the etched feature were largely maintained with respect to the original pattern described above). With this adaptation,

identical machine settings could be applied, resulting in nearly the same etching rate and side-wall angle (87.8º ± 0.4º, see Figure 3b,c,g for differently-sized cylinders).

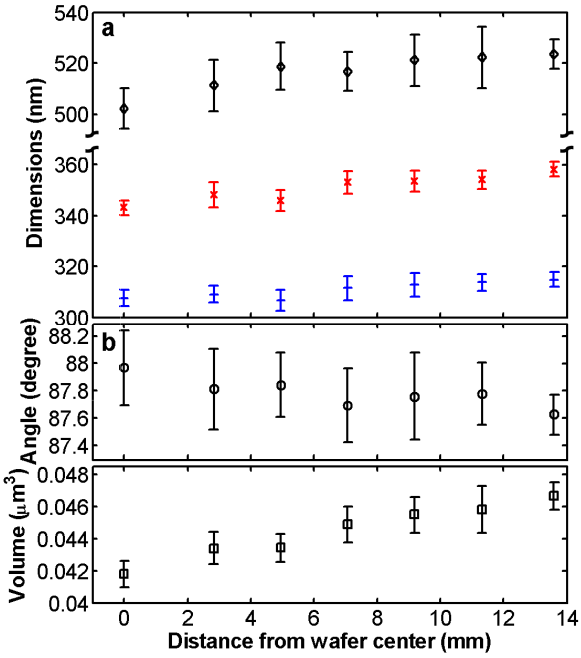

Figure 4. Dimensions of fabricated cylinders on a quartz wafer as a function of radial distance from the wafer center. The nominal top diameter equals 300 nm. (a) Average cylinder heights (black), diameters of cylinder tops (blue), and diameters of cylinder bottoms (red), determined from SEM images. (c) Average cylinder sidewall angles and (d) average cylinders volumes were calculated using the data in (a). The error bars in all panels represent one standard deviation from the mean.

To examine the variability in cylinder geometries across a wafer, we have performed quantitative SEM measurements (Methods). Here, cylinders were fabricated using a 300 nm defocused electron spot that patterned a resist mask with a thickness of 380 nm; the hexagonal array pitch equaled 1 μm; a circular area of about 14 mm in radius was employed, yielding ~0.7 billion cylinders; and the dry etching time was 3 min. Overall, the cylinders are highly uniform as shown in Figure 4: the cylinder height increases by 4.3% (± 2.0%) from wafer center to the outmost pattern position (14 mm from wafer center); the relative standard deviation (RSD) in top diameter is estimated to be 1.5% and 1.7% in bottom diameter; and the computed cylinder side-wall angle is nearly constant: 87.8º ± 0.3º. Overall, the RSD in the volume of quartz cylinder is estimated to be ~4.2% for whole cylinder population. Note that for applications of quartz cylinders in an OTW, the variation in the volume is the most appropriate indicator of cylinder dispersity, as both the optical torque exerted on the cylinder and the rotational drag are approximately proportional to the cylinder volume.

Selective Functionalization of Fabricated Quartz Cylinders: To employ quartz cylinders for biophysical experiments in an OTW, DNA (or other biomolecules) should be controllably bound to the top surface of quartz cylinder (Figure 1b), and ideally specifically to only the center of the top surface.[13] Our selective functionalization (Figure 2, Steps 10-13, 11a-13a) is demonstrated by its application to both cylinders without protrusions and cylinders with protrusions (Figure 5).

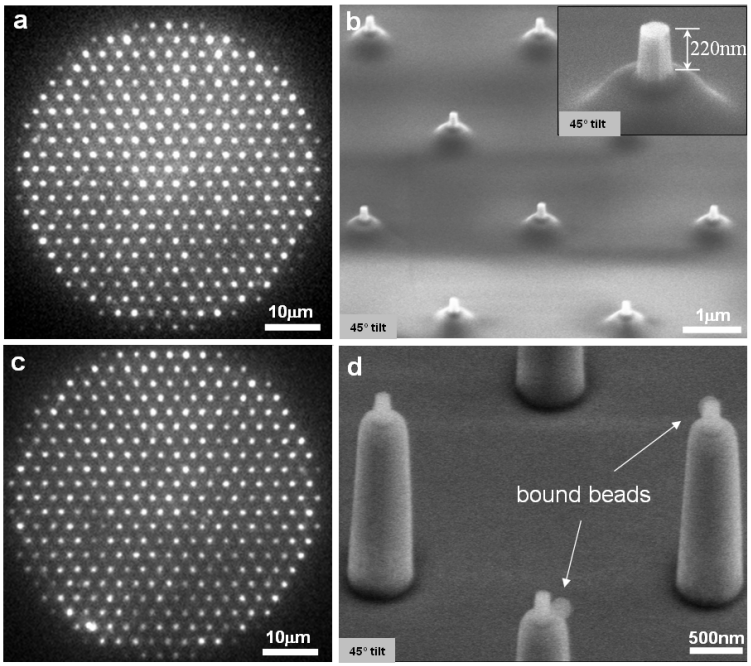

Figure 5. Selective functionalization of micron-scale quartz cylinders. (a) Fluorescence image of surface-bound biotinylated, TAMRA-labeled oligonucleotides on a wafer of quartz cylinders without protrusions. The hexagonal pattern of the fluorescent spots (white) indicates that the oligonucleotides specifically bind to the functionalized portion of cylinder surface (primarily the top surface). (b) The centered protrusions of quartz cylinders are exposed for chemical functionalization, while the rest of cylinder surface remains buried and protected in PMMA resist. The inset shows a zoom on a single centered protrusion. (c) Same as (a), with the difference that the quartz cylinders have centered protrusions. (d) SEM image of biotinylated microspheres specifically bound to the functionalized centered protrusions of quartz cylinders.

We have tested the selective functionalization of cylinders without protrusions by examining their ability to specifically bind fluorescently-labeled biotinylated oligonucleotides (Methods). As shown in Figure 5a, the fluorescence of bound oligonucleotides appears nearly exclusively at positions that arrange into a hexagonal array, indicating that labeled oligonucleotides do not aspecifically bind to the wafer surface. As both the cylinder's side-wall and the cylinder-free area of the wafer were similarly protected during chemical functionalization, it is likely that the formerly protected portion of the cylinder's sides should

lack any specific binding sites. Thus, the chemical functionalization appears limited to the exposed portion of cylinder surface, which is predominantly the top surface.

The selective functionalization of cylinders with centered protrusions was tested similarly. However, to carry out the functionalization a critical step is involved, namely exposing the centered protrusion for chemical functionalization while the rest of the cylinder surface remains buried in PMMA resist (Figure 5b). Given the variability in cylinder height discussed above, one might expect the degree of exposure of the centered protrusion to vary with the radial position on the wafer. While this was indeed the case, the variation in the height of the exposed portion of centered protrusions was interestingly far smaller than the variation in the cylinder height. For example, we find the height of cylinder main body to increase by ~300 nm (from ~1.7 μm at wafer center to ~2 μm 30 mm from wafer center), while the height of the exposed portion of centered protrusion increases by only about 100 nm (from ~120 nm to ~220 nm). This may be explained by an inhomogeneity in the thickness of the PMMA coating that would partly compensate the variation in cylinder height. We have indeed observed that the PMMA layer displays a slightly undulatory pattern, with maxima on the individual buried cylinders that additionally correlate with their height. With this in mind, we simply designed protrusions of sufficient height (~250-300 nm), thereby ensuring that all centered protrusions were partly exposed and that the remainder of surface was well-protected by PMMA. The selective functionalization of cylinders with centered protrusions was then tested by the specific binding of fluorescently-labeled biotinylated oligonucleotides as above (Figure 5c). Again, a hexagonal array of fluorescent spots (of specifically-bound oligonucleotides) indicates the chemical functionalization was specific to the selectively-functionalized portion of the centered protrusions. Further evidence for the selectivity of the chemical functionalization was evidenced by directly SEM imaging (Figure 5d), which demonstrated that biotin-labeled microspheres specifically bind to the centered protrusions of quartz cylinders.

Applications of Fabricated Cylinders in OTW: We now demonstrate the angular trapping properties of quartz cylinders in the OTW (Methods). First, for untethered cylinders of two different diameters (200 nm, 500 nm), we measured torque-rotation curves (Figure 6a; 500 nm cylinder in blue squares, 200 nm cylinder in red circles). Here, the cylinders are rotated at different speeds while measuring the mean value of the exerted torque. We clearly observe two distinct regimes in the response, separated by a threshold frequency: below the threshold frequency, the mean torque increases linearly with the imposed frequency, while subsequently the mean torque decays towards zero.[10, 22] The slope in the linear regime is equal to the rotational drag coefficient, which is itself approximately proportional to the cylinder's volume.[31] As expected, therefore, the larger cylinder presents a larger slope: the drag coefficient determined from the slope is about 3.7 pN·nm·s for the large cylinder (~ 500 nm/900 nm/2 μm, top diameter/bottom diameter/height, Figure 3d), and about 0.18 pN·nm·s for the small cylinder (~ 200 nm/300 nm/650 nm, Figure 3c). For comparison, theoretical estimation[31] of the rotational drag coefficient in water yields 3.2 pN·nm·s for a large cylinder (700 nm/700 nm/2 μm) and 0.14 pN·nm·s for a small cylinder (250 nm/250 nm/650 nm). While the drag coefficient differs greatly between the small and large cylinders, the same is not true for the threshold frequencies. This is because the maximal possible torque exerted on a cylinder is also roughly proportional to the volume of the cylinder.[23] In other words, given a

constant laser power, a larger torque always comes with a larger drag. Note that differently-sized cylinders come with distinct advantages: if large torques need to be applied, larger cylinders should be selected; however, when a fast response time is desired, smaller cylinders with their smaller drag are preferred.

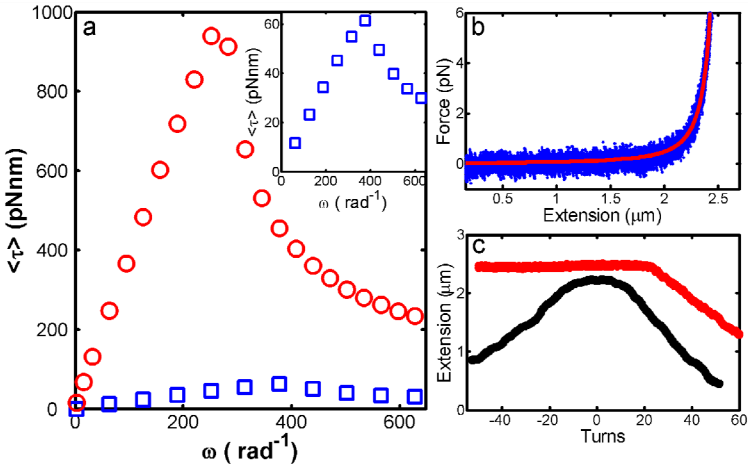

Figure 6. Characterization of quartz cylinders in an OTW. (a) The average torque exerted on an untethered quartz cylinder as a function of rotational frequency. Data are shown in red circles for a large cylinder (cone-shaped with 500 nm top diameter, Figure 3d) and in blue squares for a smaller cylinder (200 nm top diameter, Figure 3c). The inset shows a zoom on the data for the smaller cylinder. At each rotational frequency, the optical torque was recorded for 5 s. (b) Force-extension curve of a dsDNA attached to a quartz cylinder with a centered protrusion (blue points). The red curve shows a fit to the worm-like chain model. (c) Rotation–extension curves of a dsDNA attached to a quartz cylinder with a centered protrusion under stretching forces of 0.5 pN (black points) and 2 pN (red points). The rate of laser polarization rotation equaled 1 turn/s.

We then extended our measurements to cylinders tethered to dsDNA (Figure 6b,c). Here, we employed cylinders with selectively-coated centered protrusions (experiments were equally successful on cylinders selectively-coated on only a single face, data not shown). First, we varied the force applied to the cylinders by moving the flow cell by piezo-actuators at a constant speed of 1 μm/min relative to the optical trap center along the direction of laser propagation. The displacement of the tethered cylinder relative to the optical trap center was measured to determine the force and its absolute position with respect to the flow cell surface yielded the molecule's extension (Figure 6b, blue points). The excellent fit to the worm-like chain model[32] (Figure 6b, red line), yielding a persistence length L_p = 42 nm and contour length L_c = 2.6 μm, demonstrated proper attachment of a single molecule. Next, at a fixed force, we rotated the cylinder, yielding an extension-rotation curve (Figure 6c, two different forces shown; see also Methods). The rotational response of the dsDNA, with its characteristic symmetric response under low forces and asymmetric response to rotation under high forces,[33] demonstrates that the dsDNA is multiply tethered to the centered protrusion. This demonstrates that electron beam-fabricated quartz cylinders are fully capable

of manipulating single biomolecules in the OTW, providing a new tool for their subsequent study.

5.4 Conclusions

We have developed a novel method based on electron beam lithography for the fabrication of quartz cylinders. In comparison to approaches based on optical lithography, our method provides far greater versatility: a larger range of cylinder dimensions and more complex geometries were fabricated, under conditions of across-wafer uniformity. We have also developed a novel approach for the selective functionalization of quartz cylinders, which was demonstrated successfully through its use in the stretching and twisting of DNA in an OTW.

Acknowledgments: We thank M. Zuiddam for help with the C_4F_8 dry etching protocol, A. van Run for assistance in optimizing the electron beam exposure, M. van der Krogt for help with gold deposition, P. Galajda, E. van der Drift, and J. Andreasson (Stanford University) for advice on microfabrication, S. Hage and S. Donkers for DNA synthesis, J. van der Does, D. de Roos, and J. Beekman for help with instrumentation and infrastructure, F. Hol for stimulating discussions, TU Delft Nanofacility for process support, and TU Delft, FOM (Dutch Foundation for Research on Matter), NWO (Nederlandse Organisatie voor Wetenschappelijk Onderzoek), and ESF (European Science Foundation) for financial support.

5.5 References

1. Pankhurst, Q. A.; Connolly, J.; Jones, S. K.; Dobson, J., Applications of Magnetic Nanoparticles in Biomedicine. J Phys D Appl Phys 2003, 36, R167-R181.

2. Neuman, K. C.; Nagy, A., Single-Molecule Force Spectroscopy: Optical Tweezers, Magnetic Tweezers and Atomic Force Microscopy. Nat Methods 2008, 5, 491-505.

3. Walter, N. G.; Huang, C. Y.; Manzo, A. J.; Sobhy, M. A., Do-It-Yourself Guide: How to Use the Modern Single-Molecule Toolkit. Nat Methods 2008, 5, 475-489.

4. Svoboda, K.; Block, S. M., Biological Applications of Optical Forces. Annu Rev Bioph Biom 1994, 23, 247-285.

5. Kegel, W. K.; van Blaaderen, A., Direct Observation of Dynamical Heterogeneities in Colloidal Hard-Sphere Suspensions. Science 2000, 287, 290-293.

6. Pertsinidis, A.; Ling, X. S., Diffusion of Point Defects in Two-Dimensional Colloidal Crystals. Nature 2001, 413, 147-150.

7. Ghosh, A.; Fischer, P., Controlled Propulsion of Artificial Magnetic Nanostructured Propellers. Nano Lett 2009, 9, 2243-2245.

8. Bishop, A. I.; Nieminen, T. A.; Heckenberg, N. R.; Rubinsztein-Dunlop, H., Optical Microrheology Using Rotating Laser-Trapped Particles. Phys Rev Lett 2004, 92, 198104.

9. Parkin, S. J.; Knoner, G.; Nieminen, T. A.; Heckenberg, N. R.; Rubinsztein-Dunlop, H., Picoliter Viscometry Using Optically Rotated Particles. Phys Rev E 2007, 76, 041507.

10. Pedaci, F.; Huang, Z.; van Oene, M.; Barland, S.; Dekker, N. H., Excitable Particles in an Optical Torque Wrench. Nature Physics accepted Oct 2010.

11. Leach, J.; Mushfique, H.; di Leonardo, R.; Padgett, M.; Cooper, J., An Optically Driven Pump for Microfluidics. Lab Chip 2006, 6, 735-739.

12. Forth, S.; Deufel, C.; Sheinin, M. Y.; Daniels, B.; Sethna, J. P.; Wang, M. D., Abrupt Buckling Transition Observed During the Plectoneme Formation of Individual DNA Molecules. Phys Rev Lett 2008, 100, 148301.

13. Gutierrez-Medina, B.; Andreasson, J. O. L.; Greenleaf, W. J.; LaPorta, A.; Block, S. M., An Optical Apparatus for Rotation and Trapping. Method Enzymol 2010, 474, 377-404.

14. Vogel, R.; Persson, M.; Feng, C.; Parkin, S. J.; Nieminen, T. A.; Wood, B.; Heckenberg, N. R.; Rubinsztein-Dunlop, H., Synthesis and Surface Modification of Birefringent Vaterite Microspheres. Langmuir 2009, 25, 11672-11679.

15. Parkin, S. J.; Vogel, R.; Persson, M.; Funk, M.; Loke, V. L. Y.; Nieminen, T. A.; Heckenberg, N. R.; Rubinsztein-Dunlop, H., Highly Birefringent Vaterite Microspheres: Production, Characterization and Applications for Optical Micromanipulation. Opt Express 2009, 17, 21944-21955.

16. Singer, W.; Nieminen, T. A.; Gibson, U. J.; Heckenberg, N. R.; Rubinsztein-Dunlop, H., Orientation of Optically Trapped Nonspherical Birefringent Particles. Phys Rev E 2006, 73, 021911.

17. Singer, W.; Rubinsztein-Dunlop, H.; Gibson, U., Manipulation and Growth of Birefringent Protein Crystals in Optical Tweezers. Opt Express 2004, 12, 6440-6445.

18. Starr, C.; Dultz, W.; Wagner, H. P.; Dholakia, K.; Schmitzer, H., Optically Controlled Rotation of Ptcda Crystals in Optical Tweezers. Aip Conf Proc 2005, 772, 1099-1100.

19. Sun, X. D.; Zhang, H. L.; Li, X. C.; Gong, D. W.; Lee, H., Optical Rotation and Manipulation of Micro-Sized Linbo3 Crystals and Single-Walled Carbon Nanotubes Bundles. Colloid Surface A 2008, 313, 488-491.

20. Rodriguez-Otazo, M.; Augier-Calderin, A.; Galaup, J. P.; Lamere, J. F.; Fery-Forgues, S., High Rotation Speed of Single Molecular Microcrystals in an Optical Trap with Elliptically Polarized Light. Appl Optics 2009, 48, 2720-2730.

21. Deufel, C.; Forth, S.; Simmons, C. R.; Dejgosha, S.; Wang, M. D., Nanofabricated Quartz Cylinders for Angular Trapping: DNA Supercoiling Torque Detection. Nat Methods 2007, 4, 223-225.

22. La Porta, A.; Wang, M. D., Optical Torque Wrench: Angular Trapping, Rotation, and Torque Detection of Quartz Microparticles. Phys Rev Lett 2004, 92, 190801.

23. Friese, M. E. J.; Nieminen, T. A.; Heckenberg, N. R.; Rubinsztein-Dunlop, H., Optical Alignment and Spinning of Laser-Trapped Microscopic Particles. Nature 1998, 394, 348-350.

24. Ashkin, A.; Dziedzic, J. M.; Yamane, T., Optical Trapping and Manipulation of Single Cells Using Infrared-Laser Beams. Nature 1987, 330, 769-771.

25. Lipfert, J.; Kerssemakers, J. W.; Jager, T.; Dekker, N. H., Magnetic Torque Tweezers: Measuring Torsional Stiffness in DNA and Reca-DNA Filaments. Nat Methods 2010.

26. Westerheim, A. C.; Labun, A. H.; Dubash, J. H.; Arnold, J. C.; Sawin, H. H.; Yuwang, V., Substrate Bias Effects in High-Aspect-Ratio Sio2 Contact Etching Using an Inductively-Coupled Plasma Reactor. J Vac Sci Technol A 1995, 13, 853-858.

27. Karttunen, J.; Kiihamaki, J.; Franssila, S., Loading Effects in Deep Silicon Etching. P Soc Photo-Opt Ins 2000, 4174, 90-97.

28. Akashi, T.; Yoshimura, Y., Deep Reactive Ion Etching of Borosilicate Glass Using an Anodically Bonded Silicon Wafer as an Etching Mask. J Micromech Microeng 2006, 16, 1051-1056.

29. Kiihamaki, J., Deceleration of Silicon Etch Rate at High Aspect Ratios. J Vac Sci Technol A 2000, 18, 1385-1389.

30. Kokkoris, G.; Gogolides, E.; Boudouvis, A. G., Simulation of Fluorocarbon Plasma Etching Sio2 Structures. Microelectron Eng 2001, 57-8, 599-605.

31. Tirado, M. M.; Garciadelatorre, J., Rotational-Dynamics of Rigid, Symmetric Top Macromolecules - Application to Circular-Cylinders. J Chem Phys 1980, 73, 1986-1993.

32. Bustamante, C.; Marko, J. F.; Siggia, E. D.; Smith, S., Entropic Elasticity of Lambda-Phage DNA. Science 1994, 265, 1599-1600.

33. Strick, T. R.; Dessinges, M. N.; Charvin, G.; Dekker, N. H.; Allemand, J. F.; Bensimon, D.; Croquette, V., Stretching of Macromolecules and Proteins. Rep Prog Phys 2003, 66, 1-45.

Chapter 6

Calibration of the Optical Torque Wrench

Francesco Pedaci†, Zhuangxiong Huang†, Maarten van Oene, and Nynke H. Dekker

(†=equal contribution)

The optical torque wrench is a laser trapping technique that expands the capability of standard optical tweezers to torque manipulation and measurement, using the laser linear polarization to orient tailored microscopic birefringent particles. The ability to measure torque of the order of k_BT (~4 pN·nm) is especially important in the study of biophysical systems at the molecular and cellular level. Quantitative torque measurements rely on an accurate calibration of the instrument. Here we describe and implement a set of calibration approaches for the optical torque wrench, including methods that have direct analogs in linear optical tweezers as well as introducing others that are specifically developed for the angular variables. We compare the different methods, analyze their differences, and make recommendations regarding their implementations. *

* This chapter has been published as F. Pedaci†, Z. Huang†, M. van Oene, and N.H. Dekker, *Opt. Express* 20, 3787-3802 (2012), (†=equal contribution).

6.1 Introduction

The ability of optical tweezers (OT) to manipulate microscopic particles held in the focus of a laser has paved the way for many important lines of research in fields ranging from physics to biology. In single-molecule biological physics in particular, OT is one of the techniques that have ushered in a revolution in the way biological systems can be explored. In such studies, a microscopic particle is used as a force transducer and sensor through which the optical force can be transferred to a single biopolymer (*e.g.* DNA, RNA or protein). This allows one to monitor e.g. the mechanical response of a single biopolymer to linear tension (force spectroscopy), or the action of enzymes that employ the tethered molecule as substrate [1–3].

In addition to force, torque also is a physical parameter of biological relevance, as shown by its role in diverse cellular processes such as DNA replication [4], transcription [5], ATP synthesis [6, 7], and bacterial propulsion [8]. However, investigating the role of torque has proved more challenging, in part due to a lack of straightforward single-molecule manipulation techniques. Fortunately, recent efforts have focused on the development of techniques that allow the control and measurement of both force and torque on microscopic actuators [9–12].

The optical torque wrench (OTW) is one such technique and distinguishes itself by its all optical manipulation and detection of trapped microscopic birefringent particles. The OTW can easily control and detect linear and angular displacements of trapped particles with fast ms temporal resolution, allowing one to implement fast feedback loops to actively clamp the value of force or torque [10, 13]. Recent studies have continued to expand our understanding of OTW physics by focusing on the system's angular dynamics [14, 15], but already the OTW has found applications in the study of torque-induced structural transitions of single DNA molecules [16–18]. Together, these advances demonstrate that the OTW has the potential to apply and dynamically measure torque at the scale of k_BT (~4 pN·nm), opening up new applications in the study of biophysical systems.

A key component of any trapping technique, linear or angular, is the ability to properly calibrate the instrument to perform absolute quantitative measurements. Diverse methods for the calibration of linear OT can be found in the literature [19–23], while calibration of the OTW has been less fully explored [16, 24]. Here we describe several different procedures to calibrate the angular trap of an OTW, detail their experimental implementations, and compare their outcomes. As we will show, several methods have their direct analogs in the calibration of linear traps, while others are more tailored to the particularities of angular variables.

This work is organized as follows: in section 6.2 we provide an overview of OTW theory (sec. 6.2.1) and describe our experimental system in detail (sec. 6.2.2); in section 6.3 we compare the calibration principles of OT to those of OTW; in section 6.4 we detail five methods for calibrating the OTW; and in section 6.5 we discuss their outcomes.

6.2 The Optical Torque Wrench

In this section, we will describe the theoretical framework of the optical torque wrench and its experimental implementation, which together provide the necessary background for the calibration methods described subsequently.

6.2.1. Theoretical overview

In an OTW, torque is optically applied to a birefringent particle through spin momentum change in the linearly polarized laser field [10, 13]. Through its interaction with the birefringent material, the macroscopic polarization $\vec{p}$ induced in the medium is in general not parallel to the laser polarization $\vec{E}$ (Fig. 1a). Therefore the product $\vec{\tau} = \vec{p} \times \vec{E}$ is non-zero and a finite torque t is applied to the particle. The net transferred torque is measured at the trap output as an imbalance between the intensities of the left- and right-circular components of the light that propagated inside the birefringent particle.

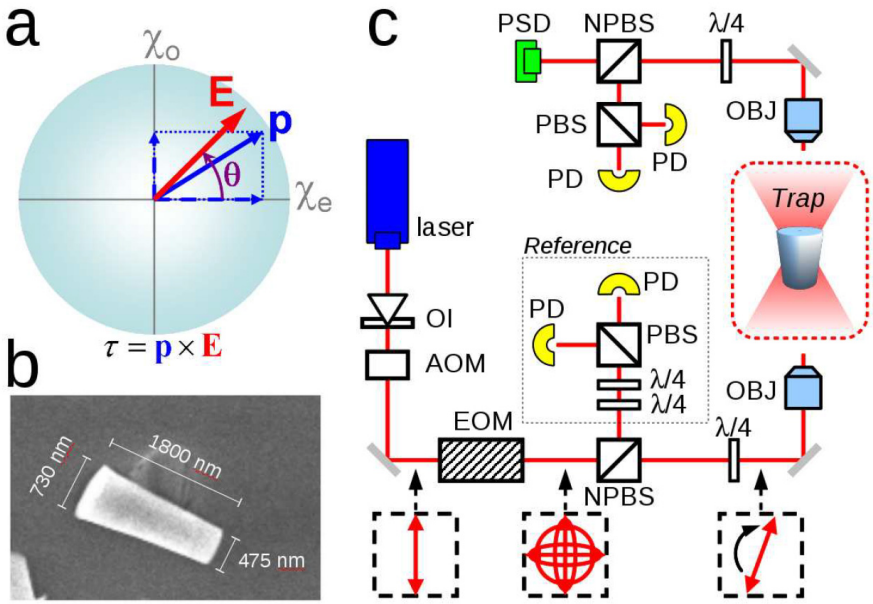

Fig. 1. *Experimental configuration*. a) Schematic depicting of the torque generation inside a birefringent crystal that has a larger susceptibility along its extraordinary axis χ_e than along its ordinary axis χ_o. b) SEM image of a nano-fabricated birefringent quartz cylinder used in the OTW. c) Diagram of the optical setup. OI: optical isolator, AOM: acousto-optic modulator, EOM: electro-optic modulator, NPBS: 50% non-polarizing beam splitter, λ/4: quarter wave-plate, PBS: polarizing beam splitter, PD: photo-detector, PSD: position sensitive detector, OBJ: 1.2NA microscope objective. The optical trap is surrounded by red dashed lines, the torque reference system is labeled and surrounded by grey dots, and the polarization state controlled by the EOM is indicated by red arrows inside the black dashed squares.

The torque transferred to a positive (negative) uniaxial birefringent particle is related to the angle $x = \theta_{cyl} - \theta_{pol}$ between the linear laser polarization θ_{pol} and the extraordinary (ordinary) axis θ_{cyl} according to

$$\tau = \tau_o \sin(2x). \tag{1}$$

where τ_o is the maximum optical torque, which depends on laser intensity, particle size, and birefringence [10]. For $x \ll 1$, linearization of the optical torque $\tau \approx 2\tau_o x$ can be used to define the angular stiffness $\kappa = 2\tau_o$.

The over-damped angular equation of motion for the birefringent particle in an OTW can therefore be written as

$$-\gamma(\dot{x} + \dot{\theta}_{pol}) - \tau_o \sin(2x) + \eta(t) = 0 \tag{2}$$

where γ is the angular drag coefficient and $\eta(t)$ is the Langevin force, a Gaussian-distributed white noise term obeying $\langle \eta(t)\eta(t') \rangle = 2k_B T\gamma\delta(t-t')$.

The dynamics of the OTW are best understood by rewriting the equation of motion to make explicit the potential landscape experienced by the particle. When the laser polarization rotates at constant frequency ω (*i.e.* $\theta_{pol} = \omega t$), the equation of motion can be written in terms of a total potential $U(x) = V(x) - Fx$, where $V(x)$ is a periodic potential tilted by an external force *F*, as

$$\gamma\dot{x} = -U'(x) + \eta(t) \tag{3}$$

which is equivalent to Adler's equation [25]. In the OTW, the periodic angular potential takes the form of $V(x) = -\frac{\tau_o}{2}\cos(2x)$, with $V(x+\pi) = V(x)$, and the tilting force is $F = -\gamma\omega$. Hence, the result of the polarization rotation is to tilt the periodic potential.

The dynamics of the OTW can be separated into two distinct dynamic regimes, separated by a saddle-node bifurcation occurring at $\omega = \omega_c = \tau_o / \gamma$. The first regime, in which $|\omega| < \omega_c$, is characterized by the existence of a potential barrier separating two successive stable states. At these low frequencies, the drag torque $\gamma\omega$ can be balanced by the optical torque $\tau(x)$, for a particular angle *x*, and the particle rotates in phase with the driving polarization. When $|\omega| <\approx \omega_c$, the presence of thermal noise can allow the system to escape the barrier between two potential minima, resulting in the appearance of regular spikes in the torque signal, a characteristic feature of the excitability of the system [15]. Physically, this corresponds to the extraordinary axis of the particle transiently slipping out of the polarization direction during rotation. In the second regime in which $|\omega| > \omega_c$, the potential barrier

disappears, the stable and unstable points merge, and a limit cycle is created giving rise to a deterministic periodic torque signal with period given by

$$T_o = \frac{\pi}{\sqrt{\omega^2 - \omega_c^2}}. \tag{4}$$

In presence of noise and for ω sufficiently greater than ω_c, the period of the torque signal becomes a statistical variable T_s distributed around its mean value T_o, hence $\langle T_s \rangle \approx T_o$.

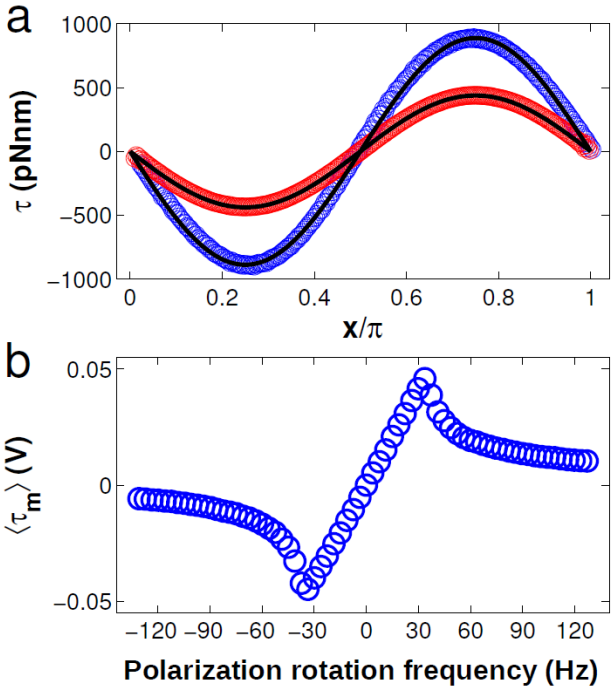

Fig. 2. *Torque on a birefringent cylinder.* a) Calibrated optical torque as a function of the angle x between the polarization and the extraordinary axis for two laser intensities (blue points: 100 mW, red points: 50 mW, power measured at the objective input). The traces are reconstructed from torque traces recorded at $\omega > \omega_c$. Calibration was performed following the method described in sec.6.4.2.1. The black lines are sinusoidal fits (eq.1) of the experimental points. b) Mean value of the measured torque as a function of the polarization rotation frequency. Within the region $|\omega| < \omega_c \approx 37 (\times 2\pi)$ Hz the torque is constant in time ($\tau_m = \beta_\tau \gamma \omega$, while for $|\omega| > \omega_c$ the torque becomes periodic, with mean period given by eq.4. Negative frequencies indicate opposite rotation direction. Note that the cylinder used here has a larger volume and lower ω_c than the one used in the subsequent figures and table.

The physics of the OTW can be experimentally verified (Fig.2). In Fig.2a, we demonstrate the excellent agreement between the theoretically predicted (eq.1) torque τ (solid lines) and the experimentally measured values (red and blue data-points), plotted over a full period of

the angle between the extraordinary axis and the laser polarization. In Fig.2b, we plot the experimentally measured mean value of the torque transferred to the trapped birefringent cylinder (Fig.1b) at different polarization frequencies (for experimental methods, see sec.6.2.2). The transition found at $|\omega| = \omega_c$ illustrates the passage between the two dynamical regimes discussed above. For $|\omega| < \omega_c$ the torque is constant in time and its value increases linearly with the frequency to balance the drag torque. Beyond the critical frequency, the drag torque $\gamma\omega$ overcomes the maximum optical torque τ_o, and the axis of the particle escapes the direction of the rotating polarization, reducing the average value of τ_m.

6.2.2. Experimental configuration

In the OTW, we employ cylindrically-shaped microscopic quartz (positive uniaxial) particles [26] fabricated by electron-beam lithography [27]. The particles have a tapered profile, with the dimensions indicated in Fig.1b, and their extraordinary axis is perpendicular to their geometrical axis. Inside the optical trap, the cylinder aligns itself parallel to the direction of laser propagation to minimize the scattering force. This, together with the three-dimensional linear trap, constrains five of the particle's degrees of freedom. The remaining degree of freedom (rotation of the cylinder around its axis) is controlled by the linear polarization of the laser, which defines the stable orientation for the extraordinary axis at $x=0(\mathrm{mod}\,\pi)$ (Fig.2a).

To control the orientation of the laser polarization, we use a fast electro optic modulator (EOM) with its axis oriented at 45º with respect to the laser polarization (Fig.1c) in combination with a quarter wave-plate (aligned at 45º with respect to the EOM axis) [24]. The resulting polarization inside the optical trap is linear (ellipticity $\lesssim$ 5%), and its angle is linearly proportional to the voltage applied to the EOM. The torque transferred to the trapped particle is deduced from the difference of the intensity signals of the two circular components of the laser light at the output of the trap.

By applying a repetitive sawtooth signal to the EOM voltage (corresponding to a rotation between 0 and π), we can quasi-continuously rotate the polarization inside the trap. We observe that rotating the laser polarization in an empty trap generates a torque signal that is modulated at the frequency of the EOM voltage, instead of the expected constant (zero) value. This can be due to imperfections of the EOM such as a small misalignment of the internal crystals. We overcome this problem by recording a torque reference signal equivalent to the torque transferred in an empty trap (Fig.1c, grey dotted box labeled *Reference*), and defining this as the zero-torque level. This reduces the spurious torque modulation to few percent of τ_o when a particle is trapped and rotated.

The optical trap is formed at the matched focus of a pair of identical microscope objectives (1.2 NA, water immersion). The intensity of the 1064 nm trapping laser is intentionally limited to 100 mW at the trap input. A calibrated position sensitive detector (PSD), placed in a plane conjugate to the back focal plane of the condenser, is used to monitor the displacement of the trapped particle in x,y,z. We employ an acousto-optic modulator to actively control the laser intensity, and we utilize two independent imaging systems to

monitor both the laser's transverse profile at the back focal plane of the condenser as well as the surroundings of the trapped particle inside the flow cell. An FPGA card runs the feedback loops that can be used to actively control the laser intensity and the torque amplitude, while a DAQ card acquires the PSD signals. The maximum overall temporal resolution is 5 μs. The flow cell is prepared with two glass slides (thickness 170 μm each) spaced by one parafilm layer, and buffer exchange is possible through inlet and outlet holes in the top glass slide.

6.3 Similarities and Differences in the Calibration of OT and OTW

In OT, quantitative force measurements can be accomplished by obtaining a complete set of three calibration parameters. First, the *sensitivity* of the detection system (in units of V/m) must be known in order to convert the measured voltage signal, proportional to the displacement of the bead inside the trap, from Volts to meters. Second, once the displacement is known in meters, the force on the trapped bead is calculated as the product between the *trap stiffness* (in units of pN/nm) and the displacement. From the analysis of the Brownian fluctuations of the particle inside the trap, one can extract the sensitivity and trap stiffness provided that the particle *drag coefficient* (in units of pN·s/nm) is known. Thus in total three independent measurements are required.

The three corresponding angular parameters that need to be quantified during the calibration of an OTW are the *torque sensitivity* β_τ (in units of V/pN·nm), the *angular stiffness* κ (in units of pN·nm/rad), or equivalently, the *maximum torque* τ_o (in units of pN·nm), and the *angular drag coefficient* γ (in units of pN·nm·s).

We can nonetheless underline several differences between the calibration of OT and OTW:

1) The quantity directly measured in an OTW is torque, from which the angle of the particle can be determined, while in OT the displacement is measured and the force is determined from it.

2) The sensitivity in OT varies outside the linear response region of the detector. In the OTW, by contrast, the measured torque signal τ_m (in Volts) is always linearly proportional to the optical torque τ applied to the birefringent particle via the sensitivity β_τ, according to

$$\tau_m = \beta_\tau \tau. \tag{5}$$

3) In OT, a single stable point for the position of the particle is defined and it is common (even though not necessary [28]) to employ only the region of the optical potential where the stiffness is constant and the linear approximation between force and displacement holds. In the OTW, the optical potential is periodic. This makes the inharmonic region of the angular potential readily accessible, because even when the particle explores angles far from the stable solution, it never escapes the 3D trap. In the following, to characterize the sinusoidal optical torque (Fig.2a) we will use the maximum available torque τ_o.

4) In both OT and OTW, when the medium viscosity is known, one has to consider how the drag coefficients depend on the particle geometry. For OT experiments, fully spherical

dielectric beads with precisely known radii are readily available, hence for calibration purposes one can safely assume the theoretical value for the linear drag given by the Stokes relation (corrected for the proximity of a surface as necessary). Calibrations with other particle geometries are also possible [29, 30]. This has the advantage of reducing the number of independent calibration measurements from three to two. By contrast, for the OTW one typically nanofabricates the birefringent particles [26, 27]. We nano-fabricated quartz cylinders with ~10% volume variation [27] that have a lightly tapered form; due to this variability in particle size and the fact that an exact analytical expression for the drag coefficient of tapered cylinders is lacking, we develop methods that allow us to directly measure the particle drag in question. Interestingly, our experimental results find quite good agreement between the values of the measured and the theoretical drag, provided that the latter is computed for a perfect cylinder with a volume equivalent to that of the cylinders employed in the experiments.

6.4 Approaches for Angular Calibration

We now discuss different approaches to perform the three independent measurements needed for OTW calibration. The approaches have in common that they provide independent measurements of the angular thermal fluctuations, of the angular response of the system to controlled modulations of the direction of the laser polarization, and of the characteristic time-scale of the system. The interplay between these three measured quantities then serves to fix the three calibration parameters. The main experimental control parameter is the frequency ω at which the polarization is rotated, also referred to as the polarization rotation frequency (which may be zero or even negative). For convenience, we classify the different calibration methods by the number of polarization rotation frequencies employed.

6.4.1. Calibration approach involving measurement over the full range of frequencies: fitting the standard deviation of the torque signal

In this first approach, we rotate the laser polarization over a wide range of frequencies to probe the system's complete dynamic response while recording the torque transferred to the trapped cylinder. For each polarization rotation frequency ω, we determine the standard deviation $\delta\tau_m$ (in Volts) of the measured optical torque signal τ_m (Fig.3, blue squares). Similar to the data shown in Fig.2a, an abrupt transition in the particle's response at $\omega = \omega_c$ is evident.

We can derive an analytical expression for $\delta\tau_m$ (Appendix I), for which the correct form depends on whether ω is above or below the critical frequency ω_c

$$\delta\tau_m = \beta_\tau \sqrt{2\tau_o k_B T}\left[1-(\omega/\omega_c)^2\right]^{\frac{1}{4}} \text{ for } \omega < \omega_c \tag{6}$$

$$= \beta_\tau \tau_o \left[\frac{\sqrt{(\omega/\omega_c)^2 - 1}}{(\omega/\omega_c) + \sqrt{(\omega/\omega_c)^2 - 1}} \right]^{\frac{1}{2}} \quad \text{for } \omega > \omega_c \tag{7}$$

Fitting the experimentally determined standard deviation of the torque to eq.6 and eq.7, as shown by the red line in Fig.3, we obtain the complete set of calibration parameters β_τ, τ_o and $\gamma = \tau_o / \omega_c$. Alternatively, the fit can be used to find the three quantities $\delta\tau_m(\omega = 0)$, $\delta\tau_m(\omega = \infty)$ and ω_c, from which the calibration parameters can be subsequently deduced according to:

$$\tau_o = 4k_B T \delta\tau_m^2(\infty) / \delta\tau_m^2(0) \tag{8}$$

$$\gamma = \tau_o / \omega_c \tag{9}$$

$$\beta_\tau = \sqrt{2}\delta\tau_m(\infty) / \tau_o \tag{10}$$

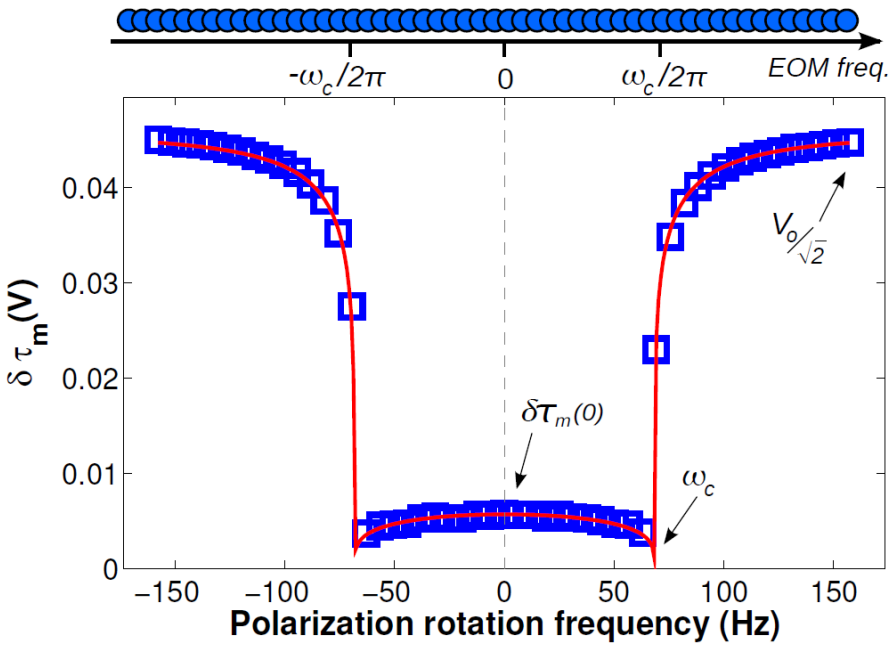

Fig. 3. *Calibration approach involving measurement over the full range of frequencies*. We plot the standard deviation of the measured torque (in Volts) as a function of the polarization rotation frequency. The quantities needed for calibration are indicated by arrows. The red line is a fit of the data to eqs. 6 and 7, yielding ω_c = 429 rad/s, $\delta\tau_m(0)$ = 5.7 mV, and $\sqrt{2}\delta\tau_m(\infty) = V_o$ = 64.9 mV (see text). The top diagram uses blue circles to schematically indicate the polarization frequencies generated by the EOM in this method.

6.4.2. Calibration approaches involving separate measurements at two frequencies

In this second approach, we perform separate measurements at two different polarization rotation frequencies. Within this approach, there are two variants that we describe in turn.

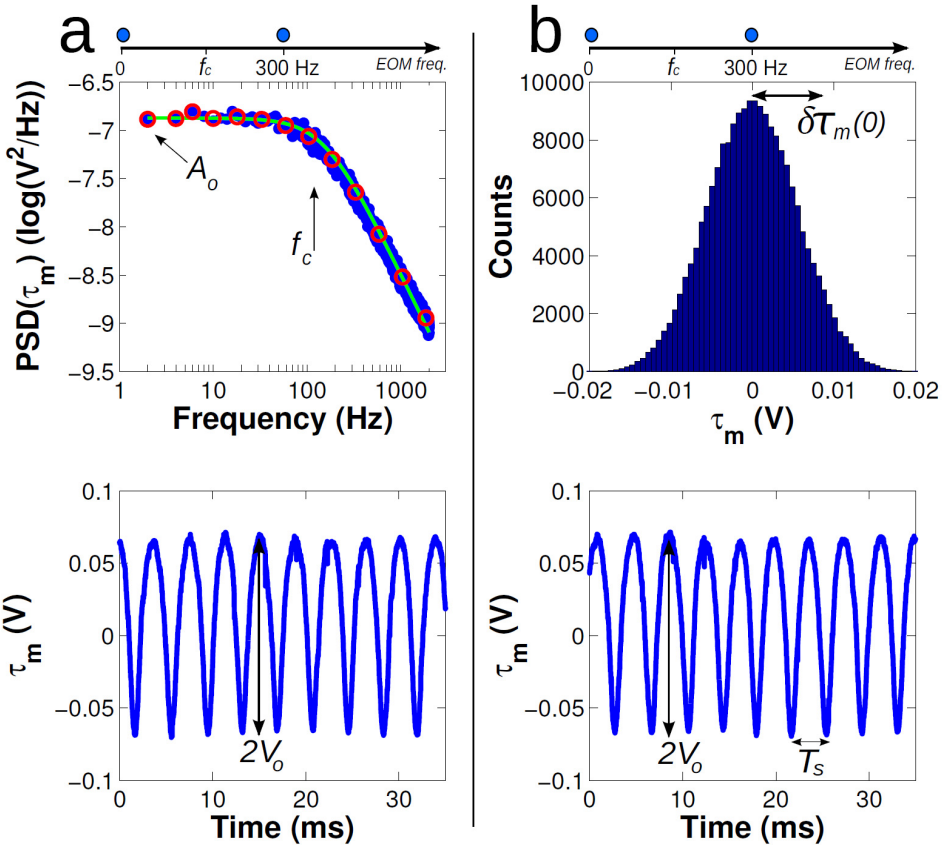

Fig. 4. *Calibration approaches involving separate measurements at two frequencies*. a) Power spectrum analysis at $\omega = 0$ followed by fast rotation at $\omega > \omega_c$. From top to bottom: a schematic of the EOM frequencies used (blue circles), the power spectrum at = 0 (where the red points result from inning the experimental points (blue) into bins of variable size and the green line is a fit of the red points to a Lorentzian), and a segment of the torque trace acquired at $\omega/2\pi$ = 300Hz. For this dataset, the measured variables (indicated by arrows) are f_c =152 Hz, A_o =3.1E-3 V^2Hz, and V_o =67 mV. b)Measurement of the torque variance, period, and amplitude. From top to bottom: a schematic of the EOM frequencies used (blue circles), the probability distribution of the torque readout at ω=0, and a segment of the torque trace acquired at $\omega/2\pi$=300Hz. For this dataset, the measured variables (indicated by arrows) are $\delta\tau_m$ = 5.5 mV, $\langle T_s \rangle$ = 3.8 ms, and V_o = 66 mV.

6.4.2.1. *Power spectrum analysis at* $\omega = 0$ *followed by fast polarization rotation at* $\omega > \omega_c$

In this method [13], one first considers the power spectral density of the measured torque signal at $\omega = 0$, which is a measurement that yields two independent quantities (Fig.4a). To see this, we note that at fixed laser polarization the power spectral density of the measured torque signal is described by a Lorentzian (provided that linearization around the particle's stable point is possible, *i.e.* $\tau_o >> k_B T$). This Lorentzian, $P_o(\tau_m, f) = A_o / (f^2 + f_c^2)$, is parameterized by an amplitude $A_o = 4\beta_\tau^2 \tau_o^2 k_B T / (\pi^2 \gamma)$ and a corner frequency $f_c = \tau_o / (\pi\gamma) = \omega_c / \pi$. Fitting the experimental spectrum to this function therefore yields two independent variables A_o and f_c (Fig.4a *top*).

To determine the third independent variable, a subsequent measurement is performed at $\omega > \omega_c$, the regime where the torque experienced by the particle is periodic as a function of time. A typical trace showing the amplitude of the torque signal V_o (defined as half of the peak-to-peak value in Volts) is shown in Fig.4a *bottom*. In practice, the value of V_o can vary along the torque trace due to the small spurious modulation discussed in sec.6.2.2. Therefore, to systematically determine an accurate average value of V_o from the entire recorded torque signal, we measure the standard deviation $\delta\tau_m$ and invert eq.7 to obtain $V_o = \beta_\tau \tau_o$.

From the measurement of the three independent variables A_o, f_c, and V_o, the calibration parameters are deduced according to:

$$\gamma = 4k_B T V_o^2 / (\pi^2 A_o) \tag{11}$$

$$\tau_o = \pi\gamma f_c \tag{12}$$

$$\beta_\tau = V_o / \tau_o \tag{13}$$

6.4.2.2. *Calibration by measurement of the torque variance, period and amplitude*

A second method that probes the response of the birefringent particle at two polarization rotation frequencies follows a similar approach. Again, we start by examining the regime in which the polarization direction is fixed ($\omega = 0$), but now we measure the standard deviation of the torque signal $\delta\tau_m(\omega = 0) = \beta_\tau \sqrt{2k_B T \tau_o}$ (eq.6). This yields the first independent variable (Fig.4b *top*).

In a subsequent step, we consider the regime in which the polarization rotation frequency is set to $\omega > \omega_c$. From the resulting periodic torque trace in the temporal domain (Fig.4b *bottom*), we can extract the torque amplitude $V_o = \beta_\tau \tau_o$ as before. In addition we extract the

mean period $\langle T_s \rangle$ of the oscillating torque experienced by the particle. Using eq.4, we can extract the value of $\omega_c = \tau_o / \gamma$ from $\langle T_s \rangle$.

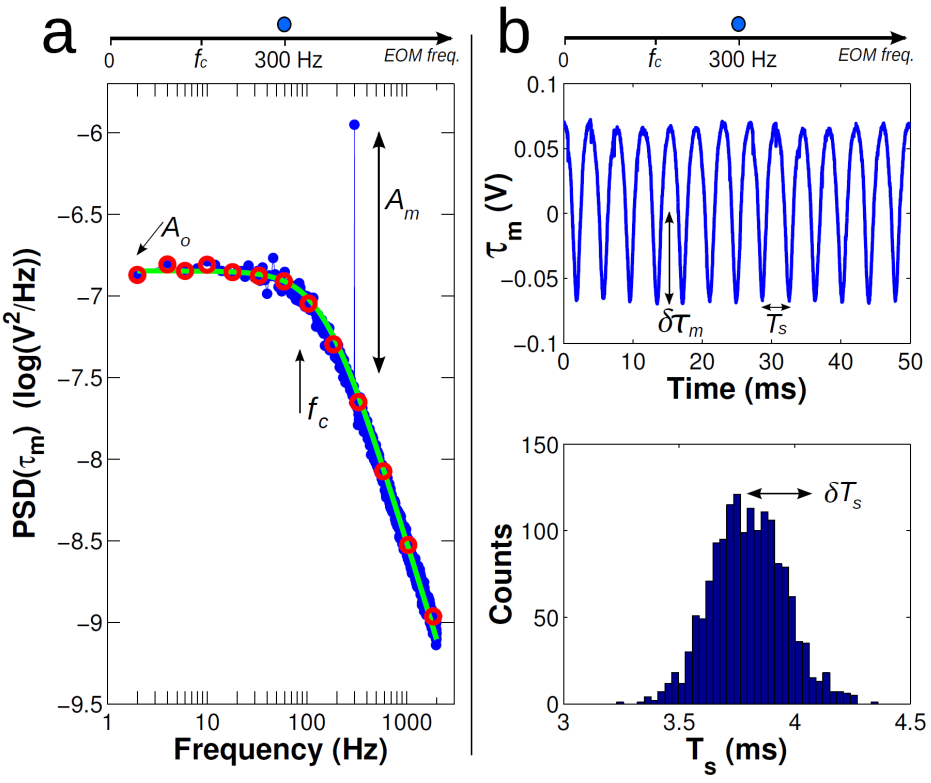

Fig. 5. *Calibration approaches using measurements at a single frequency*. a) Sinusoidal modulation of the laser polarization direction. *Top*: schematic of the EOM frequency used (the blue circle indicates the frequency of the sinusoidal modulation). *Bottom*: power spectrum of the measured torque signal including the contribution from the imposed modulation of the direction of the laser polarization (f_{mod} = 300Hz, A = 0.018 rad, Δf = 2 Hz); red points result from binning the experimental points (blue) into bins of variable size and the green line fits the red points to a Lorentzian. From the data shown, we obtain f_c = 150 Hz, A_o = 3.2E-3 V^2Hz, and A_m = 2.18E-6 V^2/Hz. b) Analysis of the diffusion in a tilted potential landscape. From top to bottom: schematic of the EOM frequency used (blue circle), a segment of the torque trace recorded at $\omega > \omega_c$, and a histogram of the measured torque period T_s. From these data, we obtain $\langle T_s \rangle$ = 3.8 ms, δT_S = 0.16 ms, and $\delta\tau_m$ = 45.3 mV.

Hence, from the measurement of the three independent variables V_o, $\langle T_s \rangle$ and $\delta\tau_m(0)$, the calibration parameters are then given by

$$\tau_o = 2k_B T\left[V_o / \delta\tau_m(0)\right]^2 \tag{14}$$

$$\gamma = \tau_o\left[\omega^2 - \left(\pi / \langle T_s \rangle\right)^2\right]^{-\frac{1}{2}} \tag{15}$$

$$\beta_\tau = V_o / \tau_o \tag{16}$$

6.4.3. Calibration approaches using measurements at a single frequency

Lastly, we discuss calibration approaches that yield all three calibration parameters from a measurement performed at a single polarization rotation frequency. As we will show, the two variants presented rest on quite different theoretical approaches.

6.4.3.1. *Sinusoidal modulation of the laser polarization direction*

The first method in this category closely follows a strategy that has been used successfully for the calibration of linear traps [31]: we insert a small sinusoidal modulation of amplitude A and frequency f_{mod} into the voltage driving the EOM, which produces a polarization that oscillates about θ_{pol} at a fixed frequency: $\theta_{pol} = A\sin(2\pi f_{\mathrm{mod}} t)$. Provided that A is sufficiently small, the power spectral density $P(\tau_m, f)$ of the measured torque τ_m experienced by the particle can be described as the sum of two components: a Lorentzian with cutoff frequency $f_c = \frac{\tau_o}{\pi\gamma}$ as in sec.6.4.2.1 and, superimposed on this, a peak centered at $f = f_{\mathrm{mod}}$. Mathematically, this is expressed as

$$P(\tau_m, f) = 2\tau_o^2\beta_\tau^2\left[\frac{2k_BT}{\gamma\pi^2(f^2 + f_c^2)} + \frac{A^2}{(1 + f_c^2/f_{\mathrm{mod}}^2)}\delta(f - f_{\mathrm{mod}})\right] \tag{17}$$

Under these conditions, three independent variables can be measured from the experimental spectrum (Fig.5a), to directly yield the three calibration parameters. First, a fit of the background power spectral density $P_o(\tau_m, f) = A_o/(f^2 + f_c^2)$ to a Lorentzian (performed excluding the peak at f_{mod}) provides the plateau value A_o and the cutoff frequency f_c as in sec.6.4.2.1. Second, the peak power A_m at the modulation frequency, given by $A_m = P(\tau_m, f_{\mathrm{mod}}) - P_o(\tau_m, f_{\mathrm{mod}})$, is measured.

From the measurement of A_o, f_c, and A_m one then obtains the calibration parameters according to

$$\gamma = \frac{2k_BTA_m}{\pi^2A^2A_o}(1 + f_c^2/f_{\mathrm{mod}}^2)\,\Delta f \tag{18}$$

$$\tau_o = \pi\gamma f_c \tag{19}$$

$$\beta_\tau = \sqrt{\frac{A_m\Delta f}{2\tau_o^2A^2}(1 + f_c^2/f_{\mathrm{mod}}^2)} \tag{20}$$

where $\Delta f = 1/t_{msr}$ and t_{msr} is the measurement time, chosen as a multiple of the period of the applied modulation [31].

6.4.3.2. *Analysis of the diffusion in a tilted potential landscape*

A second single-frequency approach for calibration relies on detailed analysis of the diffusion of a particle in the periodic optical potential tilted by the polarization rotation (eq.3).

The diffusion of a particle in a periodic potential tilted by an external force has been the object of numerous analytical and numerical studies as a result of its interesting physics and recurrence in scientific phenomena [32]. In such a system, which is at steady-state but not at the thermodynamic equilibrium, the effective diffusion coefficient D_{eff} depends on the tilt of the potential and differs from that provided by the Einstein relation $D_o = k_B T/\gamma$ [33].

In the case of the optical periodic potential $U(x)$ of the OTW, tilted by the rotation of the polarization as described by eq.3, the theoretical results can be effectively used for calibration. In Appendix II we show that the effective diffusion coefficient for the OTW, when $\omega > \omega_c$, can be expressed as [32]

$$D_{eff} = \frac{\pi^2 \delta T_s^2}{2\langle T_s \rangle^3} = \frac{k_B T}{\gamma} f(r) \tag{21}$$

where δT_s^2 is the variance of the torque period and $f(r)$ is a function of $r = \omega_c/\omega$ (see Appendix II).

To carry out a calibration measurement, we fix $\omega > \omega_c$ and record the resulting periodic torque signal (Fig.5b *top*). From this single time-trace, we directly measure the average value of the torque period $\langle T_s \rangle$ and its variance δT_s^2 in the temporal domain. The distribution of the period T_s is shown (Fig.5b *bottom*). The value of ω_c can then be determined from eq.4 using $\omega_c = \tau_o/\gamma = \sqrt{\omega^2 - (\pi/\langle T_s \rangle)}$, allowing us to calculate *r* and $f(r)$. The drag coefficient is then found from eq.21 as

$$\gamma = \frac{2 k_B T \langle T_s \rangle^3}{\pi^2 \delta T_s^2} f(r) \tag{22}$$

and the maximum optical torque is then easily calculated from γ and ω_c using

$$\tau_o = \gamma \omega_c \tag{23}$$

Finally, the standard deviation of the same torque signal $\delta\tau_m$ is measured (Fig.5), in order to yield the angular sensitivity β_τ (eq.7)

$$\beta_\tau = \frac{\delta\tau_m}{\tau_o}\sqrt{\frac{(\omega/\omega_c)+\sqrt{(\omega/\omega_c)^2-1}}{\sqrt{(\omega/\omega_c)^2-1}}} \tag{24}$$

6.5 Discussion

Using the experimental configuration described in sec. 6.2.2, we have experimentally implemented the five different calibration methods for the OTW described in the previous section on the same trapped birefringent cylinder. The resulting values of the calibration parameters (γ, β_τ, τ_o) are summarized in Table 1. Overall the numbers obtained with the different approaches agree well with one another. The errors shown in the table, indicated by the notation $\pm_b^a$, reflect the precision obtained repeating the same measurement (a) and the single measurement error that results from error propagation of experimental uncertainties in the analytical expressions (b).

Method	*Drag* γ $(pN nm s)$	Eq.	*Sensitivity* β'_τ $(pN nm/mV)$	Eq.	*Max. Torque* τ_o $(pN nm)$	Eq.
Fit of the standard deviation of the torque ($N = 2$, sec. 4.1, Fig. 3)	$2.4 \pm {}^{0.1}_{0.2}$	(9)	$15.9 \pm {}^{0.3}_{0.9}$	(10)	$1041 \pm {}^{7}_{63}$	(8)
Spectrum at $\omega = 0$ and fast rotation at $\omega > \omega_c$ ($N = 6$, sec. 4.2.1 Fig. 4a)	$2.1 \pm {}^{0.2}_{0.3}$	(11)	$15.7 \pm {}^{0.6}_{2.9}$	(13)	$1008 \pm {}^{37}_{189}$	(12)
Torque variance, period and amplitude ($N = 6$, sec. 4.2.2, Fig. 4b)	$2.1 \pm {}^{0.1}_{0.1}$	(15)	$16.7 \pm {}^{0.6}_{0.1}$	(16)	$1100 \pm {}^{41}_{25}$	(14)
Sinusoidal modulation of the polarization direction ($N = 2$, sec. 4.3.1, Fig. 5a)	$2.2 \pm {}^{0.1}_{0.3}$	(18)	$16.0 \pm {}^{0.3}_{2.9}$	(20)	$1044 \pm {}^{22}_{129}$	(19)
Diffusion in a tilted potential landscape ($N = 6$, sec. 4.3.2, Fig. 5b)	$2.4 \pm {}^{0.1}_{0.1}$	(22)	$15.9 \pm {}^{0.6}_{1.4}$	(24)	$1046 \pm {}^{40}_{47}$	(23)

Table 1. *Experimental results of the different calibration methods obtained with the same trapped birefringent cylinder*. For every method, the notation $m \pm_b^a$ indicates the mean value m, obtained in N successive measurements, the standard deviation a of the N measurements, and the error propagated from the uncertainties of the parameters measured in the method and calculated from the analytical expression of m. Here $\beta'_\tau = \beta_\tau^{-1}$. References to sections, figures and equations of this work for each method and parameter are provided.

For an absolute and independent check of the measurements, we can compare the experimentally determined values for the particle drag to the theoretically determined value for an appropriately-shaped cylinder (Fig. 1b). For a cylinder in water of length 1.8 μm and diameter 0.6 μm, a theoretical value of γ = 2.3 pN·nm·s is expected for the drag coefficient [34], which is well within the range of experimentally measured values for γ, and therefore validates our results.

When using these different methods, it is important to minimize potential sources of systematic errors. For example, there is a first source of error that primarily affects the methods that measure torque fluctuations during rotation of the laser polarization (sec. 6.4.1, 6.4.2, 6.4.3.2). This is due to the fact that it is not straightforward to obtain a torque signal that is fully free of spurious modulation (at the frequency of the EOM) in torque when $\omega > 0$, despite the improvements offered through the use of a reference signal as discussed in sec. 6.2.2. We find that the precise alignment of the axes of the two quarter-waveplates surrounding the optical trap is the critical parameter in achieving a flat torque signal when the polarization is rotated at a finite frequency below ω_c. Once such alignment is optimized, the residual amount of spurious torque modulation depends also on the trapped particles, probably reflecting small differences in their geometries and scattering. The data presented in this work correspond to a particle for which the spurious modulation could be reduced below the thermal noise. For other particles this was not always possible, and as a consequence the precision with which the parameters were obtained by the different methods was significantly lower (with deviations from the mean value up to ±20%).

If the torque modulation is appreciable, the first method introduced, relying on the use of multiple frequencies (sec. 6.4.1) and measurement of the standard deviation of the torque, suffers from a systematic error particularly strongly. This is due to the fact that for the part of the measurement that is conducted at $0 < \omega < \omega_c$, the spurious modulation can be relatively large compared to the predicted value of the standard deviation (see Fig.3), artificially increasing the value of $\delta\tau_m$; this effect is less pronounced when $\omega > \omega_c$.

A second source of error is the accuracy of the fit of the experimental power spectrum to the theoretical Lorentzian curve [21], affecting the two methods described in "Power spectrum analysis at $\omega = 0$ followed by fast rotation at $\omega > \omega_c$" (sec. 6.4.2.1) and "Sinusoidal modulation of the laser polarization direction" (sec. 6.4.3.1). This is reflected in the relatively large propagated uncertainty of these two methods. Variations in the fitting parameters critically depend on the weight given to different frequency regions, which can be controlled by binning the data with a variable bin size (as done in Fig.4a and Fig.5a to increase the weight of the Lorentzian plateau), and on the value of the maximum frequency present in the fitted spectrum, which delimits the region to which an f^{-2}-dependence is fitted.

Which type of calibration method would be most useful to the experimentalist? Based on the above considerations of sources of error, it seems likely that the methods that rely on the analysis of torque fluctuations for $0 < \omega < \omega_c$ (sec.6.4.1) and the methods that rely on spectral analysis (sec. 6.4.2.1 and sec. 6.4.3.1) should be the most prone to inaccuracies. To reduce systematic errors, one would preferably acquire and analyze torque traces in the time domain using either a fixed ($\omega = 0$) or rapidly rotating ($\omega >> \omega_c$) polarization (methods of

sec. 6.4.2.2 and 6.4.3.2). On this basis, we recommend these two methods. For the practical implementation in an experimental setup, the rapidity with which calibration can be performed is also an important consideration. Among the methods presented here, the one based on the use of multiple polarization rotation frequencies (sec.6.4.1) is surely the most time consuming; conversely, the single-frequency methods of sec. 6.4.3.1 and 6.4.3.2, which only require acquisition at a single polarization rotation frequency, are the most rapid. When high throughput is required, these two methods are preferred. Taking both speed and accuracy into account, we conclude that the single-frequency method of sec. 6.4.3.2 will be typically the most suitable. This method also has the advantage of allowing one to dynamically measure possible variations of the drag coefficient within few polarization cycles, which can be useful in micro-rheology measurements.

In conclusion, we have described and performed various methods of OTW calibration, some with direct OT analog and others developed specifically for the angular variables. Overall, the different methods lead to close results, which also agree with the theoretical prediction for the particle drag coefficient. However, the absolute values of the variables measured by the instrument should be expected to depend on the details of calibration method chosen. We hope this work can contribute to a wider use of the OTW, a versatile technique with many potential applications in physical and biophysical studies.

Acknowledgements: We thank J. Lipfert and M. Versteegh for fruitful discussions, J. van der Does, D. de Roos and J. Beekman for help with instrumentation and infrastructure, and TU Delft, FOM (Dutch Foundation for Research on Matter), and the European Science Foundation for financial support.

6.6 Appendix I: Derivation of the Standard Deviation of the Torque

We derive here the analytical expressions (eq.6 and eq.7) for the standard deviation of the torque (sec. 6.4.1). We recall that $\tau_m = \beta_\tau \tau$ (eq.5), where τ_m is the measured torque signal in Volts, β_τ is the sensitivity, $\tau = \tau_o \sin(2x)$ is the optical torque (eq.1), and x is the angle between the laser polarization and the extraordinary axis of the birefringent cylinder. When the laser polarization rotates at a constant frequency ω, the noise-free equation of motion can be written as

$$\dot{x} = -\frac{\tau_0}{\gamma}\sin(2x) - \omega \tag{25}$$

(see eq.3). We treat the two cases $\omega < \omega_c$ and $\omega > \omega_c$ separately.

For $\omega < \omega_c = \tau_o / \gamma$, the cylinder rotates in phase with the polarization. At equilibrium, when $x = x_{eq}$, the mean torque is given by

$$\langle \tau \rangle = -\tau_o \sin(2x_{eq}) = \gamma\omega \tag{26}$$

from which we deduce the equilibrium position $x_{eq} = \frac{1}{2}\arcsin(\frac{\omega}{\omega_c})$. We can express the variance of *x* from the equipartition theorem as $\delta x^2 = k_B T / \kappa$, where the angular stiffness κ can be written as $\kappa = -(\partial\tau / \partial x)_{eq} = 2\tau_o \cos(2x_{eq})$. This allows us to write the variance of the torque (see eq.28) as

$$\delta\tau^2 = \left(\frac{\partial\tau}{\partial x}\right)^2 \delta x^2 = 2k_B T \tau_o \cos(2x_{eq}) \tag{27}$$

$$= 2k_B T \tau_o \sqrt{1-(\omega/\omega_c)^2} \tag{28}$$

Equation 6 is obtained from eq.28 by multiplying by the sensitivity β_τ.

For $\omega > \omega_c$, the cylinder does not rotate in phase with the driving polarization, and the noise-free solution is a periodic torque trace with period T_o given by eq.4. In this case, the mean value of the torque is given by

$$\langle\tau\rangle = \frac{1}{T_o}\int_0^{T_o} \tau dt = \frac{1}{T_o}\int_0^{T_o} \gamma(\dot{x}+\omega)dt = \frac{1}{T_o}\gamma[x(T_o)-x(0)] + \gamma\omega = -\frac{1}{T_o}\gamma\pi + \gamma\omega$$

$$= \gamma\left(\omega - \sqrt{\omega^2-\omega_c^2}\right) \tag{29}$$

The expression of $\langle\tau\rangle$ is then used to calculate the torque variance $\delta\tau^2$ according to

$$\delta\tau^2 = \langle\tau^2\rangle - \langle\tau\rangle^2 = \frac{1}{T_\tau}\int_0^{T_\tau} \tau\gamma(dx/dt+\omega)dt - \langle\tau\rangle^2 = \gamma\omega\langle\tau\rangle - \langle\tau\rangle^2 \tag{30}$$

$$= \tau_0^2 \frac{\sqrt{(\omega/\omega_c)^2-1}}{(\omega/\omega_c)+\sqrt{(\omega/\omega_c)^2-1}} \tag{31}$$

Equation 7 is obtained from eq.31 by multiplying by the sensitivity β_τ.

6.7 Appendix II: Diffusion in a Tilted Periodic Potential

We discuss here the theoretical results used in the calibration method based on analysis of the diffusion of a particle in a tilted periodic potential (sec. 6.4.3.2). Specifically, we consider the diffusion in a total potential $U(x)=V(x)-Fx$ formed by a periodic potential $V(x)$, tilted by an external force *F*. In the case of the OTW, the motion of the over-damped particle is described by eq.3.

When the polarization rotation frequency is set to $\omega > \omega_c$, the system is far from the thermodynamic equilibrium as there is a non-zero probability flux resulting from the disappearance of the energy barrier between successive minima. In this case, the Einstein relation $D_o - \mu k_B T = 0$ (expressed in terms of the mobility $\mu = 1/\gamma$) is not valid. Rather, the following approximate expression can be derived for the effective values of the diffusion coefficient D_{eff} and the effective mobility μ_{eff}, provided $\gamma\omega >> k_B T$ [33]:

$$D_{eff} - k_B T \mu_{eff} \approx \frac{k_B T}{\gamma} \frac{\sqrt{\omega^2 - \omega_c^2}}{\omega} \left[\frac{2\langle \tau^2 \rangle}{\gamma^2 \omega^2} + \frac{5\langle \tau^3 \rangle}{\gamma^3 \omega^3} \right] \tag{32}$$

The effective mobility is in general defined by $\mu_{eff} = dv/dF$ [31], where *v* is the speed of the particle under the action of the force *F*. In our case, recalling that for $\omega > \omega_c$ the torque is a periodic function of time with period $\langle T_s \rangle$ (eq.4) and $F = -\gamma\omega$ (eq.3), the effective mobility can be expressed as

$$\mu_{eff} = -\frac{1}{\gamma} \frac{d}{d\omega} \langle v(\omega) \rangle = \frac{1}{\gamma} \frac{d}{d\omega} \frac{\pi}{\langle T_s \rangle} \approx \frac{\omega}{\gamma \sqrt{\omega^2 - \omega_c^2}} \tag{33}$$

Next, we use the expressions for $\langle \tau^2 \rangle$ (see eq.30), and derive $\langle \tau^3 \rangle = -(\gamma/2)\tau_o^2 \sqrt{\omega^2 - \omega_c^2} + \gamma^3 \omega^2 (\omega - \sqrt{\omega^2 - \omega_c^2})$. Substituting these expressions together with eq.33 into eq.32, we find that the effective diffusion coefficient can be written as

$$D_{eff} = \frac{k_B T}{\gamma} f(r) \tag{34}$$

where $r = \frac{\omega_c}{\omega}$ and where $f(r)$ is given by

$$f(r) \approx \frac{1}{\sqrt{1-r^2}} + \frac{2\sqrt{1-r^2}}{1+\sqrt{1-r^2}} \left[r^2 + \frac{5}{4} r^4 \left(1 + \frac{1}{1+\sqrt{1-r^2}} \right) \right]. \tag{35}$$

6.8 References

1 F. M. Fazal and S. M. Block, Optical tweezers study life under tension, Nature Photonics **5**, 318-321 (2011).

2 K. C. Neuman and A. Nagy, Single-molecule force spectroscopy: optical tweezers, magnetic tweezers and atomic force microscopy. Nature Methods **5**, 491-505 (2008).

3 K. Svoboda and S. M. Block, Biological applications of optical forces, Annu. Rev. Biomol. Struct. **23**, 247 (1994).

4 B. E. Funnell, T. A. Baker, and A. Kornberg, In vitro assembly of a prepriming complex at the origin of the escherichia coli chromosome, J. Biol. Chem. **262**, 10327-10334 (1987).

5 L. F. Liu and J. C. Wang, Supercoiling of the DNA template during transcription. PNAS **84**, 7024-7027 (1987).

6 M. Yoshida, E. Muneyuki, and T. Hisabori, ATP synthase, a marvellous rotary engine of the cell, Nat. Rev. Mol. Cell Biol. **2**, 669-677 (2001).

7 S. Saroussi and N. Nelson, The little we know on the structure and machinery of V-ATPase, J Exp Biol **212**, 1604-1610 (2009).

8 Y. Sowa and R. M. Berry, Bacterial flagellar motor, Quarterly Reviews of Biophysics **41**, 103-132 (2008).

9 J. Lipfert, J. W. J. Kerssemakers, T. Jager, and N. H. Dekker, Magnetic torque tweezers: measuring torsional stiffness in DNA and RecA-DNA filaments, Nature Methods **7**, 977-980 (2010).

10 M. E. J. Friese, T. A. Nieminem, N. R. Heckenberg, and H. Rubinsztein-Dunlop, Optical alignment and spinning of laser-trapped microscopic particles, Nature **394**, 348-350 (1998).

11 M. Padgett and R. Bowman, Tweezers with a twist, Nature Photonics **5**, 343-348 (2011).

12 A. Celedon, I. M. Nodelman, B. Wildt, R. Dewan, P. Searson, D. Wirtz, G. D. Bowman, and S. X. Sun, Magnetic tweezers measurement of single molecule torque, Nano Lett. **9**, 1720-1725 (2009).

13 A. LaPorta and M. D. Wang, Optical torque wrench: Angular trapping, rotation, and torque detection of quartz microparticles, Phys. Rev. Lett. **92**, 190801 (2004).

14 J. Inman, S. Forth, and M. Wang, Passive torque wrench and angular position detection using a single-beam optical trap, Optics Lett. **35**, 2949-2951 (2010).

15 F. Pedaci, Z. Huang, M. v. Oene, S. Barland, and N. H. Dekker, Excitable particle in an optical torque wrench, Nature Physics **7**, 259-264 (2011).

16 S. Forth, C. Deufel, M. Y. Sheinin, B. Daniels, J. P. Sethna, and M. D. Wang, Abrupt buckling transition observed during the plectoneme formation of individual DNA molecules, Phys. Rev. Lett. **100**, 148301 (2008).

17 B. C. Daniels, S. Forth, M. Y. Sheinin, M. D. Wang, and J. P. Sethna, Discontinuities at the DNA supercoiling transition, Phys. Rev. E **80**, 040901 (2009).

18 S. Forth, C. Deufel, S. S. Patel, and M. D. Wang, Direct measurements of torque during Holliday junction migration, Biophysical Journal **101**, L05-L07 (2011).

19 K. Visscher and S. M. Block, Versatile optical traps with feedback control, Methods in Enzymology **298**, 460-489 (1998).

20 M. Capitanio, G. Romano, R. Ballerini, M. Giuntini, F. S. Pavone, D. Dunlap, and L. Finzi, Calibration of optical tweezers with differential interference contrast signals, Review of scientific instruments **73**, 1687 (2002).

21 K. Berg-Sørensen and H. Flyvbjerg, Power spectrum analysis for optical tweezers, Review of scientific instruments **75**, 594-612 (2004).

22 K. C. Neuman and S. M. Block, Optical trapping, Review of scientific instruments **75**, 2787-2809 (2004).

23 C. Deufel and M. D. Wang, Detection of forces and displacements along the axial direction in an optical trap, Biophysical Journal **90**, 657-667 (2006).

24 B. Gutierrez-Medina, J. O. L. Andreasson, W. J. Greenleaf, A. LaPorta, and S. M. Block, An optical apparatus for rotation and trapping, Methods in Enzymology **475**, 377-404 (2010).

25 R. Adler, A study of locking phenomena in oscillators, Proceedings of the IRE **34**, 351-357 (1946).

26 C. Deufel, S. Forth, C. R. Simmons, S. Dejgosha, and M. D. Wang, Nanofabricated quartz cylinders for angular trapping: DNA supercoiling torque detection, Nature Methods **4**, 223-225 (2007).

27 Z. Huang, F. Pedaci, M. Wiggin, M. v. Oene, and N. H. Dekker, Electron beam fabrication of micron-scale birefringent quartz particles for use in optical trapping, ACS Nano **5**, 1418-1427 (2011).

28 W. J. Greenleaf, M. T. Woodside, E. A. Abbondanzieri, and S. M. Block, Passive all-optical force clamp for high-resolution laser trapping Phys. Rev. Lett. **95**, 208102 (2005).

29 O. M. Marag`o, P. H. Jones, F. Bonaccorso, V. Scardaci, P. G. Gucciardi, A. G. Rozhin and A. C. Ferrari, "FemtoNewton force sensing with optically trapped nanotubes," Nano Lett. 8, 3211–3216 (2008).

30 P. J. Reece, W. J. Toe, F. Wang, S. Paiman, Q. Gao, H. H. Tan, C. Jagadish, "Characterization of semiconductor nanowires using optical tweezers," Nano Lett. 11, 2375–2381 (2011).

31 S. F. Tolic-Nørrelykke, E. Schffer, J. Howard, F. S. Pavone, F. Jlicher, and H. Flyvbjerg, Calibration of optical tweezers with positional detection in the back focal plane Review of scientific instruments **77**, 103101 (2006).

32 P. Reimann, C. V. den Broeck, H. Linke, P. Hanggi, J. M. Rubi, and A. Perez-Madrid, Giant acceleration of free diffusion by use of tilted periodic potentials Phys Rev. Lett. **87**, 010602 (2001).

33 K. S. Asakia and S. A. Mari, Diffusion coefficient and mobility of a brownian particle in a tilted periodic potential J.Phys.Soc. Japan **74**, 2226-2232 (2005).

34 M. M. Tirado and J. Garciadelatorre, Rotational-dynamics of rigid, symmetric top macromolecules; application to circular-cylinders J. Chem. Phys. **73**, 19861993 (1980).

Chapter 7

Excitable Particles in an Optical Torque Wrench

Francesco Pedaci†, Zhuangxiong Huang†, Maarten van Oene, Stephane Barland,

and Nynke H. Dekker (†=equal contribution)

The optical torque wrench is a laser trapping technique capable of applying and directly measuring torque on microscopic birefringent particles using spin momentum transfer, and has found application in the measurement of static torsional properties of biological molecules such as single DNAs. Motivated by the potential of the optical torque wrench to access the fast rotational dynamics of biological systems, a result of its all-optical manipulation and detection, we focus on the angular dynamics of the trapped birefringent particle, demonstrating its excitability in the vicinity of a critical point. This links the optical torque wrench to nonlinear dynamical systems such as neuronal and cardiovascular tissues, nonlinear optics and chemical reactions, all of which display an excitable binary ('all-or-none') response to input perturbations. On the basis of this dynamical feature, we devise and implement a conceptually new sensing technique capable of detecting single perturbation events with high signal-to-noise ratio and continuously adjustable sensitivity.*

* This chapter has been published as F. Pedaci†, Z. Huang†, M. van Oene, S. Barland, and N.H. Dekker, *Nature Physics* **7**, 259–264 (2011), (†=equal contribution)

7.1 Introduction

The past two decades have witnessed the development of new physical techniques such as atomic force microscopy, magnetic tweezers and optical tweezers that allow the mechanical manipulation and measurement of microscopic actuators. When connected to individual biomolecules, these actuators, which control physical parameters such as the applied force at the piconewton level and molecular extension at the nanometre scale, directly report on their physical properties allowing biological systems to be studied in a direct, quantitative manner in real time[1, 2]. Torque is a further physical parameter of biological relevance, as witnessed by its role in diverse cellular processes such as DNA replication[3] and transcription[4], ATP synthesis[5] and bacterial propulsion[6]. For this reason, there is growing interest in the development of single-molecule techniques that allow modification and simultaneous measurement of force and torque[7, 8, 9, 10, 11]. To achieve this, one method is to combine the high spatio-temporal resolution of optical tweezers with the angular control of tailored microscopic birefringent particles in the so-called optical torque wrench[8, 12, 13, 14] (OTW). However, although much knowledge has been gained about linear optical tweezers, its angular counterpart remains largely unexplored, a consequence of its more recent development and remaining technical challenges.

Here we focus on the fast dynamical capabilities of optical tweezers and show that the torque dynamics of the system casts the OTW within the general class of excitable dynamical systems. Both analytically and experimentally, we show that the OTW is dynamically equivalent to a microscopic version of the Adler system[15], one of the simplest and most widely studied models for the excitable spiking of a neuron[16]. Since its discovery in the seminal studies of spiking neurons[17], excitability has been identified as a feature of several nonlinear dynamical systems ubiquitous in science[18, 19, 20, 21, 22, 23, 24, 25]. The excitable character of a system is defined by its response to external perturbations: perturbations smaller than a certain value produce a small linear response around the stable (or 'rest') state, whereas large perturbations force the system to undergo a large deterministic excursion in the phase space before returning to the stable state again. This excursion, often measured as a spike, is deterministic and independent of the perturbation, provided that it overcomes the so-called excitability threshold.

7.2 Rotational Dynamics of Birefringent Particles

Our demonstration that the angular dynamics of a birefringent particle trapped in an OTW can be described by these physical principles starts by rotationally forcing a nano-fabricated quartz cylinder by applying a linear laser polarization rotating at constant frequency $f=\omega/2\pi$ in an OTW (Fig. 1a). The response of the mean value of the transferred torque as a function of f (Fig. 1b) clearly indicates the presence of two distinctive regimes: for frequencies $|f|<f_c^{exp}$=35.5 (±0.5) Hz, the absolute value of the mean torque increases linearly with the

imposed frequency; however, further increasing $|f|$ beyond f_c^{exp} results in a decay of the absolute value of the mean torque to zero (negative frequencies indicate rotation in the opposite direction). This behaviour is typical of rotationally forced systems, with optical[12, 26, 27, 28], magnetic[29, 30] or magneto-mechanic[24] forcing. The physical reason for the decrease of the average torque for $|f|>f_c^{exp}$ becomes clear by looking at its temporally resolved signal: beyond the linear region (Fig. 1c), the drag torque acting on the rotating cylinder exceeds the maximum torque that can be transferred by the laser polarization, inducing a phase slip between the particle's extraordinary axis and the polarization. This event appears as a spike in the torque signal (Fig. 1d). At higher frequencies the particle is incapable of following the polarization and remains quasi-static under the scanning polarization, giving rise to a quasi-sinusoidal torque signal (Fig. 1e).

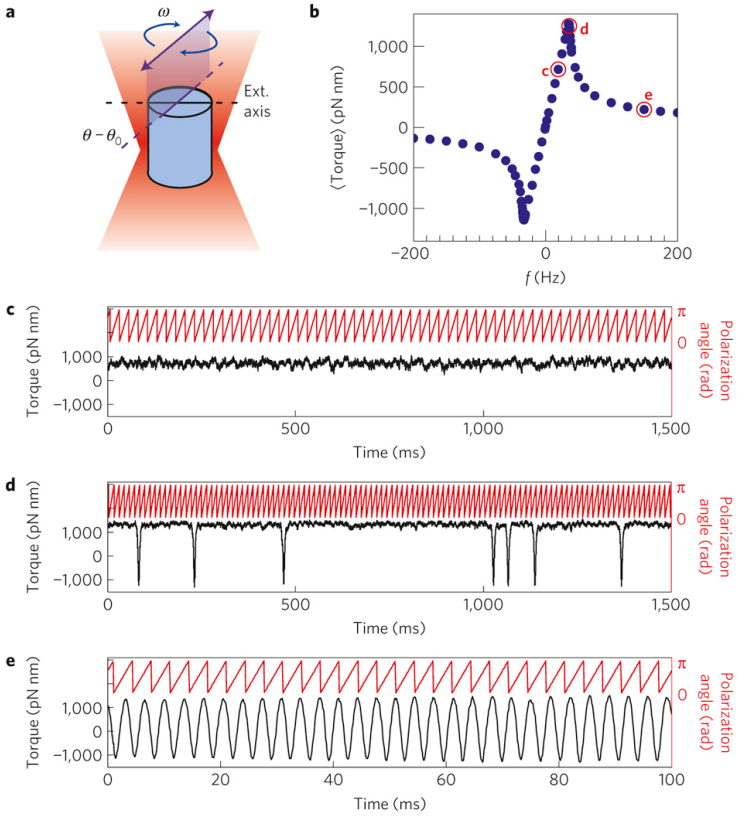

Figure 1. Measurements of torque on a birefringent particle. a, Schematic of a birefringent cylinder forced by a rotating linear polarization in an optical trap. **b**, Mean value of the measured torque as a function of the polarization rotation frequency *f*. **c–e**, Torque as a function of time (black) corresponding to the points indicated by red circles in b. The relative polarization angle is depicted in red.

These observations can be quantitatively understood by starting from the analytical expression for the torque optically transferred to the birefringent particle, which can be written[7] as

$$\tau_{opt} = -\tau_o \sin(2(\theta - \theta_o))$$

where $\tau_o = \mathrm{S}\varepsilon/(2\Omega)E_o^2 \sin(kL\Delta n)$. Here S is the particle cross-sectional area, ε is the permittivity, Ω is the laser optical frequency, $\theta-\theta_o$ is the angle between the extraordinary axis of the particle (θ) and the polarization (θ_o), k is the wave vector, L is the length of the cylindrical particle, Δn=0.009 is the quartz birefringence and a linear input polarization is assumed. When the input polarization is rotated such that $\theta_o=\omega t$, the equation of motion can be rewritten in the rotating reference frame by defining $x=\theta-\omega t$, yielding

$$\dot{x} = -\frac{\tau_o}{\gamma}\sin(2x) - \omega \tag{1}$$

where γ is the rotational drag coefficient and where inertial effects are neglected as the Reynolds number is $\approx 10^{-4}$. Equation (1) was introduced by Adler in his seminal study of locking phenomena in oscillators[15] and is a classic example of how complex behaviour can arise from a relatively simple law.

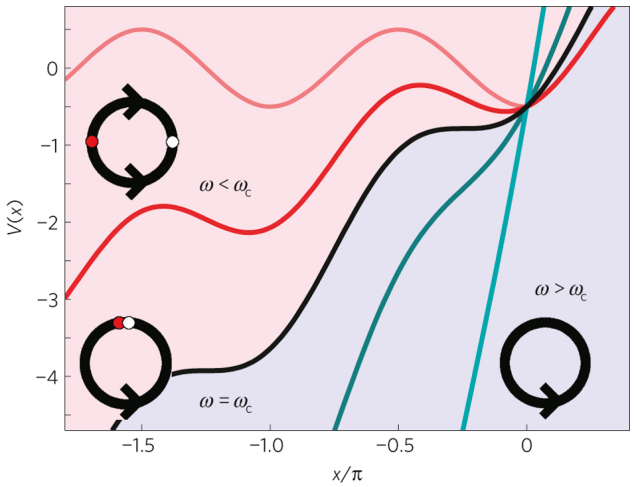

Figure 2. The potential experienced by the birefringent particle, and corresponding phase plots. For different values of ω, we plot the potential *V(x)* experienced by the birefringent particle ($\omega<\omega_c$, red lines; $\omega=\omega_c$, black line; $\omega>\omega_c$, blue lines) as a function of the angular coordinate in the rotating reference frame *x*. For these three regimes, we plot representative circular phase plots and indicate the system's fixed points by coloured dots (where a white dot represents the stable fixed point and a red dot represents the unstable fixed point). In a noise-free system, the bifurcation at $\omega=\omega_c$, evidenced by both the lack of a potential minimum and by the merging of the two fixed points in the phase plot, separates the excitable region at $\omega<\omega_c$ from the periodically modulated one at $\omega>\omega_c$. Here τ_o/γ=1 and ω=[0,0.5,1,2,6]ω_c from light-red to light-blue.

From this equation, we expect that the behaviour of the rotationally forced microscopic system, which is periodic in x and therefore analogous to the motion of a particle on a circle, can be described in terms of the potential $V(x)$, defined as $\dot{x} = -V'(x)$ (Fig. 2). For $\omega<\omega_c=\tau_o/\gamma$, one stable and one unstable stationary solution coexist (Fig. 2, red lines and corresponding phase plots). In this regime the system is excitable: a perturbation on the stable solution that overcomes the threshold (defined by the potential barrier between the two stationary points) will be followed by a large deterministic trajectory (the 'firing state') back to the stable point (the 'resting state') in which the rotation of the particle is once more in phase with the polarization. On further increasing ω, the two stationary solutions merge through saddle-node bifurcation at $|\omega|=\omega_c$ (Fig. 2, black line and corresponding phase plot), giving rise to a limit cycle (Fig. 2, blue lines), that is, to periodic spiking at constant amplitude that is initially at infinitely low frequency and becomes sinusoidal in the limit of infinite ω (Supplementary Information SI). Thus, the observed dynamical response (Fig. 1) is captured well by the behaviour predicted by equation (1).

7.3 Experimental Demonstration of Excitability

To further test the validity of this model, which predicts excitability in the region $\omega<\omega_c$, we study the response of the system to controlled external perturbations (Fig. 3). Thus we first prepare the system below the critical point ($f \lesssim f_c^{exp}$) where torque spikes are not present. A perturbation is then periodically inserted into the EOM voltage at the times indicated by red dots in the top-left time traces (Fig. 3a–c). As a result of the perturbation, the polarization phase θ_o undergoes a sudden jump (in less than 10 μs) of controlled amplitude ϕ_P ($\theta_o=\omega t + \phi_P$ with ϕ_P = [0, 1.08] rad). We observe that small amplitude perturbations (ϕ_P < 0.2 rad, Fig. 3a) do not trigger torque spikes in the system's response, whereas stronger perturbations do induce torque spikes whose amplitude does not depend on the perturbation (Fig. 3b,c). The probability of triggering torque spikes rises steeply with increased perturbation amplitude (blue circles in Fig. 3d), indicating the existence of a threshold separating a 'resting' from a 'firing' state. In the right panels of Fig. 3a–c we zoom in on a collection of torque signals acquired after repeatedly imposing single perturbations triggered at t=0. This shows that the response of the system to sufficiently strong perturbations varies only in the delay between the trigger and the response. This delay has both a deterministic component (larger perturbations leading to shorter delay), and a stochastic one due to thermal noise (Supplementary Information SIV). Importantly, the superposition of all the excited torque spikes (Fig. 3e) reveals that the pulse shape is highly conserved even when a strong stochastic component is present in the timing, which shows that the path followed by the system during an event is deterministic, as expected for an excitable response. These measurements clearly indicate a binary ('all-or-none') response to external perturbations as well as the existence of a threshold beyond which a deterministic path drives the system back to the stable state, both characteristic features of an excitable system.

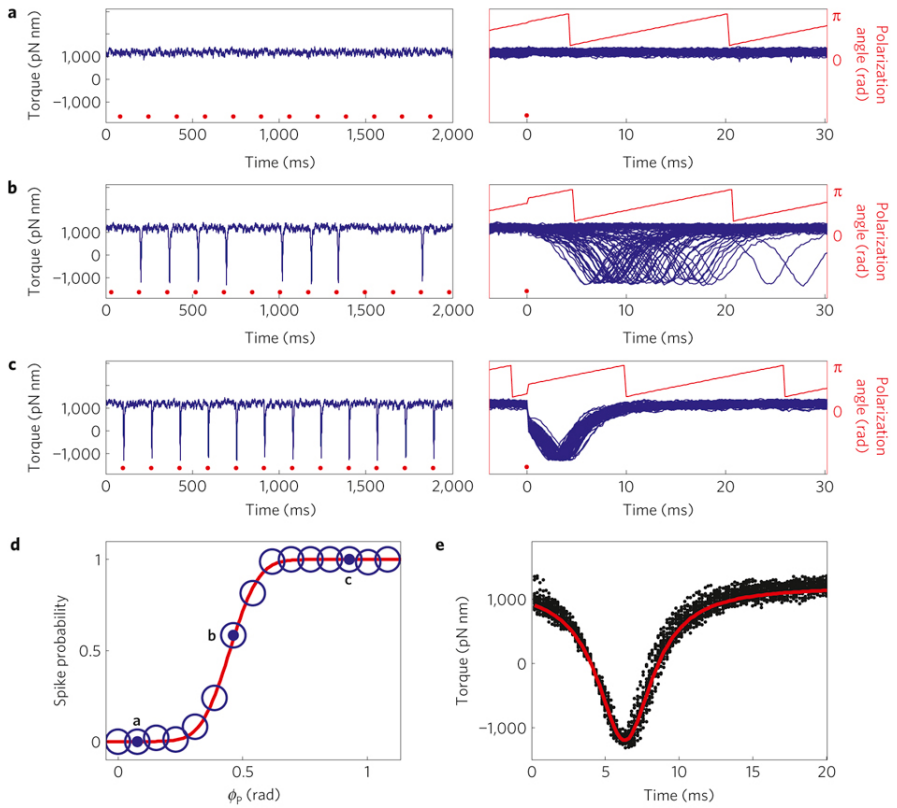

Figure 3. Demonstration of the excitability of a rotating birefringent cylinder in an optical torque wrench. **a–c** (left): while keeping f fixed at 31.25 Hz, a perturbation ϕ_P is inserted into the rotating polarization at time-points indicated by the red dots, with its amplitude increasing from **a** to **c**. **a–c** (right): a zoomed-in region of the left panels, showing both the rotating polarization including its perturbation (red line) as well as the torque response (blue line). Here, the occurrence of each perturbation is defined as t=0 (red line), and the torque response from a large number of collected responses is plotted. One can readily observe that the response is binary in the amplitude of the torque signal, and that the amplitude of the perturbation influences only the timing of the response. **d**, The probability of successful excitation of one spike as a function of the perturbation amplitude ϕ_P. The red line is the fit to equation (2). **e**, The superposition (dots) of the events (triggered in **b**) is fitted by equation (3) (red line), with τ_o=1,200 pN·nm, ω_c=(2π)38 rad·s^{-1} and to=6.3 ms.

We can deepen our understanding of this physical system by modeling both the excitation probability as a function of the amplitude ϕ_P of the imposed perturbation as well as the temporal behaviour of the deterministic torque trajectory. Following previous work on stochastic effects in excitable systems[31], we derive an analytical expression for the probability to excite a torque spike as a function of the amplitude ϕ_P of the imposed perturbation (Supplementary Information SII), as

$$P(\phi_P) = \frac{1}{2}[-\mathrm{erf}(-A(\phi_P - B))] \tag{2}$$

where $A = \sqrt{\tau_o/(2k_BT)}\left[1-(\omega/\omega_c)^2\right]^{1/4}$, $B=arccos(\omega/\omega_c)$ and k_BT = 4.1 pN·nm is the thermal energy. Fitting the data in Fig. 3d with equation (2) (red line), we find that ω=0.90 ω_c and τ_o= 1,150 pN·nm, where the latter is in excellent agreement with the maximum value of the torque measured experimentally (Fig. 1d,e). We note that the response of an externally driven excitable system can in general be more complex than the 1:1 locking ratio between the perturbation frequency and the system's torque spike response observed in Fig. 3d (ref. 20). The sigmoidal response observed is a particular case that can be successfully modeled by the dephasing action of thermal noise over the long perturbation period chosen (two orders of magnitude longer than the deterministic pulse duration). On reduction of the perturbation period, different locking ratios can be observed (Supplementary Information SIII). Furthermore, one can derive an expression for the deterministic trajectory of a torque spike by solving equation (1) (Supplementary Information SI), which yields

$$\frac{\tau}{\tau_0} = -\sin(2x) = \frac{\cot^2\left(x+\frac{\pi}{4}\right)-1}{\cot^2\left(x+\frac{\pi}{4}\right)+1} \tag{3}$$

where $\cot\left(x+\frac{\pi}{4}\right) = -\sqrt{\frac{\omega_c+\omega}{\omega_c-\omega}}\left[\frac{\exp\left(2\sqrt{\omega_c^2-\omega^2}\,(t-t_o)\right)-1}{\exp\left(2\sqrt{\omega_c^2-\omega^2}\,(t-t_o)\right)+1}\right] \cong (\omega_c+\omega)(t-t_o)$, t_o is the time at which the peak torque is reached, and the approximation is valid when $\omega \lesssim \omega_c$. The measured torque trajectory during one 'firing' event is excellently fitted by this analytical expression, as shown by the red line in Fig. 3e.

7.4 Effects of Thermal Noise

Interestingly, the microscopic scale at which these experiments are carried out implies that thermal noise itself can also act as a perturbation to trigger the excitable response of the system, provided that the excitability threshold is comparable to the amplitude of thermal fluctuations. Such thermally-excited events triggered below the critical point are indeed observed (Fig. 1d). Their interspike time probability distribution, a characteristic feature of noise-driven excitable pulses[23], is shown in Fig. 4. At long time intervals, this distribution displays the typical exponential tail described by Kramer's escape rate, whereas at short time intervals the low probabilities indicate that two successive spikes are always separated by at least a minimum amount of time, proportional to the period of revolution of the polarization. This minimum time interval corresponds to the time needed for the system to return to the rest state after the emission of a spike and is termed the refractory time, t_o. For $\omega<\omega_c$, the probability distribution of interspike times is given by[31]

$$P(t) = A\,\widetilde{W}_{tr}\,e^{-Kt} \tag{4}$$

where $\tilde{W}_{tr} = \exp\left(-\frac{e^{2\lambda(s-t_o)}-1}{e^{2\lambda(s-t_o)}-1}\ln 2\right)\left(1-e^{-2\lambda(t-t_o)}\right)^{-1/2}$, $\lambda = 2\sqrt{\omega_c^2-\omega^2}$, K is the Kramer decay rate, s is the midpoint of the step-like function $\tilde{W}_{tr}$, and A is a normalization constant (Supplementary Information SIV). This expression describes the experimentally-determined probability distribution very well (red line in Fig. 4).

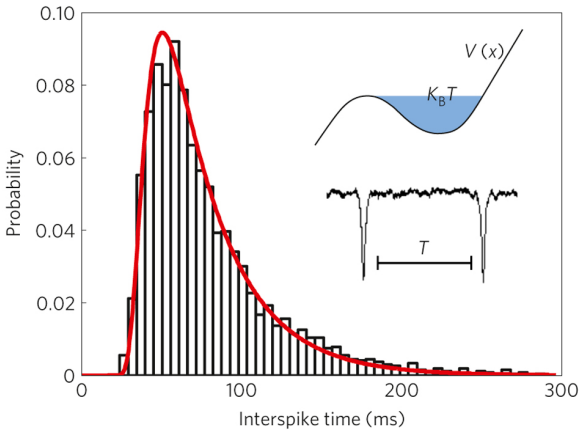

Figure 4. Probability distribution for the interspike time of events triggered by thermal noise. Here, the value of f (34.5 Hz) is selected such that the excitability threshold is readily overcome by thermal events (see sketch of the potential $V(x)$ and of the torque interspike time T in the inset). The red line fits the data using equation (4) with s=42 ms, t_o=13 ms, λ=60 Hz, K=(35 ms)$^{-1}$. The observed probability distribution also confirms the negligible role of inertia in the dynamics of this system, as otherwise a second peak would become observable[31].

A further effect of thermal noise is to strongly perturb the periodicity of the deterministic solution for values of ω slightly greater than ω_c, where particularly shallow regions of the potential near $x=N\pi$ render the system sensitive to thermal fluctuations[24]. As a consequence, clear periodicity is experimentally observed only for frequencies much higher than ω_c, as shown in Fig. 1e. Thus, we have clarified the origin of the nonlinear response of birefringent cylinders rotated in an optical torque wrench to perturbations, whether externally applied or of thermal origin.

7.5 Sensing Through Excitability

We now demonstrate the use of this excitable opto-mechanical system as a new technique for the detection of transient changes in the particle's environment (Fig. 5). In particular, we demonstrate how the rotating cylinder can detect changes in the local drag resulting from the nearby presence of objects (for example surfaces and micrometre-sized spheres), whose proximity effects can be therefore quantified. The sensing principle relies on the readout of identical torque spikes that span the entire torque range from its minimum to its maximum

value, optimizing signal-to-noise. As the observation of spikes in the torque signal does not depend strongly on imperfections in the detection and calibration (in contrast to linear detection approaches), this approach is also robust. Interestingly, as torque spikes can be excited by perturbations that overcome the excitability threshold, sensitivity can be continuously tuned by varying the threshold value, which is experimentally accessible using the parameter ω. Furthermore, we demonstrate that torque spike frequency increases with increased perturbations, a generic feature of systems that present a saddle-node bifurcation on an invariant circle (for example 'integrator' neurons, which encode the intensity of the stimulation received into their mean firing rate16).

By first monitoring the approach of a cylinder with respect to the bottom surface of the flow cell (Fig. 5a, red line and inset), we analyse the full spectrum of torque responses, and, in doing so, demonstrate a measurement of the local drag encountered by the cylinder (Fig. 5a–d). Setting $\omega<\omega_c^{exp}$ so that the isolated excitable cylinder will be insensitive to thermal fluctuations, we record both the position of the cylinder in the optical trap (Fig. 5a, blue points) and the corresponding torque signal (Fig. 5b). When the cylinder is far from the surface, it is located at the trap centre and the torque signal is initially featureless. However, as the cylinder approaches the surface, torque spikes make their appearance (Fig. 5b, region near 8 s). Subsequently, as the cylinder starts to enters into contact with the surface (at the positions indicated by dashed grey lines in Fig. 5a–d), it is displaced relative to the centre of the optical trap (Fig. 5a, blue points in region labeled 'contact'). These torque spikes report on the occurrence of the bifurcation in this excitable system (that is $\omega=\omega_c$). Their frequency, ω_{spike}, depends on the relative distance between the rotating cylinder and the surface (Fig. 5b, blue spikes in insets). By local averaging, we determine the dependence of the nearly-instantaneous spike frequency ω_{spike} on the relative distance from the surface (Fig. 5c, blue points), which illustrates that ω_{spike} approaches ω as the cylinder is pressed into the surface.

The varying character of the torque spikes as the cylinder approaches a surface can be understood as follows. First, the spike frequency encodes information on the system's critical frequency, $\omega_c(z)$: specifically, $\omega_{spike} \propto \sqrt{\omega^2 - \omega_c^2}$ (Supplementary Information SI). As the cylinder is brought into contact with the surface, the system's critical frequency decreases, becoming equal to ω and then dropping beneath it (Fig. 5c, red points). Hence, the torque signal displays thermally excited spikes when the cylinder is close to the surface (where $\omega\approx\omega_c(z)$) and periodic spikes when it is pressed into tight contact with the surface (where $\omega>>\omega_c(z)$).

We can use the relationship $\gamma(z)=\tau_o/\omega_c(z)$ to determine how the drag γ varies with the relative position of the particle and the surface (Fig. 5d). According to Faxén's law, the rotational drag should increase in the vicinity of a surface[32], as observed (Fig. 5d, regions before contact indicated by grey lines). Further increase of the drag is measured as the cylinder is brought into contact with the surface and the pressure is increased. As the measurement of the drag (Fig. 5d) and the position signal (Fig. 5a) demonstrate, we do not observe permanent sticking of the particle after contact is reached, probably as a result of the proteinaceous coating applied to the inner flow cell surfaces in these experiments.

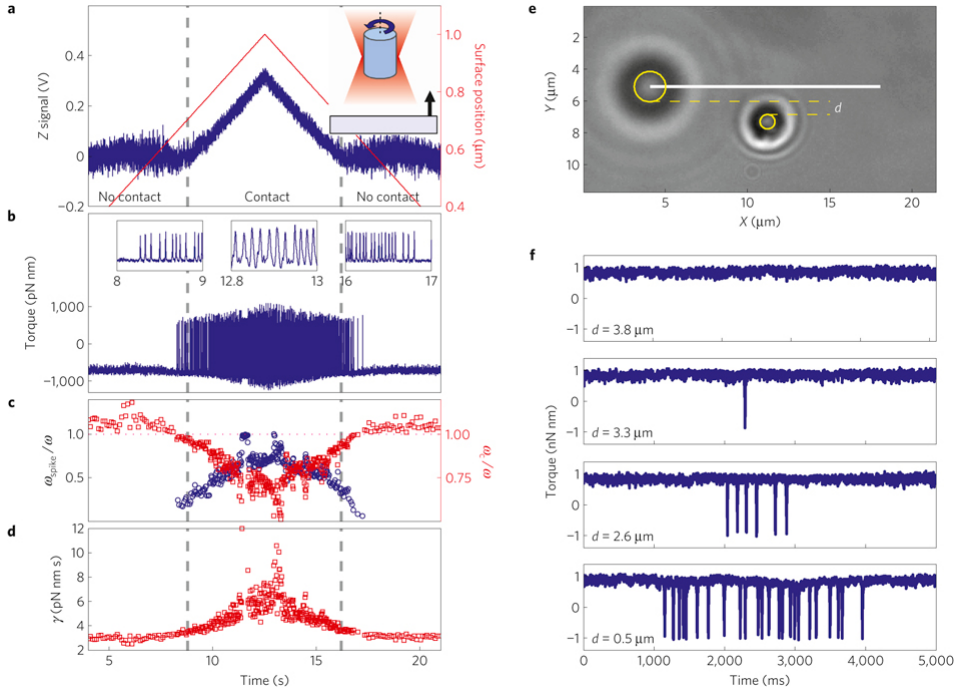

Figure 5. Sensing through excitability. a–d, Vertical motion of the excitable particle towards a surface (followed by its reverse trajectory). **a**, A trapped birefringent cylinder is constantly rotated at a sub-critical frequency ($\omega/2\pi$=35 Hz, 80% of ω_c measured in bulk) while the trap is approached towards the glass surface of the flow cell (inset). The relative distance of the trap from the surface is shown in red. The recorded signal of the vertical displacement of the cylinder from the trap centre is shown in blue and its deviations from zero indicate contact with the surface, in which the particle exerts a restoring force on the surface of maximally a few piconewtons. **b**, Torque signal recorded during the vertical movement. Insets: Zooms of the trace at three different points along the trajectory and its reversal; timescales for zooms are indicated in seconds. **c**, (Blue points) Ratio of the measured quasi-instantaneous spike frequency and polarization rotation ω. An increase in this ratio corresponds to a decrease in ω_c or equivalently an increase in drag. Transient sticking to the surface (or equivalently a transiently infinite drag) is visible at the points where this ratio becomes equal to 1. (Red points) Ratio of the measured critical frequency $\omega_c(z)$ and the polarization rotation frequency ω. The critical frequency can be deduced from the torque signal in **b**, both before and after the bifurcation at ω_c/ω=1 (Supplementary Information SVII). **d**, Rotational drag along the trajectory, calculated using the value of ω_c in **c**. **e**, **f**, Sensing a moving object through proximity effects. **e**, A 2 μm diameter bead fixed to the glass surface (large yellow circle, left) is moved at constant speed along the white line, while the excitable cylinder (small yellow circle, right) is kept in rotation at a sub-critical frequency. **f**, The torque traces along the path are shown for different values of distance d. Proximity effects (for example transient increases of the drag coefficient) effectively lower the potential barrier, which keeps the rotation of the cylinder in phase with the laser polarization, translating into large torque spikes. For all figure panels, we have fixed the maximum applicable torque τ_o as well as the cylinder rotation frequency ω dictated by the EOM.

This well-understood sensitivity of the torque signal to changes in the local drag can be employed for the detection of particles in the cylinder's vicinity. To demonstrate this, we employ a polystyrene bead (2 μm diameter, large yellow circle in Fig. 5e) fixed to the glass surface as the source of the perturbation and scan the microscope piezo-stage at constant

velocity (over a total distance of 14 μm along x, white line in Fig. 5e), thereby simulating the presence of a flow-driven bead in the sensor's proximity. While doing so, we control the lateral distance d (along y) between the surfaces of the cylinder and the bead, while the trap is maintained ≈2 μm from the glass surface. As above, we select $\omega<\omega_c^{exp}$ and record the torque signal during the movement of the stuck bead for decreasing values of d.

As shown in the temporal traces (Fig. 5f), the proximity of the bead can be easily recognized from the appearance of spikes, which are excited in a region where the distance between the bead and the cylinder is minimized. As expected, such a response by the cylinder to an approaching object is observed only in the nonlinear regime: when ω is reduced so as to induce a linear response, spikes are absent and only a barely visible perturbation of the torque signal is visible (data not shown). As such, a rotating birefringent particle can be employed as a sensitive nonlinear detector, whereby spatial localization of the sensor is assured with great accuracy by the three-dimensional optical trap and its sensitivity exploits the sensor's excitable character.

7.6 Methods

To constitute the optical trap, the laser light (100 mW at a wavelength of 1,064 nm) is focused by a 1.49 N.A. objective in a glass flow cell mounted on piezo-actuators. We use a fast (~MHz) electro-optical modulator (EOM) in combination with a quarter-wave plate as a polarization control system[14]. As a result, the angle of the linear polarization of the trapping laser field (ellipticity smaller than 5%) is proportional to the voltage applied to the EOM in the angular range 0–π. To continuously rotate the polarization at a constant rate $f=\omega/2\pi$, we use a sawtooth voltage signal of controlled frequency $2f$. The torque transferred to the trapped particle is measured optically by fast intensity detectors from the imbalance of the two circular components of the polarization at the output of the trap[7]. The total bandwidth of the detection system is 200 kHz, which readily allows sensitive torque detection on sub-millisecond timescales and is key to our experiments. An input polarization reference and a calibration procedure (similar to the one carried out for linear optical tweezers[12, 33]) are necessary to obtain the absolute value of the applied torque in physical units. The birefringent particles employed are cylinders of slightly conical shape (1.7 μm height, 0.9 μm larger diameter, 0.6 μm smaller diameter), obtained by electron beam lithography on a quartz wafer. The advantage of this technique over optical lithography[13] lies in its finer control over dimensions and accuracy. A detailed description of cylinder fabrication has been published elsewhere (Ref. 43). The glass surface of the flow cell is coated with BSA proteins immobilized by use of a nitrocellulose layer, to prevent sticking with the quartz surface of the particles. The 2 μm bead is stuck to the glass surface via the nitrocellulose layer.

Acknowledgements: We thank A. La Porta for graciously sharing key aspects of the construction of OTW, M. Wang for discussion of polarization, E. van der Drift, M. Zuiddam, A. van Run and M. van der Krogt of the Delft Nanofacility and J. Andreasson of Stanford University for advice on the microfabrication of quartz cylinders, M. Wiggin for help in

fabricating them, J. van der Does, D. de Roos and J. Beekman for help with instrumentation and infrastructure, J. Kerssemakers, I. de Vlaminck, M. van Loenhout, S. Klijnhout and J. Lipfert for stimulating discussions, and the TU Delft, FOM (Dutch Foundation for Research on Matter), NWO (Nederlandse Organisatie voor Wetenschappelijk Onderzoek) and the European Science Foundation for financial support.

7.7 Supplementary Information

S.I. Deterministic Trajectory of a Torque Spike

The deterministic behavior of a birefringent particle in OTW can be understood from its noise-free equation of motion (eq.1 in the main text):

$$\dot{x} = -\frac{\tau_0}{\gamma}\sin(2x) - \omega \tag{S.1}$$

S.I.1 Case: $\omega < \omega_c = \frac{\tau_0}{\gamma}$

For $\omega < \omega_c$, eq.S.1 has two stationary solutions (one is stable and the other one is unstable), and one non-stationary solution which describes the trajectory of the system.

Solution 1 (a stable fixed point, or node position):

$$x_n = N\pi - \frac{1}{2}\arcsin\left(\frac{\omega}{\omega_c}\right) \tag{S.2}$$

Solution 2 (an unstable fixed point, or saddle position):

$$x_s = N\pi + \frac{1}{2}\arcsin\left(\frac{\omega}{\omega_c}\right) - \frac{\pi}{2} \tag{S.3}$$

Solution 3 (describing the relaxation from the saddle position to the node position):

$$x = N\pi - \arctan\left(\frac{\omega_c}{\omega} - \sqrt{\left(\frac{\omega_c}{\omega}\right)^2 - 1} + \frac{2\sqrt{\left(\frac{\omega_c}{\omega}\right)^2 - 1}}{1 - C\exp\left(2\sqrt{\omega_c^2 - \omega^2}\,t\right)}\right) \tag{S.4}$$

where $N \in \mathbb{Z}$, and $C \neq 0$. For $x_n - \pi < x < x_s$, solution 3 can be rewritten as:

$$\cot\left(x + \frac{\pi}{4}\right) = -\sqrt{\frac{\omega_c + \omega}{\omega_c - \omega}}\left[\frac{1 - \exp\left(2\sqrt{\omega_c^2 - \omega^2}\,(t - t_0)\right)}{1 + \exp\left(2\sqrt{\omega_c^2 - \omega^2}\,(t - t_0)\right)}\right] \tag{S.5}$$

where t_0 is the time at which $x = \left(N - \frac{3}{4}\right)\pi$ is reached, and it is rewritten from constant C as:

$$t_0 = \frac{1}{2\sqrt{\omega_c^2 - \omega^2}}\left[\ln\left(\frac{\omega_c}{\omega} + \sqrt{\left(\frac{\omega_c}{\omega}\right)^2 - 1}\right) - \ln C\right] \tag{S.6}$$

When $\omega \lesssim \omega_c$, eq.S.5 can be approximated as:

$$\cot\left(x + \frac{\pi}{4}\right) \approx (\omega_c + \omega)(t - t_0) \tag{S.7}$$

Under this approximation, the deterministic trajectory of a torque spike (fig. 3e in the main text) is given by:

$$\frac{\tau}{\tau_0} = -\sin 2x = \frac{\cot^2\left(x + \frac{\pi}{4}\right) - 1}{\cot^2\left(x + \frac{\pi}{4}\right) + 1} \approx \frac{(\omega_c + \omega)^2 (t - t_0)^2 - 1}{(\omega_c + \omega)^2 (t - t_0)^2 + 1} \tag{S.8}$$

S.I.2 Case: $\omega > \omega_c = \frac{\tau_0}{\gamma}$

For $\omega > \omega_c$, there are no stationary solutions to eq.S.1 anymore since they have merged and disappeared through the saddle-node bifurcation. The only solution of the system is periodic and is described by:

$$\cot\left(x + \frac{\pi}{4}\right) = \sqrt{\frac{\omega + \omega_c}{\omega - \omega_c}} \tan\left[\sqrt{\omega^2 - \omega_c^2}\,(t - t_0)\right] \tag{S.9}$$

where t_0 is the time at which $x = \left(N - \frac{3}{4}\right)\pi$ is reached. The corresponding expression for torque is then given as:

$$\frac{\tau}{\tau_0} = -\sin 2x = \frac{\left(\frac{\omega + \omega_c}{\omega - \omega_c}\right)\tan^2\left[\sqrt{\omega^2 - \omega_c^2}\,(t - t_0)\right] - 1}{\left(\frac{\omega + \omega_c}{\omega - \omega_c}\right)\tan^2\left[\sqrt{\omega^2 - \omega_c^2}\,(t - t_0)\right] + 1} \tag{S.10}$$

which indicates the torque signal becomes a periodic function with a period given as:

$$T_{torque} = \frac{\pi}{\sqrt{\omega^2 - \omega_c^2}} \tag{S.11}$$

S.II. Torque Spike Probability as a Function of Perturbation Amplitude

In the following we consider the behavior of the system under the effect of single external perturbations and we find the expression for the probability to trigger a torque spike as a function of the perturbation amplitude. We note that this statistical approach can explain our

experimental data (Fig. 3 maintext) where the perturbation is inserted periodically at very long intervals of time, however a more complete model is needed to explain the more complex behavior which appears in forced excitable systems (section S.III)[29].

In the presence of thermal noise, the equation of motion for a birefringent particle (eq.S.1) is rewritten as:

$$\dot{x} + \frac{\tau_0}{\gamma}\sin 2x + \omega + F(t) = 0 \tag{S.12}$$

where $F(t)$ is thermal noise given by:

$$\langle F(t)F(t')\rangle = \frac{2k_BT}{\gamma}\delta(t-t') \tag{S.13}$$

When a birefringent particle in the OTW is subjected to external perturbations as demonstrated in fig. 3 (main text), its dynamical response is affected by thermal noise in two principal ways:

First, even before the application of a perturbation, the position of the birefringent particle, x_0, is broadened by thermal noise around the node position. Specifically, the distribution of x_0 is given by Maxwell-Boltzmann statistics as:

$$P_i(x_0) = \frac{1}{\sqrt{\pi\frac{2k_BT}{\kappa}}}\exp\left(-\frac{\frac{1}{2}\kappa(x_0-x_n)^2}{k_BT}\right) \tag{S.14}$$

where the subscript *i* at the left-hand side indicates 'initial position' (*i.e.* the particle position prior to the application of perturbation), and κ is the angular trap stiffness at the node position given as:

$$\kappa = -\left.\frac{d\tau}{dx}\right|_{x=x_n} = \left.\frac{d}{dx}\tau_0\sin(2x)\right|_{x=x_n} = 2\tau_0\cos(2x_n) = 2\tau_0\sqrt{1-\left(\frac{\omega}{\omega_c}\right)^2} \tag{S.15}$$

Second, when a perturbation of sufficient amplitude is applied, the position of the birefringent particle can undergo a sudden jump into the proximity of the saddle position, where the dynamics of the birefringent particle are mainly governed by thermal diffusion (see section S.V, below). In this case, the thermally-driven particle may diffuse further away and trigger a torque spike, or alternatively, may diffuse back towards the node position without triggering a torque spike. The precise spike probability can be derived analytically by expanding the equation of motion around the saddle position as:

$$\dot{\xi} = \lambda\xi + F(t) \tag{S.16}$$

where $\xi = x - x_s$ is a small quantity, and $\lambda = 2\sqrt{\omega_c^2 - \omega^2}$.

Following the same approach in ref. 40, we can derive from eq.S.16 the probability that at time *t* the particle still remains in a semi-infinite box $(-\delta,+\infty)$ (a torque spike will be triggered if the particle diffuse out of this semi-infinite box as described in ref. 40) given an initial condition $\xi = \xi_0$, as:

$$G_s(\xi_0,t) = \frac{1}{2}\left[1 + \mathrm{erf}\left(z(\xi_0,t)\right)\right] \tag{S.17}$$

where $z(\xi_0,t)$ is given by:

$$z(\xi_0,t) = \left(\delta + \xi_0 e^{\lambda t}\right)\left[2\frac{k_B T}{\gamma\lambda}\left(e^{2\lambda t} - 1\right)\right]^{-1/2} \tag{S.18}$$

where -δ is the leftmost side of the imaginary box defined as in ref. 40.

Putting this all together, the probability that a torque spike is triggered following a perturbation is given by:

$$P(\phi_P) = \int P_i(x_0)\left[1 - G_s(\xi_0,\tau_p)\right]dx_0 \tag{S.19}$$

$$\xi_0 = x_0 - x_s - \phi_P$$

where x_0 is the initial position of the particle before perturbation, $P_i(x_0)$ is the distribution of x_0 given by eq.S.14, ϕ_P is the perturbation amplitude, and τ_p is the interval between perturbation events. Since in our experimental configuration, $\lambda\tau_p >> 1$ the expression for *z* (eq.S.18) can be simplified to:

$$z(\xi_0,\tau_p) \approx \xi_0\sqrt{\frac{\gamma\lambda}{2k_B T}} = \sqrt{\frac{\tau_0}{k_B T}}\left[1 - \left(\frac{\omega}{\omega_c}\right)^2\right]^{1/4}\left(x_0 - x_s - \phi_P\right) \tag{S.20}$$

Then computing the integral in eq.S.19, the probability that a torque spike is triggered by a given perturbation amplitude can be written as:

$$P(\phi_P) = \frac{1}{2}\left[1 - \mathrm{erf}\left\{-\sqrt{\frac{\tau_0}{2k_B T}}\left[1 - \left(\frac{\omega}{\omega_c}\right)^2\right]^{1/4}\left[\phi_P - \arcsin\left(\frac{\omega}{\omega_c}\right)\right]\right\}\right] \tag{S.21}$$

This is the functional relationship to which the data in fig. 3d (main text) is fitted.

S.III. Phase Locking Under Periodic Perturbations

Forcing an excitable system with a periodic perturbation, as done in fig. 3 (main text), may lead to a complex behaviors including phase locking, quasi-periodicity and deterministic chaos[29]. In particular, regions of different locking ratio between perturbations and excited

spikes are expected when varying both the perturbation amplitude and period. These regions are indicated with the symbol *n:m*, where *n* is the number of excited responses in an interval of time which contains *m* periods of the exciting perturbation. Even richer phenomena may take place in systems that also include stochastic effects[44], such as the micrometer-sized cylinder immersed in fluid under investigation in our experiments.

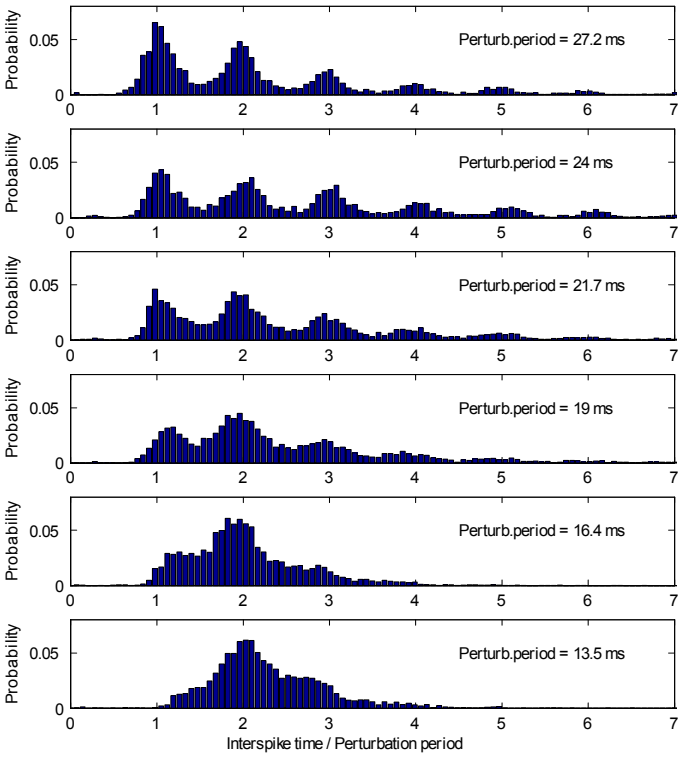

Figure S. I. Probability distribution for the interspike time of events triggered by a periodic external perturbation. The period of the perturbation is indicated in each panel. Different locking ratios, indicated by the peaks at integer multiples of the perturbation period, are visited by the system forced by long perturbation periods. Decreasing the period of the perturbation changes the relative probability, leaving the 2:1 ratio as the most probable at short period. The amplitude of the perturbation is kept fixed at a value (ϕ_P = 0.38 rad) at which the probability to excite one spike with a single perturbation is less than 0.5.

In the experiments described in Fig. 3d of the main text, we probe the driven response of our rotating cylinder at fixed forcing frequency but variable amplitude. Here we find that the spike probability as a function of excitation amplitude follows a sigmoidal response that can

be fit by an analytical expression based on a statistical escape model (section S.II), justified by the long period chosen for the experimental perturbation.

Here, we briefly explore the combined effects of noise and periodic forcing in our system in Fig.S.I, specifically varying the perturbation period. We plot the probability distribution of the measured interspike time under the application of perturbations of decreasing periods when the system is in the excitable regime. The amplitude of the perturbation is kept fixed at a value (ϕ_P = 0.38 rad) at which the probability to excite one spike with a single perturbation is less than 0.5 (compare with Fig. 3d, main text). For relatively long perturbation periods, we observe the presence of multiple peaks in the histograms. Their precise relative amplitudes may warrant further study taking into account both the external periodic forcing and the presence of thermal noise along the lines of studies such as reference 29. However, as the forcing period is gradually reduced, one can observe that the probability distribution shifts, until a forcing period of short enough duration is achieved that the response of the system mostly happens close to the 1:2 locking ratio (bottom panel), indicating that deterministic effects strongly dominate the dynamics.

S.IV. Thermal-Noise-Driven Interspike Time Distribution

Eguia *et al.*[40] have shown that the interspike time distribution (in the high friction approximation, which is also the case in our experiments) can be written as a product of a step-like function and a Kramers exponential decay function (eq.4 in the main text):

$$P(t) = A W_{tr} e^{-Kt} \tag{S.22}$$

where the step-like function W_{tr} describes the transient behavior that the particle undergoes following its injection into the imaginary box, as defined in ref. 40, and prior to reaching a stationary distribution. The expression for W_{tr} is given in ref. 40 as:

$$W_{tr}(x_0,t) = \frac{1}{\sqrt{2\pi\left(\frac{R}{\lambda}\left(1-e^{-2\lambda t}\right)\right)}} \exp\left[-\frac{\left(x_h + x_0 e^{-\lambda t}\right)^2}{2\frac{R}{\lambda}\left(1-e^{-2\lambda t}\right)}\right] \tag{S.23}$$

where all the parameters are defined in ref. 40. However, it is difficult to apply this functional form of W_{tr} directly to the data in fig. 4 (main text), because it has too many free parameters. Fortunately, it is possible to derive an alternative expression for W_{tr} suited to our experimental conditions that includes fewer free parameters and facilitates data fitting, as we now demonstrate.

The maximum value of the step-like function is:

$$W_{tr}(x_0,\infty) = \frac{1}{\sqrt{2\pi\frac{R}{\lambda}}} \exp\left(-\frac{x_h^2}{2\frac{R}{\lambda}}\right) \tag{S.24}$$

allowing us to rescale W_{tr} as:

$$\tilde{W}_{tr}(t) = \frac{W_{tr}(x_0,t)}{W_{tr}(x_0,\infty)} = \frac{1}{\sqrt{1-e^{-2\lambda t}}}\exp\left\{\frac{x_h^2}{2\frac{R}{\lambda}}\left(\left[\left(\frac{x_0}{x_h}\right)^2+1\right]-\frac{\left[\left(\frac{x_0}{x_h}\right)^2+1\right]-2\frac{x_0}{x_h}e^{-\lambda t}}{1-e^{-2\lambda t}}\right)\right\} \quad \text{(S.25)}$$

Since $|x_h| << |x_0|$, especially when the excitable system is close to the critical point (as in our experiments), we have:

$$\tilde{W}_{tr}(t) \approx \frac{1}{\sqrt{1-e^{-2\lambda t}}}\exp\left[-\left(\frac{\lambda x_0^2}{2R}\right)\frac{1}{e^{2\lambda t}-1}\right] \quad \text{(S.26)}$$

which can be further simplified using the midpoint of the step-like function (*i.e.* half height of the step-like function at $t = s$):

$$\tilde{W}_{tr}(s) = \frac{1}{2}. \quad \text{(S.27)}$$

Then we have:

$$\frac{\lambda x_0^2}{2R} = \left(e^{2\lambda s}-1\right)\ln\frac{2e^{\lambda s}}{\sqrt{e^{2\lambda s}-1}} \approx \left(e^{2\lambda s}-1\right)\ln 2 \quad \text{(S.28)}$$

Putting this all together, we have:

$$\tilde{W}_{tr}(t) \approx \frac{1}{\sqrt{1-e^{-2\lambda t}}}\exp\left[-\frac{e^{2\lambda s}-1}{e^{2\lambda t}-1}\ln 2\right] \quad \text{(S.29)}$$

Now there are only two free parameters in the expression for the step-like function.

In the spirit of ref. 40, when the evolution time interval (also called the refractory time t_0) from the saddle point to the next injection point is taken into account, the step-like function can be rewritten approximately as:

$$\begin{cases} \tilde{W}_{tr}(t) \approx \frac{1}{\sqrt{1-e^{-2\lambda(t-t_0)}}}\exp\left[-\frac{e^{2\lambda(s-t_0)}-1}{e^{2\lambda(t-t_0)}-1}\ln 2\right] & \text{if } t \geq t_0 \\ \tilde{W}_{tr}(t) = 0 & \text{if } t < t_0 \end{cases} \quad \text{(S.30)}$$

which is the expression of step-like function employed in the data fitting in fig. 4 (main text).

S.V. The Average Delay Time of Torque Spike Following a Perturbation

As shown in fig.S.II, when subjected to a perturbation of a certain amplitude, the birefringent particle will suddenly jump from its original position around the node point

(region IIB in fig.S.II) into the proximity of the saddle position where the dynamics are dominated by thermal noise (region IIA in fig.S.II). However, if the perturbation amplitude is either too small or too large, the particle may jump into other regions where the thermal noise is not a dominant dynamical factor (region IA and IB in fig.S.II). Below we will derive the expressions for the average delay time between the application of the perturbation and the detection of a torque spike, for different ranges of perturbation amplitudes. The application of the analytical expressions to our experimental data is also shown in fig.S.III.

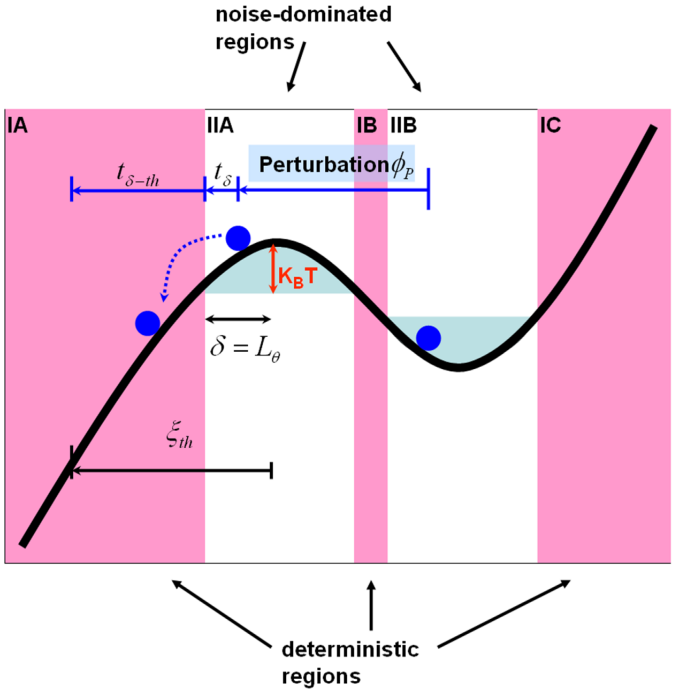

Figure S. II. Evolution of a birefringent particle subject to a perturbation. The thick black sinuous curve represents the potential experienced by a birefringent particle (blue circle). The potential profile can be divided into two types of regions. In regions of Type I (deterministic regions, in pink), the behavior of the particle is basically determined by the potential profile only, while in regions of Type II (noise-dominated regions, in white), the behavior of the particle is dominated by the thermal noise. The boundaries between Type I and Type II regions are approximated by going out by one thermal length L_θ beyond the stable or unstable fixed points. When the system is subjected to a perturbation, the particle may jump from its original position in region IIB to other regions, depending on the amplitude of the perturbation. If the particle jumps into region IIA, it may diffuse (indicated by t_δ) across the boundary ($-\delta$) between region IIA and region IA and evolve into a torque spike, or alternatively the particle may diffuse back towards its original position without triggering any torque spike. The threshold position where a triggered torque spike can be detected is indicated by ξ_{th}. The evolution time from the boundary (δ) between region IIA and IA to the threshold position (ξ_{th}) is indicated by $t_{\delta-th}$.

S.V.1. The Boundaries of the Noise-Dominated Region Around the Saddle Point

Using a rough approximation, we can define the boundaries of the noise-dominated region around the saddle point at the positions of:

$$\left|\xi\right| = \delta = L_\theta \tag{S.31}$$

where $L_\theta = \sqrt{\frac{2k_BT}{\kappa}}$ is called the thermal length. Beyond these boundaries, *e.g.* $\xi < -\delta$ (region IA in fig.S.II), the particle is unlikely to roll back by thermal force because the energy barrier that the particle needs to overcome is larger than thermal energy k_BT. So in region IA (fig.S.II), the particle will evolve deterministically away from the saddle point and trigger a torque spike.

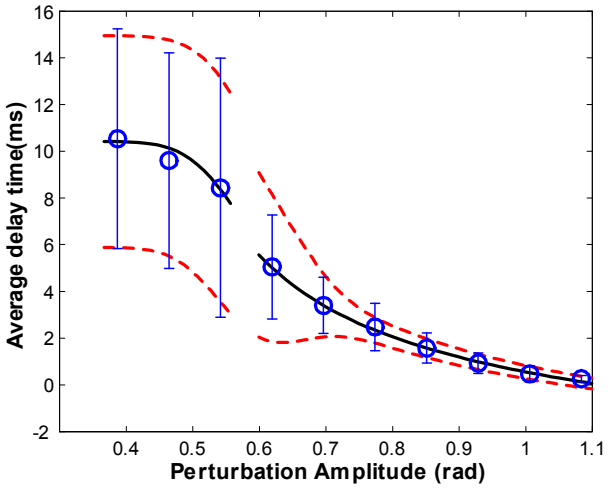

Figure S. III. Average delay time of a torque spike as a function of perturbation amplitude (ϕ_P). The experimental data is shown in blue circles. The error bars (blue) represent one standard deviation in the delay time, as determined from experimental data. The black line is the fit to eq.S.43 (curve at left) and eq.S.35 (curve at right) using λ = 230 Hz, ω/ω_c = 0.8862 and τ_0 = 1150 pN·nm. The envelope (upper and lower red dashed lines) represents the theoretical values of one standard deviation from the mean, calculated using eq.S.51 (curves at left) and eq.S.52 (curves at right) using the same parameters as the black line.

S.V.2. The Average Delay Time for Perturbation Amplitudes $\phi_P > \arccos\left(\frac{\omega}{\omega_c}\right) + L_\theta$

If the particle jumps directly into region IA (fig.S.II) when subjected to the perturbation, the delay time of the deterministic torque spike ($t_{d,d}$, the first subscript *d* indicates 'delay time', and the second subscript *d* indicates 'deterministic') can be derived from eq.S.7 as:

$$t_{d,d} = \frac{1}{\omega_c + \omega}\left[\cot\left(\xi_{th} + \frac{1}{2}\arcsin\left(\frac{\omega}{\omega_c}\right) - \frac{\pi}{4}\right) - \cot\left(\xi_0 + \frac{1}{2}\arcsin\left(\frac{\omega}{\omega_c}\right) - \frac{\pi}{4}\right)\right] \tag{S.32}$$

where $\xi_0 = x_0 - x_s - \phi_P$ is the initial position of the particle right after perturbation and ξ_{th} is the threshold position (the subscripts *th* are short for 'threshold') where a torque spike

can be detected. To analyze our experiments, we set $\xi_{th} = -\frac{1}{2}\arcsin\left(\frac{\omega}{\omega_c}\right)$ for the convenience of data processing and analysis. Then we have:

$$t_{d,d} = \frac{1}{\omega_c + \omega}\left[\cot\left(\frac{\pi}{4} - \frac{1}{2}\arcsin\left(\frac{\omega}{\omega_c}\right) - \xi_0\right) - 1\right] \tag{S.33}$$

From the previous section (section S.II), we know that for a given perturbation amplitude ϕ_P, ξ_0 is not a fixed value; instead, due to thermal broadening of x_0 around the node position, ξ_0 has a distribution given by eq.S.14 as:

$$P_\theta(\xi_0) = \frac{1}{\sqrt{\pi L_\theta^2}}\exp\left[-\frac{\left(\xi_0 - \overline{\xi_0}\right)^2}{L_\theta^2}\right] \tag{S.34}$$

$$\overline{\xi_0} = \arccos\left(\frac{\omega}{\omega_c}\right) - \phi_P$$

When subjected to a perturbation of $\phi_P > \arccos\left(\frac{\omega}{\omega_c}\right) + L_\theta$ (i.e. $\overline{\xi_0} < -\delta$, region IA in fig.S.II), the birefringent particle is much less likely to jump into the noise-dominated region IIA (fig.S.II). In this case, the average delay time $\langle t_d \rangle_{P,b}$ (the first subscript *d* indicates 'delay time', the second subscript *P* indicates an average for a given 'perturbation amplitude' and the last subscript *b* indicates that the perturbation amplitude is 'big', $\phi_P > \arccos\left(\frac{\omega}{\omega_c}\right) + L_\theta$.) between the application of the perturbation and the detection of a torque spike (when the particle evolves to ξ_{th}) is approximately given by:

$$\langle t_d \rangle_{P,b} \approx \int t_{d,d}(\xi_0) P_\theta(\xi_0) d\xi_0$$

$$\langle t_d \rangle_{P,b} \approx \frac{\int_{\overline{\xi_0}-L_\theta}^{\overline{\xi_0}+L_\theta} t_d(\xi_0) d\xi_0}{\int_{\overline{\xi_0}-L_\theta}^{\overline{\xi_0}+L_\theta} d\xi_0} \approx \frac{1}{\omega_c + \omega}\left[\cot\left(\phi_P - \frac{1}{2}\arccos\left(\frac{\omega}{\omega_c}\right) - L_\theta\right) - 1\right] \tag{S.35}$$

This expression is used to fit to the experimental data in fig.SIII (black curves at right).

S.V.3. The Average Delay Time for Perturbation Amplitudes $\arccos\left(\frac{\omega}{\omega_c}\right) - L_\theta < \phi_P < \arccos\left(\frac{\omega}{\omega_c}\right) + L_\theta$

If the particle jumps into the noise-dominated region IIA ($-\delta < \xi_0 < \delta$, fig.S.II) following the perturbation, it may evolve into a torque spike, or alternatively diffuse back into the node position. Events which successfully evolve into torque spikes must first diffuse into

the deterministic region IA (fig.S.II) and then take the deterministic path to ξ_{th}. Thus the delay time ($t_{d,n}$, the first subscript *d* indicates 'delay time', and the second subscript *n* indicates 'noise-dominated') between the application of the perturbation and the detection of a torque spike is given as:

$$t_{d,n} = t_{\delta} + t_{\delta-th}. \tag{S.36}$$

Here $t_{\delta-th}$ which represents the deterministic evolution time from the boundary of region IA ($\xi_0 = -\delta$, fig.S.II) to the threshold position where a torque spike can be detected (ξ_{th}, fig.S.II), can be calculated using eq.S.33 as:

$$t_{\delta-th} = \frac{1}{\omega_c + \omega}\left[\cot\left(\frac{\pi}{4} - \frac{1}{2}\arcsin\left(\frac{\omega}{\omega_c}\right) + \delta\right) - 1\right] \tag{S.37}$$

t_{δ} is the stochastic escape time that the particle evolves out of the noise-dominated region IIA (fig.S.II), which has a distribution that can be derived from eq.S.17 as:

$$P_d(\xi_0, t_{\delta}) = -\frac{d}{dt}G_s(\xi_0, t) = W_{tr}(\xi_0, t_{\delta})\frac{\left(\xi_0 + \delta e^{\lambda t_{\delta}}\right)\lambda}{\left(e^{2\lambda t_{\delta}} - 1\right)} \tag{S.38}$$

where $W_{tr}(\xi_0, t_{\delta})$ is a step-like function given as:

$$W_{tr}(\xi_0, t_{\delta}) = \frac{1}{\sqrt{\pi L_{\theta}^2\left(1 - e^{-2\lambda t_{\delta}}\right)}}\exp\left[-\frac{1}{L_{\theta}^2}\frac{\left(\delta e^{-\lambda t_{\delta}} + \xi_0\right)^2}{\left(1 - e^{-2\lambda t_{\delta}}\right)}\right] \tag{S.39}$$

The midpoint (t_m) of this step-like function can be derived approximately as:

$$t_m \approx \frac{1}{2\lambda}\ln\left(\frac{\delta^2}{(\ln 2)L_{\theta}^2} + 1\right) = \frac{1}{2\lambda}\ln\left(\frac{1}{\ln 2} + 1\right) \tag{S.40}$$

In the spirit of ref. 40, if we further approximate the step-like function by a Heaviside function, then the average escape time <t_{δ}> for a particle that jumps into noise-dominated region following a perturbation.) can be calculated as:

$$\begin{aligned}\langle t_{\delta}\rangle &= \frac{\int t_{\delta} P_d(\xi_0, t_{\delta})dt}{\int P_d(\xi_0, t_{\delta})dt} \\ &\approx \frac{W_{tr}(\xi_0, \infty)\int_{t_m}^{\infty} t_{\delta}\frac{\left(\xi_0 + \delta e^{\lambda t_{\delta}}\right)\lambda}{\left(e^{2\lambda t_{\delta}} - 1\right)}dt}{W_{tr}(\xi_0, \infty)\int_{t_m}^{\infty}\frac{\left(\xi_0 + \delta e^{\lambda t_{\delta}}\right)\lambda}{\left(e^{2\lambda t_{\delta}} - 1\right)}dt} \approx \frac{\int_{t_m}^{\infty} t_{\delta}\frac{e^{\lambda t_{\delta}}}{e^{2\lambda t_{\delta}} - 1}dt}{\int_{t_m}^{\infty}\frac{e^{\lambda t_{\delta}}}{e^{2\lambda t_{\delta}} - 1}dt} \approx t_m + \frac{1}{\lambda}\end{aligned} \tag{S.41}$$

Therefore for a particle that jumps into the noise-dominated region IIA ($-\delta < \xi_0 < \delta$, fig.S.II) following the perturbation, the average delay time <$t_{d,n}$> between the application of the perturbation and the detection of a torque spike is given as:

$$\begin{aligned}\left\langle t_{d,n}\right\rangle &= \left\langle t_{\delta}\right\rangle + t_{\delta-th} \\ &= \frac{1}{2\lambda}\ln\left(\frac{1}{\ln 2}+1\right)+\frac{1}{\lambda}+\frac{1}{\omega_c+\omega}\left[\cot\left(\frac{\pi}{4}-\frac{1}{2}\arcsin\left(\frac{\omega}{\omega_c}\right)+L_\theta\right)-1\right]\end{aligned} \quad \text{(S.42)}$$

As discussed above, due to the thermal broadening of x_0 around the node position (section S.II), for a given perturbation amplitude ϕ_P (and thus given $\overline{\xi_0}$), not all particles can jump into region IIA ($-\delta < \xi_0 < \delta$, fig.S.II). So events that the particle jumps into region IA ($\xi_0 < -\delta$, fig.S.II) should also be taken into account. Using a rough approximation, we can assume all the particles (given $-\delta < \overline{\xi_0} < \delta$) that jumps into the deterministic region IA ($\xi_0 < -\delta$, fig.S.II) have the same characteristic delay time given by $t_{\delta-th}$. Then for the perturbation amplitude range of $\arccos\left(\frac{\omega}{\omega_c}\right)-L_\theta < \phi_P < \arccos\left(\frac{\omega}{\omega_c}\right)+L_\theta$, the average delay time $\left\langle t_d\right\rangle_{P,m}$ (the first subscript *d* indicates 'delay time', the second subscript *P* indicates an average for a given 'perturbation amplitude', and the last subscript *m* indicates that the perturbation amplitude is in the 'medium range') between the application of the perturbation and the detection of a torque spike is given as:

$$\left\langle t_d\right\rangle_{P,m} = \left\langle t_{d,n}\right\rangle - \left\langle t_{\delta}\right\rangle\left(r\left(\phi_P\right)\right) \quad \text{(S.43)}$$

where $r\left(\phi_P\right)$ is the probability that the particle jumps into the region IA ($\xi_0 < -\delta$,fig.S.II) following a perturbation given as:

$$\begin{aligned} r\left(\phi_P\right) &= \int_{-\infty}^{-\delta} P_\theta\left(\xi_0\right)d\xi_0 = \frac{1}{2}\left\{\operatorname{erf}\left[\frac{-\delta-\overline{\xi_0}}{L_\theta}\right]+1\right\} \\ &= \frac{1}{2}\left\{\operatorname{erf}\left[\frac{\phi_P-\arccos\left(\frac{\omega}{\omega_c}\right)-L_\theta}{L_\theta}\right]+1\right\}\end{aligned} \quad \text{(S.44)}$$

This expression for $\left\langle t_d\right\rangle_{P,m}$ (eq.S.43) is used to fit to the experimental data in fig.S.III (black curves at left).

S.V.4. The Average Delay Time for Perturbation Amplitudes $\phi_P < \arccos\left(\frac{\omega}{\omega_c}\right) - L_\theta$

If the perturbation amplitude is too small ($\phi_P < \arccos\left(\frac{\omega}{\omega_c}\right) - L_\theta$), the particle is much more likely to either jump into the deterministic region IB ($\xi_0 > \delta$, fig.S.II), where the particle will evolve deterministically back to the node position without triggering a torque spike, or alternatively, not even jump out of region IIB (fig.S.II), where the particle is originally located. Since the analysis of the delay time of torque spike is only valid for the events that trigger a torque spike, the discussion on this range of perturbation amplitude is not relevant.

S.VI. Standard Deviation in Delay Time of Torque Spike

Using the results in the previous section (section S.V), we can also derive the standard deviation in the delay time of torque spike separately for different ranges of perturbation amplitudes.

S.VI.1. Case: The Particle Jumps into the Deterministic Region IA

If the particle jumps into the deterministic region IA ($\xi_0 < -\delta$, fig.S.II) following a perturbation, the standard deviation in the delay time of torque spike can be derived as:

$$\begin{aligned}\sqrt{\left\langle \left(\delta t_{d,d}\right)^2 \right\rangle} &= \sqrt{\left\langle t_{d,d}^2 \right\rangle - \left\langle t_{d,d} \right\rangle^2} \\ &\approx \frac{1}{\sqrt{2}} \left[\dot{t}_{d,d}\left(\overline{\xi_0}\right) \right] L_\theta = \frac{L_\theta}{\sqrt{2}\left(\omega_c + \omega\right)} \sin^{-2}\left(\phi_P - \frac{1}{2}\arccos\left(\frac{\omega}{\omega_c}\right) \right)\end{aligned} \tag{S.45}$$

where $\left\langle t_{d,d} \right\rangle$ and $\left\langle t_{d,d}^2 \right\rangle$ are approximately given as:

$$\left\langle t_{d,d} \right\rangle = \int t_{d,d}\left(\xi_0\right) P_\theta\left(\xi_0\right) d\xi_0 \approx t_{d,d}\left(\overline{\xi_0}\right) + \frac{1}{4} L_\theta^2 \ddot{t}_{d,d}\left(\overline{\xi_0}\right) \approx \left\langle t_d \right\rangle_{P,b} \tag{S.46}$$

$$\left\langle t_{d,d}^2 \right\rangle = \int t_{d,d}^2\left(\xi_0\right) P_\theta\left(\xi_0\right) d\xi_0 \approx t_{d,d}^2\left(\overline{\xi_0}\right) + \frac{1}{2}\left\{ t_{d,d}\left(\overline{\xi_0}\right) \ddot{t}_{d,d}\left(\overline{\xi_0}\right) + \left[\dot{t}_{d,d}\left(\overline{\xi_0}\right) \right]^2 \right\} L_\theta^2 \tag{S.47}$$

S.VI.2. Case: The Particle Jumps into the Noise-Dominated Region IIA

If the particle jumps into the noise-dominated region IIA ($\left|\xi_0\right| < \delta$, fig.S.II) following a perturbation, the standard deviation in the delay time of torque spike is given as:

$$\sqrt{\left\langle \left(\delta t_{d,n}\right)^2 \right\rangle} = \sqrt{\left\langle \left(\delta t_\delta\right)^2 \right\rangle + \left\langle \left(\delta t_{\delta - th}\right)^2 \right\rangle} \tag{S.48}$$

where $\left\langle \left(\delta t_{\delta-th}\right)^2 \right\rangle$ can be calculated directly from eq.S.45 as:

$$\left\langle \left(\delta t_{\delta-th}\right)^2 \right\rangle \approx \frac{L_\theta}{\sqrt{2}\left(\omega_c+\omega\right)} \sin^{-2}\left(\frac{1}{2}\arccos\left(\frac{\omega}{\omega_c}\right)+L_\theta\right) \tag{S.49}$$

and $\left\langle \left(\delta t_{\delta}\right)^2 \right\rangle$ can be derived approximately as:

$$\left\langle \left(\delta t_{\delta}\right)^2 \right\rangle = \left\langle t_\delta^2 \right\rangle - \left\langle t_\delta \right\rangle^2 \approx \frac{\int_{t_m}^{\infty} t^2 \frac{e^{\lambda t}}{e^{2\lambda t}-1} dt}{\int_{t_m}^{\infty} \frac{e^{\lambda t}}{e^{2\lambda t}-1} dt} - \left(\frac{\int_{t_m}^{\infty} t \frac{e^{\lambda t}}{e^{2\lambda t}-1} dt}{\int_{t_m}^{\infty} \frac{e^{\lambda t}}{e^{2\lambda t}-1} dt}\right)^2 = \frac{1}{\lambda^2} \tag{S.50}$$

S.VI.3. The Standard Deviation in the Delay Time for Perturbation Amplitudes $\arccos\left(\frac{\omega}{\omega_c}\right)-L_\theta < \phi_P < \arccos\left(\frac{\omega}{\omega_c}\right)+L_\theta$

As discussed in previous section (section S.V), in the range of perturbation amplitudes $\arccos\left(\frac{\omega}{\omega_c}\right)-L_\theta < \phi_P < \arccos\left(\frac{\omega}{\omega_c}\right)+L_\theta$ (*i.e.* $-\delta < \overline{\xi_0} < \delta$), the particle still has a certain probability to jump into the deterministic region IA ($\xi_0 < -\delta$, fig.S.II). This probability is given by $r\left(\phi_P\right)$ (eq.S.44). Again, using a rough approximation, we can assume all the events (given $-\delta < \overline{\xi_0} < \delta$) that the particle jumps into region IA ($\xi_0 < -\delta$, fig.S.II) have the same standard deviation in delay time given by $\left\langle \left(\delta t_{\delta-th}\right)^2 \right\rangle$, then the standard deviation in the total delay time $\sqrt{\left\langle \left(\delta t_d\right)^2 \right\rangle_{P,m}}$ (the first subscript *d* indicates 'delay time', the second subscript *P* indicates that the standard deviation is calculated for a given 'perturbation amplitude', and the last subscript *m* indicates that the perturbation amplitude is 'medium': $\arccos\left(\frac{\omega}{\omega_c}\right)-L_\theta < \phi_P < \arccos\left(\frac{\omega}{\omega_c}\right)+L_\theta$) is found as:

$$\sqrt{\left\langle \left(\delta t_d\right)^2 \right\rangle_{P,m}} \approx \sqrt{\left[1-r\left(\phi_P\right)\right]\left\langle \left(\delta t_\delta\right)^2 \right\rangle + \left\langle \left(\delta t_{\delta-th}\right)^2 \right\rangle + r\left(\phi_P\right)\left[1-r\left(\phi_P\right)\right]\left\langle t_\delta \right\rangle^2} \tag{S.51}$$

This expression is used to fit to the experimental data in fig.S.III (red dashed envelope curves at left).

S.VI.4. The Standard Deviation in the Delay Time for Perturbation Amplitudes $\phi_P > \arccos\left(\frac{\omega}{\omega_c}\right)+L_\theta$

Similarly, for a given perturbation amplitude ϕ_P that satisfies $\overline{\xi_0} < -\delta$ (region IA in fig.S.II), the chance that the particle jumps into noise-dominated region IIA (fig.S.II) should

also be taken into account. Then the standard deviation in the total delay time $\sqrt{\left\langle \left(\delta t_d\right)^2 \right\rangle_{P,b}}$ (the first subscript *d* indicates 'delay time', the second subscript *P* indicates that the standard deviation is calculated for a given 'perturbation amplitude', and the last subscript *b* indicates that the perturbation amplitude is 'big': $\phi_P > \arccos\left(\frac{\omega}{\omega_c}\right) + L_\theta$) can be calculated as:

$$\sqrt{\left\langle \left(\delta t_d\right)^2 \right\rangle_{P,b}} \approx \sqrt{\left(1-r(\phi_P)\right)\left\langle \left(\delta t_{d,n}\right)^2 \right\rangle + r(\phi_P)\left\langle \left(\delta t_{d,d}\right)^2 \right\rangle + r(\phi_P)\left(1-r(\phi_P)\right)\left(\left\langle t_{d,d} \right\rangle - \left\langle t_{d,n} \right\rangle\right)^2} \quad \text{(S.52)}$$

This expression is used to fit to the experimental data in fig.S.III (red dashed envelope curves at right).

S.VII. Measurement of the Cylinder's Rotational Drag through Analysis of the Torque Signal

The torque signal of a quartz cylinder in OTW encodes information on the rotational drag (γ) experienced by the cylinder. This allows us to extract γ through analysis of the torque signal, both when $\omega > \omega_c$, and when $\omega < \omega_c$, as demonstrated in fig. 5d in the main text.

When $\omega > \omega_c$, the torque signal appears as (quasi-) periodic spikes. The period of torque spikes is given in eq.S.11, from which we can determine ω_c. Since the maximum torque τ_0 that can be applied can be read off directly from the torque spike as half of the peak-to-peak amplitude, it follows that we can calculate γ using:

$$\gamma = \frac{\tau_0}{\omega_c} = \tau_0 \left(\omega^2 - \frac{\pi^2}{T_{torque}^2}\right)^{-\frac{1}{2}} \quad \text{for } \omega > \omega_c \quad \text{(S.53)}$$

When $\omega < \omega_c$, no spikes appear in the torque signal (except when ω is very close to ω_c, in which case thermal noise can induce torque spikes as shown in fig. 4 in the main text.). In this case, γ can be determined via one of two alternative approaches. One approach is to use the equation: $\gamma = \frac{\tau}{\omega}$, where τ is the measured torque signal. Alternatively, one can employ the relationship $\gamma = \frac{\tau_0}{\omega_c}$, where τ_0 is the maximum torque that can be applied, and ω_c is determined from the variance in (non-spike) torque signal $\left\langle \delta\tau^2 \right\rangle$ as follows:

First $\left\langle \delta\tau^2 \right\rangle$ can be rewritten as:

$$\left\langle \delta\tau^2 \right\rangle = \kappa^2 \left\langle \delta x^2 \right\rangle \quad \text{(S.54)}$$

where $\kappa = 2\tau_0\sqrt{1-\left(\frac{\omega}{\omega_c}\right)^2}$ is the angular trapping stiffness at the node position (x_n), and $\left\langle \delta x^2 \right\rangle$ is the variance in angular displacement around x_n, which can be calculated by partition function theory from eq.S.14 as:

$$\left\langle \delta x^2 \right\rangle = \frac{k_B T}{\kappa} \tag{S.55}$$

Putting this together, we have an expression for ω_c:

$$\frac{\left\langle \delta\tau^2 \right\rangle}{2\tau_0 k_B T} = \sqrt{1-\left(\frac{\omega}{\omega_c}\right)^2} \tag{S.56}$$

and the expression for γ:

$$\gamma = \frac{\tau_0}{\omega_c} = \frac{1}{\omega}\sqrt{\tau_0^2 - \left(\frac{\left\langle \delta\tau^2 \right\rangle}{2k_B T}\right)^2} \quad \text{for } \omega < \omega_c \tag{S.57}$$

7.8 References

10 Neuman, K. C. & Nagy, A. Single-molecule force spectroscopy: Optical tweezers, magnetic tweezers and atomic force microscopy. Nature Methods 5, 491-505 (2008).

11 Bustamante, C., Macosko, J. & Wuite, G. Grabbing the cat by the tail: Manipulating molecules one by one. Nat. Rev. Mol. Cell Biol. 1, 130-136 (2000).

12 Funnell, B. E., Baker, T. A. & Kornberg, A. In vitro assembly of a prepriming complex at the origin of the Escherichia coli chromosome. J. Biol. Chem. 262, 10327-10334 (1987).

13 Liu, L. F. & Wang, J. C. Supercoiling of the DNA template during transcription. Proc. Natl Acad. Sci. USA 84, 7024-7027 (1987).

14 Yoshida, M., Muneyuki, E. & Hisabori, T. ATP synthase, a marvellous rotary engine of the cell. Nat. Rev. Mol. Cell Biol. 2, 669-677 (2001).

15 Sowa, Y. & Berry, R. M. Bacterial flagellar motor. Q. Rev. Biophys. 41, 103-132 (2008).

16 Friese, M. E. J., Nieminen, T. A., Heckenberg, N. & Rubinsztein-Dunlop, H. Optical alignment and spinning of laser-trapped microscopic particles. Nature 394, 348-350 (1998).

17 Forth, S. et al. Abrupt buckling transition observed during the plectoneme formation of individual DNA molecules. Phys. Rev. Lett. 100, 148301 (2008).

18 Bryant, Z. et al. Structural transitions and elasticity from torque measurements on DNA. Nature 424, 338-341 (2003).

19 Celedon, A. et al. Magnetic tweezers measurement of single molecule torque. Nano Lett. 9, 1720-1725 (2009).

20 Lipfert, J., Kerssemakers, J. W. J., Jager, T. & Dekker, N. H. Magnetic torque tweezers: Measuring torsional stiffness in DNA and RecA-DNA filaments. Nature Methods published online doi:10.1038/nmeth.1520, (17 October 2010).

21 La Porta, A. & Wang, M. D. Optical torque wrench: Angular trapping, rotation, and torque detection of quartz microparticles. Phys. Rev. Lett. 92, 190801 (2004).

22 Deufel, C., Forth, S., Simmons, C. R., Dejgosha, S. & Wang, M. D. Nanofabricated quartz cylinders for angular trapping: DNA supercoiling torque detection. Nature Methods 4, 223-225 (2007).

23 Gutierrez-Medina, B., Andreasson, J. O. L., Greenleaf, W. J., La Porta, A. & Block, S. M. An optical apparatus for rotation and trapping. Methods Enzymol. 475, 377-404 (2010).

24 Adler, R. A study of locking phenomena in oscillators. Proc. IRE 34, 351-357 (1946).

25 Izhikevich, E. M. Neural excitability, spiking and bursting. Int. J. Bifurc. Haos 10, 1171-1266 (2000).

26 Hodgkin, A. L., Huxley, A. F. & Katz, B. Measurement of current-voltage relations in the membrane of the giant axon of Loligo. J. Physiol. 116, 424-448 (1952).

27 Rush, A. M. et al. A single sodium channel mutation produces hyper- or hypoexcitability in different types of neurons. Proc. Natl Acad. Sci. USA 103, 8245-8250 (2006).

28 Izhikevich, E. M. Dynamical Systems in Neuroscience (MIT Press, 2006).

29 Feingold, M., Gonzalez, D. L., Piro, O. & Viturro, H. Phase locking, period doubling, and chaotic phenomena in externally driven excitable systems. Phys. Rev. A 37, 4060-4063 (1988).

30 Glass, L., Hunter, P. & McCulloch, A. Theory of Heart: Biomechanics, Biophysics, and Nonlinear Dynamics of Cardiac Function (Springer, 1991).

31 Barland, S., Piro, O., Giudici, M., Tredicce, J. R. & Balle, S. Experimental evidence of van der Pol-Fitzhugh-Nagumo dynamics in semiconductor optical amplifiers. Phys. Rev. E 68, 036209 (2003).

32 Yacomotti, A. M. et al. Interspike time distribution in noise driven excitable systems. Phys. Rev. Lett. 83, 292-295 (1999).

33 Coullet, P., Gilli, J. M., Monticelli, M. & Vandenberghe, N. A damped pendulum forced with a constant torque. Am. J. Phys. 73, 1122-1128 (2005).

34 Epstein, I. R. & Pojman, J. A. An Introduction to Nonlinear Chemical Dynamics: Oscillations, Waves, Patterns, and Chaos (Oxford Univ. Press, 1998).

35 Shelton, W. A., Bonin, K. D. & Walker, T. G. Nonlinear motion of optically torqued nanorods. Phys. Rev. E 71, 036204 (2005).

36 Rothmayer, M., Tierney, D., Frins, E., Dultz, W. & Schmitzer, H. Irregular spin angular momentum transfer from light to small birefringent particles. Phys. Rev. A 80, 043801 (2009).

37 Rodriguez-Otazo, M., Augier-Calderin, A., Galaup, J-P., Lamère, J-F. & Fery-Forgues, S. High rotation speed of single molecular microcrystals in an optical trap with elliptically polarized light. Appl. Opt. 48, 2720-2730 (2009).

38 McNaughton, B. H., Agayan, R. R., Clarke, R., Smith, R. G. & Kopelman, R. Single bacterial cell detection with nonlinear rotational frequency shifts of driven magnetic microspheres. Appl. Phys. Lett. 91, 224105 (2007).

39 Helgesen, G., Pieranski, P. & Skjeltorp, A. T. Nonlinear phenomena in systems of magnetic holes. Phys. Rev. Lett. 64, 1425-1428 (1990).

40 Eguia, M. C. & Mindlin, G. B. Distribution of interspike times in noise-driven excitable systems. Phys. Rev. E 61, 6490-6499 (2000).

41 Leach, J. et al. Comparison of Faxén's correction for a microsphere translating or rotating near a surface. Phys. Rev. E 79, 026301 (2009).

42 Tolić-Norrelykke, S. F. et al. Calibration of optical tweezers with positional detection in the back focal plane. Rev. Sci. Instrum. 77, 103101 (2006).

43 Huang, Z., Pedaci, F., van Oene, M., Wiggin, M., & Dekker, N.H., Electron Beam Fabrication of Micron-Scale Birefringent Quartz Cylinders for Use in Optical Trapping, ACS Nano 5, 1418–1427 (2011).

44 Longtin, A., and Chialvo, D.R., Deterministic and Stochastic resonances for excitable systems. Phys. Rev. Lett. 81, 4012-4015 (1998).

Chapter 8

Miscellany on Flagellar Motor Study in Optical Torque Wrench

Zhuangxiong Huang, Francesco Pedaci, Maarten van Oene, and Nynke H. Dekker

The bacterial flagellar motor, in which torque generation plays a crucial role, is one of the most interesting and most complex molecular machines. We have been developing an optimized Optical Torque Wrench (OTW) to overcome the limitations of the existing techniques used to study flagellar motor. This chapter discusses several topics related to advancing of such technique, namely:

- The development of the appropriate surface treatment for quartz micro-cylinders (Chapter 5) to permit their attachments to a rotating flagellar motor in OTW;

- The development of a theory to describe the rotational kinetics of a birefringent particle attached to an active flagellar motor in OTW;

- A novel fabrication approach to develop micro-fabricated birefringent particle from TiO_2 rutile, which has a birefringence 32 times larger than quartz. This will enlarge the range of rotational frequency in which the flagellar motor can be studied in OTW;

- Additionally, I discuss a possible alternative construction of OTW based on circular polarized light for producing constant torque, and I describe the theoretical background underlying a method for the calibration of such an approach.

8.1 Introduction

Torque generation plays a crucial role in the functioning of bacterial flagellar motor, a rotary motor that is used to rotate a long flagellar filament (for reviews, see [1, 2]). In order to propel themselves forward in a viscous environment, microorganisms such as the bacterium Escherichia coli bundle several co-rotating flagellar filaments into the flagellum, generating nonreversible cork-screw motion that permits propagation in this low Reynolds number environment (Figure 1a) [3]. Interestingly, when one of the filaments in the bundle reverses the direction of its rotary motion, the bundle falls apart and motion ceases, allowing the bacterium to tumble and change its orientation.

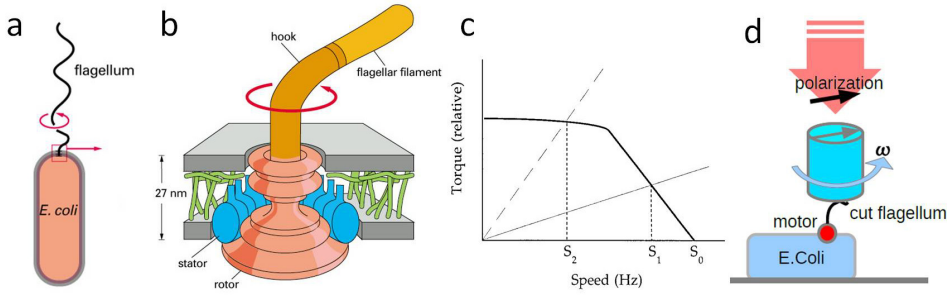

Figure 1. (a) A flagellated bacterium can propel itself in a low-Reynolds number environment through (concerted) rotary motion of filament(s). (b) The motor powering this rotary motion is known as the bacterial flagellar motor. Powered by the flux of protons flowing along a trans-membrane chemical gradient, the motor consists of a stator, a rotor, and a flexible hook. These are joined to a long flagellar filament. (c) A sketch of the torque-speed curve as measured in the first quadrant (positive torque and positive speed). When fully loaded, the motor exerts maximal torque and rotates at low speeds. A torque plateau is observed until a 'knee' indicates a decrease in the torque supplied by the motor (here between S2 and S1). (d) The experimental configuration for investigating the rotary motion of the bacterial flagellar motor using the OTW. An E.coli cell is tethered to a glass surface after its flagellar filaments have been sheared to reduce their length (increasing their effective torsional stiffness). The flagellar filaments, which are hydrophobic, can be tethered to birefringent cylinders whose centered protrusions are made hydrophobic. The cylinders are held in the optical torque wrench (laser beam simply indicated by a red arrow).

The bacterial flagellar motor is one of the most complex molecular machines, exceeding a size of 50 nm (Figure 1b). It consists of a motor unit consisting of a stator and a rotor, a flexible hook (whose compliance has been measured to equal 400 $pN{\cdot}nm{\cdot}rad^{-1}$ [4]), and a long filament with a diameter of approximately 30 nm. While it has been studied using a number of techniques, including structural studies [5] and single-molecule methods [1, 2], the mechanism by which this molecular complex generates torque remains poorly understood.

To understand the mechanism of torque generation, the relationship between the torque generated by the motor and the angular velocity at which it spins (generally referred to as a torque-speed curve) provides crucial insight (Figure 1c) [6]. To vary the speed of the bacterial flagellar motor, two approaches have been employed to date: varying the viscous load, or applying an external torque [2]. Varying the viscous load is possible by tethering differently-

sized beads to cells and observing the ensuing motor speed via optical detection [7]; here, typically the response of many cells is averaged in order to correct for cell-to-cell variations prior to the construction of the torque-speed curve. To avoid said averaging, it is also possible to vary the viscosity once the smallest detectable beads have been attached to the flagellar motor [7]. The most recent iteration of this approach was performed using 60-nm-diameter gold spheres were attached to the hook, thereby reducing the lowest load ever studied by more than two orders of magnitude and observing a rotation speed near 300 Hz [8]. The application of an external torque has been achieved by tethering the flagellar motor itself to a glass surface while using electrodes to polarize and spin the bacterial cell body according to the principle of electrorotation [9, 10], but this method suffers from the need of a special low conductivity medium, from large differences between cells, from a torque that is not constant with angle, and from the lack of a method to directly calibrate the applied torque [11, 12, 13].

We have started to perform experiments with the instrumentation provided by the Optical Torque Wrench (OTW), as it promises numerous advantages. First, use of the OTW provides the ability to more broadly explore the torque-speed curve: for instance, it makes it possible to measure the torque generated by the motor when forced to rotate backwards or forwards faster than its zero-load speed [2]. This is interesting because theoretical models that yield similar predictions for forward rotation under positive torque can diverge under these conditions. Furthermore, the behavior of the motor when forced to counter-rotate (corresponding to the second quadrant in the plot of Figure 1c) may shed light on what happens when a motor in a bundle switches. Second, as torque can be easily varied and readily measured in the OTW (distinguishing it from experiments in which bead size must be varied and from electro-rotation experiments [10], respectively), using this approach should greatly increase the rate at which experiments can be performed, yielding a vastly higher throughput. This allows one to test many mutants and many different conditions. Thirdly, use of the torque wrench will permit us to study the motor's stepping behavior and the switching behavior of flagellar filaments as a function of the external torque.

The layout of this assay is shown in Figure 1d. Here, the laser is shown in red, with its attendant polarization direction indicated by the black arrow. The laser traps a quartz birefringent cylinder shown in blue. The cylinder itself is in turn attached to the flagellar filament, which couples to the flagellar motor attached to a live E. coli cell. The cell itself is firmly anchored to a glass surface.

In the absence of any anchoring of the cylinder to the bacterial cell, and given a rotating laser polarization, the following torque balance applies: $T_{opt} = T_{drag}$. In the presence of anchoring of the cylinder to the bacterial cell, and assuming that the flagellar motor is active, the following torque balance applies: $T_{opt} + T_{motor} = T_{drag}$. Using the readout provided by the OTW, we can vary and read out the optical torque T_{opt}. Furthermore, from this readout we can access the cylinder's orientation with respect to the laser polarization and as such deduce its rotation speed; together with knowledge of the cylinder's geometry, we can compute its rotational drag (which is likely by the largest contribution to the rotational drag) and hence deduce T_{drag}, which in turn yields T_{motor}.

Using the tunability of the OTW (allowing us to vary the effective load $-T_{drag} + T_{opt}$), it should be possible to fully and rapidly reconstruct torque-speed curves, including

measurements of the motor's speed under full load, partial load, zero load, and negative load. Ultimately, in future experiments that are not described in this thesis, it should be possible to vary experimental conditions such as stator number and protonmotive force, and to study a range of rationally designed mutants designed to test models of the motor mechanism. Together, these studies should allow us to unravel the full mechanism underlying the activity of the bacterial flagellar motor.

In this chapter, several efforts that we have made towards the study of bacterial flagellar motor in the OTW will be discussed. First a controlled functionalization of quartz cylinders has been developed for attaching a cylinder to a spinning flagellum, and importantly with the flagellum tethered to the cylinder's center to avoid precession. Second, a theory has been developed to describe the rotational kinetics of a flagellum-tethered cylinder in the OTW. Third, I discuss the development of a novel micro-fabricated birefringent particle made of TiO_2 rutile, which has a birefringence 32 times larger than quartz. This is of interest because it enlarges the range of rotational frequencies over which the flagellar motor can be studied in the OTW. Last, a possible alternative construction of OTW based on circular polarized light for producing constant torque has been considered, and a method for calibration of such construction is also been discussed theoretically.

8.2 Attaching Quartz Cylinders to Spinning Flagella

Our method of attaching a quartz cylinder to a flagellum is based on hydrophobic interaction, *i.e.*, the micro-cylinder is coated on its surface with $C_8H_4C_{l3}F_{13}Si$ vapor ((Tridecafluoro-1,1,2,2-tetrahydrooctyl)trichlorosilane, AB111444, ABCR GmbH & Co. KG), resulting in a hydrophobic coating. This will then bind strongly with a flagellum that is genetically modified to also have a hydrophobic surface [15].

The main challenge in this approach is that the hydrophobic cylinders tend to form clusters due to hydrophobic interactions amongst themselves. One possible strategy to overcome this problem is to coat only a small portion of the cylinder surface, so that the cylinder still appears mainly hydrophilic. Another important concern is the flagellum should be tethered preferably to the cylinder's center to avoid precession. As discussed in Chapter 5, cylinders with centered-protrusions are very suitable for both purposes, as a coating can specifically be applied to the tiny protrusion alone [16].

The general steps of the selective coating protocol are described in Chapter 5 (Fig.2, Steps 11a-13a). After a controlled exposure to O_2 plasma, only the small protrusions are accessible for surface coating, while the remaining portion of cylinder surface is buried in PMMA as protection mask (Chapter 5, Step 11a). For hydrophobic surface coating (Step 12a), the wafer is then placed immediately (within 30 min, otherwise it is necessary to re-activate the quartz surface in O_2 plasma briefly for ~4 s) into a vacuum desiccator, and ~10 µl of fresh $C_8H_4C_{l3}F_{13}Si$ liquid is pipetted into a small open beaker that is placed in the same desiccator. Then, as quickly as possible, the desiccator is sealed and a vacuum pump is switched on to reduce the vapor pressure in the desiccator. The vacuum pumping is kept running for ~10 min until the pressure in the desiccator is reduced to ~1-10 mbar. Then, we close the vacuum

valve and switch off the vacuum pump (also disconnecting it from the desiccators if necessary). At this point, the $C_8H_4C_{l3}F_{13}Si$ liquid will have evaporated, leaving the desiccator full of $C_8H_4C_{l3}F_{13}Si$ vapor that can bind to the quartz surface and render it hydrophobic. The $C_8H_4C_{l3}F_{13}Si$ vapor is kept in the desiccator for about 2 hr (this time-period is necessary for the quartz surface to become very hydrophobic with a contact angle of water > 90º). Following the hydrophobic vapor coating, the wafer is treated with a sonication bath of acetone for 10 min to remove the PMMA coating layer and expose the un-coated quartz surface (Step 13a). At this point, the wafer is ready for microtome shaving to release individual cylinders for use.

The quartz cylinders with selectively-coated protrusions have successfully attached to genetically-modified flagella via hydrophobic interaction. As demonstrated in Figure 2, a flagellum-attached cylinder can be driven by the flagellar motor.

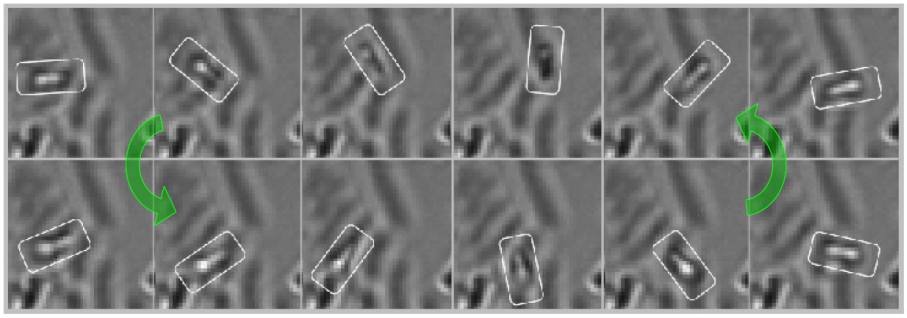

Figure 2. Time-lapse series of images showing a quartz cylinder (in white box) being dragged by a rotating flagellar motor (~ 1Hz). The movie was recorded when the trapping laser was off. The measurement sample was prepared as following: cells were grown in Luria-Bertani medium until the end of exponential phase, harvested by centrifugation and sheared as through gauge 26 needles fifty times to truncate flagella; the cells were then loaded into a polylysine-coated flow-cell (assembled from cleaned cover slips with a parafilm spacer), wait for sedimentation and immobilization; after 20 min, unattached cells were washed away, and a suspension of selectively-coated quartz cylinders was added; after 20 min, unattached quartz cylinders were washed away and the flow-cell sample was ready for optical measurement.

8.3 Kinetics of a Flagellum-Tethered Cylinder in OTW

Using the quartz cylinders with hydrophobic protrusions (detailed in Sec. 8.2), we have been able to study the kinetics of single flagellar motor in OTW. Here we will briefly present the preliminary results of this study, and then focus on a possible theoretical model for understanding these results.

8.3.1. Estimating the Stall Torque of Flagellar Motor

The experimental configuration for the study of the flagellar motor in the OTW is shown in Figure 1d. If the angular trap is strong enough, the motor will be stalled at a fixed laser polarization. In this case, the optical torque that is applied to the tethered cylinder is equal to the stall torque of the motor (but with opposite direction or opposite sign). Therefore, the

readout of the optical torque signal is a direct measurement of the stall torque. Figure 3 (*right*) shows a real-time measurement of the stall torque of an active flagellar motor in the OTW. Note that we observe a stepwise transition of the stall torque (between 2 s and 3 s). It is thought that this might reflect the stator dynamics (*i.e.* the number of active stators associated to the flagellum changes in time, see Ref. [17]). This topic is still under extensive investigation, and will be discussed in more details elsewhere. This chapter we will focus on another interesting observation: as the measured torque increases (in absolute value), the noise in the torque signal decreases (e.g. in Figure 3 (*right*), the noise between 0 s and 2 s is much larger than the noise between 3 s and 4 s). Here I will provide a possible theoretical explanation for this noise increase.

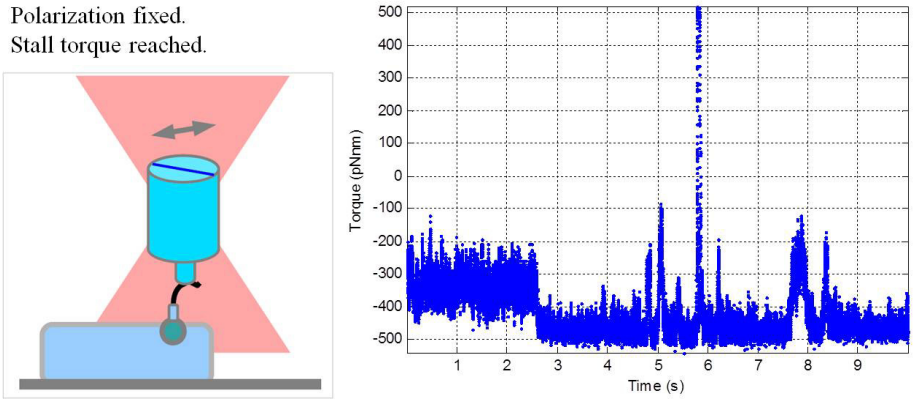

Figure 3. Measurement of stall torque of a bacterial flagellar motor using the OTW. (*Left*) When the laser polarization is fixed, the cylinder held in the optical trap will stall the flagellar motor, and the stall torque of the motor will equal the optical torque applied on the cylinder. Therefore, the stall torque can be measured directly from the optical torque signal (*right*).

In my model, I assume the noise is mainly due to thermal fluctuation of the angular position of the cylinder, which is attached to the flagellum in an ideal geometric configuration (so that the system is symmetric and simple). Mathematically, noise can be quantified by computing the variance in the signal. The variance in torque signal can be further expressed as $\left\langle \delta\tau^2 \right\rangle = \kappa_{opt}^2 \left\langle \delta x^2 \right\rangle$, where κ_{opt} is the optical angular trapping stiffness, x is angle between the laser polarization and the extraordinary axis of the cylinder, and $\left\langle \delta x^2 \right\rangle$ denotes the variance in x. Now I will derive the expressions for κ_{opt} and $\left\langle \delta x^2 \right\rangle$ separately.

The expression for κ_{opt} can be found from its physical definition as $\kappa_{opt} = -(\partial\tau / \partial x)_{eq} = 2\tau_o \cos(2x_{eq})$, where x_{eq} is the equilibrium position of the cylinder at stall torque. The expression of x_{eq} can be further derived by solving the equation

$\tau_{mot} = \tau_{opt}^{eq} = \tau_o \sin(2x_{eq})$ as $x_{eq} = \frac{1}{2}\arcsin(\tau_{mot}/\tau_o)$, where τ_{mot} is the stall torque of the motor, τ_{opt}^{eq} is the optical torque at equilibrium position x_{eq}, and τ_o is the maximum optical torque (which is ~ 2000 pN·nm·rad^{-1}, see Figure 3 *middle*). Pluging the expression of x_{eq} into κ_{opt} we have $\kappa_{opt} = 2\tau_o\sqrt{1-(\tau_{mot}/\tau_o)^2}$.

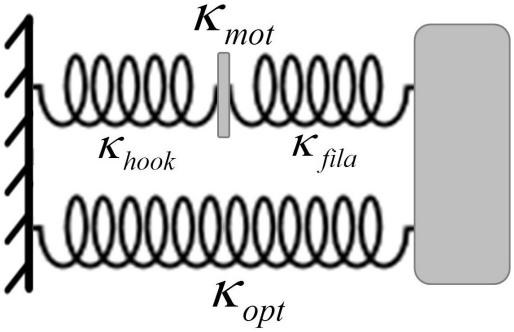

Figure 4. Spring model for a flagellum-tethered birefringent cylinder in OTW. The equivalent spring of the angular trapping of the OTW (represented by κ_{opt} as its spring constant) is connected in parallel with the flagellar motor (κ_{mot}), in which the hook (κ_{hook}) and the flagellar filament (κ_{fila}) in connected in series.

The expression for $\langle \delta x^2 \rangle$ can be given by equipartition theorem as $\langle \delta x^2 \rangle = k_B T / \kappa_{tot}$, where κ_{tot} is the total angular stiffness that the cylinder experiences. As shown in Figure 4, κ_{tot} can be derived from a parallel spring model as $\kappa_{tot} = \kappa_{opt} + \kappa_{mot}$. Note that κ_{mot} is itself the effective angular stiffness of the flagellar motor, given by a series spring model as $1/\kappa_{mot} = 1/\kappa_{fila} + 1/\kappa_{hook}$, where κ_{fila} and κ_{hook} represent the angular stiffness of the flagellar filament and the hook (see Figure 1b and Figure 4), respectively. κ_{fila} can be further expressed as $\kappa_{fila} = B_{fila}/l_{fila}$, where B_{fila} and l_{fila} are the bending stiffness and the length of the filament respectively. B_{fila} can be found in Ref. [161] as ~3.5 pN·μm^2, and l_{fila} is typically only few hundred nanometers in our experiment (the flagellum was pre-cut, see Figure 1d). Therefore, κ_{fila} can be estimated in the order of 10^4 pN·nm·rad^{-1}, which is about one or two orders of magnitude larger than κ_{hook} (measured to be ~ 400 pN·nm·rad^{-1} [4]). Consequently, we can simply ignore the contribution of the flagellar filament, and make the following approximations: $\kappa_{mot} \approx \kappa_{hook}$, and thus $\kappa_{tot} \approx \kappa_{opt} + \kappa_{hook}$.

To sum up, the variance in torque signal can be expressed as a function of κ_{hook} and κ_{opt} according to:

$$\left\langle \delta\tau^2 \right\rangle = k_B T \kappa_{opt} \left(1 + \kappa_{hook} / \kappa_{opt}\right)^{-1} \quad (1)$$

where $\kappa_{opt} = 2\tau_o \sqrt{1 - \left(\tau_{mot} / \tau_o\right)^2}$. Accordingly, when the motor stall torque τ_{mot} increases (in absolute value), this results in a decrease in optical angular trapping stiffness κ_{opt} , and hence a decrease in $\left(1 + \kappa_{hook} / \kappa_{opt}\right)^{-1}$, and ultimately a decrease in $\left\langle \delta\tau^2 \right\rangle$. We can therefore understand the observation from the data in Figure 3 (the noise between 0 s and 2 s is much larger than the noise between 3 s and 4 s).

Interestingly, I note equation 1 can also be used to calculate the angular stiffness of the hook κ_{hook} . A possible procedure to do so is as following: first from the torque trace (as in Figure 3, *right*), calculate κ_{opt} and plot $\left\langle \delta\tau^2 \right\rangle$ as a function of κ_{opt} . Then least-square fit the equation 1 to the $\left\langle \delta\tau^2 \right\rangle$ - κ_{opt} plot, with κ_{hook} as fitting parameter. The best fit result provides the value of κ_{hook} , which was found as 1000±600 pN·nm·rad^{-1} from the single trace of data in Figure 3. Systematic measurement for determining a more accurate value of κ_{hook} is still in progress.

8.3.2. Mapping Flagellar Motor's Torque-Speed Curve by Rotating Laser Polarization

Still in the same experimental configuration (Figure 1d), we rotated the laser polarization and recorded the mean value of the optical torque transferred to the tethered cylinder at different polarization frequencies, as plotted in Figure 5 (*right*). For comparison, the same measurement on an un-tethered cylinder was also plotted in Figure 5 (*left*). The curve for tethered cylinder appears to have the same characteristic shape as that for un-tethered cylinder, but is shifted to the left. Here we will present a theoretical model to explain and quantify this shift.

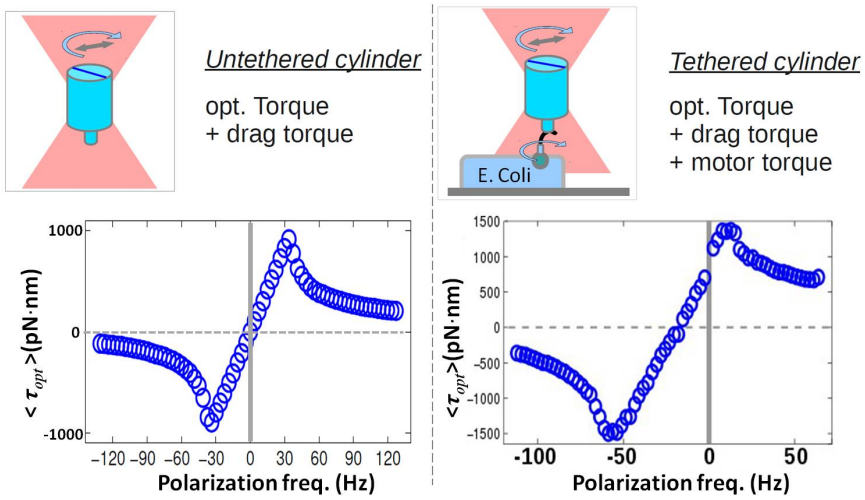

Figure 5. The mean value of the optical torque transferred to a quartz cylinder trapped in OTW as a function of the rotational frequency of laser polarization. (*Left*) the cylinder is un-tethered. (*Right*) the cylinder is tethered to a flagellum filament on an active flagellar motor.

As discussed in Chapter 7, the <Torque> - Polarization frequency relationship for an un-tethered cylinder can be found as a solution to its noise-free equation of motion in OTW:

$$\dot{x} = -\frac{\tau_o}{\gamma}\sin(2x) - \omega \tag{2}$$

where x is the angle between the extraordinary axis of cylinder θ_{cyl} and the laser polarization θ_{pol} given as $x = \theta_{cyl} - \theta_{pol}$, τ_o is the maximum optical torque (positive number in any case), γ is the rotational drag of the cylinder, and ω is the angular frequency ($\omega = 2\pi f$) of the polarization rotation. For the tethered cylinder, the torque generated by the flagellar motor τ_{mot} enters equation 8.2 as:

$$\dot{x} = -\frac{\tau_o}{\gamma}\sin(2x) - \omega + \frac{\tau_{mot}}{\gamma} \tag{3}$$

where we assume that the torque generated by the motor τ_{mot} is approximately constant* over the applied frequency range [2]. Note that in this coordinate system τ_{mot} is a (positive) negative number if the motor intends to rotate (counter-) clockwise. By defining $\omega' = \omega - \tau_{mot} / \gamma$, equation 3 can be rewritten as:

$$\dot{x} = -\frac{\tau_o}{\gamma}\sin(2x) - \omega' \tag{4}$$

which is in exactly the same form as equation 2. Therefore all the expressions derived from equation 2 also holds for equation 3, provided that ω is replaced by ω', or $\omega - \tau_{mot} / \gamma$. In other words, all the plots with ω as horizontal axis will be shifted to the right/left (for positive/negative motor torque) by an amount of τ_{mot} / γ for the case of tethered cylinder. In our experiment, the motor have a negative torque (*i.e.* clockwise), so the curve was shifted to the left (Figure 5, *right*).

As discussed in Chapter 6 (Appendix I, eqs.26 and 29), the mean value of the optical torque $\langle \tau_{opt} \rangle$ applied to an un-tethered cylinder as a function of ω can be approximated as:

$$\langle \tau_{opt} \rangle = \begin{cases} \gamma\left(\omega - \sqrt{\omega^2 - \omega_c^2}\right) & \text{if } \omega > \omega_c \\ \gamma\omega & \text{if } |\omega| < \omega_c \\ \gamma\left(\omega + \sqrt{\omega^2 - \omega_c^2}\right) & \text{if } \omega < -\omega_c \end{cases} \tag{5}$$

where $\omega_c = \tau_o / \gamma$. This is the expression that should describe the data in the plot in the left panel of Figure 5.

Accordingly the expression of $\langle \tau_{opt} \rangle$ on a tethered cylinder can be derived as:

$$\langle \tau_{opt} \rangle = \begin{cases} \gamma\omega - \tau_{mot} - \sqrt{(\gamma\omega - \tau_{mot})^2 - \tau_o^2} & \text{if } \omega > \omega_c + \tau_{mot} / \gamma \\ \gamma\omega - \tau_{mot} & \text{if } -\omega_c + \tau_{mot} / \gamma < \omega < \omega_c + \tau_{mot} / \gamma \\ \gamma\omega - \tau_{mot} + \sqrt{(\gamma\omega - \tau_{mot})^2 - \tau_o^2} & \text{if } \omega < -\omega_c + \tau_{mot} / \gamma \end{cases} \tag{6}$$

This is the expression that describes the data in the plot in the right panel of Figure 5.

* Note that this assumption implies that there is no energy barrier when the motor is forced to rotate in the direction opposite to intended direction. In other words, the motor torque stays approximately the same for both positive and negative frequencies near the zero frequency.

Equation 6 can be further used to derive the expression for the rotational speed of the tethered cylinder (and thus the motor) as:

$$\left\langle \dot{\theta}_{cyl} \right\rangle = \frac{\left\langle \tau_{opt} \right\rangle + \tau_{mot}}{\gamma} = \begin{cases} \omega - \sqrt{\left(\omega - \tau_{mot}/\gamma\right)^2 - \omega_c^2} & \text{if } \omega > \omega_c + \tau_{mot}/\gamma \\ \omega & \text{if } -\omega_c + \tau_{mot}/\gamma < \omega < \omega_c + \tau_{mot}/\gamma \\ \omega + \sqrt{\left(\omega - \tau_{mot}/\gamma\right)^2 - \omega_c^2} & \text{if } \omega < -\omega_c + \tau_{mot}/\gamma \end{cases} \quad (7)$$

One interesting prediction from this expression is that when $\tau_o > \left|\tau_{mot}\right|$, there are two polarization rotation frequencies at which the motor is stalled: at zero, as expected, and at:

$$\omega_{\text{stall}} = -\frac{\tau_o^2 - \tau_{mot}^2}{2\gamma\tau_{mot}} \quad (8)$$

where the negative sign indicates that at this stall frequency, the laser polarization rotates opposite to the motor torque direction. As a result, the motor fluctuates around a fixed position at the same frequency as laser polarization, and does not produce any net rotation. Also, it can be easily proved mathematically that ω_{stall} is always beyond the transition frequency where the maximum (or minimum if $\tau_{mot} > 0$) torque is achieved. In other words, a non-zero stall frequency always exists as long as $\tau_o > \left|\tau_{mot}\right|$. Between the transition frequency and the stall frequency, the motor rotates in the same direction as the polarization, while beyond the stalling torque, the motor rotates in a direction opposite to the polarization rotation, and the motor speed increases towards to τ_{mot}/γ as $\omega \to \infty$.

Another important prediction from this model is the range of motor frequencies that can be probed (ω_{probe}) using this method. This is straightforwardly expressed as:

$$\frac{\left\langle \tau_{opt} \right\rangle_{\min} + \tau_{mot}}{\gamma} < \omega_{\text{probe}} < \frac{\left\langle \tau_{opt} \right\rangle_{\max} + \tau_{mot}}{\gamma} \quad (9)$$

where $\left\langle \tau_{opt} \right\rangle_{\max} = -\left\langle \tau_{opt} \right\rangle_{\min} \approx \tau_o$. Thus, eq.9 can be rewritten as:

$$-\omega_c + \tau_{mot}/\gamma < \omega_{\text{probe}} < \omega_c + \tau_{mot}/\gamma \quad (10)$$

which indicates that the motor torque-speed curve measured using this method will be restricted to a small frequency window of width ω_c/π centered at $\tau_{mot}/2\pi\gamma$. This more or less agrees with our experimental data as shown in Figure 6. In our measurements using quartz cylinder, this frequency window was very small compare to the entire motor torque-speed curve that we wish to measure. Therefore, it is absolutely essential to find a way of increasing ω_c of the birefringent particle, which is the topic of the next section.

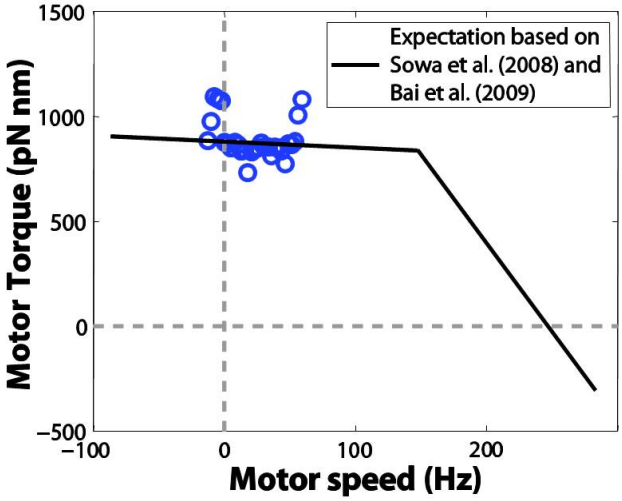

Figure 6. Motor torque-speed relationship (blue circles) calculated from the same data set as in Figure 5 (right panel) using equation 6. Note that here we plot the absolute value of the motor torque (which was clockwise, negative) for convenience of comparison with existing model in literature. The black line sketches an expectation of torque-speed curve extended to the entire range of motor speed [2].

8.4 Fabrication of TiO_2 Particles

As discussed previously, using the OTW to measure the relationship between the torque and spinning speed of a flagellar motor can provide important insights into the mechanism of torque generation by the flagellar motor. Figure 7 summarizes the torque–speed relationship of flagellar motors from different species measured by different methods. As can be seen, to be able to measure the entire spectrum of torque-speed relationship, an OTW should ideally be able to apply torque up to 4000 pN·nm, and the birefringent particle should be able to spin at speeds up to 1000 Hz. In reality, as indicated in Figure 7 (red area), the quartz cylinders we fabricated [16] typically can only apply torque less than 2000 pN·nm and spin at a speed of less than 100 Hz.

The maximum optical torque τ_o that can be applied to a quartz particle is a function of the laser power, the particle size, and its birefringence [18]. And the maximum spinning speed of a birefringent particle in OTW is determined by its critical frequency [18] given as $f_c=\tau_o/2\pi\gamma$, where γ is the rotational drag coefficient. Since γ is also roughly proportional to the particle size and does not depend on laser power or birefringence, this implies that f_c can only be tuned by laser power and/or the birefringence. In other words, increasing the particle size can increase the maximum torque, but basically has no effect on the maximum spinning frequency. In order to increase the maximum spinning speed, one should either increase the laser power, or use a material with a higher birefringence, or both.

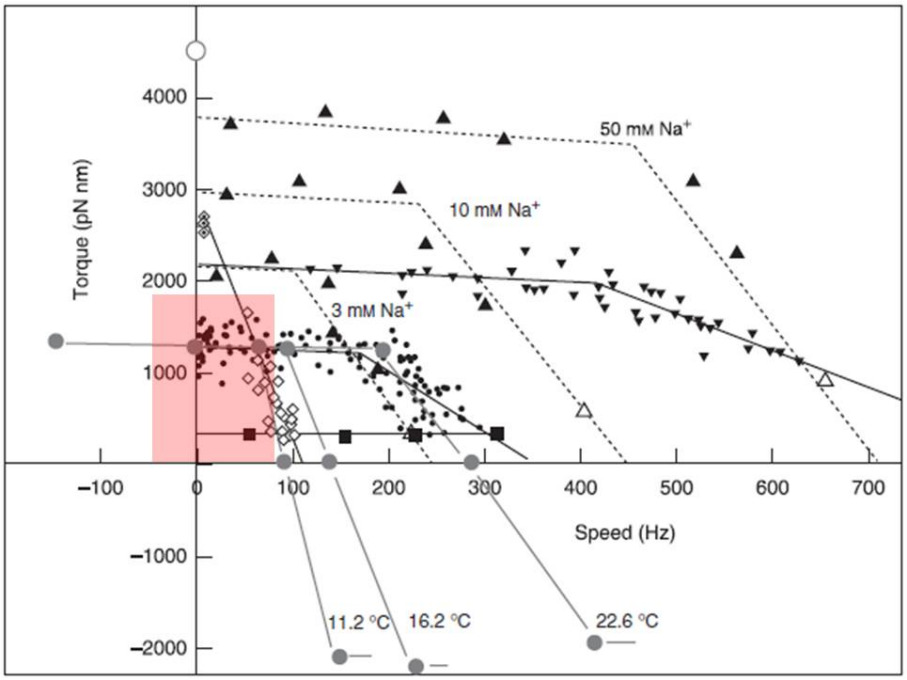

Figure 7. Summary of the measured torque–speed relationship of flagellar motors from different species using different methods (adapted from Ref. [2]). The regime that our quartz cylinders are typically applicable (with oxygen scavenger) is indicated in red.

Though increasing laser power sounds like an easier solution, we find in reality there is a limit to the amount of laser power that can be used. This is because intense illumination will generate a significant amount of reactive oxygen species and other reactive radicals that will quickly damage (known as phototoxicity) the flagellar motor and the bacterium under investigation [19]. Actually, we have applied enzymatic oxygen scavenging system (50 nM protocatechuate dioxygenase and 2.5 mM protocatechuic acid (Sigma-Aldrich), see Ref. [20]) to the flow-cell where the bacteria were immobilized for investigation in OTW, in order to mitigate the phototoxicity. We found that such an oxygen scavenger successfully extended the life-span of flagellar motors in OTW several-fold. However, even with the oxygen scavenger, to maintain a meaningful condition for measurement (life-span of flagellar motors > 0.5 hr), the trapping laser power still has to be maintained lower than 50 mW, which results in a maximum spinning speed of particle typically less than 100 Hz (Figure 7, red area).

Therefore, in order to increase the maximum spinning speed of a birefringent particle, we need to use a material with a much higher birefringence than quartz. We have been exploring the possibility of using single-crystal TiO_2 rutile for this purpose. TiO_2 rutile has a birefringence of +0.287, which is 32 times higher than quartz. In other words, the maximum spinning speed of birefringent particle can be potentially increased by a factor of 32 times using TiO_2 rutile. Equally importantly, controlled fabrication and functionalization of TiO_2

rutile particles is practically possible: first, single-crystal TiO_2 rutile wafer is commercially available (*e.g.* Semiconductor Wafer Inc., Taiwan); second, it has been reported that TiO_2 can be dry-etched in fluorine plasma [21]; and last but not least, TiO_2 surfaces can be functionalized using silanization chemistry, in the same way as quartz surfaces [22].

Here we present the preliminary result of nano-fabrication of TiO_2 rutile particles based on electron-beam lithography, adapted from our previous protocol for quartz cylinder fabrication (Chapter 5).

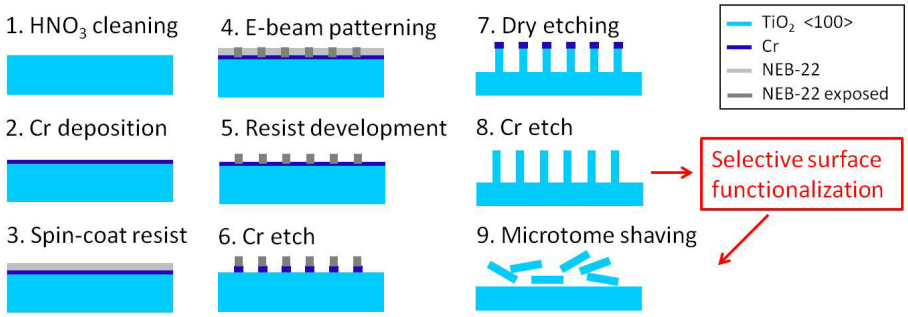

Figure 8. Schematic of the fabrication of TiO_2 particles using electron beam lithography. (Step 1) A single-crystal TiO_2 Rutile wafer is cleaned and prepared for patterning. (Steps 2-6) Pattern Cr hard etch mask using electron beam lithography. (Steps 7-8) Dry etching and formation of the TiO_2 cylinders. (Step 9) Shaving off and collecting of the TiO_2 cylinders.

Fabrication of the TiO_2 particles was performed on 10x10 mm^2 square single-crystal TiO_2 rutile <100> wafers (0.5 mm thickness, one side polished, Supplier: Semiconductor Wafer Inc., Taiwan) and comprised 9 principal steps (Figure 8).

In the first step, the wafers were ultrasonically cleaned in fuming nitric acid (100% HNO_3) for 10 min (Figure 8, Step 1), rinsed in deionized (DI) water and spun dry. Then a 50 nm Cr layer is deposited on the polished side of the wafer (Figure 8, Step 2) using a Temescal FC-2000 evaporation system. The pressure set-point to start evaporation was $2x10^{-6}$ mbar, and the evaporation rate was kept at 1 Å/s. Followed the Cr deposition, a 350-nm layer of NEB-22A2E negative electron-beam resist (Sumitomo Chemical Co.) was spin-coated onto the wafer at 2000 rpm for 55 s and baked for 3 min at 110°C. At this point, the sample is ready for patterning (Figure 8, Step 3).

Feature patterning (Figure 8, Step 4) is performed on a Leica EBPG 5000+ (acceleration voltage 100 kV, aperture 400 µm). The particles were exposed as single pixels, whereby the pixel size was adjusted by defocusing a small electron beam spot to reduce the irregularity of the feature shape. Nominal pixel diameters of 300 nm were achieved by defocusing electron beam spots with currents of 18 nA (corresponding to estimated 14 nm before defocusing). Doses equaled 1300 µC/cm^2 with a 50 nm beam step size (BSS). The beam settling time was set to 10 µs to minimize the overall patterning time (per billion particles, machine time was ~8 h). Particles were arranged in a hexagonal array with pitches of 600 nm, yielding a total of ~0.2 billion particles in an 8x8 mm^2 square area on each wafer.

Following electron beam exposure, the resist was baked at 105 °C for 3 min, and then was developed in Microposit MF322 solution (Rohm and Haas) for 1 min, followed by a 15 s soaking in 1:10 diluted MF322 solution (Figure 8, Step 5). The wafer was then rinsed in DI water and spun dry. Next the patterns in the resist was transferred to the underneath Cr layer by immersing the wafer in Selectipur chromium etchant (BASF) for ~30 s until the Cr in unmasked area is completely etched off (Figure 8, Step 6). Then the wafer was rinsed in DI water and spun dry. Due to the isotropic nature of wet etching, undercutting occurs underneath the mask layer. To minimize the undercutting, Cr etching was stopped as soon as the etching on unmasked area was complete (the process was visually monitored). The resulting Cr mask structures appear as truncated cone shapes with a bottom diameter of ~220 nm (Figure 9a).

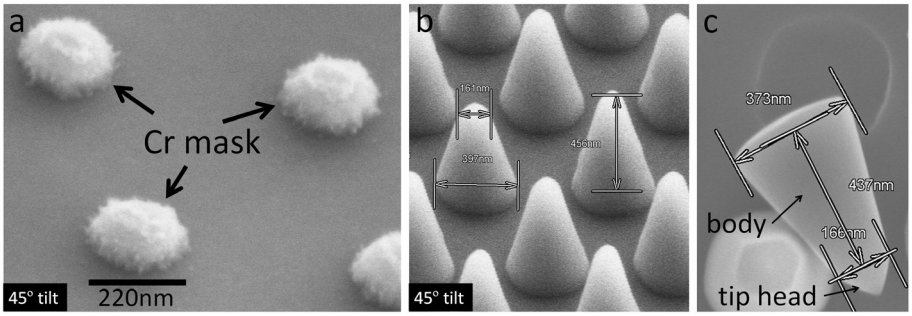

Figure 9. SEM images of Cr masks and fabricated TiO_2 particles. (a) Cr mask structures. The e-beam resist above the Cr structures was removed by oxygen plasma before SEM imaging to avoid confusion. (b) Fabricated TiO_2 conical particles arranged in a hexagonal array pattern on the wafer. (c) A single TiO_2 conical particle released from the wafer by microtome blade shaving (from the same wafer as in (b)). The microtome shaving consistently produces an evenly cut surface at the base of the TiO_2 conical particle. The body of TiO_2 particle was etched using high flow rate of passivation gas (30 sccm CH_4), and the tip head was formed using less passivation gas (15 sccm CH_4).

The wafers were then dry-etched (Figure 8, Step 7) in an inductively-coupled-plasma (ICP) reactive-ion etcher (Adixen AMS100 I-speeder) with a mixture of 15 sccm SF_6 and 30 sccm CH_4. The ICP source power equaled 1500 W and the substrate bias RF power equaled 250 W. The pressure was maintained as low as possible, ~1 Pa. The temperature was maintained at 0 °C for the sample holder and 200 °C for the chamber. Under these settings, the etching rate of TiO_2 was ~70 nm/min, and the etch selectivity of TiO_2 relative to the Cr masks was ~10:1. The resulting TiO_2 particles are quite homogeneous in size, and appear identically as conical shapes with a side-wall angle of ~77° (the particle body, Figure 9b). The side-wall angle could be tuned by changing the flow rate of CH_4, which was added to the etching gas SF_6 to form Teflon-like polymer for side-wall passivation. We made use of this effect, in combination with the effect of mask erosion, to form the tip head structure of the particle (Figure 9b) by a second plasma etching (CH_4 flow was reduced from 30 sccm to 15 sccm, while other settings were remained the same). The tip head is an analogue of center protrusion in quartz cylinder, specifically designed for selective surface functionalization (Chapter 5).

Following the plasma etching, the wafer was immersed in Selectipur chromium etchant (BASF) for ~20 s to remove possible residue of Cr mask (Figure 8, Step 8). At this point the

wafer was ready to proceed with selective surface functionalization, which is now under development (indicated as red box in Figure 8). In the final step of the protocol, the TiO_2 particles were shaved off from the wafer (Figure 8, Step 9) using a clean microtome blade (DT315D50, C. L. Sturkey, Inc.), collected and stored in DI water. Figure 9c shows an example of TiO_2 particle released from the wafer by microtome blade shaving.

The test of fabricated TiO_2 particles in OTW is in progress, and the test results will be reported elsewhere.

8.5 Simplified OTW Applying Constant Torque

In this section, we propose a simplified version of OTW that can in principle also be used for the study of the flagellar motor using birefringent particles. The diagram of the proposed optical setup is shown in Figure 10. Briefly, circularly polarized light is used for the generation of an optical torque [23] on a trapped birefringent particle. Due to torque transfer, the output light of the trap becomes elliptically polarized, with a long axis rotating in phase with the trapped particle (that is, the angle between the long axis of the elliptic output light and the particle's extraordinary axis is fixed at 45°). Therefore, the angular position of the trapped particle can be obtained by detecting the intensity imbalance between the horizontal and vertical projections of the elliptically polarized output. Here we present the theoretical framework for the detection of the trapped particle's angular position, and for calibration of the setup.

The input laser beam of the trap consists of circular-polarized light given as:

$$\vec{E}_{in} = \frac{\sqrt{2}}{2}\begin{pmatrix} \exp\left(i\frac{\pi}{2}\right) \\ 1 \end{pmatrix} E_0 \tag{11}$$

where E_0 is the amplitude of the electric field. Then the output of the trap can be found as:

$$\begin{aligned} \vec{E}_{out} &= \begin{pmatrix} \cos\alpha & -\sin\alpha \\ \sin\alpha & \cos\alpha \end{pmatrix}\begin{pmatrix} \exp\left(i\frac{\phi}{2}\right) & 0 \\ 0 & \exp\left(-i\frac{\phi}{2}\right) \end{pmatrix}\begin{pmatrix} \cos\alpha & \sin\alpha \\ -\sin\alpha & \cos\alpha \end{pmatrix}\vec{E}_{in} \\ &= \frac{\sqrt{2}}{2}\begin{pmatrix} \left(\sin\frac{1}{2}\phi - 2\sin\frac{1}{2}\phi\cos^2\alpha\right) + i\left(\cos\frac{1}{2}\phi + \sin\frac{1}{2}\phi\sin 2\alpha\right) \\ i\left(\sin\frac{1}{2}\phi - 2\sin\frac{1}{2}\phi\cos^2\alpha\right) + \left(\cos\frac{1}{2}\phi - \sin\frac{1}{2}\phi\sin 2\alpha\right) \end{pmatrix} E_0 \end{aligned} \tag{12}$$

where α is the angular position of the particle's extraordinary axis with respect to a laboratory frame of reference, and ϕ is the phase retardation in the birefringent particle given as:

$$\phi = 2\pi\frac{\Delta n h}{\lambda_0} \tag{13}$$

Here h is the length of the birefringent particle, Δn is the degree of birefringence over the particle length, and λ_0 is the wavelength of the light in free space. In this case, the intensity imbalance between the horizontal and vertical projections of the output light is given by:

$$\Delta I = I_x - I_y \propto E_0^2 \sin\phi \sin 2\alpha \tag{14}$$

This is the expression for converting the measured signal (ΔI) into the angular position of the particle (α). In practice, we can record a long trace of ΔI (provided that the particle has rotated at least half a turn) and first determine the amplitude (ΔI_{max}) from the modulation of ΔI. Then, each data point in the trace can be converted into α using

$$\alpha = \frac{1}{2}\arcsin\left(\frac{\Delta I}{\Delta I_{\max}}\right) \tag{15}$$

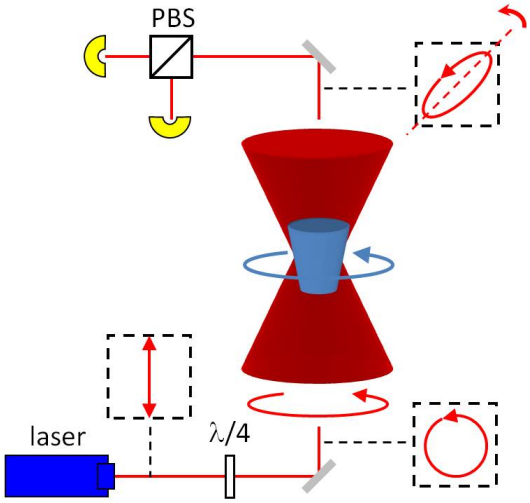

Figure 10. Diagram of the optical setup. A linear-polarized laser beam is converted to a circular polarized light using a quarter wave-plate (λ/4). A birefringent particle (blue) is trapped in the focus spot (red surrounding) of the circular polarized light, which generates a constant torque on the birefringent particle and thus drives the particle to rotate [23]. Due to the torque transfer, the output light of the trap becomes elliptic, with a long axis 45° with respective to the particle's extraordinary axis. The elliptic output is then separated into horizontally and vertically polarized beams using a polarizing beam splitter (PBS). The intensity of the two beams is measured using two identical photo-detectors (yellow). The difference in the intensity between two beams encodes the information of the angular position of the trapped particle.

Once the temporal evolution of the particle's angular position (eq.15) is known, the rotational drag coefficient of the particle (γ) and the optical torque applied (τ_{opt}) can be calibrated. For example, γ can be obtained from the diffusion equation as

$$\frac{k_B T}{\gamma} = D = \frac{\left\langle \alpha^2(t) \right\rangle - \left\langle \alpha(t) \right\rangle^2}{2t} \tag{16}$$

where $\alpha(t)$ is the angular displacement of the particle for a given time period t. Then τ_{opt} is given accordingly as:

$$\tau_{opt} = \gamma \frac{\langle \alpha(t) \rangle}{t} \tag{17}$$

in which the trapped particle is assumed untethered so that the optical torque τ_{opt} equals the drag torque.

Experimental verification of this proposal and the accompanying theory is in progress.

8.6 References

1 Berg, H.C., The rotary motor of bacterial flagella. Annu Rev Biochem, 2003. 72: p. 19-54.

2 Sowa, Y. and R.M. Berry, Bacterial flagellar motor. Q Rev Biophys, 2008. 41(2): p. 103-32.

3 Purcell, E.M., Life at low Reynolds number. American Journal of Physics, 1977. 45(1): p. 3-11.

4 Block, S.M., D.F. Blair, and H.C. Berg, Compliance of bacterial flagella measured with optical tweezers. Nature, 1989. 338(6215): p. 514-8.

5 Lee, L.K., et al., Structure of the torque ring of the flagellar motor and the molecular basis for rotational switching. Nature, 2010. 466(7309): p. 996-1000.

6 Xing, J., et al., Torque-speed relationship of the bacterial flagellar motor. Proc Natl Acad Sci U S A, 2006. 103(5): p. 1260-5.

7 Chen, X. and H.C. Berg, Torque-speed relationship of the flagellar rotary motor of Escherichia coli. Biophys J, 2000. 78(2): p. 1036-41.

8 Yuan, J. and H.C. Berg, Resurrection of the flagellar rotary motor near zero load. Proc Natl Acad Sci U S A, 2008. 105(4): p. 1182-5.

9 Washizu, M., et al., Dielectrophoretic measurement of bacterial motor characteristics. IEEE Transactions on Industry Applications, 1993. 29: p. 286-294.

10 Berg, H.C. and L. Turner, Torque generated by the flagellar motor of Escherichia coli. Biophys J, 1993. 65(5): p. 2201-16.

11 Berry, R.M., L. Turner, and H.C. Berg, Mechanical limits of bacterial flagellar motors probed by electrorotation. Biophys J, 1995. 69(1): p. 280-6.

12 Berry, R.M. and H.C. Berg, Torque generated by the bacterial flagellar motor close to stall. Biophys J, 1996. 71(6): p. 3501-10.

13 Berry, R.M. and H.C. Berg, Torque generated by the flagellar motor of Escherichia coli while driven backward. Biophys J, 1999. 76(1 Pt 1): p. 580-7.

14 Darnton, N.C. and H.C. Berg, Force-Extension Measurements on Bacterial Flagella: Triggering Polymorphic Transformations. Biophys J, 2007. 92:p. 2230 - 2236.

15 Sowa Y., et al., Direct observation of steps in rotation of the bacterial flagellar motor. Nature, 2005. 437: 916-919.

16 Huang, Z., et al., Electron beam fabrication of birefringent microcylinders. ACS Nano, 2011. 5(2): p. 1418-27.

17 Leake M.C., et al., Stoichiometry and turnover in single, functioning membrane protein complexes. Nature, 2006, 443:p.355-358.

18 Pedaci, F., et al., Excitable particles in an optical torque wrench. Nature Physics, 2011. 7: p. 259-264.

19 Neuman, K. C., et al., Characterization of Photodamage to Escherichia coli in Optical Traps. Biophysical Journal, 1999. 77: p. 2856-2863.

20 Aitken, C. E., et al., An Oxygen Scavenging System for Improvement of Dye Stability in Single-Molecule Fluorescence Experiments. Biophysical Journal, 2008. 94: p. 1826-1835.

21 Norasetthekul, S., et al., Dry etch chemistries for TiO2 thin films. Applied Surface Science, 2001. 185: p. 27-33.

22 Ye, L., et al., Biotinylation of TiO2 nanoparticles and their conjugation with streptavidin. Langmuir, 2007, 23 (10), pp 5630–5637

23 Friese, M. E. J., et al., Optical alignment and spinning of laser-trapped microscopic particles. Nature 394, 348-350 (1998).

Summary

Heterogeneity is a general feature in biological system. In order to avoid possible misleading effects of ensemble averaging, and to ensure a correct understanding of the biological system, it is very important to look into individuals, such as a single bio-molecule or a single cell, for details. The size of a single bio-molecule/cell typically ranges from nanometer to micrometer scale. Therefore, the tools for study single-molecule/cell often consist of nano- and micro-features. The power of nanotechnology is such that it is possible to fabricate a wide variety of nano- and micro-scale structures and devices, which find more and more frequent application as powerful tools for biophysical studies of single-molecule/cell.

This thesis reports several nano- and micro-fabricated structures that I, together with my colleagues, have developed for biophysical studies at single-molecule/cell level: (1) Nanofabricated zero-mode waveguides for single-molecule fluorescence experiments at biologically-relevant high concentrations; (2) Microfabricated mirrors for three-dimensional fluorescence imaging and tracking of single molecule / particle; (3) Microfabricated polydimethylsiloxane-based microfluidics device for studying submicron-scale bacteria (4) Microfabricated birefringent cylinders for use in optical torque wrench to study torsional properties of single biomolecules.

Our main interest in zero-mode waveguide lies in its powerful potential to study single telomerase at work by visualizing individual incorporation of dye-labeled nucleotides. We have successfully developed several key fundamental elements towards single-molecule fluorescence studies of telomerase in ZMW: we have designed a biotin-labeled oligonucleotide specifically for human telomerase assay in ZMW - it can be immobilized on the ZMW floor via its biotin group, and it has the highest affinity for base-pairing with telomerase. We have also designed and acquired two types of special modified nucleotides for this assay: fluorescently phospholinked nucleotides (TMR-γ-dATP and Atto532-dG6P), and we have demonstrated that both phospholinked nucleotides can be incorporated processively by human telomerase. We have constructed an optical setup specifically for single-molecule fluorescence studies in ZMWs. This setup can operates in two different modes, namely, massive parallel detection mode (using wide-field illumination and EMCCD detection), and high-speed single spot mode (using focused illumination spot and APD for high speed detection). We have successfully developed methods for nano-fabrication of ZMWs. We have also performed extensive characterizations on our ZMW devices using SEM (device geometric profiles), and FCS (detection volume, fluorophore working concentration). Our characterization results show that we are able to controlledly fabricate ZMWs with a suitable size (*ca.* 80nm in diameter) for single-molecule fluorescent studies at biologically relevant concentration (> 1μM), which is very important for meaningful studies of telomerase kinetics. Finally, we have demonstrated a method for successful surface treatment of ZMWs, by which the DNA substrates can be tethered specifically onto the glass floor of ZMWs, and more

importantly, the non-specific transient adsorption of labeled nucleotides on ZMW surfaces has been reduced to a sufficient low level (one order of magnitude lower than the typical rate of nucleotide incorporation).

Microfabricated mirror is one of the most promising tools for high-precision 3D imaging and particle tracking. We have developed a method based on electron beam lithography and wet etching of single-crystal silicon for the fabrication of V-groove micromirrors. 54.7°-symmetric V-groove micromirror was fabricated using regular (100) silicon wafer. To fabricate a mirror facet 45° relative to wafer surface, an off-axis cut silicon wafer (<100> off 9.7° to <110>) was used. We have demonstrated that our V-groove micromirrors could be assembled into flow cell structures for imaging single fluorescent particles. We have also been developing a novel algorithm based on maximum likelihood estimation (MLE) for 3D tracking of single molecule/particle using micromirrors. Our simulation results demonstrated that our MLE tracking method outperformed center-of-mass tracking method as developed by Berglund *et al.*

The ability to restrict the movement of cells in a controlled manner using microfluidics, allows one to study individual cells and gain added insight into aspects of their physiology and behaviour that can potentially be hidden in ensemble averaging experiments. We have developed a novel protocol based on electron beam lithography together with specific dry etching procedures for the fabrication of a microfluidic device suited to study submicron-sized bacteria. In comparison to approaches based on conventional optical lithography, our method provides greater versatility and control of the dimensions of the growth channels while satisfying the rapid-prototyping needs in a research environment. The widths of the submicron growth channels allow for the potential immobilization and study of different size bacteria with widths ranging from 0.3 μm to 0.8 μm. We verified by means of SEM that these structures are successfully transferred from Si into polydimethylsiloxane (PDMS) as well as from PDMS into PDMS. As a proof-of-principle, we demonstrated that the bacterium L. lactis can successfully be loaded and imaged over a number of generations in this device. Similar devices could potentially be used to study other submicron-sized organisms under conditions where the height and shape of the growth channels are crucial to the experimental design.

The Optical Torque Wrench (OTW) is a special type of optical tweezers (OT) that uses birefringent dielectric particles, and has proved to be one of the most promising tools for torsional manipulation and torque measurement of single biomolecules. The main difference between OTW and conventional OT is that OTW uses a birefringent dielectric particle, which can be rotated by controlling the polarization of trapping laser, and therefore is able to apply and measure torque on the biomolecule attaching to the particle. We describe the use of electron beam lithography for the design, fabrication and functionalization of micron-scale birefringent quartz cylinders. We demonstrate excellent control of the cylinders' geometry, fabricating cylinders with heights of 0.5–2 μm and diameters of 200–500 nm with high precision while maintaining control of their side-wall angle. The flexible fabrication allows cylinders to be selectively shaped into conical structures or to include centered protrusions for the selective attachment of biomolecules. The latter is facilitated by straightforward functionalization targeted either to a cylinder's face or to the centered protrusion alone. The fabricated quartz cylinders are characterized in an optical torque wrench, permitting correlation of their geometrical properties to measured torques. In addition, we tether

individual DNA molecules to the functionalized cylinders and demonstrate the translation and rotational control required for single-molecule studies.

By using micron-scale birefringent particles, OTW has the ability to measure torque of the order of k_BT (~4 pN·nm), which is especially important in the study of biophysical systems at the molecular and cellular level. Quantitative torque measurements rely on an accurate calibration of the instrument. We have described and performed various methods of OTW calibration, some with direct OT analog and others developed specifically for the angular variables. Overall, the different methods lead to close results, which also agree with the theoretical prediction for the particle drag coefficient. However, the absolute values of the variables measured by the instrument should be expected to depend on the details of calibration method chosen.

Motivated by the potential of the OTW to access the fast rotational dynamics of biological systems, a result of its all-optical manipulation and detection, we focus on the angular dynamics of the trapped birefringent particle, demonstrating its excitability in the vicinity of a critical point. This links the optical torque wrench to nonlinear dynamical systems such as neuronal and cardiovascular tissues, nonlinear optics and chemical reactions, all of which display an excitable binary ('all-or-none') response to input perturbations. On the basis of this dynamical feature, we devise and implement a conceptually new sensing technique capable of detecting single perturbation events with high signal-to-noise ratio and continuously adjustable sensitivity.

Last but not least, we describe our efforts towards the study of single bacterial flagellar motor in OTW, which is one of our main interests in developing OTW technology. Bacterial flagellar motor is one of the most interesting and most complex molecular machines. Torque generation plays a crucial role in its functionality. Our progresses towards the study of torque generation in flagellar motor using OTW include: (1) A controlled functionalization of quartz cylinders has been developed for attaching a cylinder to a spinning flagellum, and importantly with the flagellum tethered to the cylinder's center to avoid precession; (2) A theoretical framework has been developed to describe the rotational kinetics of a flagellum-tethered cylinder in the OTW. (3) A novel fabrication approach has been developed for nano-fabrication of birefringent particles using TiO_2 rutile, which has a birefringence 32 times larger than quartz. This will enlarge the range of rotational frequency in which the flagellar motor can be studied in OTW; (4) A possible alternative construction of OTW based on circular polarized light for producing constant torque has been considered, and a method for calibration of such construction is also been discussed theoretically.

Samenvatting

Heterogeniteit is een algemeen verschijnsel in biologische systemen. Om de mogelijk misleidende effecten van middeling op heterogene systemen te ontwijken, waardoor een beter begrip van een biologisch systeem mogelijk is, is het van groot belang om de details van individuele moleculen of cellen te bestuderen. De grootte van een individueel molecuul of een enkele cel varieert in de orde nanometers tot micrometers. Het gereedschap om een individueel molecuul of een enkele cel bevat om deze reden vaak onderdelen op deze lengte-schalen. De kracht van de nanotechnologie ligt in de mogelijkheid om een groot scala aan nanometer- en micrometer-schaal structuren en devices te ontwikkelen. Op dusdanige wijze ontwikkeld gereedschap vindt steeds vaker toepassingen in biofysische studies van individuele moleculen of enkele cellen.

Dit proefschrift beschrijft verschillende structuren op nano- en micrometerschaal die ik, samen met mijn collega's, ontwikkeld heb voor biofysische studies aan individuele moleculen of enkele cellen: (1) optische golfgeleiders (waveguides) op nanometerschaal die het mogelijk maken om fluorescentie experimenten aan enkele moleculen uit te voeren in de aanwezigheid van een hoge achtergrondconcentratie van gelabelde moleculen; (2) optische spiegels op micrometerschaal voor het opnemen van fluorescentie plaatjes in drie dimensies; (3) microfluidische systemen van kanalen die het mogelijk maken om fluorescentie experimenten uit te voeren op de allerkleinste bacteriën; (4) cilinders op microschaal die vervaardigd zijn uit materialen die een dubbele brekingsindex bevatten en het mogelijk maken om de torsionele eigenschappen van individuele biomoleculen in kaart te brengen.

Onze interesse in nanometerschaal zero-mode optische golfgeleiders heeft te maken met de potentie om via deze techniek de werking van het telomerase eiwit te visualiseren. Wij hebben met succes verschillende onderdelen die vereist zijn voor fluorescentie studies op enkel-molecuul niveau van dit eiwit: wij hebben bijvoorbeeld oligonucleotides ontworpen die aan een kant aan de onderkant van de golfgeleider zijn te bevestigen terwijl ze aan te andere kant een hoge affiniteit voor telomerase hebben. We hebben ook twee speciale nucleotides voor dit experiment ontworpen: lichtgeven nucleotides (TMR-γ-dATP en Atto532-dG6P) waarbij het lichtgevende label aan de uiterste fosforgroep is bevestigd. We hebben aangetoond dat deze nucleotides door het telomerase eiwit gebruikt kunnen worden. Vervolgens hebben we een optische opstelling ontwikkeld voor studies op enkel-molecuul niveau in zero-mode optische geleiders. De opstelling kan in een parallelle toestand meerdere geleiders detecteren middels EMCCD camera's maar tevens ook met hoge tijdsresolutie de voortgang in een enkele geleider volgen via fotodetectoren. De zero-mode optische geleiders voor deze opstelling zijn in de cleanroom ontwikkeld en zijn uitgebreid gekarakteriseerd in optische opstelling. Vervolgens is het ons gelukt om de niet-specifieke adsorptie van gelabelde nucleotides in de zero-mode optische geleiders tot een minimum te beperken, een vereiste voor experimenten aan telomerase.

Optische spiegels op micrometerschaal zijn een van de meest veelbelovende technieken voor precisie imaging en deeltjesdetectie in drie dimensies. Om deze spiegels te ontwikkelen hebben we een methode ontwikkeld die gebaseerd is op elektronenbundel lithografie en natte etstechnieken van enkel-kristals silicium. Dit leidt tot V-vormige microspiegels, waarbij de V-hoek verschillende waardes kon aannemen. Wij hebben aangetoond dat de V-vormige microspiegels in een flow-cell gemonteerd konden worden om individuele lichtgevende deeltjes te detecteren. Vervolgens hebben we speciaal voor deze microspiegels nieuwe algoritmes ontwikkeld die gebruik maken van maximum likelihood estimation (MLE) om de positie van de gedetecteerde deeltjes nauwkeurig te bepalen en aangetoond dat onze methodes veel nauwkeuriger zijn die de algoritmes van bijvoorbeeld Berglund et al.

De mogelijkheid om de bewegingen van cellen nauwgezet te beheersen via microfluidische systemen maakt het mogelijk om individuele cellen te bestuderen. We hebben een nieuwe methode ontwikkeld voor het maken van microfluidische kanalen die het mogelijk maken om fluorescentie experimenten uit te voeren op de allerkleinste bacteriën. Deze methode is tevens gebaseerd op elektronenbundel lithografie en maakt gebruik van droge etstechnieken. Vergeleken met technieken die gebruik maken van meer conventionele optische lithografie is onze methode veelzijdiger: de afmetingen van de kanalen kunnen nauwkeuriger gecontroleerd worden maar tevens ook sneller gewijzigd worden. In deze kanalen kunnen bacteriën met afmetingen van 0.3 μm tot 0.8 μm bevestigd worden. Wij hebben eerste experimenten gedaan waarin de kleine bacterie L. lactis over verschillende generaties in ons microfluidische device gevolgd kon worden.

De optische torsiepincet (optical torque wrench, OTW) is een special vorm van een optische pincet die gebruik maakt van microdeeltjes met een dubbele brekingsindex. Dit maakt het mogelijk om met behulp van de pincet torsie uit te oefenen en te meten. Voor gebruik in deze techniek hebben wij elektronenbundel lithografie gebruikt voor het ontwikkelen, maken en coaten van kwartscilinders. Wij kunnen de afmetingen van de microcilinders nauwgezet controleren: het is zelfs mogelijk om in het midden van de cilinder een speciaal bevestigingspunt voor biologische moleculen aan te brengen, zodat alle rotatie langs de optische as van de torsiepincet plaatsvindt. Wij hebben deze deeltjes volledig gekarakteriseerd in de torsiepincet, wat ook heeft geleid tot de ontwikkeling van nieuwe methodes voor de kalibratie van de torsiepincet zelf. Bovendien hebben wij de fysica van de rotatie van een deeltje in de torsiepincet volledig uitgewerkt, ook theoretisch, en aangetoond dat deze overeenkomsten toont met een zogeheten exciteerbaar systeem, een bekend concept uit de niet-lineaire dynamica. Met deze kennis in hand zijn wij niet alleen beter in staat om de rol van draaiing in biologische systemen te begrijpen, zoals wij in het laatste hoofdstuk van dit proefschrift aantonen met studies aan de rotatiemotor die het mogelijk maakt voor bacteriën om te zwemmen, maar tevens tonen wij aan dat ons fysische begrip van de torsiepincet het mogelijk maakt om dit instrument als een omgevingssensor te gebruiken.

Acknowledgements

Hereby, I would like to express my gratitude towards those who helped me make this thesis possible.

Above all, I want to thank my wife Ruyin Lin for her understanding and support all the time.

Then, I want to say this thesis would have not been possible without the guidance and patience of my supervisor Professor Nynke Dekker. I have learned many valuable things from her. For example, she has taught me the art of setting ambitious goals with realistic plans. She has also guided me with a great patience to understand the value of focusing, which I believe I will benefit from for the rest of my life. Moreover, her tremendous passion for her job has greatly inspired me to stay in what I feel passion for. I am happy to say that the big difference between my chaotic nature and her precise character has turned out to be a complementary and productive co-work relationship, as evidenced by this thesis. Last but not least, I would also like to thank her for offering me a position in her group, first as a master student (2006-2007) and later as a PhD student (2007-2011). I very much enjoyed the life in her group, which counts more than 20% of my life so far.

Many of the works presented in this thesis have actually been carried out in cleanroom (Kavli Nanolab). For this, I wish to express my gratitude to the cleanroom supervisor Dr. Emile van der Drift, not only for his hospitality and tolerance – to allow a "mess-maker" like me to play around in his cleanrom, but also for the friendly atmosphere he nurtures in his group, which somehow makes the ugly yellow light very attractive to me. It is always a joyful experience talking to Emile, who always smiles and speaks softly, friendly and wisely.

Besides Nynke and Emile, during my PhD study in BN, I have also greatly benefited from the interactions with other teachers. Professor Cees Dekker has inspired me with enthusiasm and optimism, which has helped me through some difficult times. I have also been inspired by Dr. Juan Keymer and Dr. Christophe Danelon to have fun with tedious routine labwork. Dr. Bertus Beaumont and Dr. Chirlmin Joo have increased my confidence in my cleanroom work and in its potential influence on other fields. Dr. Elio Abbondanzieri and Dr. Anne Meyer set a good example of how to harmoniously balance career and family.

There are many people who have directly contributed to the work presented in this thesis. First and foremost, I would like to thank my best collaborator Francesco Pedaci. By inviting me to join his OTW project, Francesco has helped me through my mid-PhD crisis and got me back on the right track towards this thesis. I deeply appreciate his great listening skill and his willing and patience to understand my arrogance and sometimes nonsense complains, which I believe is the key to our pleasant and successful collaboration. I would also like to thank Maarten van Oene, a quiet, smart and organized guy who could always follow my scattered thoughts, for the fun we had together in OTW project. Ilja Westerlaken, I want to thank her for her continuous patience in explaining bacteria work to me. Charl Moolman, Funny Charl,

I would like to thank him for synchronizing with me so well that I very much enjoy his phone calls at any unreasonable time and on any trivial topic. I hope he also enjoys my random calls during his holiday time as well. David Dulin, Mr. French, another funny person to work with, I very much like his random walk in the lab, and his way of talking. Somehow I quite enjoy his experimental plans, which are resonant very well with my chaotic nature. Jelmer Cnossen, I was very impressed by his critical thinking, which was quite important for Micromirror simulation project. Jacob Kerssemakers, I would like to thank him for his kindly sharing of knowledge and experience, not only in science but also in many aspects of life, which still have been inspiring to me. Yun-Hsuan Chen, a highly self-motivated girl, ZMW project has greatly benefited from her excellent step-by-step execution of experimental plan. Aurélien Crut and Daniel Koster, I want to thank them for the valuable trainings they gave me. Susanne Hage, one of the first persons I met in old MB (early 2006), I would thank her for her constantly making impossible (to me) possible in biolab for ZMW project. Serge Donkers, it's absolutely unbelievable how much noise he could take from me! He is probably the only person on this planet who can actually work together with me in biolab. It is really incredible that after so many messes I made in biolab, he was still happy to help me through and get something useful done! He was the man who kept ZMW project still bio-related, as it should be. Jelle van der Does, he is a role model for me to stay happy, excited and proud of what I think I am capable of. Actually I was indeed very proud that somebody told me I was somehow a cleanroom version of Jelle, or "nano-Jelle". I would like to thank Jelle, and his successor Dimitri de Roos, for all the handy tools they made, which really made life much easier! Jaap Beekman, who has an office I like to visit most often, I want to thank him for his constant patience in helping me to solve all kind of IT problems, and to build all kind of handy stuffs. I have been missing his quick-response support.

There are also many people who have indirect but equally important contributions to the work presented in this thesis. First and foremost, I would like to thank Marc Zuiddam for treating me as a brother (so my name becomes Sjoerd Zuiddam in this case). Indeed we have many things in common: impatient, talking fast, not very precise, and always have crazy ideas about how to torture the AMS Bosch etcher so as to make it useful again. Without his visionary and friendly support, the development of etching recipe for birefringent microcylinder fabrication would have not been possible. I would also like to thank Marco van der Krogt for many things he has helped me with. I am not sure how annoyed he felt about my phone call on Christmas day when he was shopping with his girlfriend. But I deeply appreciated that he still answered to my call and explained every technical details patiently to me as usual. I quite miss the efficiency in the work we did together on his evaporators. I wish to thank Arnold van Run for his always overwhelming information for any question I asked. It turned out to be very useful for optimizing my use of EBPG. Anja van Langen-Suurling, I appreciate her for friendly sharing a lot of critical information about processing of NEB resist, which became fundamental to most of my cleanroom work. Hozan Miro, I want to thank her for teaching me so well to operate SEM, and for her being "strict but not very strict" about my user behaviors. Roel Mattern, I would like to thank him for his advices on all kind of chemicals I dealt with in cleanroom. Those advices were not only necessary to keep me alive and healthy, but also to make me comfortable and feel safe to work in cleanroom. Ewan Hendriks, his importance to me is not only about keeping my beakers clean and supplying

chemicals in time; it is more about keeping the cleanroom noisy and lovely. I greatly appreciate him for talking loud and dirty to me in cleanroom. I could not imagine how much fun would have been lost if there was no such big Sjoerdinator (Sjoerd terminator) shouting in cleanroom. Marco Bakker, I appreciate his technical support during 'evenings' when most people were off the cleanroom.

There are also many people who were much less involved in the work presented to this thesis, while still very important to my PhD life. First, I would like express my gratitude towards my ex-roommates, who were naturally parts of my PhD life. Felix Hol, Holy Hol, I greatly appreciate him for his always honest, straight but not unfriendly comments on whatsoever I was doing or about to do. I personally have benefited a lot from his dare-to-speak nature. Marijn van Loenhout, I want to thank him for sharing his philosophy on career and life, which has still been inspiring to me. Rifka Vlijm, I very much appreciate her for listening to my constant compalins about my mid-PhD crisis. I also wish her all the best for her own PhD work and for the arrival of Hannah's brother/sister. Sriram Krishnan, he was so quiet that I often felt guilty about making noise in the office. I sincerely appreciate his tolerance of my noisy nature.

Next, I would like to give my gratitude to 'corridor' or 'coffee-table' people, who have helped me a lot through my PhD from different aspects. Fabai Wu, we have shared a lot of opinions about academic career and Chinese life in Holland. Marcel Zevenbergen, I would like to thank him for training me in cleanroom. Michiel van den Hout, my 'Big Brother' in Nynke's lab, I want to thank him for his always willing to help with all kind of problems, even if I ask in a very annoying way. Greg Schneider, Mr. Chemistry, I am very happy to know such a smart and knowledgeable chemist. He is basically a Wikipedia of surface chemistry to me. My chemical work has directly benefited from his knowledge. Xander Janssen, Mr. Careful, I have a lot of fun in brainstorming with him about all kind of cleanroom problems, such as my crazy idea about selective functionalization of magnetic particles. Stefan Kowalczyk, I am very happy about our nice collaboration in the teaching of Nynke's optical tweezers course. Gary Skinner, I enjoyed the time playing video game together with him. Besides, the exploration on RNA buckling transition together with Gary and Jan Lipfert was one of my best off-track experiences. Iwijn De Vlaminck, I felt safer and less lonely when I often saw him also working in the lab during weekends. I also greatly appreciate his help with my job interview and many other things. Tim Blosser, I want to thank him for his suggestion on how to reduce dye blinking, which had saved us quite some "try-error" time. Marijn Versteegh, I was very impressed by his strong physics background. I wish him a great success in Nynke lab. Emmylou van Hartrop and Dijana Boric, I would like to thank them for their supports in past few years. They have saved me significant amount of time in figuring out how things should be arranged properly. Ji Li, it is too bad that we don't eat out together as often as before. I greatly appreciate for his being available any time for going to cleanroom together, which was really helpful to speed up my training in cleanroom processing. Rabah Hanfoug, I want to thank him for sharing his abundant experience in cleanroom processing, which greatly accelerated my research progress in cleanroom. Carel Heerkens, although he claimed himself not a nice guy, I am very sure he is. I appreciate his help with the knowledge of plasma dry etching. Vladimir Kutchoukov, Mr. Library, I wish his MEMS Library grows exponentially. Peipei Chen, although her presence in cleanroom brought a lot of fun to us, I still sincerely hope she could stop Bian Tai as soon as possible.

She deserves more beautiful things than the ugly white coat and boring yellow light. C.K. Yang, I want to thank him for kindly sharing his experience in job interview.

Then, I would like to thank my Chinese friends: Xu Qiang, Liu Xinglan, Song Bo, Gao Bo, Xie Hangxing, Chen Ping, Li Zhen, Guo Zhe, Dong Jianfei, Leng Xin, Jia Qi, Qin Yu, Ye Qinghua, Chen Yue, Zuo Kun, and many others for making me feel home in Holland.

Last but not least, I want to give my gratitude to my colleagues in Philips: Ashoka Sathanur, Marc Notten, Ronald van Langevelde, Sandra Spoor, Ke Wang, Alwin Verschueren, Vincent Henneken, Ronald Dekker, Freek Suijver, Johan Marra, Thanh Trung Nguyen, Bo Liu, and many others for their supports on my thesis writing.

Curriculum Vitae

Zhuangxiong Huang

02-05-1982	Born in Raoping, Guangdong, China
1997-2000	Secondary school Guangdong Shantou Jinshan Middle School, China
2000-2004	B.Sc. in Microelectronics, with Honors Nanjing University, China
2004-2005	M.Sc. Candidate in Microelectronics (Major: VLSI Design) Nanjing University, China
2005-2007	M.Sc. in NanoScience, Cum Laude Leiden University & TU Delft, Netherlands
2007	Research Internship in Harvard University, USA
2007-2012	PhD. Candidate in TU Delft, Netherlands under Supervision of Prof. dr. N.H. Dekker
2011- present	Research Scientist, Philips Research Eindhoven, Netherlands

List of Publications

1. M.C. Moolman*, Z. Huang*, S. Tiruvadi Krishnan, and N.H. Dekker, *Electron-beam Fabrication of a Microfluidics Device for Submicron-scale Bacteria,* **Submitted** (2012).
   [*=equal contribution]

2. F. Pedaci*, Z.X. Huang*, M. van Oene, and N.H. Dekker, *Calibration of Optical Torque Wrench*, **Optics Express**, 20, 3787 (2012).
   [*=equal contribution]

3. Z.X. Huang*, F. Pedaci*, M. van Oene, M. Wiggin, and N.H. Dekker, *Electron Beam Fabrication of Birefringent Microcylinders*, **ACS Nano**, 5, 1418 (2011)
   [*=equal contribution]

4. F. Pedaci*, Z.X. Huang*, M. van Oene, S. Barland, and N.H. Dekker, *Excitable Particles in an Optical Torque Wrench*, **Nature Physics**, 7, 259 (2011).
   [*=equal contribution]

5. A. Crut, D.A. Koster, Z.X. Huang, S. Hage, and N.H. Dekker, *Controlling the surface properties of nanostructures for studies of polymerases*, **Nanotechnology**, 19, 465301 (2008).

6. Y. Xu, L. Li, M.L. Gao, Z.X. Huang, and S.G. Yang, *Static Power Mechanism and Low-Power Design Techniques in Nanometer CMOS Circuits*, **Microelectronics & Computer (China)**, 24, 184 (2007). [in Chinese].

7. Y. Xin, Y. Shi, H. Liu, Z. X. Huang, L. Pu, R. Zhang, and Y. D. Zheng, *Effect of NH3 flow rate on growth, structure and luminescence of amorphous silicon nitride films by electron cyclotron resonance plasma*, **Thin Solid Films**, 516, 1130 (2008).

8. Z. X. Huang*, Y. Shi*, Y. Xin, L. Pu, R. Zhang, and Y. D. Zheng, *Generation and amplification of confined acoustic phonons in a quantum wire via the Cerenkov effect*, **Physics Letters A**, 342, 181 (2005).
   [*=Corresponding author]

9. Y. Xin, Z. X. Huang, Y. Shi, L. Pu, R. Zhang, and Y. D. Zheng, *Structural evolution of SiNx films deposited by ECR and its light emission*, **Physica E**, 30, 41(2005).

10. Y. Xin, T. Lu, Z. X. Huang, L. Pu, Y. Shi, Z. Y. Ning, and Y. D Zheng, *Microstructures and optical properties of SiNx*, **Journal of Vacuum Science and Technology (China)**, 25, 36 (2005). [in Chinese]

11. Z. Yang, Y. Shi, J. L. Liu, B. Yan, Z. X. Huang, L. Pu, Y. D. Zheng, and K. L. Wang, *Strain and phonon confinement in self-assembled Ge quantum dot superlattices*, **Chinese Physics Letters (IOP publishing)**, 20, 2001 (2003).

12. H. Zhu, and Z. X. Huang, *Navigation in a small world with local information*, **Physical Review E**, 70, 036117 (2004).
[Selected in **Virtual Journal of Biological Physics Research**, vol. 8, issue 7 (2004)]

13. Z. X. Huang*, X. R. Wang, and H. Zhu*, *Pair correlations in scale-free networks*, **Chinese Physics (IOP publishing)**, 13, 273 (2004).
[*=Corresponding author]

14. Z. X. Huang*, Y. H. Pan, W. Song, and J. Zhou, *Improvement on the shape of light-beat in measurement of tiny displacement by double-grating using laser*, **College Physics (China)**, 23, 59 (2004). [in Chinese].
[*=Corresponding author]